

ABSTRACT

Title of dissertation: MEASURING TOPOLOGY OF BECS
IN A SYNTHETIC DIMENSIONAL LATTICE

Dina Genkina
Doctor of Philosophy, 2019

Dissertation directed by: Professor Ian Spielman
Joint Quantum Institute,
National Institute of Standards and Technology,
and
Department of Physics, University of Maryland

We describe several experiments performed on a two species apparatus capable of producing Bose-Einstein condensates (BECs) of ^{87}Rb and degenerate Fermi gases (DFGs) of ^{40}K .

We first describe computational results for observed optical depths with absorption imaging, in a regime where imaging times are long enough that recoil-induced detuning introduces significant corrections. We report that the observed optical depth depends negligibly on the cloud shape. We also find that the signal-to-noise(SNR) ratio for low atom numbers can be significantly improved by entering this regime and applying the appropriate corrections. We take advantage of this SNR improvement in our subsequent experiment colliding two clouds of ^{40}K for different values of background magnetic field in the vicinity of a Feshbach resonance. We directly imaged the fraction of scattered atoms, which was low and difficult to detect. We used this method to measure the resonance location to be $B_0 = 202.06(15)$

Gauss with width $\Delta = 10.(5)$ Gauss, in good agreement with accepted values.

Next, we describe experiments creating an elongated effectively 2D lattice for a BEC of ^{87}Rb with non-trivial topological structure using the technique of synthetic dimensions. We set up the lattice by applying a 1D optical lattice to the atoms along one direction, and treating the internal spin states of the atoms as lattice sites in the other direction. This synthetic direction is therefore very short, creating a strip geometry. We then induce tunneling along the synthetic direction via Raman coupling, adding a phase term to the tunneling coefficient. This creates an effective magnetic flux through each lattice plaquette, in the Hofstadter regime, where the flux is of order the flux quantum h/e . We detect the resulting eigenstate structure, and observe chiral currents when atom are loaded into the central synthetic site. We further launch analogues of edge magnetoplasmons and image the resulting skipping orbits along each edge of the strip.

We then applied a force along the real dimension of the 2D lattice and directly imaged the resulting motion in the transverse, synthetic, direction. We performed these measurements with 3 and 5-site width lattices along the synthetic direction. We used these measurements to identify the value of the Chern number, the topological invariant in 2D, by leveraging the Diophantine equation derived by Thouless, Kohomoto, Nightingale, and den Nijs. We measure Chern numbers with typical uncertainty of 5%, and show that although band topology is only properly defined in infinite systems, its signatures are striking even in extremely narrow systems.

Measuring topology of BECs in a synthetic dimensions lattice

by

Dina Genkina

Dissertation submitted to the Faculty of the Graduate School of the
University of Maryland, College Park in partial fulfillment
of the requirements for the degree of
Doctor of Philosophy
2019

Advisory Committee:

Professor Ian Spielman, Advisor

Professor Mohammad Hafezi, Dean's representative

Professor Steven Rolston, Chair

Professor Trey Porto

Professor Christopher Lobb

© Copyright by
Dina Genkina
2019

Acknowledgments

This thesis describes work that was carried out by many people, in a way that the multitude of authors on each of the papers only begins to convey. However, as this is the acknowledgement section of *my* thesis, I will endeavor to thank all the people that guided and supported me during my admittedly long tenure as a graduate student.

I would first and foremost like to thank my adviser, Dr. Ian Spielman, for taking a chance on a lab-averse recovering theorist. Ian's mentorship style was always patient and supportive, but without compromising on standards. Ian would never ask 'why isn't this done?', but instead ask 'how are things going this fine morning?' and offer insight and advice regarding whatever I happened to be working on. He was a role model to aspire to, both in his unique combination of intuition and rigor in physics and his unparalleled coffee consumption.

The first 'trial' semester of my lab work was spent in the RbLi lab at UMD. During that time, I am grateful to have learned from Dan Campbell, who voluntarily took on teaching me about the BEC production process one step every day, and Ryan Price, whose magical skills with all equipment and dark humor got me through that time. When I first joined the NIST lab, I had the great fortune of learning from a team of outstanding postdocs—the 'old guard'—consisting of Lindsey LeBlanc, Ross Williams, and Matthew Beeler. I thank them for an excellent introduction to not only laboratory techniques and the physics under study but also the art of working as a team.

An unparalleled debt of gratitude goes to Lauren Aycock, who shared the lab with me from day one and taught me most of what I know being an experimentalist. She endured my clumsiness and obstinance and continued teaching and supporting me throughout my time at NIST. Beyond the lab, she helped teach me how to drive and pushed me to do my first half-marathon. I cannot imagine what my graduate career would have been like without her. I would also like to thank post-docs Ben Stuhl and Hsin-I Lu for the role they played in my physics training. Ben's enthusiasm for electronic design was infectious and it was an honor to learn from him, be it about feedback loops or version control. Hsin-I's unparalleled productivity in her own work didn't stop her from taking lots of time to help me in mine. Her wisdom for knowing what the root of a problem is and how to prioritize tasks was invaluable, and she remains a role model for me today.

I am happy to have had the opportunity to work with several visiting German students: Marcell Gall, Max Schemmer, and Martin Link. Marcell excelled in balancing hard, productive work in the lab with fun in his free time, and was generally a joy to be around. Max jumped into the research with a running start, and it was exciting to see what he accomplished in a short amount of time. Martin (Marcell III) forced me to give up my belief that all crossfitters are annoying. It was a pleasure to work with him as well as to exercise and hang out with him.

My later years in the lab were spent with post-doc Mingwu Lu and fellow grad student Alina Escalera. Mingwu has taught me so much about physics, electronics, western philosophy and wine. I am grateful for having the opportunity to learn from him and get to know him. It has been a pleasure to watch Alina grow in the lab,

and to have her understanding support during the rougher parts of paper and thesis writing. Her tenacity and drive are to be admired. I have had few opportunities to spend time with new lab recruits, post-doc Amilson Fritsch and graduate student Graham Reid, but even from our limited interactions I am confident the lab will be left in good hands.

During the writing of this thesis, I have had amazing help and support from my roommates, fellow students and friends. I would like to thank Ana Valdes-Curiel, Paco Salces-Carcoba, Chris Billington, Kristen Voigt and Jon Hoffman for bravely reading through entire chapters of my thesis when I couldn't bare to even look at it. I am extremely grateful to have been part of the amazing living community that is the international house of physicists (IHOP)—it has felt more like a large family than a housing arrangement. I would like to thank both the current IHOPers, Ana, Paco, Chris and Daniel, and notable past IHOPers, Dimitry Trypogeorgos and Rory Speirs. A special thank you to Ana and Paco for unpromptedly feeding me during the final thesis writing days and to them and Chris for continued moral support. Extra special thank you to Kristen, my oldest graduate school friend, for teaching me how to drive, housing me in my times of need, providing me with thesis writing space and support, feeding me uncountable times, and telling me its okay to take a nap.

I would also like to thank Jenna Beckwith for her help at the beginning of my graduate journey, Taylor Cole for her insightful support in the last year that has allowed me to work on my thesis almost without panic, and Dr. Diane Stabler for her constant presence and support throughout my time here and for offering

deceptively simple advice. I would also like to thank the good people at Eli Lily and Company without whose pioneering research my work would not have been possible.

Above all I would like to thank my family. If it wasn't for my parents' upbringing, graduate school would never have been a possibility for me. I am grateful to them for teaching me all that they have, supporting me throughout my time as a graduate student, but prioritizing my happiness above graduate success. I would like to thank them, my sister Alya, and my brother Pten, for everything.

Table of Contents

Acknowledgements	ii
List of Tables	ix
List of Figures	x
1 Introduction	1
1.1 Condensed matter context	1
1.1.1 Topology	2
1.1.2 Band topology in materials	4
1.1.3 Magnetic field in 2D and the Aharonov-Bohm phase	6
1.1.4 Hofstadter regime	8
1.1.5 Diophantine equation	9
1.2 Ultracold atoms for quantum simulation	11
1.3 Structure of the thesis	13
2 Atom-Light Interactions	14
2.1 Level structure of alkali atoms	14
2.1.1 Fine and hyperfine structure	15
2.1.2 Interaction with static magnetic fields	19
2.2 Near-resonant atom-light interaction	22
2.2.1 Rabi oscillations	22
2.2.2 Scattering	25
2.2.3 Adiabatic rapid passage	26
2.3 Far-off-resonant atom-light interaction	28
2.4 Absorption imaging	29
2.4.1 Time-of-flight and in situ imaging	31
2.5 One-dimensional optical lattices	32
2.5.1 Lattice Hamiltonian	32
2.5.2 Tight-binding approximation	36
2.5.3 Pulsing vs adiabatic loading of the lattice	37
2.6 Raman and rf coupling	41

2.6.1	Rf coupling Hamiltonian	41
2.6.2	Raman coupling Hamiltonian	44
2.6.3	Calibration of Raman and rf dressed states	49
3	Ultracold Gases and the RbK apparatus	53
3.1	Bose-Einstein condensation	53
3.1.1	Phase transition of a non-interacting Bose gas	53
3.1.2	Interacting Bose gas	59
3.2	Degenerate Fermi Gas	61
3.2.1	Fermi statistics and the onset of degeneracy	63
3.2.2	Interactions and Feshbach resonances	65
3.3	RbK apparatus	67
3.3.1	Laser beams	68
3.3.2	Magnetic coils	72
3.3.3	Procedure for making a BEC	73
3.3.4	Changes to apparatus for Rubidium	76
3.3.4.1	Master laser setup	76
3.3.4.2	Alignment imaging path	78
3.3.4.3	FPGA quad servo	82
3.3.4.4	ODT beam shaping	86
3.3.5	Procedure for making a DFG	87
3.3.6	Current status of Potassium apparatus	90
4	Absorption Imaging with Recoil Induced Detuning	97
4.1	Recoil-induced detuning	97
4.2	Perturbative treatment	98
4.3	Stationary atom model	99
4.4	Traveling atom model	104
4.5	Calibration of saturation intensity	105
4.6	SNR optimization	108
5	Imaging of Scattering Near a Feshbach Resonance	111
5.1	Experimental procedure	112
5.2	Data analysis	115
5.3	Results	118
6	Synthetic Magnetic Fields in Synthetic Dimensions	120
6.1	Synthetic dimensions setup	121
6.2	Hamiltonian of the effective 2-D system	124
6.2.1	Hamiltonian	124
6.2.2	Band structure	128
6.2.3	Calibration	131
6.2.4	Tight binding approximation	134
6.3	Eigenstates of the synthetic 2-D lattice	136
6.4	Chiral edge currents	138

6.5	Observation of skipping orbits	141
7	Measuring Chern Number in Synthetic Dimensions	144
7.1	Experimental procedure	145
7.1.1	Loading procedures	147
7.1.2	Application of force and measurement	149
7.1.3	Density reduction	152
7.1.4	Rf correction	153
7.2	Quantum Hall Effect interpretation	155
7.2.1	Microscopic view of QHE	155
7.2.2	Chern number from Hall conductivity	156
7.2.3	Inadequacy for narrow systems	158
7.3	Measuring Chern number via Diophantine equation	160
7.3.1	TKNN Diophantine equation in synthetic dimensions	161
7.3.2	Prescription for identifying Chern number	162
7.3.3	Properties of the method	164
7.4	Results and conclusion	165
A	Brownian motion of solitons in a Bose–Einstein Condensate	168
B	Geometrical pumping with a Bose–Einstein condensate	175
	Bibliography	181

List of Tables

List of Figures

1	Topology of baked goods	3
2	Hall effect setup	7
3	Aharanov-Bohm experiment	7
4	Hofstadter butterfly	10
1	Atomic structure of the ground and first excites states	17
2	Energy structure of hyperfine states of ^{87}Rb and ^{40}K	21
3	Adiabatic rapid passage (ARP)	27
4	Absorption imaging	30
5	Lattice band structure in the extended zone scheme	35
6	Lattice pulsing	39
7	Lattice pulsing for calibration	40
8	Adiabatic lattice loading	42
9	Raman and rf coupling schematic	43
10	Band structure of the rf Hamiltonian	45
11	Band structure of the Raman Hamiltonian	48
12	Pulsing on rf coupling	50
13	Pulsing on Raman coupling	52
1	Occupation of energy states of a 3-D harmonic oscillator	57
2	Time-of-flight images of atoms	58
3	In situ measurement of a fraction of bose condensed atoms	62
4	Occupation number as a function of energy for a Fermi gas	65
5	Schematic of a Feshbach resonance	67
6	Photograph of RbK apparatus at NIST Gaithersburg	69
7	Schematic of RbK apparatus	70
8	Schematic of magnetic coils on the RbK apparatus	72
9	New master board layout	76
10	Schematic of the bottom half of the alignment imaging system	79
11	Schematic of the new imaging lens	80
12	Schematic of the top half of the alignment imaging system	81
13	Turn on and off curves of the quad coils	84
14	Output current as a function of computer command voltage	85

15	Schematic of beam shaping optics in the path of the 0th order ODT beam	86
16	Beam waist as a function of propagation distance	88
17	Schematic of the 2D MOT setup	92
18	Picture of 2D MOT cell	93
19	Schematic of 2D MOT optics	95
20	Picture of current 2D MOT apparatus	96
1	Recoil induced detuning	100
2	Optical depth as a function of probe intensity	102
3	Checking stationary atom assumption	103
4	Phase space evolution of the atomic cloud	106
5	Comparison of stationary and moving atom simulations	107
6	Signal-to-noise optimization	110
1	An sample absorption image after 6.8 ms TOF	115
2	Experimental setup and inverse Abel transform	116
3	Normalized scattered population vs bias field B	119
1	Setup of effective 2-D lattice	123
2	Band structure of the synthetic dimensions Hamiltonian	129
3	Calibration of synthetic dimensions lattice	132
4	Band structure of the tight binding versus full Hamiltonian	135
5	Eigenstates of the synthetic dimensions lattice	137
6	Measuring chiral currents in synthetic dimensions	140
7	Imaging skipping orbits	142
1	Quantum Hall effect in Hofstadter ribbons	146
2	Band structure of the lattice-coupled system in $F = 2$	148
3	Application of a constant force by displacing a Gaussian beam potential	150
4	Band structure in a 5-site wide ribbon	151
5	Correction of oscillations in rf coupled data	154
6	Hall displacement	157
7	Band structure of the synthetic dimesnions lattice with flux $\Phi/\Phi_0 = -4/3$	159
8	Chern number from the TKNN equation	161
9	Calculating Chern number	163
10	Chern number dependence	165
11	Chern number measurement	166

Chapter 1: Introduction

Although quantum mechanics has been well established since the early 20th century, there are still many quantum phenomena that are not well understood and are not easy to calculate. These include high temperature superconductivity [1, 2], fractional quantum Hall physics [3, 4], and ground states of frustrated amorphous materials [5]. One of the reasons these problems are proving elusive is that calculation of properties of many-body quantum mechanical systems is computationally intensive enough to be completely prohibitive in a large class of problems.

Quantum simulation provides an attractive alternative to direct computation. In it, a test quantum system, here ultracold atoms, is used to simulate a more complicated, less experimentally accessible quantum system, such as a non-trivial material from condensed matter physics. In order to get to the point where unsolved problems can be solved with quantum simulation, tools must be built up to create and verify Hamiltonians in the test system that are relevant to the more complex target system. In this thesis, we present a technique for creating topologically non-trivial Hamiltonians for ultracold atoms and experimentally measuring their topological properties.

1.1 Condensed matter context

Topology has been a field of mathematics since the 17th century. Its importance in physics, particularly in the study of crystalline materials in condensed matter, was first discovered by Thouless, Kohmoto, Nightingale and den Nijs [6].

They used topology to explain the shockingly precise quantization of resistivity in the quantum Hall effect. Since then, topology has been central to condensed matter, from topological insulators [7] to fractional quantum hall physics [3]. There have been many excellent pedagogical texts written on this matter. Here, we include only a brief overview of the physics that is relevant for motivating Chapters 6 and 7 of this thesis.

1.1.1 Topology

Topology is the study of how things can be continuously transformed into other things without tearing or gluing parts together. Things that can be continuously transformed into each other under those rules are called homeomorphic to each other. Classes of objects that are all homeomorphic to each other belong to the same topological class. These classes are characterized by a topological invariant, an integer. Surfaces in 3D can be characterized by their genus g , essentially the number of holes in the shape. Since holes cannot be opened up or closed by a continuous transformation, the number of holes is a topological invariant that can be used for classification.

Figure 1.1.1 shows some examples of objects with different genus g . A loaf of bread has no holes, and is therefore topologically equivalent to a sphere, with $g = 0$. A bagel has one hole, and is topologically equivalent to a torus, or a coffee mug, or any other number of things with a single through hole, with $g = 1$. A pretzel has 3 through holes, and is therefore topologically distinct from both the loaf and the bagel, with $g = 3$.

More formally, the Gauss-Bonnet theorem proves the discrete topology of 2D surfaces. It uses the Gaussian curvature, K , defined at every point on the surface. The Gaussian curvature is defined as follows [8]: at any point on the surface, there is a normal vector, perpendicular to that point's tangent plane. The set of planes



Figure 1: Topology of baked goods. They are classified according to genus g , the number of holes. Baking credit: genus 0—Ana Valdes-Curiel, genus 1&3—Whole Foods Market Riverdale.

containing the normal vector are called normal planes. Each normal plane intersects the surface at a curve, with an associated curvature given by the coefficient of the quadratic term in a Taylor expansion of said curve. There is then a normal plane giving the maximal curvature k_{max} and a normal plane giving the minimal curvature k_{min} (if all the curvatures are the same k , as on a sphere, then $k_{max} = k_{min} = k$). The Gaussian curvature is just the product of the two, $K = k_{min}k_{max}$. The Gauss-Bonnet theorem [8] then states that the integral of the Gaussian curvature K over a closed surface S is an integer multiple of 2π :

$$\chi = \frac{1}{2\pi} \int_S K dA, \quad (1.1)$$

where the integer χ is called the Euler characteristic, and is related to the genus via $\chi = 2 - 2g$. Essentially, the total curvature of a closed surface is quantized to integer values, and any closed surface can be classified by that integer. Surfaces with equal χ can be continuously transformed into each other.

1.1.2 Band topology in materials

The same general principles can be applied to the bands within the band structure of a crystalline material [9]. Crystalline materials are characterized by a spatially periodic Hamiltonian. The primitive unit cell, or the minimal repeating unit of the lattice, can be parametrized by primitive unit vectors \vec{a}_i , where i indexes from 1 to the number of dimensions d . In momentum space, the repeating structure is parametrized by reciprocal lattice vectors \vec{K}_i . The eigenstates of are labeled by a momentum k and an energy E , with energies grouped into bands. According to Bloch's theorem [10], the eigenstate wavefunction for some band in a periodic potential in d dimensions can be written as

$$|\Psi(\vec{k})\rangle = e^{i\vec{k}\cdot\vec{r}} |u(\vec{k})\rangle, \quad (1.2)$$

where \vec{k} is the crystal momentum, \vec{r} is the spatial coordinate, and $|u(\vec{k})\rangle$ is periodic with the reciprocal lattice periodicity. Reciprocal lattice space is continuously well defined for an infinite system. In a finite system, the reciprocal space becomes discrete. In the limit where the system is large compared to the primitive unit cell, one can still approximate a sum over k states with an integral for many applications. However, the rigorous theorems of continuous mathematics no longer apply.

There is a phase ambiguity in the definition of the Bloch wavefunction, such that the physics remains invariant under the transformation [9]

$$|u(\vec{k})\rangle \rightarrow e^{i\phi(\vec{k})} |u(\vec{k})\rangle, \quad (1.3)$$

which is reminiscent of gauge invariance in electrostatics. The corresponding gauge-

dependent potential is called the Berry connection \vec{A} , and is given by

$$\vec{A} = -i \langle u(\vec{k}) | \nabla_{\vec{k}} | u(\vec{k}) \rangle. \quad (1.4)$$

Under the transformation eq. 1.3, the Berry connection \vec{A} goes to $\vec{A} + \nabla_{\vec{k}}\phi(\vec{k})$. The gauge invariant field, in 2 dimensions, is given by $\mathcal{F} = \frac{\partial A_y}{\partial k_x} - \frac{\partial A_x}{\partial k_y}$, where \mathcal{F} is known as the Berry curvature.

From this, the geometric phase, or Berry phase γ_c [11], can be defined as the phase acquired over a closed curve c in parameter space that is independent of the rate at which the curve is traversed:

$$\gamma_c = \int_c \vec{A} \cdot d\vec{k} = \int_S \vec{\mathcal{F}} \cdot dS, \quad (1.5)$$

where S is a surface bounded by the curve c , and in the second equality we have invoked Stoke's theorem.

The Berry curvature integrated over the entire Brillouin zone, or primitive cell in reciprocal lattice space, is quantized in units of 2π and in 2D given by:

$$C = \frac{1}{2\pi} \int_{BZ} \mathcal{F} d\vec{k}, \quad (1.6)$$

where C is an integer [12, 13]. This bears a strong similarity to the Gauss-Bonnet theorem, eqn. 1.1, with the Gaussian curvature replaced by the Berry curvature, and the closed surface in real space replaced by the Brillouin zone in momentum space. Similarly, the integer C is a topological invariant and can be used to classify the topological properties of the bands. For periodic structures in 2D, this invariant is called the Chern number.

In finite systems, the transition to momentum space is necessarily discretized. The integral in eqn. 1.5 is no longer continuous, and the identification of the Chern

number can only be made in the continuous limit. In short, the Chern number corresponds to the Chern number of the system in the imaginary scenario where its bulk was extended indefinitely. In finite systems, the edges of the system become important. The edge of the system is an interface between a topologically non-trivial region (the system in question) and a topologically trivial region (the surrounding air or other material). These edges support conducting edge modes. The number of these conducting edge modes is equal to the total Chern number of the filled bands in the bulk. This is known as the bulk-edge correspondence [6, 14], and has been widely used to experimentally detect the effective Chern number.

1.1.3 Magnetic field in 2D and the Aharonov-Bohm phase

Without the constraint of a lattice, the behavior of electrons in a magnetic field is well known. They experience a force $F = -e\vec{v} \times \vec{B}$, where e is the electron charge, \vec{v} is their velocity, and \vec{B} is the magnetic field. If the electrons are confined to a 2D slab, as in the classical Hall effect, and the magnetic field is perpendicular to the slab (see Figure 1.1.3), they perform orbits with frequency $\omega_B = eB/m$. These orbits are called cyclotron orbits, and ω_B is known as the cyclotron frequency. The chirality of the orbits, i.e. whether they are clockwise or counterclockwise, is prescribed by the direction of the magnetic field. If the system is finite, as is the case in all reality, the electrons at the edge of the system will not be able to complete cyclotron orbits. However, the chirality of the orbits must till be preserved, and electrons reflected off the edge will continue semi-orbits in a defined direction along each edge, as shown in Figure 1.1.3. These are known as skipping orbits.

In the same geometry, the presence of an underlying crystal lattice constrains the motion of the electrons. In order to understand the effect of a magnetic field in this case, particularly in the quantum limit, it is useful to think of the field in terms of the Aharonov-Bohm effect. The setup for the Ahoranov-Bohm effect is shown in

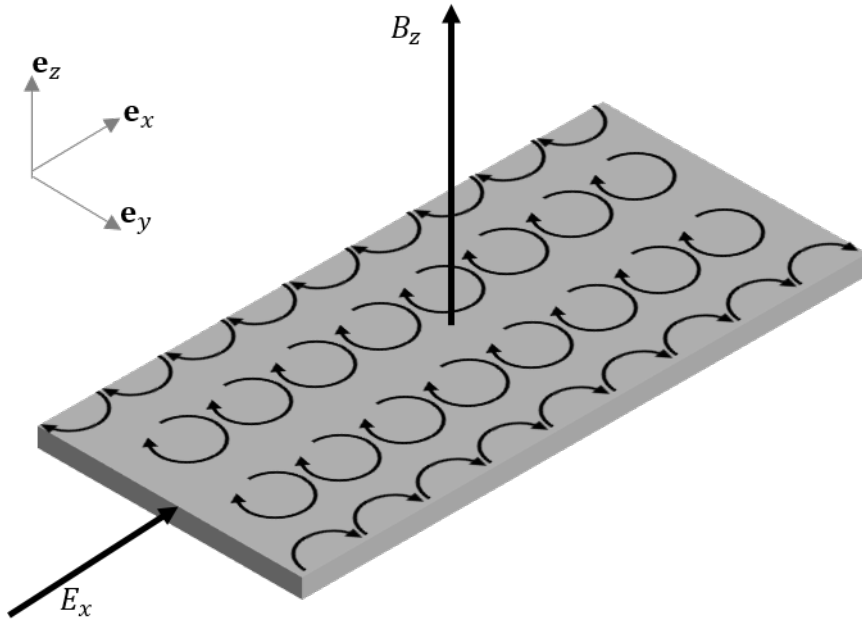


Figure 2: Hall effect setup. A slab of metal very thin along one axis acts as a 2D constraint for the electrons to travel in. A magnetic field normal to the plane pierces the metal. Electrons travel in cyclotron orbits in the bulk and perform skipping orbits along the edges.

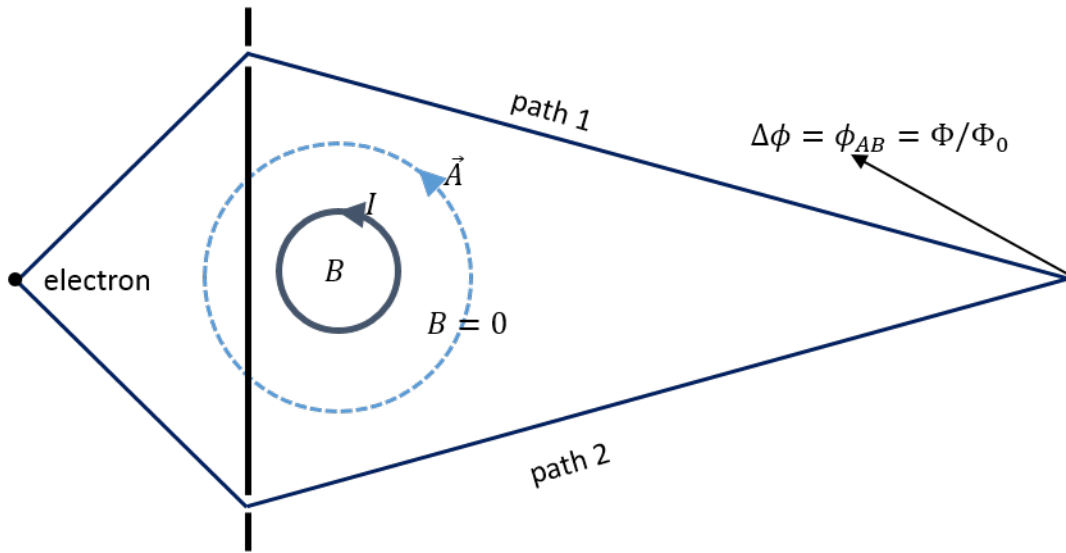


Figure 3: Aharonov-Bohm experiment. An electron is sent through two possible paths around an infinite solenoid with a magnetic field B and corresponding flux Φ going through the solenoid, and no field outside. An interference pattern is observed on the other side, corresponding to a phase difference between the two paths proportional to the enclosed flux.

Figure 1.1.3. There is an infinite solenoid with a current running through it, resulting in a uniform magnetic field $\vec{B} = B_z e_z$ inside the solenoid. Outside the solenoid, the field is zero. However, the vector potential \vec{A} , which defines a magnetic field through $\vec{B} = \vec{\nabla} \times \vec{A}$ can be non-zero, as long as its curl remains zero. In the experiment [15], two electrons were sent around the solenoid, never experiencing a magnetic field. Classically, the electrons should pass unaffected. In reality, though the electron's trajectory was unchanged, the quantum mechanical phase was effected. Two electrons that started out in phase acquired a phase difference $\phi_{AB} = 2\pi\Phi/\Phi_0$, where $\Phi = A \times B_z$ is the flux through the solenoid given by the field B_z times the area inside the solenoid A , and $\Phi_0 = h/e$ is the flux quantum.

For electrons on a 2D lattice, this provides a way to treat interpret a magnetic field quantum mechanically. The smallest unit of the lattice, called a plaquette, will have some magnetic flux through it $\Phi = A \times B_z$. As far as the electron is concerned, which is only constrained to move around the plaquette, it is as if there is an infinite solenoid with magnetic flux Φ through it is piercing the center of the plaquette. Therefore, an electron hopping in a closed loop around the plaquette will acquire a phase $\phi_{AB} = 2\pi\Phi/\Phi_0$. We will use this treatment in the next section.

1.1.4 Hofstadter regime

The Hofstadter regime [16] for 2D electrons in a magnetic field occurs when the magnetic flux per individual lattice plaquette is a non-negligible fraction of a flux quantum. This regime is hard to reach experimentally, since the typical plaquette size in crystalline material is of order a square Angstrom, and the magnetic field necessary to thread a magnetic flux of Φ_0 through such a narrow area is of order $\approx 10^4$ Tesla, not accessible with current technology. Several platforms have however reached the Hofstadter regime by engineering systems with large effective plaquette size in engineered materials [17, 18].

For a square lattice with sites along e_x labeled by index j and sites along e_y labeled by k , in the tight binding limit, the Harper-Hofstadter Hamiltonian can be written in the Landau gauge as

$$H = - \sum_{j,k} t_x e^{i\phi_{AB} k} |j+1, k\rangle \langle j, k| + t_y |j, k+1\rangle \langle j, k| + h.c., \quad (1.7)$$

where t_x and t_y are the tunneling amplitudes along e_x and e_y , and h.c. is the Hermitian conjugate. Here, we have labeled the states by site indexes along both directions $|j, k\rangle$ and included only nearest neighbor tunneling. The choice of Landau gauge is here represented by the phase factor $e^{i\phi_{AB} k}$ being only on the tunneling term along e_x .

This Hamiltonian can be solved to find its eigenenergies for a range of phases ϕ_{AB} , and therefore different fluxes per lattice plaquette Φ/Φ_0 . Note that the Hamiltonian is invariant to changes of phase in integer units of 2π , and therefore the physics is invariant under changes of magnetic flux per plaquette of Φ_0 .

The spectrum of the Hamiltonian for a range of flux values is shown in Figure 1.1.4. This is known as the Hofstadter butterfly, and is remarkable for its fractal structure. In the limit of flux $\Phi/\Phi_0 \rightarrow 0$, the fractal bands come together to form equally spaced composite bands, Landau levels underlying the quantum Hall effect [19–21]. The topology of each energy level for each flux value, as defined by the Chern number, can be found through eqn. 1.6. In the quantum Hall effect limit, the Chern number of each Landau level is $C = 1$.

1.1.5 Diophantine equation

In their seminal paper explaining the topological nature of the quantum Hall effect [6], Thouless, Kohmoto, Nightingale and den Nijs also defined an alternative way to compute the Chern number, without resorting to eqn. 1.6. This equation

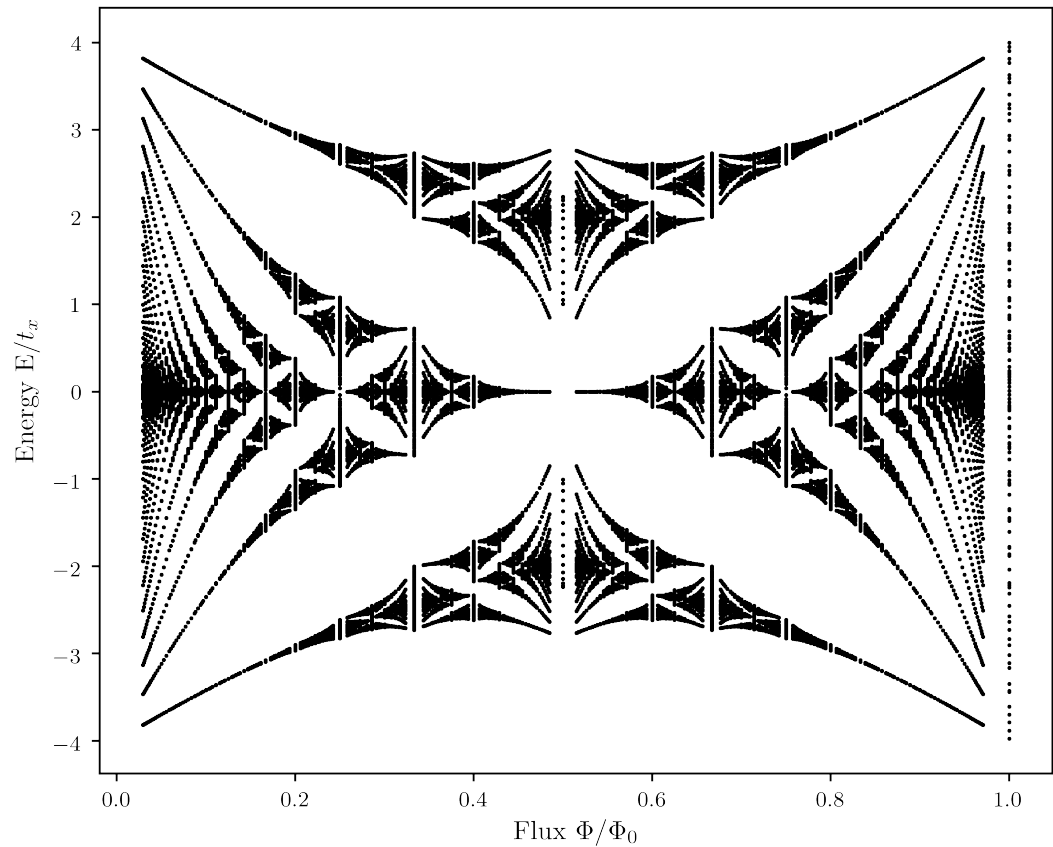


Figure 4: Hofstadter butterfly calculated in 2D momentum space for isotropic tunneling $t_x = t_y$.

states that for rational flux $\Phi/\Phi_0 = P/Q$ (for relatively prime integers P and Q) the integer solutions s and C to the Diophantine equation

$$1 = Qs - PC, \quad (1.8)$$

under the constraint $|C| \leq |Q|/2$ [6, 22], uniquely determine the Chern number of the lowest band. We refer to this equation as the TKNN Diophantine equation, and will make use of it in Chapter 7.

1.2 Ultracold atoms for quantum simulation

The phenomenon of Bose–Einstein condensation (BEC) was first predicted in 1924 [23]. But it wasn’t until 1995 that techniques for cooling atoms down to ultracold temperatures allowed for an experimental realization of this phase of matter. The first BEC was created and observed by two labs, one at JILA [24] and one at MIT [25]. The realization of a BEC won Eric Cornell, Carl Wieman and Wolfgang Ketterle the Nobel prize in 2001. Since then, similar cooling techniques have been applied to Fermionic atomic species. Though no phase transition occurs for these atoms, at ultracold temperatures they start to differ significantly from an ideal gas. Atoms in this regime are known as a degenerate Fermi gas (DFG), and they were first experimentally realized in 1999 in the group of Deborah Jin [26, 27].

Since their realization, BECs and DFGs have become widely studied, both for their fundamental properties and as a platform for quantum simulation. A key tool that makes ultracold atoms amenable to simulating condensed matter systems is optical lattices. These lattices serve as analogues of crystal structure in a solid, with atoms serving as analogues of electrons. Optical lattices are created by laser light and can be used to create almost any geometry, from square [28] to triangular [29, 30], to hexagonal [31] to Kagome [32]. This allows for simulation of almost any crystal

structure, and even the creation of periodic structures not yet found in nature.

Moreover, these optical lattices can be tuned *in situ*, giving the experimenter dynamical control of Hamiltonian parameters far beyond what is possible in condensed matter settings. This allowed for the realization of the previously predicted [33] quantum phase transition from the superfluid to the Mott insulating phase in a BEC [34, 35].

Additionally, there are tools available to control and tune interactions between atoms. Most notable of these are Feshbach resonances [36–40]. These have been responsible for significant advances, from creating BEC of attractively interacting atoms [41], to forming molecular BECs [42–44], to allowing for realization of BEC-BCS crossover physics [44–46]. The control of inter-atomic scattering length allowed by Feshbach resonance makes them an important tool and subject of study. In Chapter 5, we describe our experiment directly imaging the scattering in the vicinity of such a resonance.

One drawback of ultracold atomic systems is that they are made with neutral atoms, limiting their interactions with magnetic fields to those arising from their magnetic dipole moment. It might seem that the interesting physics of 2D systems in magnetic fields, as described in the previous section, would not lend itself to quantum simulation in these settings. However, many techniques have emerged for creating artificial magnetic fields, or terms in the atomic Hamiltonian that are identical to the charged particle–magnetic field interaction. One proposal was rotating the atoms such that the Coriolis force takes the role of the Lorentz force [47]. Another is engineering laser coupling in a precise geometry to induce effective magnetic fields [48], which was successfully realized [49] and extended to creating a spin-orbit coupled Bose gas [50].

On a lattice, the cold atomic approach of imprinting Ahoranov-Bohm phases, rather than using large external fields, has opened the way for simulation of large

magnetic fluxes [51–53]. Several experiments have used this approach to reach the Hofstadter regime [54–59], and further applications are promised [60]. Furthermore, the approach of synthetic dimensions [61] has enabled reaching the Hofstadter regime without laser modulation. The experimental realization and detection with this technique as described in [62] is detailed in Chapter 6 of this thesis. It has also been successfully used by other groups [58, 63]. In Chapter 7 of this thesis, we further detail our experiment detecting the underlying topology of these synthetic dimensional lattices.

1.3 Strucute of the thesis

In the second chapter, I review some background atomic physics necessary to understanding the experiments that follow. In the third chapter, I review basics of Bose-Einstein condensates and degenerate Fermi gases and present an overview of the experimental apparatus, with extra detail on a few recent upgrades. In the fourth chapter, I describe numerical simulations of absorption imaging in the presence of strong recoil-induced detuning. In the fifth chapter, I describe our experiment with colliding ^{40}K atom clouds in the vicinity of a Feshbach resonance and imaging the resulting *s*-wave scattering halos. In the sixth chapter, I describe our experiment creating an effectively 2D synthetic dimensions lattice in the Hofstadter regime for ^{87}Rb , and imaging skipping orbits on its edges. In the final chapter, I describe our experiment measuring the underlying topological invariant of the same lattice. In the appendices, I include published papers to which I contributed but did not include in the body of the thesis.

Chapter 2: Atom–Light Interactions

In this chapter, we review the physics of interactions between atoms and light in so far as they are relevant to our experiments. We describe the level structure of alkali atoms in section 2.1, including the fine and hyperfine interactions and the effects of external magnetic fields. We review the interaction of atoms with near-resonant light (section 2.2), pertinent to cooling and absorption imaging as well as Raman and rf coupling. We then detail interactions of atoms with far-detuned light (section 2.3), pertinent to optical trapping and lattices.

In the following sections, we use these basic interactions to explain the tools used in our experiments. We describe absorption imaging (section 2.4), our detection scheme. We explain the basic physics of atoms in a 1D optical lattice potential (section 2.5), and the physics of Raman and rf coupling of hyperfine atomic levels (section 2.6).

2.1 Level structure of alkali atoms

Alkali atoms (those in the first column of the periodic table) are the most commonly used for laser cooling. Their level structure can be understood as primarily the energy state of the single electron in the outer shell, interacting with the rest of the atom—the nucleus and all the other electrons—as a whole. The quantum numbers that describe the energy levels of the atom are the principal quantum number N , that electron’s spin S , the orbital angular momentum L , and finally the nuclear spin I . The work described in this thesis was done with alkali species ^{87}Rb and ^{40}K .

2.1.1 Fine and hyperfine sturcutre

The fine structure of alkali atom comes from two corrections to the bare Hamiltonian. The bare Hamiltonian H_0 encompasses the kinetic energy and the Coulomb interaction between the outermost electron and the rest of the atom. The first of these corrections is due to special relativity—it's the correction to the classical kinetic term. The energy shift due to this term, to leading order in the small parameter of velocity over the speed of light v/c , is given by [64]

$$\Delta E_{\text{rel}} = -\frac{E_N^2}{2mc^2} \left(\frac{4N}{L - 1/2} - 3 \right), \quad (2.1)$$

where E_N is the unperturbed energy and m is the mass of the electron.

The second correction comes from the spin–orbit interaction. In the frame of the outermost electron, the nucleus is orbiting it, creating a magnetic field. The magnetic dipole moment of the electron—given by $\vec{\mu}_S = -g_S \mu_B \hat{\vec{S}}/\hbar$, where g_S is the spin g-factor, μ_B is the Bohr magneton, and $\hat{\vec{S}}$ is the spin angular momentum operator—interacts with this magnetic field. The Hamiltonian describing this interaction is given by [64, 65]

$$H_{\text{SO}} = \frac{Ze^2}{4\pi\epsilon_0} \frac{g_s}{4me^2c^2} \frac{\hat{\vec{L}} \cdot \hat{\vec{S}}}{r^3}, \quad (2.2)$$

where Z is a factor expressing the effective charge seen by the electron, e is the electron charge, ϵ_0 is the vacuum permittivity and r is the radial coordinate. This Hamiltonian does not commute with either $\hat{\vec{S}}$ or $\hat{\vec{L}}$, and therefore the projection quantum numbers m_S and m_L are no longer good quantum numbers. However, the total angular momentum $\hat{\vec{J}} = \hat{\vec{L}} + \hat{\vec{S}}$ does commute with the Hamiltonian, and therefore m_J is still a good quantum number. We can rewrite the coupling term in the spin–orbit Hamiltonian as $\hat{\vec{L}} \cdot \hat{\vec{S}} = \hat{\vec{J}}^2 - \hat{\vec{L}}^2 - \hat{\vec{S}}^2$. The leading order shift in

perturbation theory due to this interaction is given by

$$\Delta E_{\text{SO}} = \frac{E_N^2}{mc^2} \left(\frac{N[J(J+1) - L(L+1) - S(S+1)]}{L(L+1/2)(L+1)} \right). \quad (2.3)$$

Note that the relativistic and spin-orbit correction terms are of the same order. We therefore combine them into a total energy shift, called the fine structure shift. Using the fact that $S = 1/2$ and $J = L \pm 1/2$, this term can be written as

$$\Delta E_{\text{fs}} = \frac{E_N^2}{mc^2} \left(3 - \frac{4N}{J+1/2} \right), \quad (2.4)$$

which splits the atomic energies according to the quantum number J .

The ground state of ^{87}Rb , in term notation $N^{2S+1}L_J$ is $5^2s_{1/2}$, where s is orbital notation indicating $L = 0$. Since $L = 0$, the ground state only has one possible value of $J = 1/2$, and there is no ground state fine structure splitting. The first excited state 5^2p_J has orbital angular momentum $L = 1$ (as indicated by p in orbital notation). Therefore, J can take on two different values: $1/2$ and $3/2$, producing a hyperfine splitting between the $5^2p_{1/2}$ and $5^2p_{3/2}$. The spectral feature associated with the ground $5^2s_{1/2}$ and lower excited $5^2p_{1/2}$ energy difference is conventionally called the $D1$ line, and the feature corresponding to the splitting between $5^2s_{1/2}$ and $5^2p_{3/2}$ is the $D2$ line. For other alkalis, including ^{40}K , the ground state values of L and S are identical and only the N value is different. Therefore, even though their energies vary, $D1$ and $D2$ lines feature in all alkalis.

There is a yet smaller correction to the bare Hamiltonian, causing what's known as the hyperfine splitting. This arises from the interaction of the nuclear spin magnetic dipole moment with the magnetic field created by the electron. The Hamiltonian for this interaction is

$$H_{\text{hfs}} = -\hat{\vec{\mu}}_I \cdot \vec{B}, \quad (2.5)$$

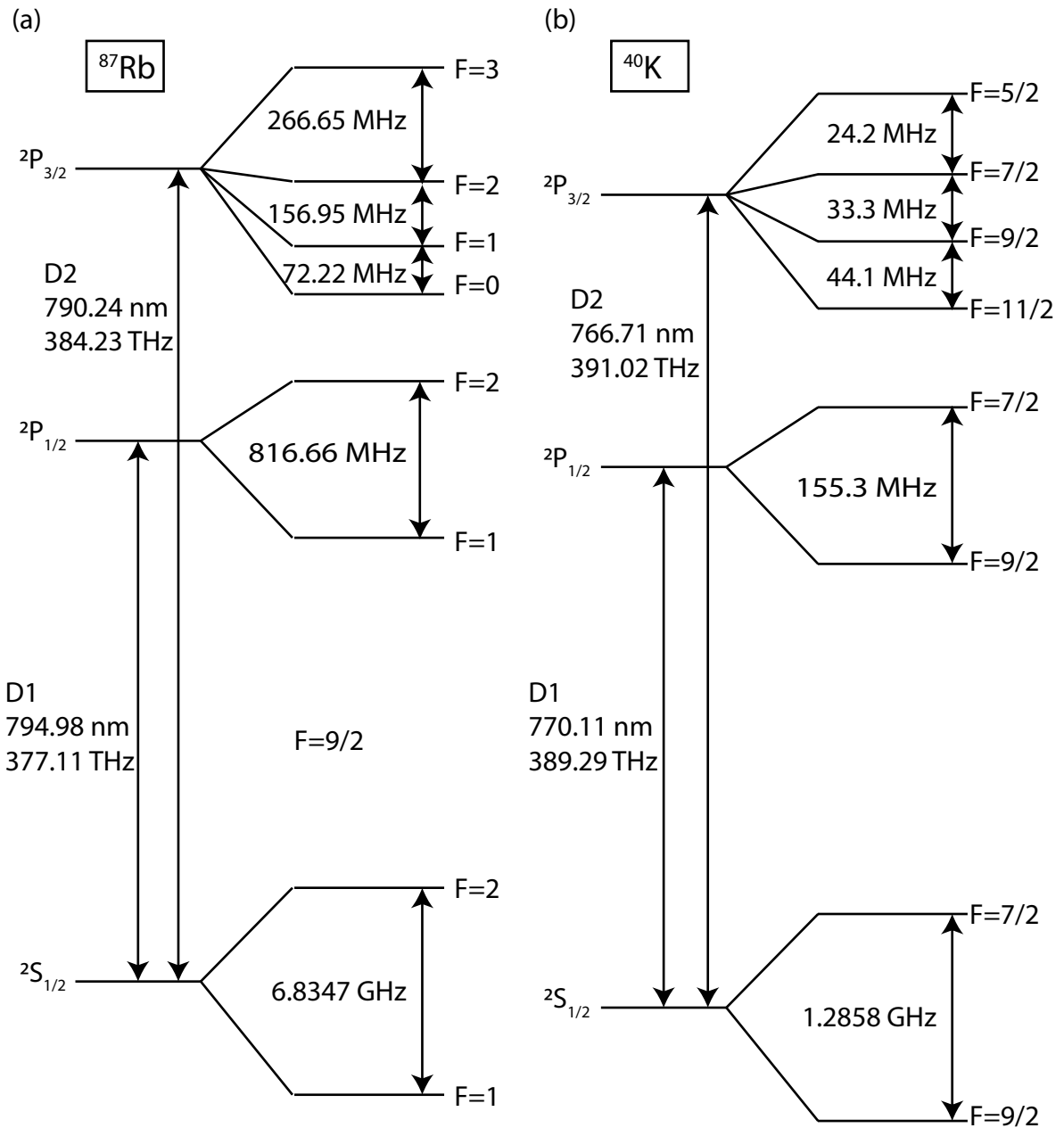


Figure 1: Atomic structure of the ground and first excites states, with fine and hyperfine splittings. (a) ^{87}Rb . Values from [66]. (b). ^{40}K . Values from [67].

where $\hat{\mu}_I = g_I \mu_B \hat{I}$ is the nuclear spin magnetic dipole moment, \hat{I} is the nuclear spin operator and \vec{B} is the magnetic field seen by the nucleus. The nuclear spin g-factor g_I encompasses the entire complex structure of the nucleons, but is generally smaller than the electron spin g-factor g_S by a factor of m_e/m_p , where m_e is the electron mass and m_p is the proton mass, making this term very small. This magnetic field, to leading order, is given by [66, 68]

$$\vec{B} = 2\frac{\mu_0}{4\pi}\mu_B \left(\frac{\hat{L}}{\hat{r}^3} - \frac{1}{\hat{r}^3} \left[\hat{S} - 3\frac{\hat{S} \cdot \hat{r}}{\hat{r}^2} \hat{r} \right] + \frac{2}{3}\delta(\vec{r})\hat{r}^2 \hat{S} \right), \quad (2.6)$$

where the first term arises from the field due to the orbital angular momentum of the electron, the second term is the field created by the electron spin magnetic dipole moment, and the final term is the contact interaction, which is only non-zero for $L = 0$ states. The hyperfine Hamiltonian eqn. 2.5 contains both $\hat{I} \cdot \hat{L}$ and $\hat{I} \cdot \hat{S}$ terms. Therefore, \hat{L} , \hat{S} and \hat{I} as well as \hat{J} no longer commute with the Hamiltonian and projection quantum numbers m_L , m_S , m_J and m_I are no longer good quantum numbers. However, the total spin including nuclear spin $\hat{F} = \hat{L} + \hat{S} + \hat{I}$ commutes with the Hamiltonian, and total spin F and its projection m_F are now good quantum numbers.

The energy shift, to lowest order in perturbation theory, due to the hyperfine interaction is given by [66, 68]

$$\Delta E_{\text{hfs}} = \frac{1}{2}A_{\text{hfs}}K + B_{\text{hfs}} \frac{\frac{3}{2}K(K+1) - 2I(I+1)J(J+1)}{2I(2I-1)2J(2J-1)}, \quad (2.7)$$

where $K = F(F+1) - I(I+1) - J(J+1)$, A_{hfs} is the magnetic dipole constant of the electron, whose values for ^{87}Rb and ^{40}K can be found in [66, 67].

For ^{87}Rb , $I = 3/2$ and for ^{40}K , $I = 4$. The interaction with the nuclear spin splits the ground state of ^{87}Rb into two manifolds, $F = 1$ and $F = 2$. Similarly for ^{40}K , it splits the ground state into $F = 9/2$ and $F = 7/2$ manifolds. The

structure of the ground and first excited states of ^{87}Rb and ^{40}K , including both the fine and hyperfine splittings, is diagrammed in Figure 1. Note that the $D1$ and $D2$ transitions are in the optical regime, making them amenable to laser cooling. The fine structure splitting of the excited states is in the far infrared, whereas the hyperfine splitting of the ground states is in the microwave regime.

2.1.2 Interaction with static magnetic fields

In a static background magnetic field \vec{B} , the atomic angular momentum interacts with the field via the Hamiltonian

$$H_B = \frac{\mu_B}{\hbar} (g_S \hat{\vec{S}} + g_L \hat{\vec{L}} + g_I \hat{\vec{I}}) \cdot \vec{B}, \quad (2.8)$$

where μ_B is the Bohr magneton, g_S , g_L and g_I are the spin, orbital and nuclear Landé g-factors correcting their respective magnetic dipole moments. Without loss of generality, we can define the magnetic field to be in the e_z direction, $\vec{B} = B_z e_z$, to obtain

$$H_B = \frac{\mu_B}{\hbar} (g_S \hat{S}_z + g_L \hat{L}_z + g_I \hat{I}_z) B_z. \quad (2.9)$$

At very low magnetic field strengths, where the energy shift due to H_B is small compared to the hyperfine splitting, the total angular momentum F remains a good quantum number, and the Hamiltonian in eqn. 2.10 can be re-written as

$$H_B = \frac{\mu_B}{\hbar} (g_F \hat{F}_z) B_z, \quad (2.10)$$

where the effective Lande g-factor is dependent on the angular momentum quantum

numbers:

$$g_F = g_J \frac{F(F+1) - I(I+1) + J(J+1)}{2F(F+1)} + g_I \frac{F(F+1) + I(I+1) - J(J+1)}{2F(F+1)}. \quad (2.11)$$

In this regime, the levels split linearly according to the \hat{F}_z projection quantum number, m_F . For the ground state of ^{87}Rb , it splits into three hyperfine states in the $F = 1$ manifold ($m_F = 0, \pm 1$) and five hyperfine states in the $F = 2$ manifold ($m_F = 0, \pm 1, \pm 2$). This regime is at fields $B \leq \approx 1$ Gauss for ^{87}Rb , as seen in Figure 2.

At fields producing energy shifts small compared to the fine structure splitting, but large compared to the hyperfine splitting, F is no longer a good quantum number, and the relevant Hamiltonian becomes

$$H_B = \frac{\mu_B}{\hbar} (g_J \hat{J}_z + g_I \hat{I}_z) B_z. \quad (2.12)$$

Here, since $g_I \ll g_J$, the energy dependence on B_z is dominated by a linear dependence on the \hat{J}_z projection quantum number, m_J , as seen in the higher field limit in Figure 2.

In the intermediate regime, there is in general no analytic solution for the eigenenergies and one must resort to numerics. However, for the specific case of $J = 1/2$ applicable to alkali ground states, there is an analytic solution given by the Breit-Rabi formula [69]:

$$E_{|J=1/2 m_J I m_I\rangle} = -\frac{\Delta E_{\text{hfs}}}{2(2I+1)} + g_I \mu_B m B \pm \frac{\Delta E_{\text{hfs}}}{2} \left(1 + \frac{4mx}{2I+1} + x^2 \right)^{1/2}, \quad (2.13)$$

where ΔE_{hfs} is the zero field hyperfine splitting, $m = m_I \pm m_J$, and

$$x = \frac{(g_J - g_I)\mu_B B}{\Delta E_{\text{hfs}}}. \quad (2.14)$$

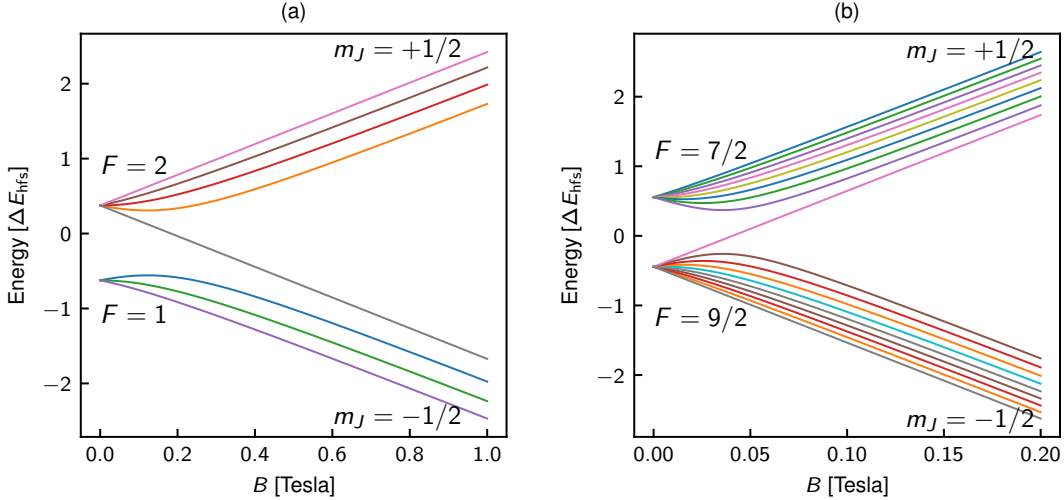


Figure 2: Energy structure of hyperfine states of the ground state of (a) ^{87}Rb and (b) ^{40}K as a function of external magnetic field strength in Gauss. Note that the zero field splitting ΔE_{hfs} by which the vertical axis is scaled is different for the two atomic species.

From this we can get a better picture of the shifts at low fields, where $\mu_{\text{B}}B \ll E_{\text{hfs}}$. Expanding eqn. 2.13 to second order in small parameter $4mx/(2I+1) + x^2$, and neglecting the field-independent terms, we obtain

$$\Delta E_{|J=1/2m_JIm_I\rangle} \approx \frac{\Delta E_{\text{hfs}}}{2} \left(\frac{1}{2} \left[\frac{4mx}{2I+1} + x^2 \right] - \frac{1}{8} \left[\frac{16m^2x^2}{(2I+1)^2} + \frac{4mx^3}{2I+1} + x^4 \right] \right). \quad (2.15)$$

We recognize the term linear in mx , $\Delta E_{\text{hfs}}mx/(2I+1) = (g_J - g_I)\mu_{\text{B}}Bm/(2I+1)$.

In addition, there is a term quadratic in mx :

$$\Delta E_{\text{hfs}} \frac{m^2x^2}{(2I+1)^2} = \frac{(g_J - g_I)^2\mu_{\text{B}}^2B^2m^2}{\Delta E_{\text{hfs}}(2I+1)^2} = \epsilon(B)m^2, \quad (2.16)$$

where in the last term we have defined $\epsilon(B)$, the magnitude of this ‘quadratic’ Zeeman energy shift. For the magnetic field strengths used in experiments described in this thesis, the linear term plus quadratic correction are sufficient for describing the energy levels.

The form of the approximate Hamiltonian in this regime for any value of F is given by

$$H_0 = H_{\text{KE}} + \hbar\omega_z \hat{F}_z + \hbar\epsilon \hat{F}_z^2, \quad (2.17)$$

where $\hbar\omega_z = \mu_B g_F B_z / \hbar$, and the kinetic energy Hamiltonian $H_{\text{KE}} = \hbar^2 \vec{k}^2 / 2m\hat{\mathcal{I}}$, and $\hat{\mathcal{I}}$ is the identity matrix.

2.2 Near-resonant atom–light interaction

In this section, we will assume the atom can be treated as a two-level system: one with a ground state of some energy $\hbar\omega_g$ and excited state with energy $\hbar\omega_e$, with an energy difference $\hbar\omega_0$. The interaction with a light source results from the electric dipole moment of the atom $\vec{d} = -\epsilon_0 \vec{r}$ interacting with the electric field of the beam $\vec{\mathcal{E}}(t, \vec{r})$, giving [70]

$$H_{\text{L}}(t) = -\vec{d} \cdot \vec{\mathcal{E}}(t, \vec{r}). \quad (2.18)$$

When very weak or no light is being shined on the atom, it still experiences the interaction with vacuum light modes. Through this mechanism, an atom in the excited state may still decay to its ground state (emitting a photon). This is called spontaneous emission, and the time scale on which the decay will happen is determined by the dipole matrix element of the transition, and is known as the natural transition linewidth of the atomic transition Γ [70].

2.2.1 Rabi oscillations

When strong laser light is present, and on timescales short compared to $1/\Gamma$, spontaneous emission can be ignored [71]. Let us consider the Hamiltonian

$$H = H_0 + H_{\text{L}}(t), \quad (2.19)$$

where H_0 is the bare atomic Hamiltonian and H_L is the interaction with the laser beam eqn. 2.18. We can write the wavefunction Ψ as a linear combination of the two eigenstates (for a two-level atom) of the bare Hamiltonian H_0 as

$$\Psi = c_g(t)\phi_g(\mathbf{r})e^{-i\omega_g t} + c_e(t)\phi_e(\mathbf{r})e^{-i\omega_e t}, \quad (2.20)$$

where $c_g(t)$ and $c_e(t)$ are the time-dependent coefficients multiplying the eigenstate wavefunctions ϕ_g and ϕ_e of the ground and excited state respectively, and \mathbf{r} is the spatial coordinate. Absorbing any diagonal elements of H_L into H_0 , multiplying both sides of the Schrödinger equation from the left by ψ_j and integrating over \mathbf{r} , we can write down the Schrödinger equation as two coupled equations:

$$i\hbar \frac{dc_g(t)}{dt} = c_e(t)H_L^{ge}(t)e^{-i\omega_0 t} \quad (2.21)$$

and

$$i\hbar \frac{dc_e(t)}{dt} = c_g(t)H_L^{eg}(t)e^{i\omega_0 t}, \quad (2.22)$$

where $\omega_0 = \omega_e - \omega_g$ is the transition frequency, $H_L^{ge}(t)$ is the off-diagonal element of the laser coupling Hamiltonian that couples the excited to the ground state and $H_L^{ge}(t) = H_L^{eg*}(t)$. For simplicity, let's consider light propagating along e_z , linearly polarized light along e_x , $\vec{\mathcal{E}} = (\mathcal{E}_0, 0, 0)\cos(\omega t)$. The coupling Hamiltonian can then be written as [70]

$$H_L^{ge}(t) = -\mu_{ge}\mathcal{E}_0\cos(\omega t), \quad (2.23)$$

where the electric dipole matrix element $\mu_{ge} = \int \phi_g^* x \phi_e$. This can be written as

$$H_L^{ge}(t) = \hbar\Omega\cos(kz - \omega_L t) \quad (2.24)$$

with

$$\Omega = \frac{\mathcal{E}_0 |\mu_{ge}|}{\hbar} \quad (2.25)$$

the Rabi frequency, characterizing the coupling strength between the laser field and the atom. Here, e is the charge of the electron.

To solve this Schrödinger equation, we make the traditional transformation to the rotating frame:

$$c'_g(t) = c_g(t) \quad (2.26)$$

$$c'_e(t) = c_e(t)e^{-i\delta t}, \quad (2.27)$$

where $\delta = \omega_0 - \omega_L$ is the detuning of laser light from resonance. In this frame, we can write the atom-light Hamiltonian in the $\begin{pmatrix} c'_g \\ c'_e \end{pmatrix}$ basis as:

$$H = \hbar \begin{pmatrix} -\delta/2 & \Omega/2 \\ \Omega/2 & \delta/2 \end{pmatrix}. \quad (2.28)$$

In the limit of no coupling, $\Omega = 0$, in the rotating frame the eigenenergies are $E_{\pm} = \pm \hbar \delta / 2$. For non-zero coupling, finding the eigenvalues of H gives

$$E_{\pm} = \pm \hbar \sqrt{\delta^2 + \Omega^2} / 2. \quad (2.29)$$

The eigenenergies are shifted in the presence of the light.

Assuming the atom starts in the ground state $c_g(t=0) = 1$, we can solve the time-dependent Schrödinger equation (TDSE) with the above Hamiltonian

$$i\hbar \frac{d}{dt} \begin{pmatrix} c'_g \\ c'_e \end{pmatrix} = H \begin{pmatrix} c'_g \\ c'_e \end{pmatrix} \quad (2.30)$$

we obtain the oscillating excited state amplitude

$$c'_e(t) = -i \frac{\Omega}{\sqrt{\Omega^2 + \delta^2}} \sin \left(\frac{\sqrt{\Omega^2 + \delta^2} t}{2} \right), \quad (2.31)$$

known as Rabi oscillations. The frequency of these oscillations is the generalized Rabi frequency $\Omega' = \sqrt{\Omega^2 + \delta^2}$. The amplitude of the oscillation is at its maximum when the laser is on-resonance, $\delta = 0$. As the detuning increases, the contrast in excited and ground populations decreases, while the frequency of the oscillation increases.

2.2.2 Scattering

In the regime where spontaneous emission cannot be ignored, Rabi oscillations of each individual atom are intermittently interrupted by decay to the ground state. Averaging over an atomic ensemble, on the time scale of a single Rabi oscillation, the overall excited state population reaches a steady state, and the rate of spontaneous emission becomes constant. Since during spontaneous emission the ejected photon can go into any vacuum mode, this process can be thought of as the scattering of photons by the atoms. This scattering rate is given by [71]

$$\gamma_{\text{sc}} = \frac{\Gamma}{2} \frac{I/I_{\text{sat}}}{1 + 4(\delta/\Gamma)^2 + I/I_{\text{sat}}}, \quad (2.32)$$

where I_{sat} is the saturation intensity. This is the intensity at which the timescale of spontaneous emission matches the Rabi oscillation rate, reducing the capacity for absorption of extra light.

2.2.3 Adiabatic rapid passage

Suppose there is a two-level atom in its ground state that an experimenter wants to transfer into the excited state. To transfer it with perfect fidelity using Rabi oscillations, one would need a perfectly on-resonant beam and very precise timing to shut off the coupling field at the maximum of the excited state population. This is challenging and not very stable to small perturbations in the level splitting between the ground and excited state (caused by small field fluctuations for the case of two Zeeman sublevels). A more robust technique is known as adiabatic rapid passage.

Suppose the two energy levels of the atom are sensitive to some external parameter. Commonly (as in the case of hyperfine sublevels), they are sensitive to an external magnetic field B , and in the small field limit are linear in B . Therefore, the detuning that goes into the Hamiltonian in eqn. 2.28 becomes $\hbar\delta = AB - \hbar\omega_L$, where A is the coupling constant in the hyperfine (or other) Hamiltonian. In the limit of zero coupling strength, diagonalizing the Hamiltonian amounts to calculating the eigenenergies in the rotating frame as a function of the control parameter B . These are represented in black in Figure 3. Note that the two levels cross each other when their energy difference matches $\hbar\omega_L$, on resonance.

Once the coupling field is turned on (in the case of the hyperfine interaction, and rf-field), the two levels split near the resonance and an avoided crossing appears, as seen in blue in Figure 3. Crucially, away from resonance towards the left, the bottom coupled state overlaps closely with the uncoupled (black state). Far from resonance, the ground state is largely unaffected by the presence of light. On the other hand, far from the resonance on the right, the lower coupled state overlaps almost perfectly with the excited uncoupled state. Adiabatic rapid passage (ARP) takes advantage of this change.

The ARP protocol is as follows. Start at a bias field (or other control parameter)

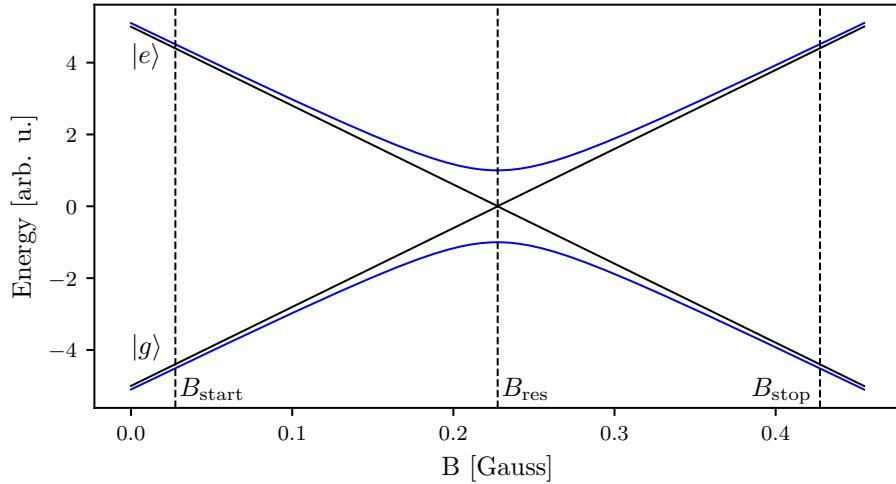


Figure 3: Adiabatic rapid passage (ARP). Black lines represent energies of the ground and excited state, in the rotating frame, with zero coupling. Blue lines represent these bands with some coupling $\hbar\Omega$ turned on. The dashed lines represent the starting point of an ARP (B_{start}), the resonant field value (B_{res}) and the end point of an ARP (B_{stop}).

ter) where turning on the coupling field does not significantly perturb the eigenstate (B_{start} in the figure). Turn on the coupling field adiabatically (slow with respect to the time scale associated with the level splitting energy at the selected detuning $\tau = \hbar/(E_e - E_g)$), such that the atom remains entirely in the ground state $|g\rangle$. Then, sweep the control parameter across the resonance, again adiabatically with respect to the coupled level splitting (blue in the figure). The sweep rate can be optimized to be faster away from resonance, where $E_e - E_g$ is large and slower closer to the avoided crossing. Then, at a final value of the control parameter where the lowest coupled state overlaps almost perfectly with the bare excited state $|e\rangle$, adiabatically turn off the coupling field, leaving the atoms in the excited state.

The ‘rapid’ part of adiabatic rapid passage refers to the procedure having to be fast with respect to the spontaneous emission timescale, since in the coupled basis there is some population in the excited state and spontaneous decay would disrupt the process. This procedure is relatively insensitive to field fluctuations (as

long as B_{res} is roughly in the middle of the relatively long sweep, the procedure will succeed). It can also be applied to multi-level situations, for example in the case of the hyperfine states of a single manifold F , where the atoms traverse multiple avoided crossings in the same sweep and can be efficiently transferred from one stretch state $m_F = F$ to the other $m_F = -F$, or vice versa.

2.3 Far-off-resonant atom–light interaction

We can infer the behavior of atoms in a far-detuned laser field by taking the solutions from eqns. 2.29 and 2.31 in the limit $\delta \gg \Omega$. First, looking at the excited state population in eqn. 2.31, the amplitude of the excited state population oscillation approaches zero. Therefore, as expected, no absorption of the light actually takes place and the atom remains in the ground state. However, the light still affects the atom by shifting the eigenenergies via eqn. 2.29. Recalling that the bare eigenenergies in the rotating frame are given by $E_{\pm} = \pm\hbar\delta/2$, the energy shift from bare is given by

$$\Delta E_{\pm} = \pm\hbar\sqrt{\delta^2 + \Omega^2}/2 - \pm\hbar\delta/2. \quad (2.33)$$

Expanding the energy shift in the small parameter Ω/δ , we obtain the shifted energies $E_{\pm} = \pm\hbar\sqrt{\delta^2 + \Omega^2}/2 \approx \pm(\delta/2 + \Omega^2/4\delta)$. The shift from bare energy levels is thus

$$\Delta E_{\pm} \approx \pm\hbar(\delta/2 + \Omega^2/4\delta) - \pm\hbar\delta/2 = \pm\hbar\Omega^2/4\delta. \quad (2.34)$$

This laser-intensity–dependent energy shift is called the AC Stark shift, and is the basis of most laser created potentials for cold atoms.

For the ground state, and a red detuned laser beam (where the laser frequency is lower than the resonant frequency), this creates energy minima in locations of maximal laser intensity. For the lattice described in this chapter, as well as for the trapping of our atoms in the final stages of cooling, we use high power (up to 10 W)

lasers with wavelength $\lambda_L = 1064$ nm.

2.4 Absorption imaging

Absorption imaging takes advantage of the on-resonant interaction described in the previous section. An on or near-resonant laser beam ($\delta/\Gamma \ll 1$) is shined at the atoms, and the absorbed light acts to create a shadow in the shape of the atoms in the laser beam. This beam with the shadow is then imaged on a camera, in our case a CCD, as depicted in Figure 4a (top). This is called the atom image, and the intensity distribution over the camera is denoted by $I_f(x, y)$, where the subscript f stands for final - the intensity after the light has encountered the atoms. To quantify the ‘shadowed out’ intensity, after the atoms have left the trap, the same laser intensity is shined directly at the camera, as in Figure 4a (bottom). This is called the probe image, and the intensity distribution over the camera is denoted by $I_0(x, y)$, where the subscript 0 indicated initial—the intensity before the light had encountered the atoms.

To recover the atom number distribution encountered by the light, consider an atomic cloud with 3D density $\rho(x, y, z)$. Since we can only obtain 2D information from the camera, we can only hope to recover a 2D atomic column density $n(x, y) = \int \rho(x, y, z) dz$. Focusing in on a single pixel of the camera, we can consider a single value of I_0 and I_f to recover a local n . As the laser light propagates through the atomic cloud, the intensity of the light will diminish due to absorption. This absorption as a function of propagation direction z can be expressed using the scattering rate equation eqn. 2.32 as the number of photons scattered by the atoms (proportional to the atomic density times the scattering rate) times the photon energy $\hbar\omega_L$:

$$\frac{d}{dz} \frac{I(z)}{I_{\text{sat}}} = -\hbar\omega_L \rho(z) \gamma_{sc}(z) = -\rho(z) \sigma_0 \frac{I(z)/I_{\text{sat}}}{1 + 4\delta^2/\Gamma^2 + I(z)/I_{\text{sat}}}, \quad (2.35)$$

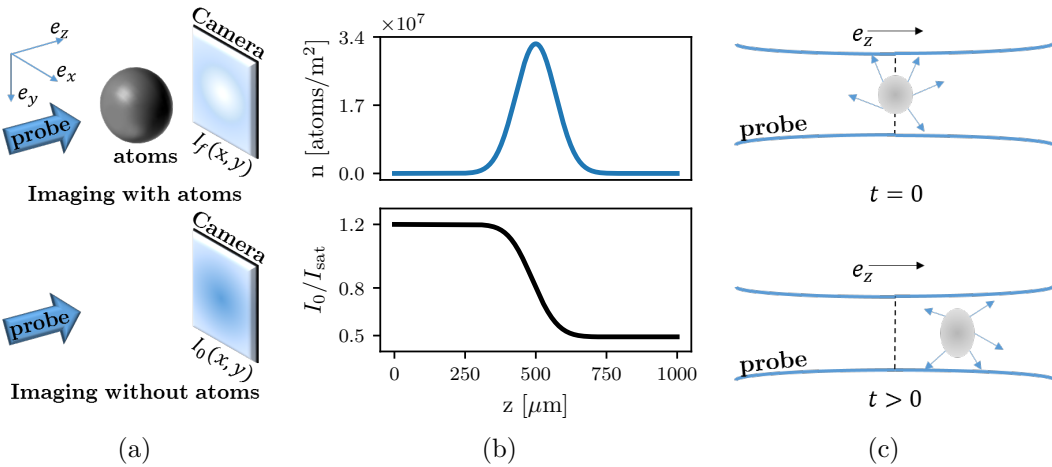


Figure 4: Absorption imaging. (a) Near-resonant probe light illuminates the atoms, and the transmitted light (containing a shadow of the atoms) is imaged on the camera. A second image taken with no atoms provides a reference. (b) The probe beam is partially absorbed as it traverses the cloud, and the intensity seen by atoms further along the imaging direction e_z is lowered. (c) An atomic cloud illuminated by a probe light field absorbs photons from the probe and re-emits them in all directions. This process results in a net acceleration of the cloud in the direction of the probe light as well as diffusive spreading in the transverse directions.

where the resonant scattering cross section is $\sigma_0 = 3\lambda_0^2/2\pi$, and λ_0 is the wavelength associated with atomic resonance.

Integrating both sides of eqn. 2.35, we obtain

$$\sigma_0 n = \left(1 + 4\delta^2/\Gamma^2\right) \ln(I_0/I_f) + (I_0 - I_f)/I_{\text{sat}}. \quad (2.36)$$

The quantity $\text{OD} = \ln(I_0/I_f)$ is called the optical depth of the cloud. When the probe intensity I_0 is much smaller than the saturation intensity, the second term in eqn. 2.36 becomes negligible. Assuming further that the probe light is on resonance, $\delta = 0$, the atomic column density becomes simply $\sigma_0 n = \text{OD}$. Figure 4b shows a Gaussian atomic density distribution (top) and the resulting probe intensity as a function of position in the cloud (bottom). The intensity drops from its initial to final value gradually as it traverses the cloud.

However, there is an important effect that the above equations do not account for. Namely, as the atoms absorb light from the probe beam, they also get a momentum kick equal to the momentum of a photon during each collision $\hbar k_r = h/\lambda_L$ in the direction of propagation. It is true that the absorbed photon will then be re-emitted by the atom, inducing a loss of momentum, but since this happens through the process of spontaneous emission into a random vacuum mode, the average momentum kick acquired this way over many re-emissions will average to zero. On average, each photon absorbed will induce a change in velocity of the atom of $v_r = \hbar k_r/m$, where m is the atomic mass, as depicted in Fig. 4c. As the velocity of the atom changes, due to the Doppler effect, the apparent laser frequency will change as well. Therefore, even if the laser light is exactly on-resonant for a stationary atom, it will become off-resonant for longer imaging times, and eqn. 2.35 will acquire a time dependence. For most experiments, this effect is small and can be neglected. However, if the imaging time becomes of order a recoil time t_r , a time after which the recoil-induced detuning δ becomes of order Γ , this effect becomes significant. We explore this effect in Chapter 4.

2.4.1 Time-of-flight and in situ imaging

There are two commonly used protocols for measuring cold atomic clouds, in situ and time-of-flight measurements. Generally, the atomic cloud is trapped (in our case by an optical dipole trap) during the experiment. In situ is Latin for in its original place. As suggested by the name, in situ measurements are taken while the cloud is still in its original trap, or immediately after the trap is turned off before any dynamics have had time to occur. These measurements measure the real spatial distribution of the atoms at the end of the given experiment. There is a difficulty associated with making in situ measurements of BECs, however. Namely, BECs in their original trap tend to be relatively dense, with optical depths often in excess of

$\text{OD} \approx 20$, requiring unrealistic probe light intensities to resolve. One way to bypass this difficulty is to selectively image only a small fraction of the condensed atoms, as was done with microwave imaging for our magnetic field stabilization feedforward protocol. Another option is to instead perform a time-of-flight measurement, which reduce the density of the cloud but don't give access to the original density distribution.

In time-of-flight measurements, the trapping potential is abruptly snapped off after the experiment, and the atoms are allowed to free fall and expand for some time t . For our experiments, t was on the order of tens of milliseconds. In the regime where time t is long enough that the atoms travel much further than the initial extent of the cloud in the directions transverse to the imaging axis, the final position of the atoms is determined almost exclusively by their in situ momentum, not their in situ position. Therefore, time-of-flight imaging in this regime measures the atomic distribution as a function of momentum, not position.

2.5 One-dimensional optical lattices

2.5.1 Lattice Hamiltonian

Our 1-D optical lattice is created by retro-reflecting the $\lambda_L = 1064$ nm laser, creating a standing wave of light. Via the AC Stark shift, this creates a periodic potential for the atoms of the form

$$V = -V_0 \sin^2(k_L x), \quad (2.37)$$

where $k_L = 2\pi/\lambda_L$ is the wavenumber associated with the lattice recoil momentum. The time-independent Hamiltonian, for some eigenenergy E_n , will be given by

$$-\frac{\hbar^2}{2m} \frac{d^2}{dx^2} \Psi_n(x) - V_0 \sin^2(k_L x) \Psi_n(x) = E_n \Psi_n(x). \quad (2.38)$$

Since the potential is spatially periodic, we can invoke Bloch's theorem [10]:

$$\Psi_{n,q} = e^{iqx} u_{n,q}(x), \quad (2.39)$$

where q is the crystal momentum restricted to $\pm\hbar k_L$, and $u_{n,q}(x)$ is the spatially-varying part of the wavefunction obeying the spatial periodicity of the lattice. Plugging this in to the Hamiltonian, we obtain

$$-\frac{\hbar^2}{2m} \left(-q^2 + 2iq \frac{d}{dx} + \frac{d^2}{dx^2} \right) u_{n,q}(x) - V_0 \sin^2(k_L x) u_{n,q}(x) = E_n u_{n,q}(x). \quad (2.40)$$

Expanding $u_{n,q}(x)$ in Fourier components commensurate with the lattice period of $2k_L$ as $u_{n,q}(x) = \sum_{j=-\infty}^{\infty} a_j e^{i2k_L j x}$, we obtain

$$\sum_j \left(\frac{\hbar^2}{2m} (q + 2k_L)^2 a_j - V_0 \sin^2(k_L x) a_j \right) e^{i2k_L j x} = E_n \sum_j a_j e^{i2k_L j x}. \quad (2.41)$$

Re-writing $\sin^2(k_L x) = (e^{-2ik_L x} + e^{2ik_L x} - 2)/4$, multiplying both sides by $e^{i2k_L j' x}$ and invoking $\sum c_j e^{ik(j-j')} = \delta_{jj'}$, where $\delta_{jj'}$ is the Kroniker delta and c_j are appropriately normalized coefficients, we get for any value of the index j

$$\frac{\hbar^2}{2m} (q + 2k_L j)^2 a_j - \frac{V_0}{4} (a_{j+1} + a_{j-1}) = E_n a_j. \quad (2.42)$$

This can be expressed in matrix form

$$H_L = \begin{pmatrix} \ddots & & & & & \\ & \frac{\hbar^2}{2m}(q + 4k_L)^2 & -\frac{V_0}{4} & 0 & 0 & 0 \\ & -\frac{V_0}{4} & \frac{\hbar^2}{2m}(q + 2k_L)^2 & -\frac{V_0}{4} & 0 & 0 \\ & 0 & -\frac{V_0}{4} & \frac{\hbar^2}{2m}q^2 & -\frac{V_0}{4} & 0 \\ & 0 & 0 & -\frac{V_0}{4} & \frac{\hbar^2}{2m}(q - 2k_L)^2 & -\frac{V_0}{4} \\ & & 0 & 0 & -\frac{V_0}{4} & \frac{\hbar^2}{2m}(q - 4k_L)^2 \\ & & & & & \ddots \end{pmatrix}, \quad (2.43)$$

in the basis of momentum orders $|k\rangle = e^{ikx}$ given by:

$$\begin{pmatrix} \vdots \\ |q + 4k_L\rangle \\ |q + 2k_L\rangle \\ |q\rangle \\ |q - 2k_L\rangle \\ |q - 4k_L\rangle \\ \vdots \end{pmatrix}. \quad (2.44)$$

This matrix can be diagonalized for every value of the crystal momentum q , with the resulting band structure shown in Figure 5. It is convenient to define the lattice recoil energy $E_L = \hbar^2 k_L^2 / 2m$. Then, we can re-write the Hamiltonian with

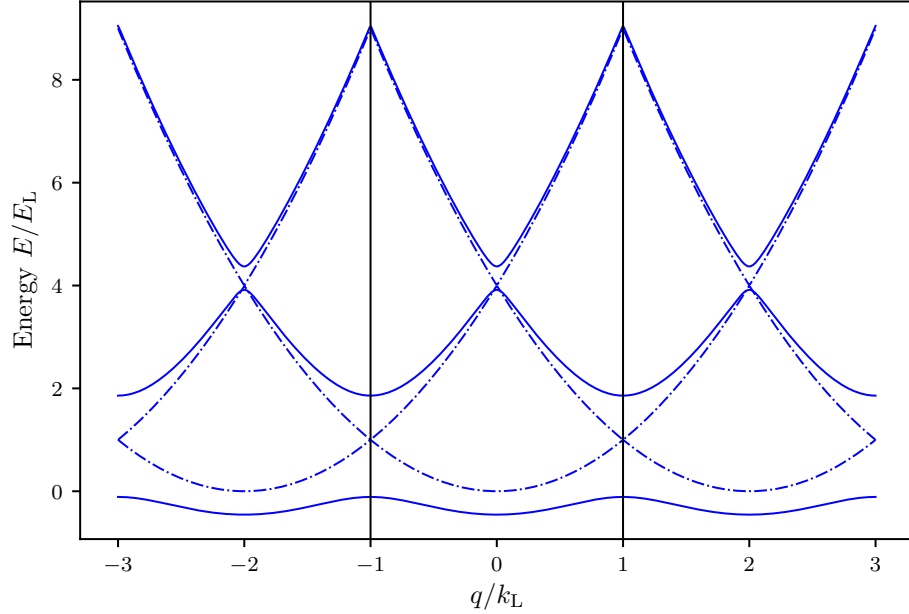


Figure 5: Lattice band structure in the extended zone scheme. The dashed lines represent the limit of zero lattice depth, with the regular parabolic dispersion relation of a free particle repeating with the reciprocal lattice period. The solid lines are the dispersion relation at $V_0 = 4.0E_L$, showing the opening of gaps at crossings of the zero lattice depth bands. The black lines demarcate the first Brillouin zone.

V_0 in units of E_L and momenta q in units of k_L as

$$H_L/E_L = \begin{pmatrix} \ddots & & & & \\ & (q+4)^2 & -\frac{V_0}{4} & 0 & 0 & 0 \\ & -\frac{V_0}{4} & (q+2)^2 & -\frac{V_0}{4} & 0 & 0 \\ & 0 & -\frac{V_0}{4} & q^2 & -\frac{V_0}{4} & 0 \\ & 0 & 0 & -\frac{V_0}{4} & (q-2)^2 & -\frac{V_0}{4} \\ & 0 & 0 & -\frac{V_0}{4} & (q-4)^2 & \ddots \end{pmatrix}. \quad (2.45)$$

In any numerical simulation, the number of momentum orders that can be included is finite. We determine the value of the parameter $n = \max(|j|)$ as the

lowest n at which the eigenvalues stop changing to machine precision from $n - 1$.

2.5.2 Tight-binding approximation

In the limit of large lattice depths, $V_0 > \approx 5E_L$, the lattice Hamiltonian is well approximated by the tight-binding model with only nearest neighbor hopping. In the tight-binding model, the basis is assumed to be a set of orthogonal functions, called Wannier functions, localized to each lattice site $|j\rangle$. The approximation lies in assuming only nearest neighbor tunnelings between the sites, forming the nearest-neighbor tight-binding Hamiltonian

$$H_{\text{tb}} = -t |j\rangle \langle j+1| + \text{H.c.}, \quad (2.46)$$

where t is the tunneling amplitude between nearest neighbor sites and H.c. stands for Hermitian conjugate. We have neglected the diagonal energy term, as it will be equal for every Wannier function $|j\rangle$ and thus represents a constant energy offset. All the information about the lattice depth is therefore reflected in the tunneling amplitude t .

This Hamiltonian can also be expressed in the momentum basis by Fourier transforming the basis functions:

$$|j\rangle = \frac{1}{\sqrt{N}} \sum_{k_j} e^{-ik_j j} |k_j\rangle, \quad (2.47)$$

giving the Hamiltonian

$$H_{\text{tb}} = -\frac{1}{N} \sum_{k_1} \sum_{k_2} t e^{-ijk_1} e^{ik_2(j+1)} |k_1\rangle \langle k_2| + \text{H.c.} = -\sum_k 2t \cos(k) |k\rangle \langle k|. \quad (2.48)$$

From this we can directly read off the band structure of the tight binding Hamiltonian. First, we notice that we only obtain one band—to approximate higher bands

with the tight-binding approximation we would need to construct a different set of Wannier functions and a different tunneling strength. Second, we see that the lowest band is simply a cosine—therefore we have solved for the band structure without even defining what the basis Wannier functions are! Third, the amplitude of the cosine function is given by the tunneling strength t . This gives us a good clue as to how to determine the appropriate tunneling given a lattice depth V_0 —simply find a t that matches the amplitude of the lowest band, which becomes cosinusoidal in the deep lattice limit.

The precise form of the Wannier functions depends on both the depth of the lattice and the band being reproduced. It is not necessary for us to find their full expression, as the band structure can be calculated without them. The definition, however, is

$$|j\rangle = \int_{\text{BZ}} e^{i\phi(q) - iqja} |q\rangle dq, \quad (2.49)$$

where the integral is over the Brillouin zone, from $-k_L$ to k_L , a is the lattice spacing $\lambda_L/2$, and $|q\rangle$ is the Bloch wavefunction at crystal momentum q , and $\phi(q)$ is the phase associated with each Bloch wavefunction. The Bloch wavefunctions individually have arbitrary phase. The phase plays an important role in combining the Bloch wavefunctions into a Wannier function, finding the proper phase relationship to make the wavefunction maximally localized at each site [72].

2.5.3 Pulsing vs adiabatic loading of the lattice

The lattice depth parameter $V_0/4$, for a range of values, can be well calibrated experimentally by pulsing on the lattice. Here, the word pulsing indicates that the lattice is turned on fully non-adiabatically, if not instantaneously, such that the original bare momentum state is projected onto the lattice eigenvector basis, as shown in Figure 8a. If the atoms start out stationary in the trap, the bare state in

the momentum basis is simply

$$|\Psi_0\rangle = \begin{pmatrix} \vdots \\ 0 \\ 0 \\ 1 \\ 0 \\ 0 \\ \vdots \end{pmatrix}, \quad (2.50)$$

as depicted in Figure 8b.

Since the lattice eigenvector basis is distinct from the bare one, instantaneously turning on the lattice will necessarily excite the atoms into a superposition of lattice eigenstates, each evolving with a different phase according to the eigenenergy while the lattice is on, as shown in Figure 8c. Then, when the lattice is snapped back off, the wavefunction is projected back into the bare basis, and the varying phase accumulation results in a beating of the different momentum orders, see Figure 8d. This can be calculated simply by using the time evolution operator

$$|\Psi(t)\rangle = e^{-iH_L t/\hbar} |\Psi_0\rangle. \quad (2.51)$$

By pulsing on the lattice for variable amounts of time t , we can obtain fractional populations in the different momentum states. Time-of-flight imaging captures the momentum distribution of the cloud, and the different entries of $\Psi(t)$ in the momentum basis will thus appear as different clouds on the absorption image, as shown in Figure 7a. The fractional population in these clouds corresponds to a measurement of $|a_j|^2$. Typically for our values of the lattice depth $V_0 < 10E_L$, it is sufficient to simply count three central momentum orders, $k = q, q \pm 2k_L$. Then, we can fit eqn.

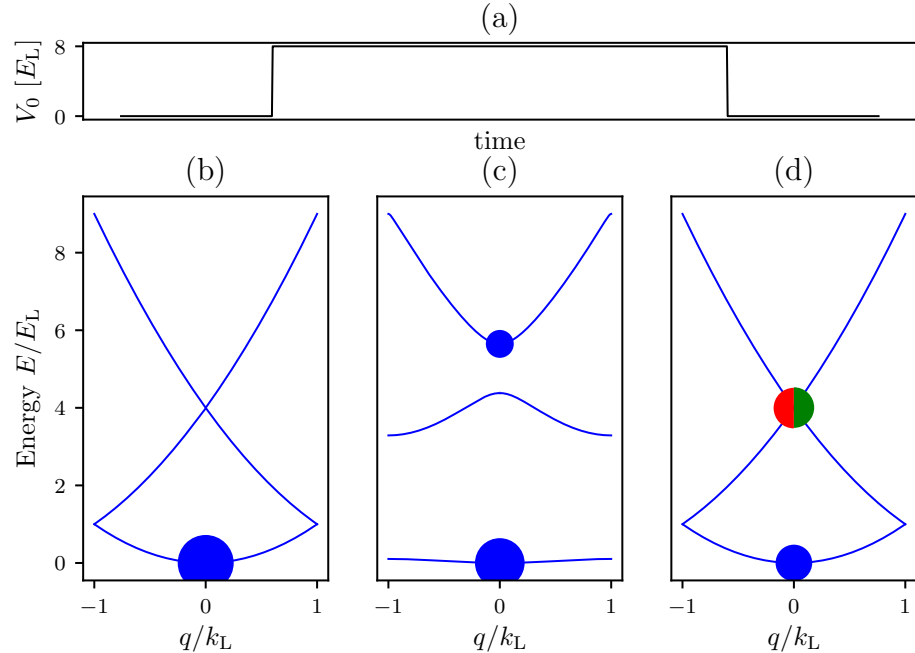


Figure 6: Lattice pulsing. (a) Lattice depth as a function of time during a pulsing experiment. The lattice is turned on instantaneously at $t = 0$ and held on for a variable amount of time until being turned off instantaneously at a final time $t = t_f$. (b) Atomic population before $t = 0$. The dispersion relation is that of a free particle, and all of the atoms start out at $q = 0$ in the lowest energy level. Here, the area of the dots is proportional to the fractional population in the energy state. (c) Atomic population after the lattice is turned on for a lattice depth of $V_0 = 8.0E_L$. The energy spectrum now shows the lattice band structure, and some atomic population is projected onto the excited bands. (d) Atomic population after the lattice is snapped off at $t_f = 150 \mu s$. The wavefunction is projected back onto the bare states, with some fraction (blue circle) in the lowest band at $k = 0$ and some fraction in the excited band, with equal population being projected onto the $k = 2k_L$ (green) and $k = -2k_L$ (red).

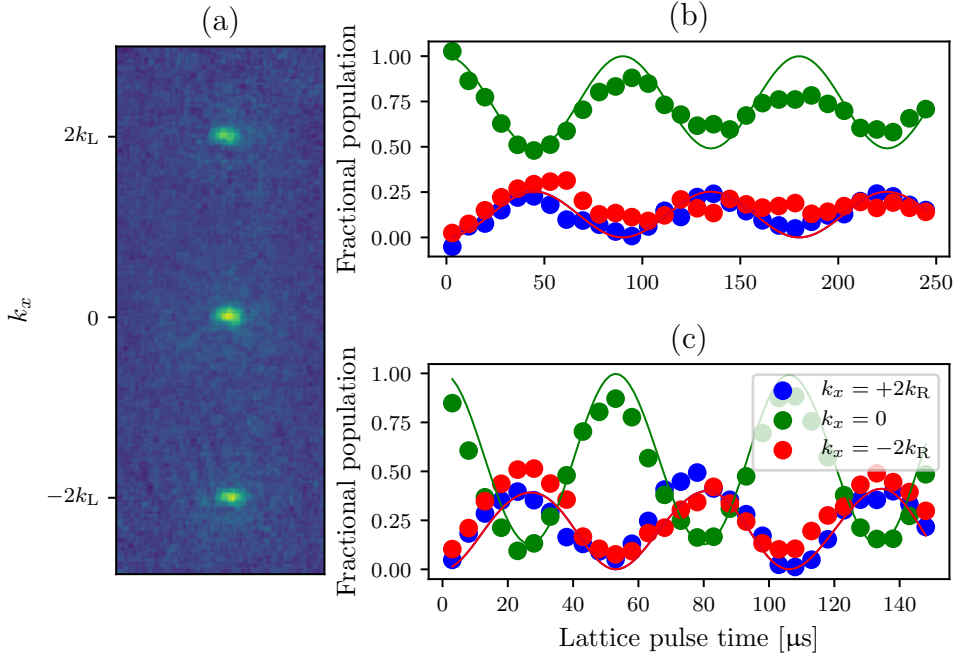


Figure 7: Lattice pulsing for calibration. (a) An example time-of-flight image from a pulsing experiment. The three different clouds are different momentum orders. (b) Fractional populations in the different momentum orders as a function of pulsing time at a low lattice power. Data is indicated by dots and best-fit theory is represented by lines. The lattice depth from fit is $V_0 = 5.57 \pm 0.07 E_L$. (c) Fractional populations in the different momentum orders as a function of pulsing time at a higher lattice power. Data is indicated by dots and best fit theory is represented by lines. The lattice depth from fit is $V_0 = 12.69 \pm 0.07 E_L$.

2.51 to the data with fitting parameter V_0 , thus deducing the lattice depth. Some examples of these pulsing experiments are presented in Figure 7b,c.

In contrast to pulsing, adiabatic loading turns the lattice on slowly, such that the atomic wavefunction starting in the bare ground state can continuously adjust to remain in the ground state of the current Hamiltonian, without projecting onto any of the higher bands. This process is illustrated in Figure 8. The adiabatic timescale depends on the spacing between the ground and next excited band (or if starting in a different eigenstate, the nearest eigenstate). If the energy difference between the ground and first excited state is ΔE , the timescale on which the lattice

is turned on must fulfill $t \gg h/\Delta E$.

2.6 Raman and rf coupling

In this section, we will introduce Raman and rf coupling between the hyperfine sublevels of the ground state of ^{87}Rb . While we will focus on the $F = 1$ and $F = 2$ manifolds of this ground state due to their relevance to the experiments described in Chapters 6 and 7, the discussion can be easily extended to any value of F .

2.6.1 Rf coupling Hamiltonian

For the $F = 1$ manifold, there are three available spin states $m_F = 0, \pm 1$. There are many ways of introducing coupling terms between the different hyperfine states. Here, we will explain two methods: rf coupling and Raman coupling. Rf coupling is a radio-frequency oscillating magnetic field, in our case produced by a pair of circular coils in series side by side above the atoms (see [73]). Assuming the rf oscillating field is polarized along the \mathbf{e}_x , with the bias field along \mathbf{e}_z , the coupling Hamiltonian is given by $H_{\text{rf}} = \mu_B g_F \hat{\vec{F}} \cdot \vec{B} = \mu_B g_F \hat{F}_x B_x \cos(\omega t)$, where $2\pi\omega$ is the rf frequency. The schematic of this setup is shown in Figure 9.

The eigenstates of the bare Hamiltonian H_0 are the constituent m_F states. The eigenstates of the coupled Hamiltonian $H_0 + H_{\text{rf}}(t)$ can be expressed as a linear superposition of the bare eigenstates $\Psi(\vec{x}, t) = \sum_{m_F} c_{m_F}(t) \phi_{m_F}(\vec{x}) e^{-i\omega_{m_F} t}$. The Hamiltonian in this basis can then be written as [71]

$$H_{\text{rf}} = H_{\text{KE}} + \hbar \begin{pmatrix} 0 & \Omega \cos(\omega t) e^{-i(\omega_z - \epsilon)t} & 0 \\ \Omega \cos(\omega t) e^{-i(\omega_z - \epsilon)t} & 0 & \Omega \cos(\omega t) e^{-i(\omega_z + \epsilon)t} \\ 0 & \Omega \cos(\omega t) e^{i(\omega_z + \epsilon)t} & 0 \end{pmatrix}, \quad (2.52)$$

where $\omega_z = (\omega_1 - \omega_{-1})/2$, ϵ is the quadratic Zeeman shift, and Ω is the Rabi fre-

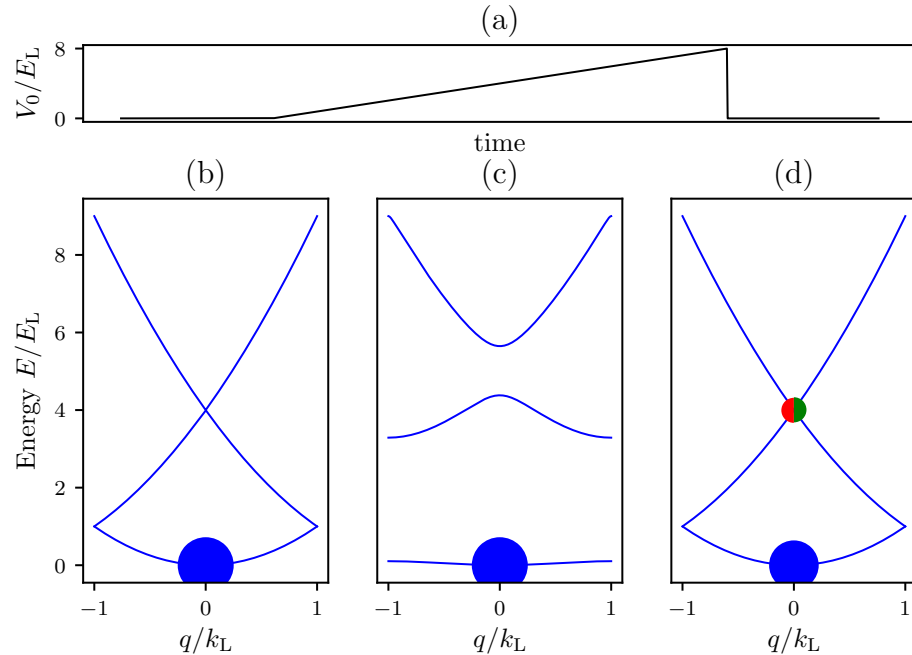


Figure 8: Adiabatic lattice loading. (a) Lattice depth as a function of time during adiabatic turn-on. The lattice is ramped on starting at $t = 0$, slowly increasing to a final lattice depth and turned off instantaneously at a final time $t = t_f$. (b) Atomic population before $t = 0$. All atoms are at $k = 0$ in the lowest bare band. (c) Atomic population after the lattice is turned on adiabatically to a lattice depth of $V_0 = 8.0E_L$. All atoms remain in the lowest band, but the band is no longer bare. (d) Atomic population after the lattice is snapped off. The wavefunction is projected back onto the bare states, with some fraction (blue circle) in the lowest band at $k = 0$ and some fraction in the excited band, with equal population being projected onto the $k = 2k_L$ (green) and $k = -2k_L$ (red). Since the lowest lattice band is a superposition of bare bands, some atoms are excited to the higher bare momentum states.

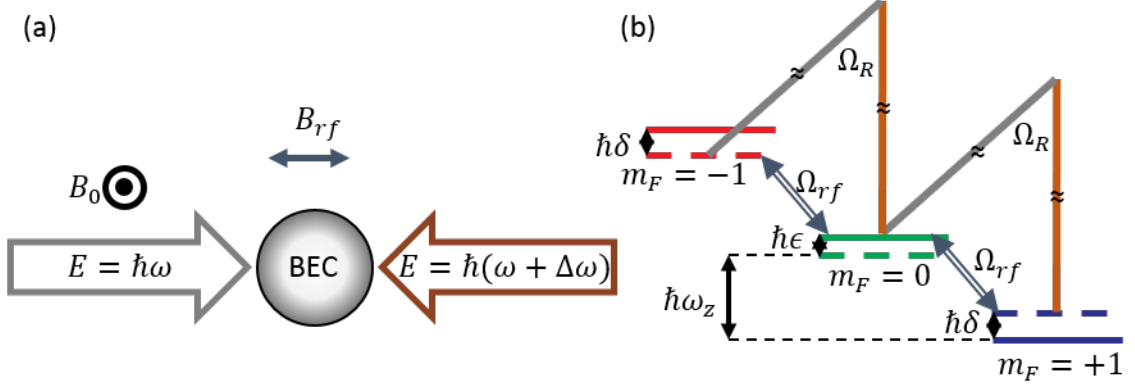


Figure 9: Raman and rf coupling schematic. (a) Beam geometry of the Raman beams and rf relative to the external field. The Raman beams have a frequency difference $\Delta\omega$, and are linearly polarized in perpendicular directions. (b) Level structure of both Raman and Rf coupling for hyperfine states of the $F = 1$ manifold. The hyperfine splitting separates the levels by an energy $\hbar\omega_z$. The quadratic Zeeman shift ϵ lowers the energy of the $m_F = 0$ state, and the detuning δ of either the Raman or the rf fields shifts the energies of the $m_F = \pm 1$ states. Raman transitions are two-photon, exciting up to a virtual state and coming back down to an adjacent hyperfine state, with an accompanying momentum transfer. Rf couples adjacent hyperfine states directly. Figure taken from ref. [74]

quency, proportional to B_x . We can then transfer into the rotating frame $c'_{m_F} = e^{-im_F\delta t+i(1-m_F^2)\epsilon t}c_{m_F}$, where $\delta = \omega_z - \omega$. Then we apply the rotating wave approximation, that the fast oscillating terms average to zero over time scales of interest $e^{2i\omega t} \approx 0$, and obtain

$$H_{\text{rf}} = H_{\text{KE}} + \hbar \begin{pmatrix} \delta & \Omega/2 & 0 \\ \Omega/2 & -\epsilon & \Omega/2 \\ 0 & \Omega/2 & -\delta \end{pmatrix}, \quad (2.53)$$

or for any value of F

$$H_{\text{rf}} = H_{\text{KE}} + \hbar\delta F_z + \hbar\epsilon F_z^2 + \Omega F_x/2, \quad (2.54)$$

which reduces to the above form for $F = 1$ with an overall energy shift of $\hbar\epsilon\mathcal{I}$.

The band structure of this Hamiltonian can be seen in Figure 10, where we have diagonalized eqn. 2.53 for a range of momenta k_x (we have isolated k_x for comparison with Raman coupling, as will be seen in the next section). The parabolas are simply the free particle dispersion relations along one dimension, with three bands arising from the three available spin states. It is convenient to define the magnetization of an eigenstate $m = \sum_{m_F} m_F p_{m_F}$, where p_{m_F} is the fractional population in the m_F state. We have indicated the magnetization of the eigenstate by coloring the eigenenergies, with $m = -1$ in red, $m = 0$ in green, and $m = +1$ in blue. In Figure 10a, both the detuning and the coupling strength are zero. Therefore, there are simply three free particle dispersion curves, each exactly correlated with a particular spin state, the $m_F = \pm 1$ are degenerate and the $m_F = 0$ state is slightly offset by the quadratic shift $\hbar\epsilon$. In Figure 10c, the coupling strength is again zero, but the detuning has been turned on, lifting the degeneracy between the $m_F = \pm 1$ states. Figure 10b,d shows the same conditions as a,c, respectively, but with the coupling strength turned on. In Figure 10b, where the detuning is zero and the quadratic shift is negligible compared to the coupling strength, all states average to a magnetization of zero—the $m_F = \pm 1$ states are symmetrically populated. In Figure 10d, this symmetry is broken by the presence of a detuning.

2.6.2 Raman coupling Hamiltonian

The counter-propagating Raman beams, as seen in Figure 9, couple the same states as the rf. They do so via the vector light shift created by the pair of beams. The electric field due to the right going beam (red in Figure 9a) is $\vec{E} = E_0 \exp(i k_R x - i\omega t) \mathbf{e}_y$, where E_0 is the amplitude of the electric field and $\hbar k_R = h/\lambda_R = \hbar\omega/c$. The electric field from the left going beam (gray in Figure 9b) is $\vec{E} = E_0 \exp(-i k_R x - i(\omega + \Delta\omega)t) \mathbf{e}_z$. This combines to give an effective field from the vector light shift [75] $B_{\text{eff}} \propto \vec{E} \times \vec{E}^* \propto -E_0^2 \cos(2k_R x + \Delta\omega t) \mathbf{e}_x$. Going through the same procedure as for

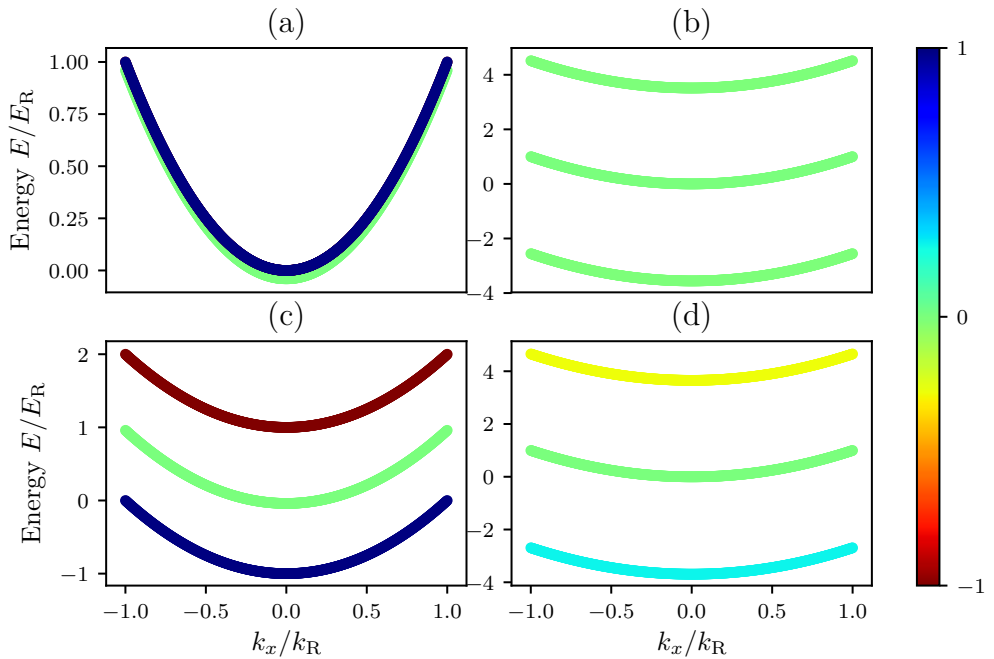


Figure 10: Band structure of the rf Hamiltonian, eqn. 2.53, in momentum space. For all plots, the quadratic Zeeman shift $\hbar\epsilon = 0.04E_R$, and the color represents magnetization, labeled by the colorbar. (a) $\hbar\Omega = 0$, $\hbar\delta = 0$. No coupling or detuning is present, so the only separation between the bands is due to the quadratic shift $\hbar\epsilon$. (b) $\hbar\Omega = 5.0E_R$, $\hbar\delta = 0$. (c) $\hbar\Omega = 0$, $\hbar\delta = 1.0E_R$. Even though the coupling strength is zero, the bands are separated by the detuning. (d) $\hbar\Omega = 5.0E_R$, $\hbar\delta = 1.0E_R$.

the rf coupling case, including the transfer into the rotating frame and the rotating wave approximation, we obtain the same Hamiltonian in the basis of bare spin states $| -1 \rangle, | 0 \rangle, | 1 \rangle$ but with an extra phase factor:

$$H_{\text{Raman}} = H_{\text{KE}} + \hbar \begin{pmatrix} \delta & \Omega/2e^{-i2k_{\text{R}}x} & 0 \\ \Omega/2e^{i2k_{\text{R}}x} & -\epsilon & \Omega/2e^{-i2k_{\text{R}}x} \\ 0 & \Omega/2e^{i2k_{\text{R}}x} & -\delta \end{pmatrix}, \quad (2.55)$$

where $\delta = \omega_z - \Delta\omega$.

This phase difference between the rf and Raman Hamiltonian has an intuitive physical explanation. In order to undergo a Raman transition, an atom first absorbs a photon from one beam, getting a momentum kick equal to the recoil momentum $\hbar k_{\text{R}}$. Then, to decay back down to an adjacent spin state, the atom undergoes stimulated emission into the field of the other (counter-propagating) beam, acquiring another recoil momentum kick in the same direction for a total of $2\hbar k_{\text{R}}\mathbf{e}_x$. Therefore, the Raman coupling Hamiltonian for $F = 1$, after transforming into the rotating frame and performing the rotating wave approximation, can be written in the same way as the rf Hamiltonian in eqn. 2.53 with the addition of a momentum kick—in real space, an acquired phase—of $e^{i2k_{\text{R}}x}$.

We can again make a basis transformation to get rid of this phase. Let us define $| -1' \rangle = \exp(-2ik_{\text{R}}x)| -1 \rangle = | k_x - 2k_{\text{R}}, -1 \rangle, | 0' \rangle = | 0 \rangle = | k_x, 0 \rangle, | 1' \rangle = \exp(2ik_{\text{R}}x)| 1 \rangle = | k_x + 2k_{\text{R}}, 1 \rangle$, where for third definition we went into the momentum basis and labeled the states by a combination of their momentum and spin state. Then, including the kinetic energy term along \mathbf{e}_x explicitly, we obtain the Hamiltonian in the new basis as:

$$H_{\text{Raman}} = H_{\text{KE}}^{(y,z)} + \begin{pmatrix} \frac{\hbar^2(k_x - 2k_{\text{R}})^2}{2m} + \hbar\delta & \hbar\Omega/2 & 0 \\ \hbar\Omega/2 & \frac{\hbar^2k_x^2}{2m} - \hbar\epsilon & \hbar\Omega/2 \\ 0 & \hbar\Omega/2 & \frac{\hbar^2(k_x + 2k_{\text{R}})^2}{2m} - \hbar\delta \end{pmatrix}. \quad (2.56)$$

It is convenient to define the Raman recoil energy as $E_R = \frac{\hbar^2 k_R^2}{2m}$. The band structure of this Hamiltonian is shown in Figure 11, for several representative parameter values, with the magnetization labeled by the color. Figure 11a shows the band structure in the limit of zero coupling and zero detuning, but where we have already gone into the basis $|k_x - 2k_R, -1\rangle, |k_x, 0\rangle, |k_x + 2k_R, 1\rangle$; therefore, the free particle parabola corresponding to the $m_F = 1$ spin states is shifted to center on $k_x = -2k_R$ and the $m_F = -1$ parabola is shifted to center on $k_x = 2k_R$. As the coupling is turned on to $\hbar\Omega = 1E_R$ in Figure 11b, the points where the parabolas cross become ‘avoided crossings’, separating into three bands where magnetization (and the underlying spin distribution) depends on the momentum k_x . As the coupling strength is turned up even further to $\hbar\Omega = 5E_R$ in Figure 11c, the lowest band goes from having three minima, one corresponding to each original spin state, to only one minimum. This transition happens at $\hbar\Omega = 4E_R$ [73]. In Figure 11d, we show the band structure again in the limit of zero coupling, but this time with a detuning of $\hbar\delta = 1.0E_R$. Note that the detuning tips the parabolas with respect to each other. Figure 11e shows the detuned system with coupling strength turned up to $\hbar\Omega = 1E_R$, still in the three minima regime but with avoided crossings creating three momentum and spin coupled bands. In Figure 11f, the detuned system is turned up to a coupling strength of $\hbar\Omega = 5E_R$, creating a single minimum, this time offset from $k_x = 0$.

We can write the general F version of the Raman coupled Hamiltonian in the basis $|k_x + m_F 2k_R, m_F\rangle$, where $-F \leq m_F \leq F$, as:

$$H_{\text{Raman}} = H_{\text{KE}}^{(y,z)} + \hbar^2(k_x \mathcal{I} + 2k_R F_z)^2 / 2m + \hbar\delta F_z + \hbar\epsilon F_z^2 + \Omega F_x / 2. \quad (2.57)$$

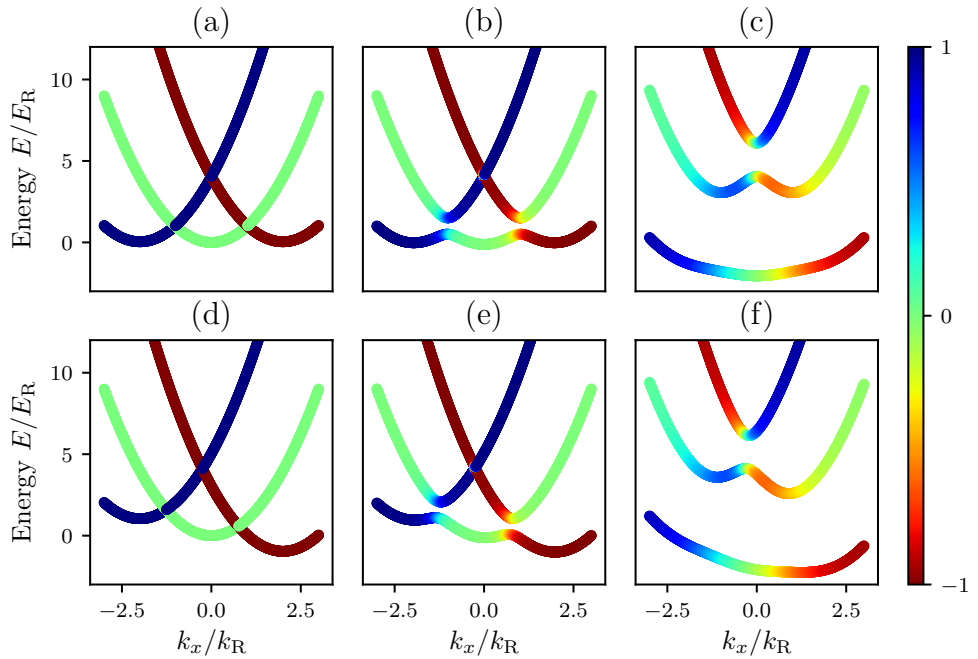


Figure 11: Band structure of the Raman Hamiltonian, eqn. 2.56, in momentum space. For all plots, the quadratic Zeeman shift $\hbar\epsilon = 0.04E_R$, and the color represents magnetization, labeled by the colorbar. (a) $\hbar\Omega = 0, \hbar\delta = 0$. (b) $\hbar\Omega = 1.0E_R, \hbar\delta = 0$. (c) $\hbar\Omega = 5.0E_R, \hbar\delta = 0.0$. (d) $\hbar\Omega = 0.0, \hbar\delta = 1.0E_R$. (e) $\hbar\Omega = 1.0E_R, \hbar\delta = 1.0E_R$. (f) $\hbar\Omega = 5.0E_R, \hbar\delta = 1.0E_R$.

2.6.3 Calibration of Raman and rf dressed states

To calibrate the rf and Raman coupling strengths, we take a similar approach to the 1-D lattice calibration: start in a pure spin state, for example $m_F = 0$, and turn the coupling on non-adiabatically to induce Rabi oscillations between the coupled states. Then, during time-of-flight, apply a Stern-Gerlach gradient pulse to separate the spin components and observe the fractional populations in different spin states as a function of Rabi oscillation time.

Figure 12a,b shows example images obtained in time-of-flight when pulsing on an rf coupling field for atoms in the $F = 1$ and $F = 2$ manifold, respectively. The Stern–Gerlach gradient pulse separates the spin components along the horizontal axis in the images. The fractional population in each state can then be obtained by summing up the optical depth in each cloud and dividing by the total optical depth. Similarly, Figure 13a shows an example time-of-flight image obtained when pulsing on a Raman coupling field on an $F = 1$ cloud initially in the $m_F = 0$ spin state. Here, the spin states are separated along the horizontal axis by the same Stern–Gerlach pulse. In addition, the recoil momentum obtained when undergoing a Raman transition separates the different spin states along the vertical axis—parallel to the Raman beams along \mathbf{e}_x . The direction of the Stern–Gerlach gradient was chosen purposefully to be perpendicular to the Raman direction \mathbf{e}_x for easy separation of the two effects.

These population oscillations can then be fit for coupling strength $\hbar\Omega$ and detuning $\hbar\delta$. Note that the quadratic Zeeman shift $\hbar\epsilon$ is set by the strength of the bias field B_0 and therefore often well known—it is not a fitting parameter. The theoretical predictions are obtained by applying the time evolution operator $U = \exp(-iH_{\text{Raman/rf}}t/\hbar)$ to an initial state Ψ in the appropriate basis. Figure 12c shows an example time series of rf pulsing in the $F = 1$ manifold, starting in the

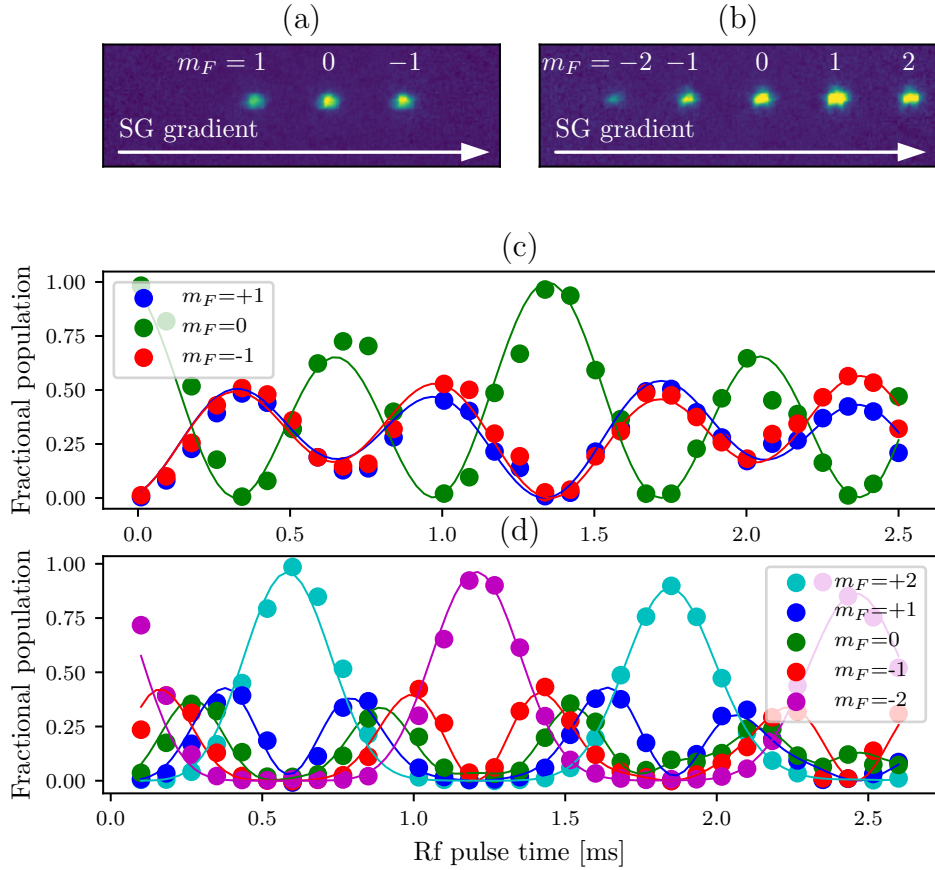


Figure 12: Pulsing on rf coupling. (a) Example time-of-flight image during an rf pulsing experiment in the $F = 1$ manifold. Spin states are separated via a Stern–Gerlach pulse along the horizontal direction. (b) Example time-of-flight image during an rf pulsing experiment in the $F = 2$ manifold. Here, 5 spin components are present. (c) Pulsing experiment in the $F = 1$ manifold. Dots represent fractional populations in different spin states measured from time-of-flight images, and lines represent best-fit theory curves. Fitted parameters are $\hbar\Omega = (0.863 \pm 0.004)E_R$, $\hbar\delta = (-0.198 \pm 0.007)E_R$. (d) Pulsing experiment in the $F = 2$ manifold. Dots represent fractional populations in different spin states measured from time-of-flight images, and lines represent best-fit theory curves. Fitted parameters are $\hbar\Omega = (1.000 \pm 0.002)E_R$, $\hbar\delta = (-0.061 \pm 0.001)E_R$. $\hbar\epsilon = 0.038E_R$ for all panels.

$m_F = 0$ state. The lines of best fit are overlayed on experimental data, extracting fit parameters $\hbar\Omega = (0.863 \pm 0.004)E_R$ and $\hbar\delta = (-0.198 \pm 0.007)E_R$. Figure 12d shows an example time series of rf pulsing in the $F = 2$ manifold, starting in the $m_F = -2$ state. Here, the extracted fit parameters were $\hbar\Omega = (1.000 \pm 0.002)E_R$ and $\hbar\delta = (-0.061 \pm 0.001)E_R$.

Figure 13b shows an example time series of Raman pulsing in the $F = 1$ manifold, starting in the $m_F = 0$ state, with fitted parameters $\hbar\Omega = (1.47 \pm 0.01)E_R$ and $\hbar\delta = (0.004 \pm 0.024)E_R$. Note that although the coupling strength is almost double the rf coupling strength in Figure 12c, the contrast (peak to peak oscillation of the fractional population in, say, the $m_F = 0$ state) is much lower in the Raman data than in the rf. This is a direct consequence of the recoil momentum transfer, and can be understood by looking at the band structure. For rf, the coupled bands at initial momentum $k_x = 0$ are separated by the coupling strength, see Figure ??b. For Raman, even at zero coupling strength, due to the shifting of the parabolas by $2k_R$, and $k_x = 0$ the higher bands are $\hbar^2(2k_R)^2/2m = 4E_R$ separated from the lower bands. Therefore, the energy difference is larger and the fraction in the excited band will be lower, leading to lower contrast.

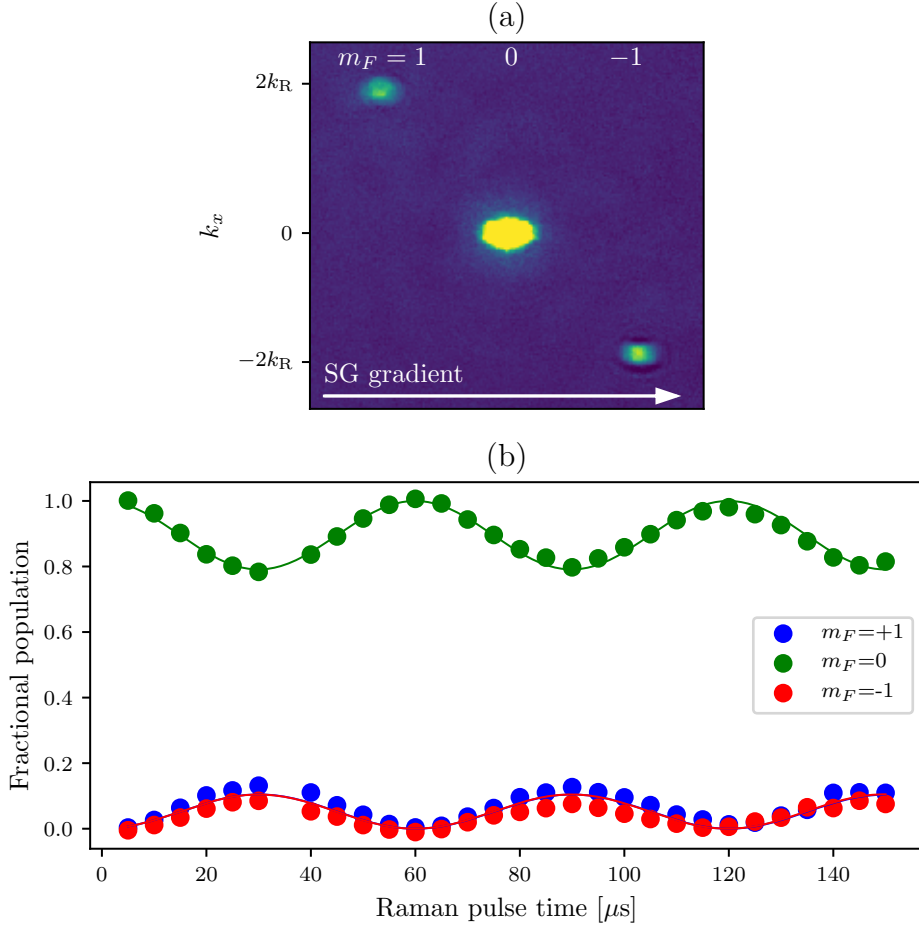


Figure 13: Pulsing on Raman coupling. (a) Example time-of-flight image during a Raman pulsing experiment in the $F = 1$ manifold. A Stern–Gerlach pulse during time-of-flight separates different spin components along the horizontal direction, and different momentum orders fly apart along the vertical direction. (b) Fractional population in different spin states during a Raman pulsing experiment as a function of time. Dots represent data and lines represent a best fit from theory. The fitted parameters are $\hbar\Omega = (1.47 \pm 0.01)E_R$, $\hbar\delta = (0.004 \pm 0.024)E_R$. The quadratic Zeeman shift was $\hbar\epsilon = 0.038E_R$.

Chapter 3: Ultracold Gases and the RbK apparatus

In this chapter we introduce the basics of ultracold quantum gases. When cooled to extremely low temperatures, bosonic atoms form Bose Einstein condensates, described in sec. 3.1. Fermionic atoms do not undergo a phase transition, but gradually become degenerate, forming what's known as a degenerate Fermi Gas, described in sec. 3.2. We then give a basic overview of the rubidium-potassium (RbK) apparatus at NIST, on which the work described in this thesis was done, in sec. 3.3. We detail some of the changes that have been made to the apparatus since it was last documented.

3.1 Bose-Einstein condensation

In this section, we give some basic background on Bose-Einstein condensation, relevant to ^{87}Rb atoms cooled in our apparatus.

3.1.1 Phase transition of a non-interacting Bose gas

Bose gases are characterized by the Bose-Einstein distribution giving the number of atoms $n(E_j)$ occupying each energy eigenstate E_j as

$$n(E_j) = \frac{1}{e^{(E_j - \mu)/k_B T} - 1}, \quad (3.1)$$

where k_B is the Boltzmann constant, T is the temperature in Kelvin, and μ is the chemical potential. Assuming the total atom number N is fixed, the chemical

potential $\mu(T, N)$ ensures that the total occupation $\sum_j n(E_j) = N$.

The Bose distribution leads to Bose-Einstein condensation, the collapse of a macroscopic fraction of the atoms into the ground state. This comes as a direct consequence of the Bose distribution's characteristic -1 in the denominator. Consider the occupation number $n(E_j)$. It must remain positive, as a negative occupation number is unphysical. This implies the quantity $e^{(E_j - \mu)/k_B T}$ must remain greater than 1, or $(E_j - \mu)/k_B T > 0$ for all E_j . Therefore, $\mu \leq E_0$, where E_0 is the ground state energy.

Then, for a given temperature T , there is a maximum occupation number for each excited state given by $n(E_j) = \frac{1}{e^{E_j/k_B T} - 1}$. The only energy state whose occupation number is unbounded is the ground state, as $n(E_0)$ tends toward infinity as μ tends towards 0. Therefore, as the temperature decreases, the maximum occupation of each excited state decreases until they can no longer support all N of the atoms. The remaining atoms then have no choice but to collapse into the lowest energy level and Bose condense.

We will show this quantitatively for the case of a 3-D harmonically trapped gas of non-interacting atoms, relevant to the experiments described in this thesis [76]. It is convenient to define the fugacity $\zeta = e^{\mu/k_B T}$, and re-write the Bose-Einstein distribution for some eigenstate E_j as

$$n(E_j) = \frac{\zeta}{e^{E_j/k_B T} - \zeta}. \quad (3.2)$$

The harmonic oscillator potential can be written as

$$V(r) = \frac{1}{2}m(\omega_x^2x^2 + \omega_y^2y^2 + \omega_z^2z^2), \quad (3.3)$$

where ω_x , ω_y and ω_z are the angular trapping frequencies along \mathbf{e}_x , \mathbf{e}_y , and \mathbf{e}_z . The

eigenenergies with this potential are

$$E(j_x, j_y, j_z) = \left(\frac{1}{2} + j_x\right)\hbar\omega_x + \left(\frac{1}{2} + j_y\right)\hbar\omega_y + \left(\frac{1}{2} + j_z\right)\hbar\omega_z. \quad (3.4)$$

In order to find μ , we must find $\sum_{j_x, j_y, j_z} n(E(j_x, j_y, j_z))$ and set it equal to N . This task is greatly simplified by going to the continuum limit and finding the density of states. To do this, we neglect the zero-point energy (setting $E_0 = 0$, the effects of the zero-point energy are discussed in [77] section 2.5) and assume there is on average one state per volume element $\hbar^3\omega_x\omega_y\omega_z$. Then, the total number of states with energy less than or equal to some value ϵ is given by the volume of a prism made between points $(j_x, j_y, j_z) = (0, 0, 0), (\epsilon, 0, 0), (0, \epsilon, 0)$ and $(0, 0, \epsilon)$ in units of the volume element:

$$G(\epsilon) = \frac{\epsilon^3}{6\hbar^3\omega_x\omega_y\omega_z}. \quad (3.5)$$

The density of states is given by

$$g(\epsilon) = \frac{d}{d\epsilon}G(\epsilon) = \frac{\epsilon^2}{3\hbar^3\omega_x\omega_y\omega_z}. \quad (3.6)$$

Note that the occupation of the ground state is not included in this continuum picture. We can therefore use it only to calculate the total number of atoms in all of the excited states:

$$N_{\text{ex}} = \int_0^\infty d\epsilon g(\epsilon)n(\epsilon) = \int_0^\infty d\epsilon \frac{\epsilon^2}{3\hbar\omega_x\omega_y\omega_z} \frac{\zeta}{e^{\epsilon/k_B T} - \zeta} = \frac{(k_B T)^3}{\hbar^3\omega_x\omega_y\omega_z} \text{Li}_3(\zeta), \quad (3.7)$$

where $\text{Li}_3(\zeta)$ is the polylogarithm function¹. We define the mean trapping frequency $\bar{\omega} = (\omega_x\omega_y\omega_z)^{1/3}$ and the harmonic oscillator energy as $\hbar\bar{\omega}$, with the thermal energy

¹This calculation was done with Wolfram Alpha, not Russian algebra skills

in harmonic oscillator units $\tau = k_B T / \hbar \bar{\omega}$, giving

$$N_{\text{ex}} = \tau^3 \text{Li}_3(\zeta). \quad (3.8)$$

Finding the occupation number of the ground state from the Bose-Einstein distribution

$$N_0 = \frac{\zeta}{1 - \zeta}, \quad (3.9)$$

we can then find the chemical potential, or equivalently the fugacity ζ , to satisfy

$$N = N_0 + N_{\text{ex}}. \quad (3.10)$$

This is a transcendental equation that can only be solved numerically. We present an example of the solution in Figure 1. Here, we have calculated the fractional population in different harmonic oscillator energy levels for three different temperatures, using trapping frequencies $\omega_x = \omega_y = \omega_z = 2\pi \times 50$ Hz, and atom number $N = 10^6$. For energies above the ground state (dots in the figure), we binned 50 energy levels together, such that each dot represents the total fractional population in 50 adjacent levels. This was obtained by integrating eqn. 3.7 from $\epsilon - 25\hbar\bar{\omega}$ to $\epsilon + 25\hbar\bar{\omega}$. The stars represent the fractional population in just the ground state, calculated from eqn. 3.9. Note that at temperature $T = 255$ nK (red), the ground state population is consistent with a continuous extrapolation from the excited state populations and is almost zero. At lower temperatures, $T = 180$ nK (blue) the ground state population is in excess of any reasonable extrapolation from the excited state fractions, and at $T = 80$ nK (green) almost all the atoms are in the ground state.

The onset of Bose-Einstein condensation occurs at a critical temperature T_c . This temperature is defined as the temperature at which the occupation number of excited states is equal to the atom number, i.e. when the atoms have occupied all

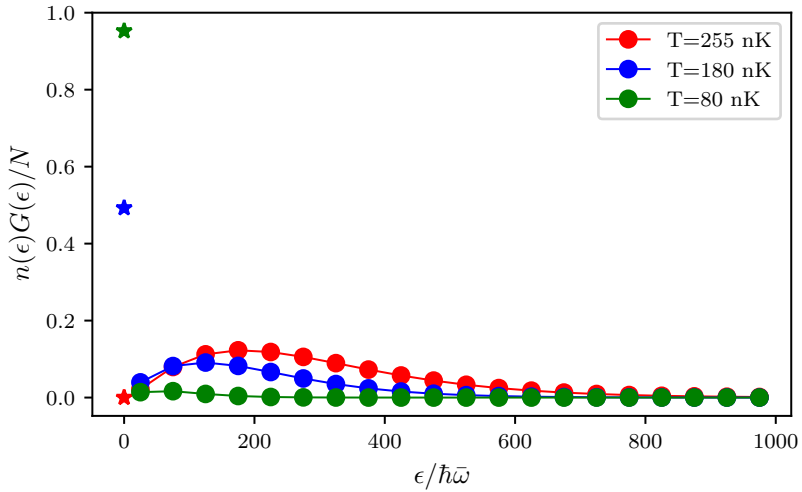


Figure 1: Occupation of energy states of a 3-D harmonic oscillator. The trapping frequencies are $\omega_x = \omega_y = \omega_z = 2\pi \times 50$ Hz, and the atom number is $N = 10^6$. Dots represent the total fractional population in 50 adjacent energy levels, including degeneracies. The stars represent the fractional population in just the ground state.

available excited states and any remaining atoms were forced to pile into the ground state. Since the maximal occupation of the excited states will occur at $\mu = 0$, the occupation of the excited state is bounded from above by $N_{\text{ex}}(\mu = 0)$, and the critical temperature is defined by

$$N = N_{\text{ex}}(\mu = 0, T = T_c) = \frac{(k_B T_c)^3}{\hbar^3 \omega_x \omega_y \omega_z} \text{Li}_3(\zeta = 1). \quad (3.11)$$

Using $\text{Li}_3(1) \approx 1.202$, we obtain for a given atom number and trapping frequencies

$$T_c = \frac{1.202 N}{k_B^3} \hbar^3 \omega_x \omega_y \omega_z. \quad (3.12)$$

For the parameters in Figure 1, $T_c = 225$ nK.

For temperatures below the critical temperature, the condensation fraction f_c —the fraction of atoms in the ground state—is directly related to the ratio of the

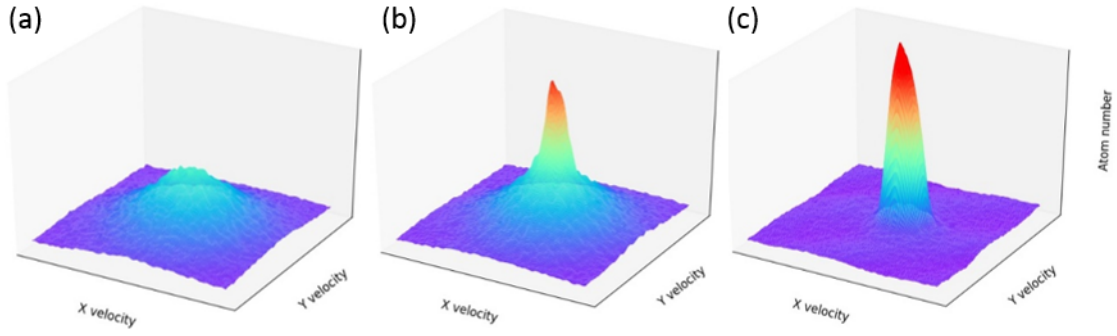


Figure 2: Time-of-flight images of atoms. (a) Above the critical temperature - the atoms are thermally distributed. (b) Below the critical temperature - about half of the atoms are condensed in the central peak. (c) Far below the critical temperature - almost all atoms are condensed in the central peak.

temperature to the critical temperature:

$$f_c = 1 - \frac{N}{N_{\text{ex}}} = 1 - \frac{(k_B T)^3}{\hbar^3 \omega_x \omega_y \omega_z} \text{Li}_3(\zeta = 1) = 1 - \left(\frac{T}{T_c} \right)^3, \quad (3.13)$$

where in the last step we have plugged in the definition of the critical temperature eqn. 3.12.

Figure 2 shows the progression towards condensation as the temperature of a cloud of ^{87}Rb is decreased below T_c . The images are obtained via a time-of-flight measurement (see section 2.4.1), where the atoms are allowed to expand freely, mapping the initial momentum to final position, imaged via absorption imaging (see section 2.4). The x and y axes represent momentum along x and y , while the z axis represents the number of atoms per spatial bin. The z axis momentum is integrated over. Figure 2a shows a cloud above the condensation temperature - the momentum distribution is nearly gaussian, given by the Maxwell-Boltzmann distribution. In fig. 2b, the temperature has been decreased below T_c , and about half the atoms have collapsed into the ground state, producing a large peak in atom number around zero momentum. In fig. 2c, the temperature has been decreased

even further and almost all the atoms populate the central peak - the distribution is no longer gaussian but a sharp peak around zero momentum.

3.1.2 Interacting Bose gas

In the previous section, we assumed there were no interaction between the atoms other than those enforced by statistics. In this section, we will relax this assumption somewhat and describe the condensed atomic state through its characteristic Gross-Pitaevskii equation.

Since condensation occurs at very low temperatures, and thus very low kinetic energies, we can assume that any scattering processes between the atoms are *s*-wave and can be described simply by a scattering length a (equivalent to assuming that the characteristic size of the atomic wavefunction, given by the thermal deBroigle wavelength, is large compared to the scale of the interatomic potential). For ^{87}Rb , relevant to experiments described in this thesis, the scattering length between two atoms in the $F = 2$ hyperfine state is $a = 95.44(7)a_0$ [78], where $a_0 = 5.29 \times 10^{-11}$ m is the Bohr radius. The short-range interaction between two particles can be approximated as a contact interaction with an effective strength U_0 as (see [77] section 5.2.1):

$$U(r_1, r_2) = U_0\delta(r_1 - r_2) = \frac{4\pi\hbar^2 a}{m}\delta(r_1 - r_2), \quad (3.14)$$

where m is the atomic mass and δ is the Dirac delta function. The full Hamiltonian of the many-body system is then

$$H = \sum_i \frac{p_i^2}{2m} + V(r_i) + U_0 \sum_{i < j} \delta(r_i - r_j), \quad (3.15)$$

where i labels the particles, p_i is the momentum, r_i is the position, and V is the external potential.

We make the mean field approximation by assuming that no interactions be-

tween two atoms take them out of the ground state, and hence all atoms can be assumed to be in the same single particle wavefunction, making the overall wavefunction

$$\Psi(r_1, r_2, \dots, r_N) = \prod_i^N \phi(r_i), \quad (3.16)$$

where ϕ is the single particle wavefunction. It is convenient to define the wavefunction of the condensed state, $\psi(r) = \sqrt{N}\phi(r)$, making the normalization $N = \int dr |\psi(r)|^2$.

The energy of this wavefunction under the Hamiltonian above is given by

$$E = \int dr \left[\frac{\hbar^2}{2m} |\nabla \psi(r)|^2 + V(r) |\psi(r)|^2 + \frac{1}{2} U_0 |\psi(r)|^4 \right]. \quad (3.17)$$

Given N particles, there are $N(N - 1)/2$ unique pairs of particles that can have a pairwise interactions, approximately equal to $N^2/2$ for large N . The N^2 is absorbed into the definition of ψ , but the factor of $1/2$ remains on the final interaction term. The task of finding the condensate eigenstate reduces to minimizing this energy under the normalization constraint $N = \int dr |\psi(r)|^2$. This can be done by using the method of Lagrange multipliers to minimize $E - \mu N$. Then, we can minimize this quantity by finding the point where the derivative with respect to ψ and ψ^* is zero. Taking the derivative with respect to ψ^* we obtain

$$-\frac{\hbar^2}{2m} \nabla^2 \psi(r) + V(r) \psi(r) + U_0 |\psi(r)|^2 \psi(r) = \mu \psi(r), \quad (3.18)$$

which is the Gross-Pitaevskii equation. This is a non-linear equation that generally needs to be solved numerically.

There is another approximation that can be made in cases where the atomic density is high enough that the interaction energy is significantly larger than the kinetic energy. Then, the kinetic term in the Hamiltonian can be neglected. This is

called the Thomas-Fermi approximation. In this approximation, the wavefunction is given simply by

$$|\psi(r)|^2 = \frac{\mu - V(r)}{U_0}. \quad (3.19)$$

Here, the probability density simply takes the shape of the inverted potential in which the atoms are held. In the case of a harmonically trapped BEC, it is shaped like an inverted parabola. The Thomas-Fermi radius, i.e. the extent of the particle wavefunction, is the point where the probability density goes to zero: $\mu - V(r_0) = 0$. For a harmonic trap, along any direction, this is given by $r_0^2 = 2\mu/m\omega^2$.

Figure 3a shows an absorption image of a small fraction of atoms in a BEC *in situ* (see section 2.4.1), meaning as it is in the trap - without expanding in time-of-flight. The x and y axes represent position, while color represents the atom number. Figure 3b shows the atom number integrated over the y -axis in blue. The red dashed lines represent the best fit line to a Thomas-Fermi distribution, here an inverted parabola. The black dashed lines represent the best fit of a Gaussian to the atomic distribution. The Thomas-Fermi distribution matches the atomic distribution more closely in the center where the density is high, but the Gaussian distribution does a better job at the tails of the distribution. This is due to the presence of some fraction of uncondensed atoms, which are well approximated by a Maxwell-Boltzmann distribution.

3.2 Degenerate Fermi Gas

In this section, we give some basic background on degenerate Fermi gases, relevant to ^{40}K atoms cooled in our apparatus.

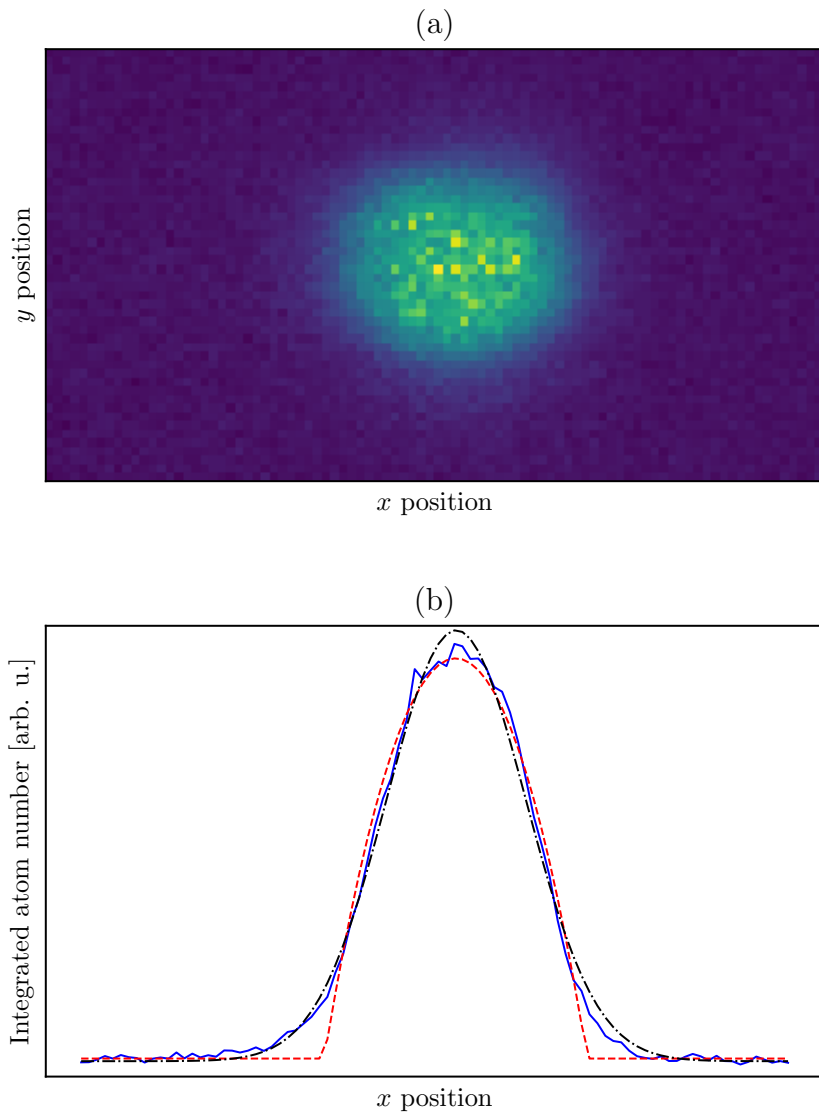


Figure 3: In situ measurement of Bose condensed atoms. (a) Absorption image taken of $\approx 1\%$ of the cloud. The x and y axes represent x and y position, while color represents the atom number. (b) The blue line represents atom number as a function of position along the x axis, integrated over the y axis. The black dashed line represents the best fit of a Gaussian function to the atomic distribution. The dashed red line represents the best fit of a Thomas-Fermi profile to the atomic distribution.

3.2.1 Fermi statistics and the onset of degeneracy

The occupation of different energy levels E_j by Fermions is given by the Fermi-Dirac distribution:

$$n(E_j) = \frac{1}{e^{(E_j - \mu)/k_B T} + 1}. \quad (3.20)$$

The difference from the Bose-Einstein distribution is simply the sign of the 1 in the denominator. This has important implications, however. First, since e^x varies between 0 and ∞ , the occupation $n(E_j)$ varies between 1 and 0 - a consequence of the Pauli exclusion principle. Second, as the temperature T tends towards 0, there become two distinct cases: $E_j - \mu > 0$ and $E_j - \mu < 0$. If $E_j - \mu > 0$, $e^{(E_j - \mu)/k_B T}$ tends towards ∞ , and $n(E_j)$ tends towards 0. If $E_j - \mu < 0$, $e^{(E_j - \mu)/k_B T}$ tends towards 0, and $n(E_j)$ tends towards 1. Therefore, at $T = 0$, the energy states below the chemical potential μ are maximally occupied (with probability 1) and the energy states above the chemical potential are unoccupied.

We can use this to determine the chemical potential at $T = 0$ by constraining the total atom number:

$$N = \sum_j n(E_j) = \sum_{E_j < \mu} 1. \quad (3.21)$$

Again, we take the common example of the 3-D harmonic trap. Then the task reduces to simply finding the number of energy levels at or below a certain energy μ . This is given by eqn. 3.5. From this, we find the chemical potential at zero energy, which is known as the Fermi energy E_F , as

$$E_F = (6N)^{1/3} \hbar \bar{\omega}, \quad (3.22)$$

where $\bar{\omega} = (\omega_x \omega_y \omega_z)^{1/3}$ is the geometric mean of the three trapping frequencies.

From the Fermi energy, we can define the associated Fermi temperature T_F as

$$T_F = \frac{(6N)^{1/3} \hbar \bar{\omega}}{k_B}, \quad (3.23)$$

and the Fermi momentum $\hbar k_F$ as

$$\hbar k_F = \sqrt{2mE_F}, \quad (3.24)$$

where m is the mass of the Fermion.

For higher temperatures, we can solve for the chemical potential, or the fugacity ζ , by integrating the Fermi-Dirac distribution weighted by the density of states (eqn. 3.6) to obtain

$$N = \int_0^\infty \frac{\epsilon^2}{2\hbar^3 \bar{\omega}^3} \frac{\zeta}{e^{\epsilon/k_B T} + \zeta} = -\frac{(k_B T)^3}{\hbar^3 \bar{\omega}^3} \text{Li}_3(-\zeta), \quad (3.25)$$

where Li_3 is again the polylogarithm function. Again, this is a transcendental equation that can be solved numerically. However, in contrast to the BEC case, we do not have to consider the ground state occupation separately, as it is bounded by 1 like every other state.

We show an example of the occupation distribution for different temperatures in Figure 4. Here, we have used the same parameter values as for the BEC case: $N = 10^6$ and $\omega_x = \omega_y = \omega_z = 2\pi \times 50$ Hz. The Fermi temperature for these parameters is $T_F = 436$ nK. For illustrative purposes, we plot $n(\epsilon)$, unweighted by the density of states $g(\epsilon)$. At zero temperature (red line in the figure), only states below the Fermi energy are occupied. At higher temperatures, the distribution is smoothed out (green and orange lines) until at the Fermi temperature there is almost no significance to the Fermi energy.

In contrast with Bose-Einstein condensation, the transition to a Degenerate

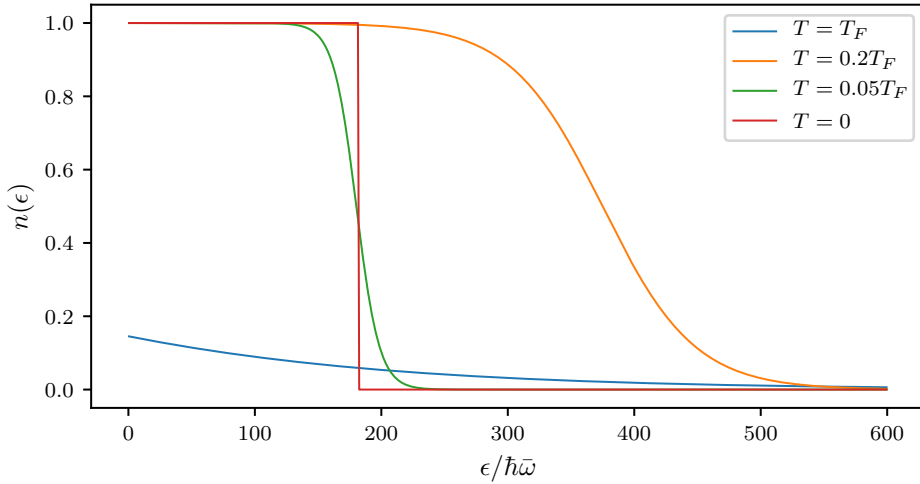


Figure 4: Occupation number as a function of energy for a Fermi gas of $N = 10^6$ atoms in a 3-D harmonic oscillator with frequencies $\omega_x = \omega_y = \omega_z = 2\pi \times 50$ Hz. The Fermi temperature for these parameters is $T_F = 436$ nK.

Fermi Gas (DFG) is not a phase transition, and there is no absolute measure of the onset of degeneracy. Instead, a Fermi gas can be considered degenerate when the occupation function $n(\epsilon)$ differs significantly from that of a thermal gas. This occurs when the temperature is of order $0.2T_F$.

3.2.2 Interactions and Feshbach resonances

Although the magnitude of the contact interaction U_0 for DFGs is not intrinsically different from that of BECs, there are two key differences. First, the Pauli exclusion principle forbids s -wave interactions between atoms of the same spin. Higher partial wave interactions are 'frozen out' at low temperatures, when the impact parameter of the collision becomes larger than the effective cross section of interactions (see [79], sec. 2.1.2). Therefore, in order to observe interactions, and indeed to cool the gas to degeneracy, another species needs to be present so that intraspecies s -wave interactions can occur. This can be a different atomic species or a different spin state of the same atom.

Second, the densities of standard DFGs ($\approx 10^{12}$ atoms/cm 3) are much lower than that of BECs ($\approx 10^{14}$ atoms/cm 3). Since the likelihood of two-body collisions is proportional to the atomic density ρ^2 , this leads to a much smaller effect of interactions in DFGs.

A widely used technique for enhancing interaction effects in DFGs (and to a more limited extent, BECs) is Feshbach resonances [80–84]. A Feshbach resonance occurs between two species (either atomic species or spin species of the same atom) when the open channel, i.e. the two particles independently in their external potential, energetically approaches a closed channel, i.e. a bound molecular state of the two species, shown schematically in Figure 5a.

Generally, the atoms in an open channel are energetically sensitive to a background magnetic field \vec{B} via the hyperfine interaction $H_B = -\vec{\mu} \cdot \vec{B}$, where μ is the magnetic dipole moment. Tuning the magnetic field should therefore tune the energy of the open channel with respect to the closed channel. The molecular bound state may also have an overall magnetic moment, but it is generally not identical to that of the two atoms in the open channel, and therefore varies differently with the background field. Figure 5b shows an example where the bound state has zero magnetic moment. Here, the energy of both the closed and open channel as a function of background magnetic field \vec{B} is plotted in the vicinity of a Feshbach resonance. The resonance occurs at a field magnitude B_0 where the energies of the two channels coincide.

Assuming there is at least infinitesimal coupling between the closed and open channels, as the energies of the two channels approach each other the perturbative correction term to the energy grows and the interaction between the atoms is affected. This is most easily seen in the *s*-wave case through changes in the scattering length a . In the case where there are no inelastic two-body channels, such as for the ${}^{40}\text{K}$ resonance discussed in this thesis, the interatomic scattering length as a

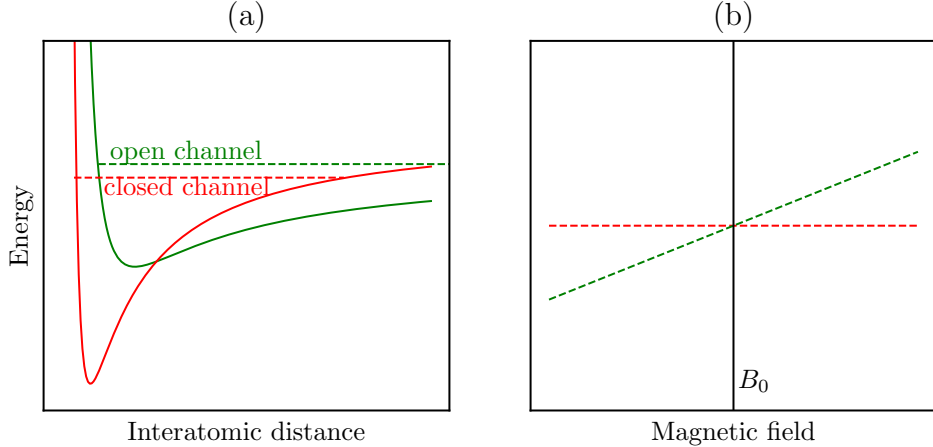


Figure 5: Schematic of a Feshbach resonance. (a) Pictoral representation of energy as a function of interatomic distance for an open channel (red) and closed channel (blue). (b) Energy as a function of background magnetic field B for the closed (blue) and open (red) channels. The energies coincide at the Feshbach resonance point B_0 .

function of background field is given by [40]

$$a(B) = a_{\text{bg}} \left(1 - \frac{\Delta}{B - B_0} \right), \quad (3.26)$$

where a_{bg} is the background scattering length, Δ is the width of the resonance, and B_0 is the field value at which the resonance occurs. The scattering length diverges at the resonance.

The tunability of interactions provided by Feshbach resonances has allowed for creation of molecular Bose-Einstein condensates from Fermi gases [42, 43, 45] as well as observation of the phase transition from the Bardeen-Cooper-Schrieffer (BCS) superconducting regime to the BEC regime at sufficiently low temperatures [44, 46, 85, 86].

3.3 RbK apparatus

The rubidium-potassium (RbK) apparatus at NIST Gaithersburg has been previously detailed in [73, 87, 88]. In this thesis, we will give a brief overview of the

apparatus and how it is used to produce BECs of ^{87}Rb and DFGs of ^{40}K , and only give detailed documentation for those parts of the apparatus that differ from previous works.

A photograph of the main experiment is shown in Figure 6. This is mounted on an optical table, with the science chamber elevated above the surface of the table. The atoms start at the ovens (off to the right, not in the photograph) and travel down the Zeeman slower until they are trapped in the science chamber. The optical dipole trap laser, as well as the 1-D optical lattice laser, are located on the optical table and coupled into optical fibers, which are output on the main floor of breadboard before being sent towards the atoms. All other lasers are located on other optical table and brought over to the experiment table via optical fibers.

3.3.1 Laser beams

Figure 7 details the beam paths of the light going through the atoms. Figure 7a shows a side view of the apparatus. The up and down going MOT cooling beams are shown in red, reaching the atoms when the flipper mirrors M_{top} and M_{bottom} are flipped in. The down going probe beam, used for imaging along the $x - y$ axis both in situ and in time-of-flight, is shown in solid blue. The probe beam is split via a polarizing beam splitter cube to allow for both in situ and time-of-flight imaging of the same cloud, shown in the inset in fig. 7b and described in greater detail in sec. 3.3.4. The dashed blue line represents the upward going probe beam introduced for alignment purposes, described in greater detail in sec. 3.3.4. The kinematic base mirror (green in the figure) is removable, and only inserted when the alignment beam is in use.

Figure 7b show's a bird's eye view of the apparatus, with optics on the main floor breadboard. The slower cooling (solid dark blue) and slower repump (dashed dark blue) are coming in from the left to slow the atoms as they are moving through

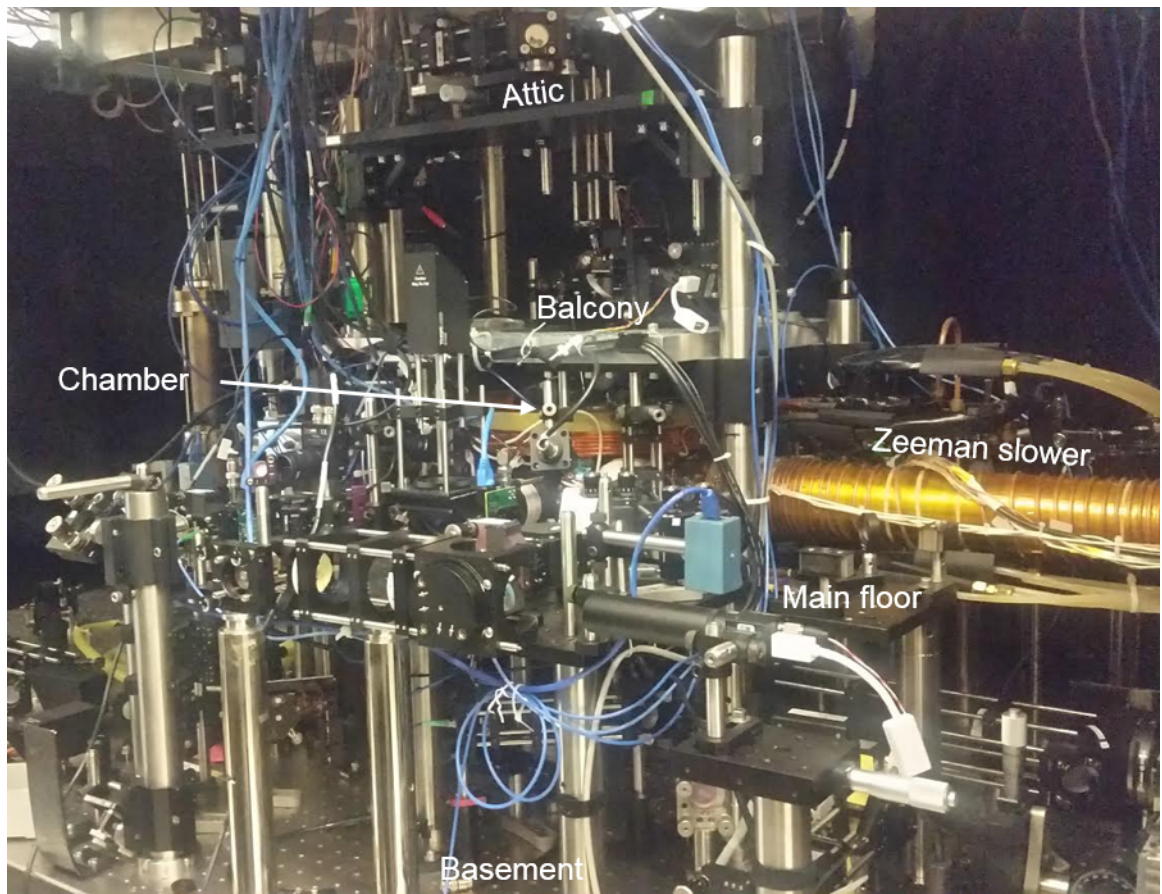


Figure 6: Photograph of RbK apparatus at NIST Gaithersburg. The main science chamber is at the center, hidden behind optics and coils. The Zeeman slower connects the atomic ovens (not shown) to the chamber. There are several levels of breadboards on which optics are mounted, labelled here as basement (surface of optical table), main floor, balcony and attic.

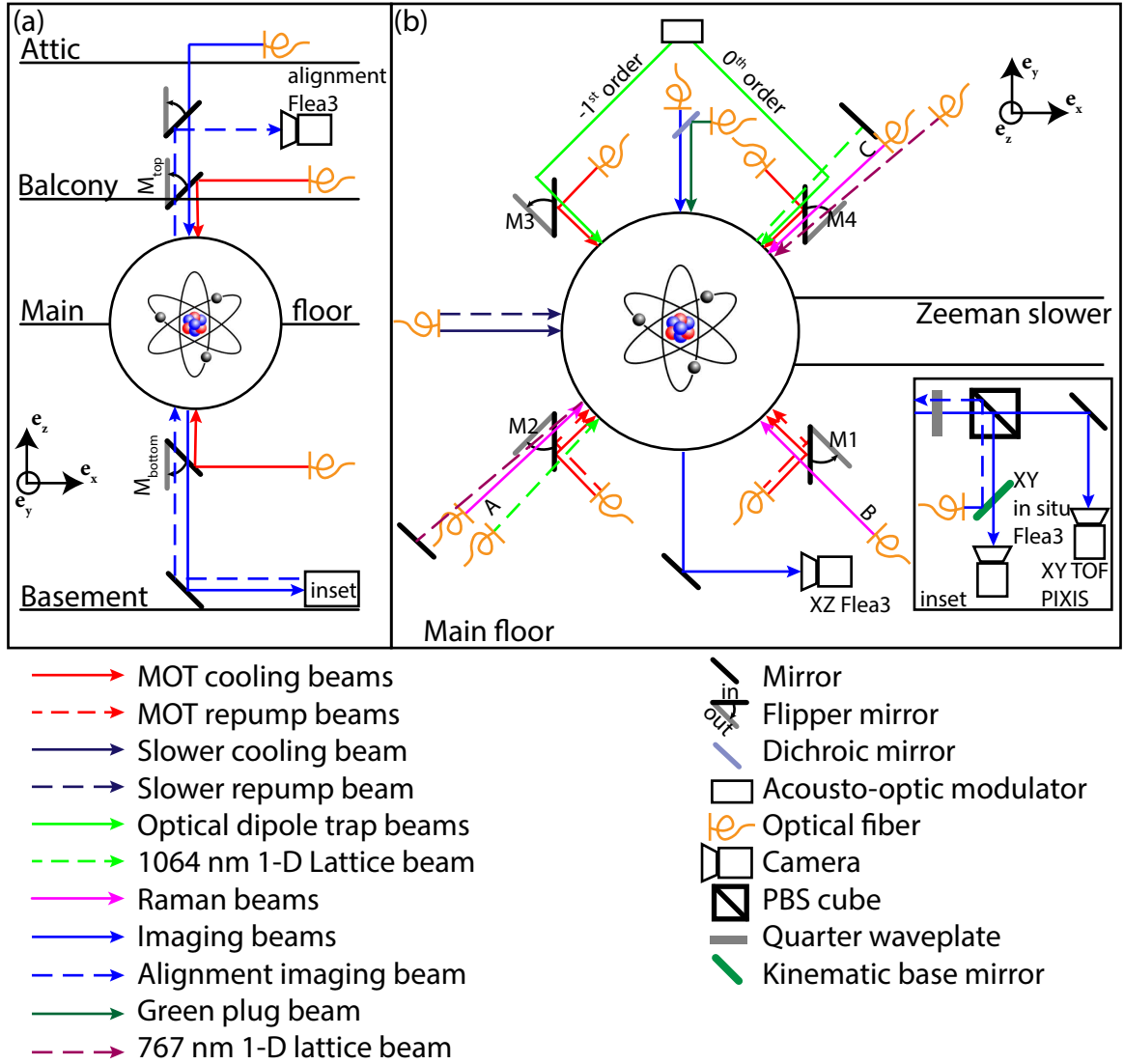


Figure 7: Schematic of RbK apparatus. (a) Side view of apparatus. Only beams propagating along the e_z direction through the atoms are pictured. (b) Top view of apparatus. Only beams propagating along the $x-y$ plane are shown. Schematic is not to scale and the angles are approximate.

the Zeeman slower. The remaining four MOT cooling beams, coming from four opposing directions, are shown in red. They reach the atoms when their flipper mirrors, $M1 - 4$, are flipped in. All six flipper mirrors are computer controlled by the same digital channel, so they can be flipped in and out together. Only the beams going in through mirrors $M1$ and $M2$ are accompanied by MOT repump light, dashed red lines. The repump light for ^{87}Rb (both MOT and slower) comes from a Toptica DL-100 laser. The cooling light (MOT, slower) as well as imaging beams, come from a Toptica TA-100 tapered amplifier system. Both lasers are frequency referenced to a master laser, a toptica DL-pro, which is frequency stabilized to a ^{87}Rb atomic transition via saturated absorption spectroscopy (see section 3.3.4).

The optical dipole trap beams (solid green) come from the same 1064 nm laser (IPG YDL-30-LP), and are split via an acousto-optic modulator into two orders, which enter from opposite directions and intersect each other at approximately a 90 degree angle, providing confinement along all three axes. There is a 1-D optical lattice beam (dashed green), also 1064 nm (IPG YAR-10K-1064-LP-SF, seeded by a pick off from an NP Photonics seed laser), sent in past the $M2$ mirror and retroreflected on the opposite end of the chamber to form a standing wave pattern. This was also used for experiments in Chapters 6 and 7. There is also another imaging beam, imaging the atoms along the x - z plane, going to a Flea3 camera.

There are three Raman beams (solid magenta): Raman A, entering past the flipped-out $M2$ mirror, Raman B, at 90 degrees to Raman A entering past the $M1$ mirror, and Raman C, counter-propagating with Raman A and entering past the $M4$ mirror. The Raman beams are derived from a tunable Coherent MBR-110 Ti:Sapphire laser seeded by a Coherent Verdi V-10 laser. For experiments described in Chapters 6 and 7, we used the Raman A and C beams.

When ^{40}K atoms are in use, the slower cooling, slower repump, MOT cooling, MOT repump and imaging beams are all a combination of frequencies for both ^{87}Rb

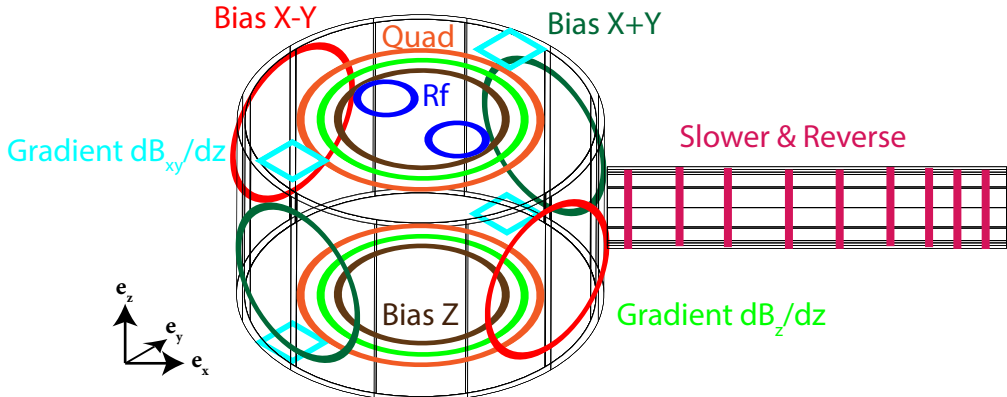


Figure 8: Schematic of magnetic coils on the RbK apparatus. The black wire frame represents the main experiment chamber, with the Zeeman slower off to the right. The Zeeman slower and reverse coils are wound around the Zeeman slower in varying spatial frequency (magenta). The quad (orange), gradient cancellation dB_z/dz (bright green) and bias Z (brown) are all pairs of identical coils on the top and bottom of the apparatus. Bias X-Y coils (red) are a pair of identical coils around the axes of the M_1 and M_3 mirrors, and the bias X+Y (dark green) are a pair of identical coils around the axes of the M_2 and M_4 mirrors. The rf coils (blue) are a pair of circular coils on top of the experimental chamber, spaced enough to allow the top MOT beam through. The gradient cancellation coils dB_{xy}/dz (cyan) are four square coils on top and bottom of the experiment along the X+Y axis.

and ^{40}K , fiber coupled before they were sent to the main experiment table. Both the ^{40}K cooling and repump lasers are Toptica TA-pro systems, with the repump laser frequency stabilized to the ^{40}K atomic transition. In addition, a green plug beam (solid dark green in 7b) is used (see section 3.3.5), derived from a Coherent Verdi V-5 laser. For ^{40}K experiments detailed in Chapter 5, we used a near resonant retroreflected optical lattice beam, shown in dashed dark magenta entering past the M_4 flipper mirror, coming out past the M_2 mirror before getting retro-reflected.

3.3.2 Magnetic coils

Figure 8 is a schematic depiction of all the coils used to produce magnetic fields on the RbK apparatus. The quad coils (orange in the figure) are a large pair of coils used to produce a quadrupole field for the MOT. The top and bottom coils are

connected through four IGBT switches, forming an h-bridge (see Figure 4.9 in [88]). This allows switching between two configurations: anti-Helmholtz and Helmholtz. In anti-Helmholtz configuration, the top and bottom coils conduct current in opposite directions, producing a quadrupole field gradient at the center. This is the configuration used for the MOT, rf evaporation, and producing a Stern-Gerlach gradient for spin resolved imaging. In Helmholtz configuration, the two coils conduct current in the same direction, producing a strong bias field along the e_z direction. This was used to get close to the Feschbach resonance in the experiment detailed in Chapter 5.

There are three pairs of bias coils, used to cancel constant background fields or provide field offsets along the three axes. All three are in Helmholtz configuration. The bias Z coils (brown) are on top and bottom of the experiment and provide a constant B_z field at the center. The bias X+Y coils (dark green) are vertical on two opposite sides of the apparatus along the e_x+e_y directions, and the bias X-Y (red) are on the other two opposing sides along the e_x-e_y directions. There are also two sets of gradient cancellation coils available, although they are not subject to feedback loops or computer control. The first is another pair of coils on top and bottom of the apparatus (bright green), connected in anti-Helmholtz configuration to produce a small gradient dB_z/dz . The second is four square coils mounted above and below each bias X+Y coil (cyan). Both vertically stacked pairs of coils are wound in Helmholtz configuration, and the two pairs are in series, providing a small gradient dB_{xy}/dz at the atoms.

3.3.3 Procedure for making a BEC

We begin with the atoms heated in the ovens, sent through a thin nozzle allowing only those atoms with a velocity towards the science chamber to enter. They are cooled via a Zeeman slower and captured in a Magneto-Optical trap (MOT)

in the science chamber. During this step, the Zeeman slower is on, with both the coils and the slower cooling and repump lights on. These beams (dark blue in Figure 7b) are -148.5 MHz red detuned from the $|F = 2\rangle$ to $|F' = 3\rangle$ transition for cooling and -8.2 MHz red detuned from the $|F = 1\rangle$ to $|F' = 1\rangle$ transition for cooling (for this, the cooling TA is locked to a 133 MHz beat note offset from the master laser). At the same time, the flipper mirrors $M1 - 4, M_{bottom}, M_{top}$ are flipped in and the MOT cooling and repump beams (red in Figure 7) are on. The quad coils are on in anti-Helmholtz configuration with 25 A of current running through them, producing a field gradient of $\frac{dB_z}{dz} \approx 13$ Gauss/cm. This step can be set to take anywhere from ≈ 0.7 s to ≈ 5 s depending on how many atoms are needed.

Next is the optical molasses step, during which sub-Doppler cooling of the atoms occurs. For this step, the Zeeman coils and slower lights are turned off. The quad coil current is also switched off, leaving just the MOT cooling light and only leakage MOT repump light. The MOT cooling light is set to 20.6 MHz below the $|F = 2\rangle$ to $|F' = 3\rangle$ transition (120 MHz beat-note command). It is then linearly ramped in 19 ms down to a red detuning of 90.2 MHz (50 MHz beat-note command). Since the repump light is all but off in this step, the atoms are also depumped into the $F = 1$ manifold. Then, the atoms are optically pumped into the $|F = 1, m_F = -1\rangle$ state to make them trappable by the quadrupole field. This is done by turning on the slower repump beam (dashed dark blue in fig. 7b) 1 ms. Then, the XZ imaging beam (blue in fig. 7b) is briefly turned on to get rid of any remaining $F = 2$ atoms.

Next, we compress the atoms and perform forced rf evaporation. To compress, the quad coils are first turned on to 130 A. After holding for 20 ms, we sweep the current linearly to 250 A in 200 ms. The forced rf evaporation is then performed by turning on the rf coupling field and sweeping the frequency from 20 MHz to 4 MHz in 4 s to couple the highest energy atoms from $|F = 1, m_F = -1\rangle$ to $|F = 1, m_F = 0\rangle$

and allow them to escape the trap. The slow ramp is designed to allow the system to rethermalize through collisions as the hottest atoms are ejected. During rf evaporation, the crossed optical dipole trap (ODT) is on at an initial command power of 2.0 V and initial split (command to AOM controlling the power split between the two crossing beams, shown in fig. 7b) of 0.01 V. This allows any atoms that are cold enough to see the optical trap to be captured by it.

Then, the atoms are decompressed and loaded into the ODT. The quad current is ramped down to 60 A exponentially with a time constant of $\tau = 1.5$ s in 3 s. This is the quad current at which the atoms are only barely suspended against gravity by the quadrupole trap. At the same time, the bias Z current is ramped down from 10 A to 8 A, lowering the center of the quadrupole trap to the ODT. Then, the atoms are further evaporated in the ODT. This is done over the course of 5 s, ramping down the depth of the ODT and allowing the hottest atoms to escape. During this step, the ODT power is ramped exponentially from the initial command of 2.0 V to a final command of 0.4 V, while the split command is ramped up linearly from 0.01 V to 0.65 V, effectively turning on the crossing -1^{st} order beam. It is during this evaporation step that the atoms are cooled below the critical temperature and Bose condense.

Finally, the quad current is ramped exponentially to 0 A in 5 s, leaving the atoms optically trapped. Then any desired experiment can be performed on the BEC. For daily checks of the BEC, no experiments are performed and the atoms are released from the trap and allowed to expand in time-of-flight for 16.2 ms before being absorption imaged in the XY plane by the PIXIS imaging camera, pictured in fig. 7b.

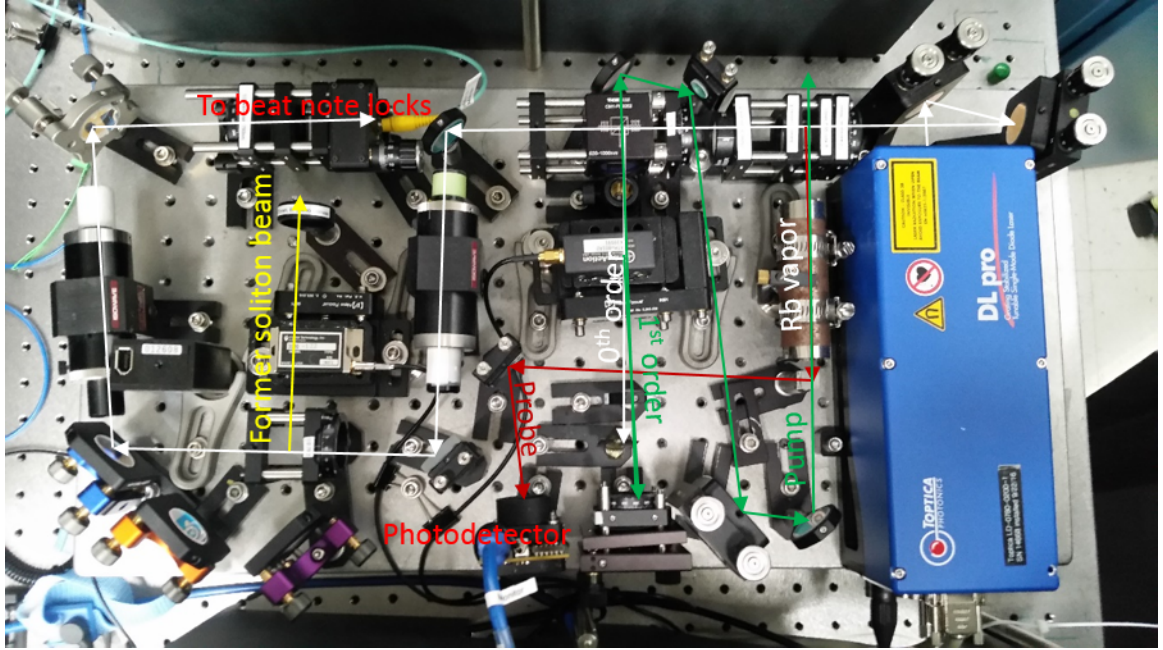


Figure 9: New master board layout.

3.3.4 Changes to apparatus for Rubidium

In this section, we describe a few of the changes that were made to the apparatus since the writing of Lauren Aycock’s thesis [88]. This is not an exhaustive list, but rather the most notable changes to the main setup affecting BEC production or adding capabilities to the apparatus.

3.3.4.1 Master laser setup

In 2014, the master laser board was replaced by a new version, with a new laser that was not dying. The laser was a Toptica DL-Pro, and it output approximately 80 mW, allowing for an extra beam arm that was used to imprint a phase shift on half the cloud to produce a soliton in the soliton project (see Appendix A) [89].

The layout of the new master laser board is shown in Figure 9. The board contains saturated absorption spectroscopy to lock the laser frequency relative to the atomic resonance, an output port to send to the cooling and repump lasers for

beat note locking and monitoring purposes, and an ouput port (partially dismantled in the figure) for any use if necessary. There are two mirrors directly in at the laser output, for easy re-alignment of the whole board if a diode is changed or other internal laser adjustments are made.

After hitting the two mirrors, the beam is used for saturated absorption spectroscopy, as described in section 8.3 of [90]. It is first split into two branches by a polarizing beam splitter cube (PBS). The power split between the branches can be adjusted by a half wavpelate (HWP) preceding the PBS. One branch is used as the probe beam in saturated absorption (red in the figure). This branch goes through the Rb vapor cell and is then sent to a photodetector. The photodetector reading is sent to a scope for monitoring and to a lock-in amplifier, used to derive the error signal for frequency locking. The rest of the beam (white) then hits another PBS cube (again preceded by a HWP to control the power split), splitting off the pump beam (green) for saturated absorption spectroscopy. This beam is sent to an acousto-optic modulator (AOM). This AOM's frequency is modulated by the lock-in amplifier, with modulation frequency of 100.0 kHz, amplitude of 0.356 V and phase shift (between the signal and photodetector response) of -115.44 degrees. The 0th order out of the AOM is blocked by a razor blade. The 1st order is retro-reflected in a cat's eye configuration [91]. Note that after retro-reflection, the second pass through the AOM also produces a 0th and 1st order beam. This 0th order beam is not blocked, but continues along the 1st order (pump beam) path at a slightly different angle - care must be taken to avoid aligning this order to counter-propagate with the probe. The double-passed beam (1st order in both directions, frequency shifted up twice) is then used as the pump and sent through the Rb vapor cell in the opposite direction of the probe beam.

The rest of the laser beam (white) then goes through an optical isolator, to avoid any subsequent reflections off of fiber tips or anything else from disturbing the

saturated absorption frequency lock. Then, the beam hits another HWP followed by a PBS, splitting off the former soliton beam (yellow). In the figure, the soliton beam launch has been partially dismantled, but can be revived at any moment if needed. The beam was double-passed through an AOM in a cat's eye configuration before being sent into a fiber launch. The rest of the laser power (white) is sent into a fiber that is connected to a fiber splitter box, providing light for beat note locking of the ^{87}Rb repump and cooling lasers as well as for monitoring the master laser on a wavemeter and Faby-Perot cavity.

3.3.4.2 Alignment imaging path

In 2016, there was a plan to carry out a project to create a 1D magnetic lattice whose topological character flips in the middle of the lattice, predicted to support localized states at the boundary. For this, two Raman beams needed to be overlapping, with one having a sharp phase change centered on the atoms. This required precise control of the beam phase as well as precise alignment of the beam center to the atoms. For optimal resolution, the Raman beams were to be sent upwards through the XY imaging system. To aid in alignment, it was decided that an additional imaging path that could detect these Raman beams directly be built. This alignment imaging path was implemented by Dr. Hsin-I Lu and is outlined in this section. All figures in this section were made by Hsin-I Lu.

The bottom part of the setup, with optics on the basement level of the experiment optical table, is diagrammed in Figure 10. One of the Raman beams, here called RamanC, first hit a spatial light modulator to imprint a phase jump. RamanC is then combined with a second beam, here called RamanD, on a PBS. Both overlapped beams are sent backwards through the XY imaging system and up towards the atoms. The dichroic filter allowed the Raman beams ($\lambda \approx 790$ nm) to be reflected while the imaging light ($\lambda \approx 780.24$ nm) passed through to the imaging

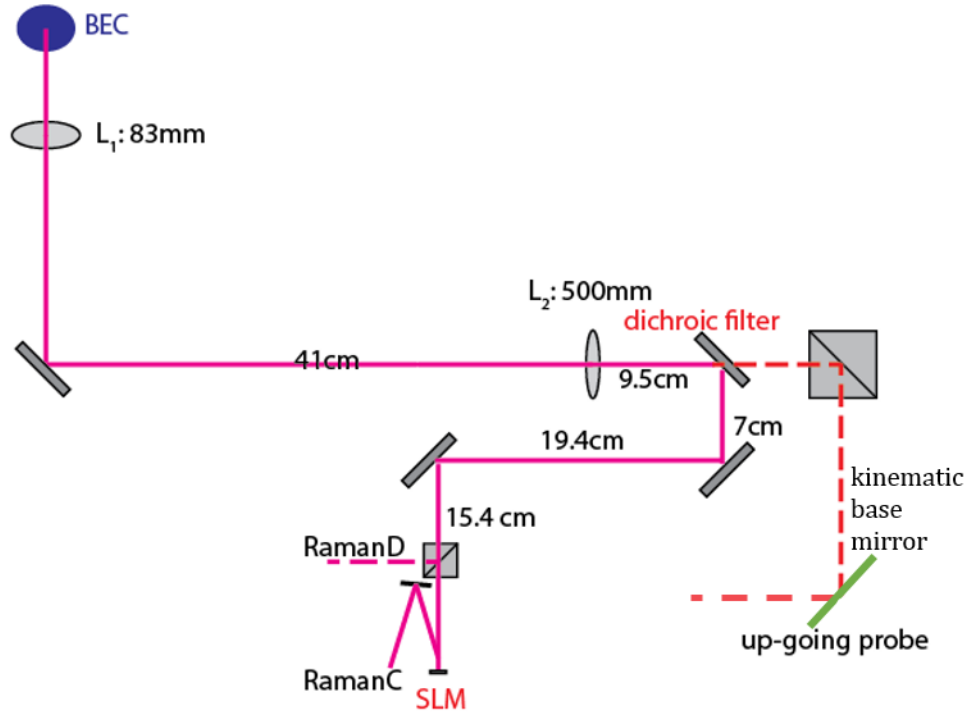


Figure 10: Schematic of the bottom half of the alignment imaging system, as well as the Raman beam set-up.

cameras. The beam for alignment imaging is sent up to the atoms backwards along the XY imaging beam path. It entered the path via a mirror on a kinematic mount, which could be removed to allow imaging through the usual camera focused in situ in XY (see Figure 7).

To set up an alignment imaging system going upwards through the chamber, it was necessary to insert a new imaging lens above the chamber, as close to the atoms as possible to maximize the numerical aperture. A schematic of this lens is shown in Figure 11, it is a 25 mm diameter $f = 50$ mm aspheric lens, a Thorlabs AL2550. This lens was placed above the printed circuit board (PCB) that contains the top bias Z coil and rf coils. It was held in a custom made mount.

The top part of the imaging system is diagrammed in Figure 12. Here, the alignment probe beam is light blue. From the atoms, the alignment probe beam hits

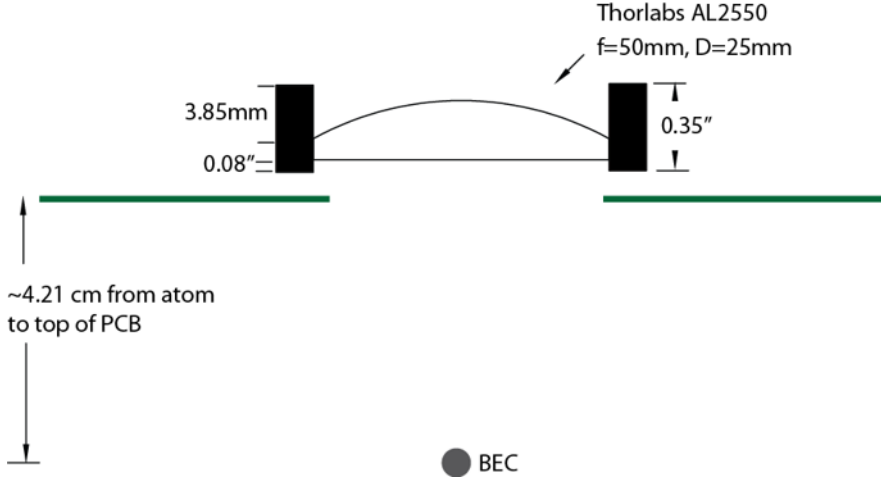


Figure 11: Schematic of the new imaging lens placed on the bucket window on top of the experimental chamber.

the new imaging lens (labelled L_1). Then, if the top MOT mirror is flipped out, it hits another additional flipper mirror (here M_2) before reaching a second lens and hitting an additional Flea3 camera, on the 'balcony' level of the experiment. Since the imaging lens on top of the chamber cannot be taken in and out, it was necessary to correct the down-going probe beam and down-going MOT beam, ensuring they retain their size at the atoms. For the down-going probe beam, this was done by installing a telescope to expand the beam by a factor of 4 (L_6 and L_5 in the figure) and then add a lens (L_4 in the figure) that forms a telescope with the imaging lens to reduce the beam back down by a factor of 4. The MOT beam was corrected by switching the focusing lens directly after the MOT fiber to an $f = 100$ mm lens (L_7), effectively expanding the beam by a factor of $\approx 2/3$, and then adding an $f = 75$ mm lens (L_2) to form a telescope with the imaging lens, reducing the beam size by a factor of $2/3$. The adjusted beams were aligned and the experiment functioned properly. The alignment imaging system was also aligned with great effort.

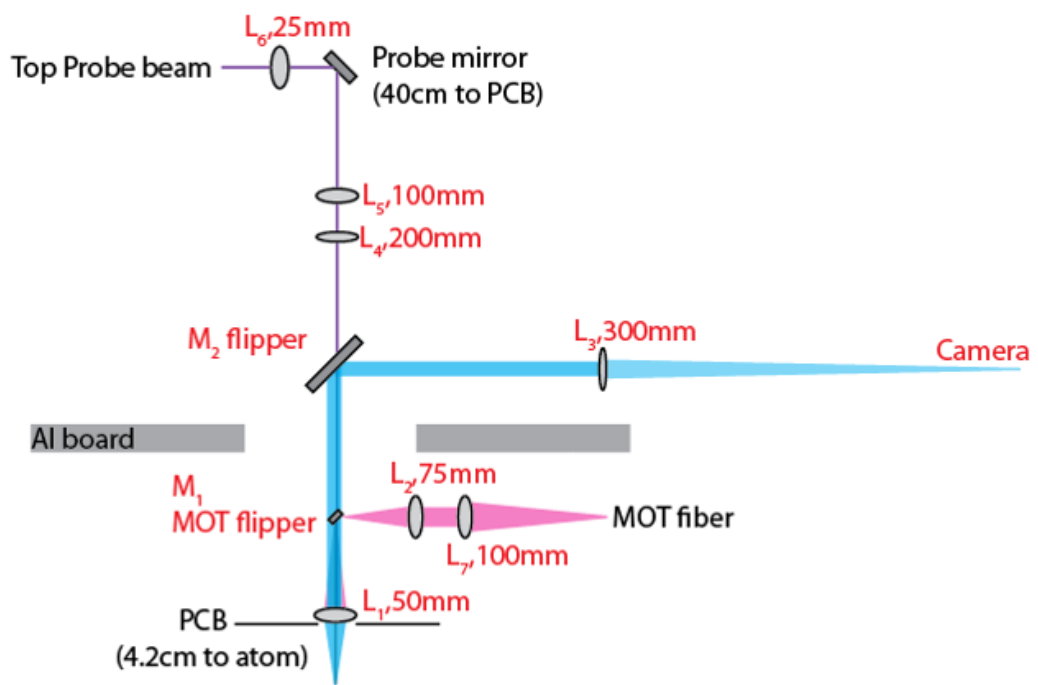


Figure 12: Schematic of the top half of the alignment imaging system, including correction optics for the MOT beam and probe beams to undo the effects of the new imaging lens.

3.3.4.3 FPGA quad servo

In 2014, the servo board that was used to stabilize the current in the quad coils had failed, and rather than replacing it with an identical one a new FPGA-based servo board design by Ryan Price was implemented. This design is described in detail in Appendix B of [92]. Here, we include a brief description of the design and implementation details for the quad servo at RbK.

The basic operation of the board is as follows. There are four SMA connections for input signals. These signals go to a 16 bit, 8 channel analog to digital converter ADAS3022BCPZ, then through a digital isolator Si8662BC-B-IS1, to the FPGA board. The outputs of the FPGA are sent through a similar digital isolator, Si8660BC-B-IS1 and into a 16 bit, 4 channel digital to analog converter AD5686R. Then, each of the four outputs is sent through a programmable gain amplifier AD8250ARMZ. The gain setting signal is derived from the FPGA board , by way of a serial shift register CD74HC4094. There are four SMA connections for outputs of each of the four amplifiers.

All of these devices are powered from a +/-18 supply voltage by way of three voltage regulators, LM2940C_KTT_3 for 5V regulation, LM2990_KTT_3 for -15V regulation, and LM2940CSX_KTT_3 for +15V regulation. The FPGA communication is set up through USB. There is a USB input port that connects to a USB chip FT232HL. The USB chip requires an EEPROM, in this case 93LC56BT is used. Clock timing for both the FPGA and the USB chip is provided by CTX292-LVCT. There is also a buffer SN2564BCT25244 available for amplifying digital FPGA outputs. The digital side of the board is also powered from a separate 5V supply by way of a 3.3V regulator LM1085_KTT_3.

For quad coil current stabilization, the board receives a computer command, in volts, through one of it's input ports, and a Hall probe reading, in amps, through

the other one. The Hall probe current sent to the servo is dropped across a stack of two 51 Ohm resistors (located inside the servo box) for a total measured resistance of 25 Ohms. The difference between the two inputs, in volts, is interpreted as the error signal by the FPGA board. The control output of the board is then sent to the gate input of a MOSFET bank. The power supply powering the quad coils is connected to this MOSFET bank and then to the coils in series. Controlling the gate voltage of the MOSFETs controls the resistance the power supply sees and thus the current it outputs (in voltage limited mode).

The optimal PID parameters, set via software and programmed in the FPGA board, have been found at a gain factor of -5 and integrator bandwidth of 400 Hz. The resulting turn-on curve is shown in pink in Figure 13 a. For this curve, the computer command was hopped to 100 A and the resulting current as detected by the Hall probe was observed. The turn-on curve using the preceding servo board is shown in gray.

The board is also equipped with a digital TTL input (on the back of the board). When this digital input is high, the output control voltage is immediately railed to its lower bound. To be compatible with the MOSFETs used, the upper and lower bounds of the control output are set to 5 and 3 V respectively. The turn-off curve when this TTL switch is activated is shown in Figure 13 b. The timescale is likely limited by eddie currents in the chamber.

We calibrated the resulting current (as measured by the Hall probe) for different command voltages. This is shown in Figure 14. Both the schematic for the servo board and the Box control program to talk to the FPGA are in the shared google drive under 'RbK/Lab Notebook/Electronics/FPGA Quad Servo (From Ryan)'. When connected, the box control program detects 'RbK Quad Servo' in its device list. In the past, several cycles of plugging and unplugging as well as turning on and off have been necessary for the connection to be successfully made.

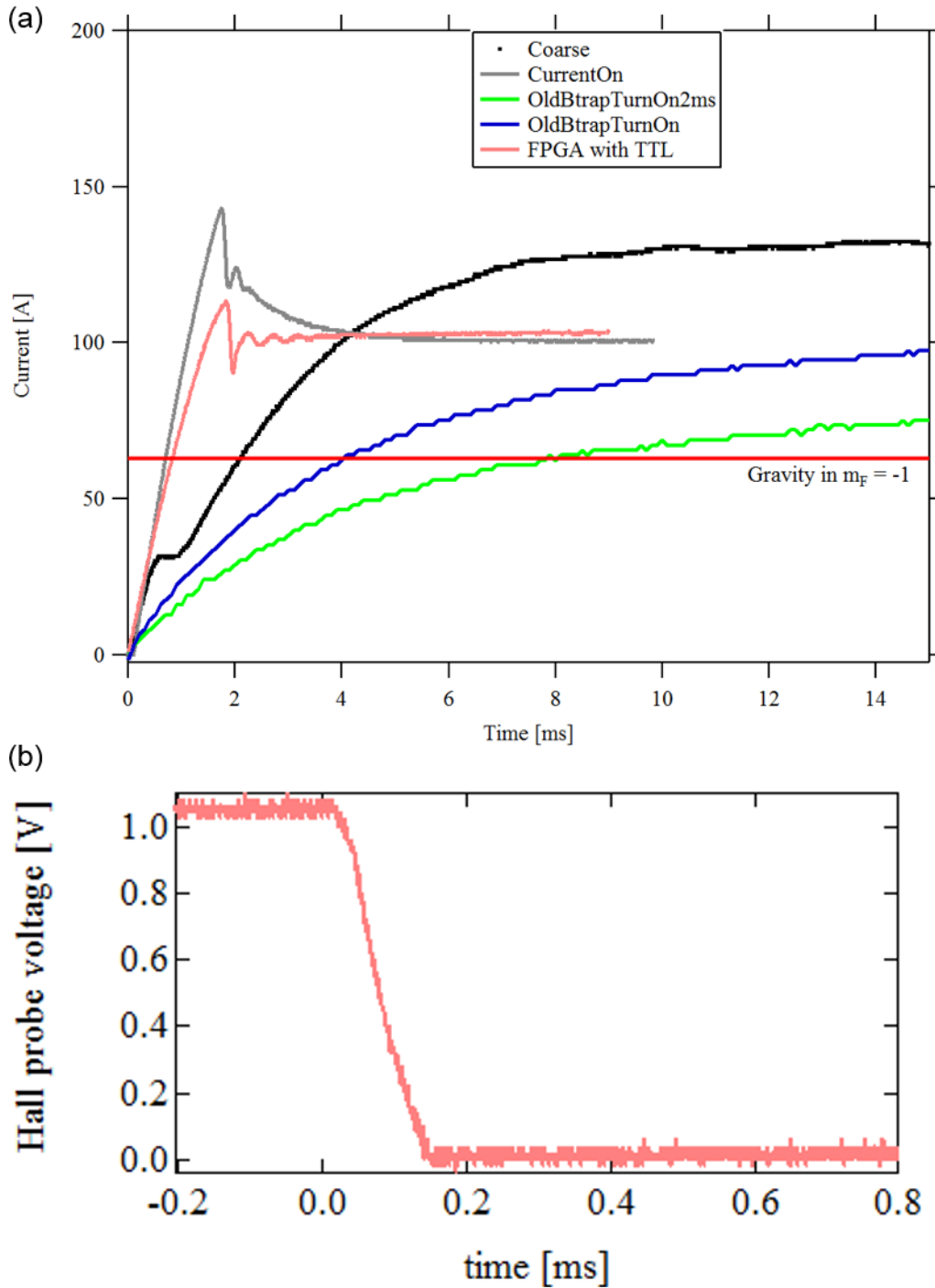


Figure 13: Turn on and off curves of the quad coils. (a) Turn-on, when computer command is jumped from 0 to 100 A . The FPGA-based servo response is in pink. The previous hardwired servo is in gray. The other curves are extraneous. (b). Turn-off with the FPGA-based servo when the TTL switch is engaged.

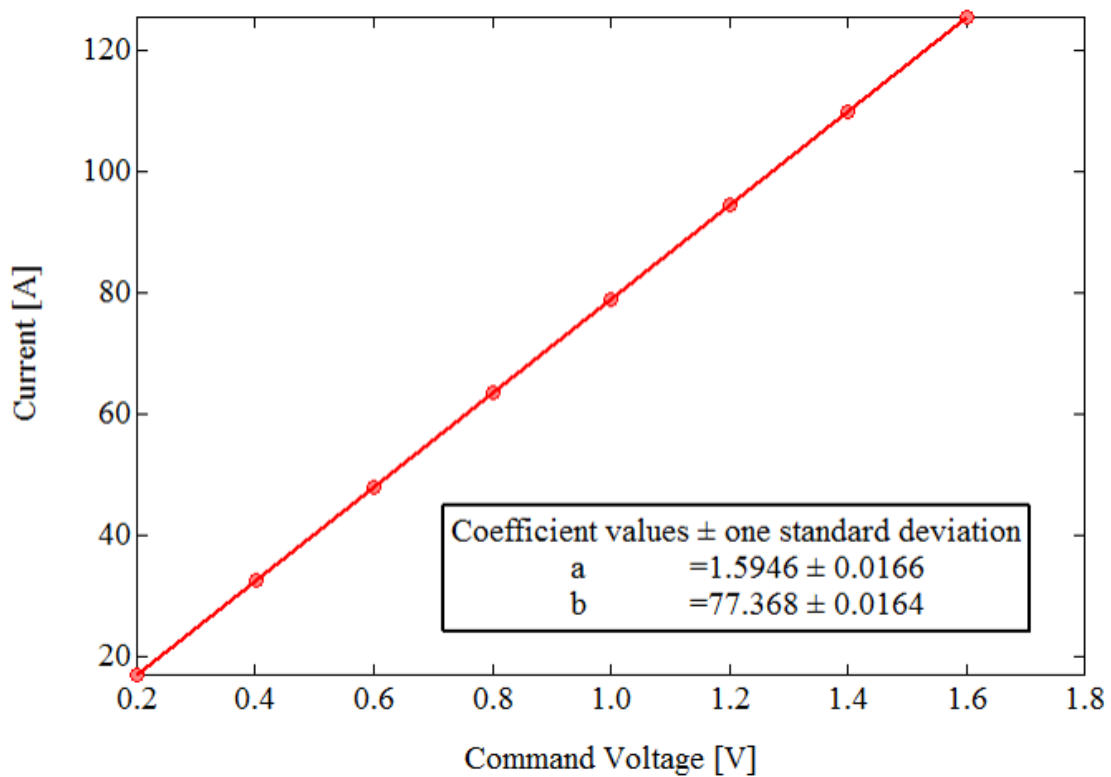


Figure 14: Output current as a function of computer command voltage for the FPGA-based servo implementation.

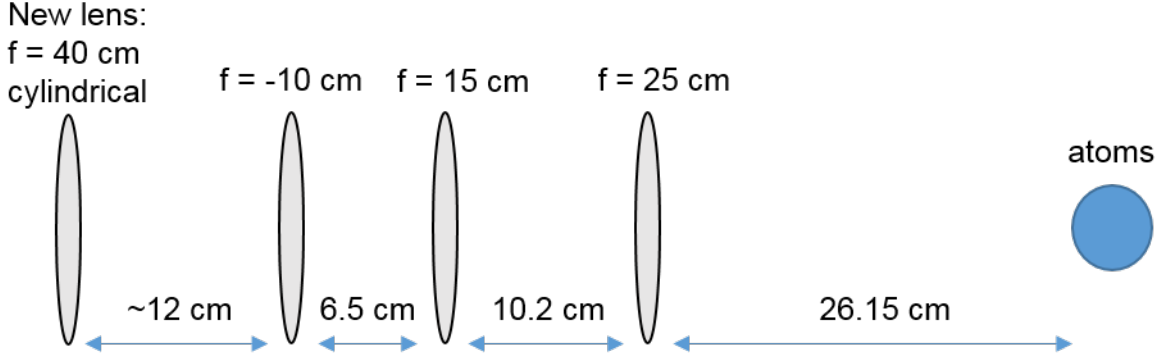


Figure 15: Schematic of beam shaping optics in the path of the 0th order ODT beam, after the split AOM. The new lens, on a removable mount, is cylindrical, shaping the beam along the horizontal axis only.

3.3.4.4 ODT beam shaping

In 2015, two projects were being carried out on the apparatus at the same time: the soliton project (see Appendix A) [89] and the synthetic dimensions project detailed in Chapter 7. The soliton project used an elongated BEC, requiring the dipole trap to be highly elongated along one direction, here $e_x + e_y$. For this, only the 0th order of the ODT was used and it was made very tight both along the horizontal and vertical directions: with 42 and 55 μm waists, respectively. The synthetic dimensions projects suffered from momentum changing collisions, and therefore needed the cloud to be as dilute as possible. For this, the 0th order ODT beam still needed to be tight in the vertical direction to suspend against gravity, but needed to be as wide as possible (while still retaining a detectable atom number) in the horizontal. Therefore, an extra cylindrical lens on a removable, rotatable mount was added in the beam path to switch between the two configurations.

The location of this new lens is detailed in Figure 15. Without this lens, the beam was sent through a telescope (the $f = -10$ and $f = 15$ cm lenses before reaching an $f = 25$ cm focusing lens, placed 25 cm away the center of the chamber to focus the beam at the atoms. The beam waist as a function of propagation distance

along this beam path is shown in blue in Figure 16 a. This graph was made by Dr. Ian Spielman from a python calculation of Gaussian beam optics. According to the calculation, the beam is focused down to a $45 \mu\text{m}$ waist at the atoms located at a displacement of 1400 mm.

The additional lens used was an $f = 40 \text{ cm}$ cylindrical lens, rotated in its rotating mount to focus the beam slightly in the horizontal direction. The effect of this lens on the horizontal beam waist along its path was calculated and plotted (again by Ian using his code) in Figure 16 b. This plot was made for a $f = 75 \text{ cm}$ lens instead of $f = 40 \text{ cm}$, but the qualitative effect is the same. As seen in the figure, the waist of the beam is not significantly impacted by the addition of the lens, but the focus is shifted away from the atoms, resulting in a larger waist at the atoms. The horizontal beam waist at the atoms with the $f = 40 \text{ cm}$ lens as measured by a beam profiler camera was $115 \mu\text{m}$. This was the configuration used in the experiments described in Chapter 7.

3.3.5 Procedure for making a DFG

To make a degenerate Fermi gas of ^{40}K , we followed a similar cooling procedure as for making a BEC, with some key differences. First, as mentioned in sec. 3.2.2, due to the Pauli exclusion principle, spin polarized ^{40}K atoms cannot undergo s -wave collisions, and therefore below a certain temperature have no method to thermalize on their own and cannot be evaporatively cooled. To overcome this problem, we cooled a mixture of ^{87}Rb and ^{40}K , effectively using ^{87}Rb as a collisional bath to allow the Fermions to thermalize. Second, ^{40}K is slightly below half the mass of ^{87}Rb . This leads to a larger magnitude of transverse velocity for ^{40}K atoms in the Zeeman slower, leading to a larger fraction of atoms missing the capture region of the MOT. To mitigate this issue, we utilized transverse cooling of ^{40}K right before the Zeeman slower. This consisted of two pairs of counter-propagating beams along the $e_z + e_y$

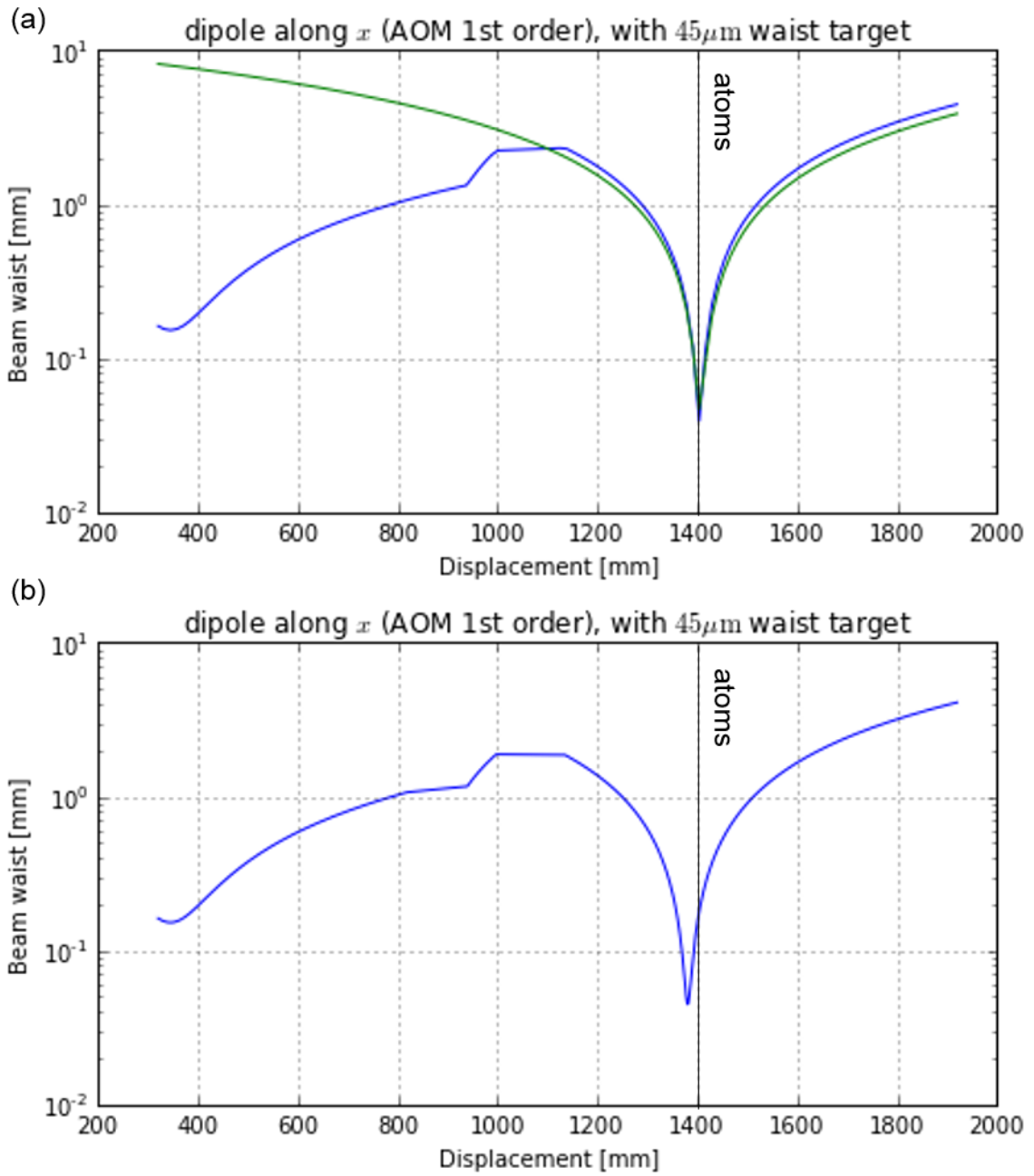


Figure 16: Beam waist as a function of propagation distance as calculated by Ian Spielman's code. Graphs also made by Ian Spielman. The atoms are at displacement = 140 cm. (a) Without additional lens. Blue line represents horizontal beam waist. (b) With an additional $f = 75$ cm lens 12 cm in before the next optic.

and e_z - e_y directions, performing Doppler cooling in the directions perpendicular to propagation (not shown in fig. 7b). The lower mass of ^{40}K , as well as the larger number of available spin states, also leads to a larger number of Majorana losses near the center of the MOT: spin flips that take the atoms out of the trappable states because they are moving too fast to adiabatically follow the changing magnetic field direction [93–95]. To mitigate this issue, for cooling ^{40}K the center of the quadrupole trap was plugged by a tightly focused green (repulsive) laser beam (dark green in fig. 7b).

First, ^{40}K atoms starting at the oven were cooled via a Zeeman slower and transverse cooling and captured in a MOT for 7 s. Then, both ^{40}K and ^{87}Rb atoms were slowed and MOT loaded for 1.5 s. The subsequent optical molasses step was only 2 ms long, with the ^{87}Rb MOT cooling light ramped linearly from 20.6 MHz below the $|F = 2, m_F = 2\rangle$ to $|F = 3, m_F = 3\rangle$ transition (120 MHz beat-note command) to 40.6 MHz below the resonance (100 MHz beat-note command). In this time, the ^{40}K cooling light was turned down in intensity but the detuning remained unaltered.

Next, ^{87}Rb was optically pumped into the $|F = 2, m_F = 2\rangle$ state using the slower cooling beam, while ^{40}K was optically pumped into the $|F = 9/2, m_F = 9/2\rangle$ state using a dedicated optical pumping beam in $250\mu\text{s}$. These are magnetically trappable states, and we subsequently turned on the quad coil current to 130 A to capture the atoms in the magnetic trap, along with the green plug beam at the center to prevent Majorana losses. Both species were compressed by a linear ramp of the quad current up to 160 A in 0.5 s. Then, forced rf evaporation was performed for 10 s, sweeping the rf frequency linearly from 18 MHz down to 2 MHz.

Then, the atoms were decompressed and loaded into the ODT, similarly to the BEC procedure. The ODT was turned on to an initial power of 2 V and an initial split command of 0.01 V. The quad current was ramped down to 25.5 A

exponentially with a time constant of $\tau = 1.5$ s in 3 s. The evaporation in the ODT was split into two steps. During the first 3 s step, the split was ramped linearly to its final command power of 0.65 V, putting more power into the (less tightly focused) crossing beam. The green plug beam was ramped off during this step. During the second, 4 s step, the overall power of the ODT was exponentially ramped down to 1.2 V, while the quad coil current was ramped exponentially to 0 A.

We then used adiabatic rapid passage (ARP, see sec. 2.2.3) to transfer the ^{87}Rb atoms from $|F = 2, m_F = 2\rangle$ to $|F = 1, m_F = +1\rangle$ using a microwave coupling field and a 50 ms ramp in bias Z coil current. Then, we pulsed on the XZ imaging beam to eject any remaining $F = 1$ atoms. Then we performed one last evaporation step in the ODT, ramping the final power down to 0.7 V. The ^{87}Rb atoms were no longer suspended against gravity and fell out of the trap. We then were free to perform experiments with the degenerate ^{40}K cloud.

3.3.6 Current status of Potassium apparatus

At the time of writing, the ^{40}K part of the apparatus as described is no longer functional. The number of ^{40}K atoms collected in the MOT started decaying significantly in January 2014, and by March was almost completely gone and could not be resurrected. The specific failure point of the setup was not clear. However, other groups have found that atomic sources are much more stable, and a higher fraction of the (expensive) ^{40}K sources can be utilized when the atoms were initially cooled with a 2-D MOT rather than with a Zeeman slower [96–98]. Therefore, rather than continuing to attempt to revive the existing set-up, the decision was made to build a 2-D MOT for both ^{40}K and ^{87}Rb .

The design of our 2D MOT is closely based on the design in Thomas Uehlinger's diplome thesis [97]. The design was developed by Dalia Ornelas, and initially implemented by Marcell Gall before it was taken over by the rest of the RbK team.

The schematic of the planned vacuum system (with attached optics) is pictured in Figure 17. On the left side of the schematic, there are optics directing the pushing beam into a miniconflat viewport. The viewport is part of a cross, with the ^{40}K and ^{87}Rb ovens attached to the two ends of the cross, with gate valves allowing one to close off one or both sources from the rest of the vacuum system. From there, the cross attaches to the main 2D MOT cell via a mini-conflat flange.

The cell is a custom machined stainless steel frame with rectangular anti-reflection (AR) coated windows on four sides and mini-conflat connectors on two ends, pictured in more detail in Figure 18. Two aluminum mounting crosses attach to either end of the cell. Four aluminum bars are connected between the crosses, and the main 2D MOT optics are mounted on those four bars. The opposite end of the cell (right in fig. 17) sandwiches a differential pumping tube in the mini-conflat connection and connects to another cross. The top of the cross connects to a small ion pump. The bottom connects to a rotatable feed-through mechanism with a 'flag', a square of metal, attached inside. The rotator rotates the flag in and out of the atomic beam path, providing a means of losing off the main chamber from the atomic beam and push beam light. The fourth end of the cross connects to another gate valve, separating the 2D MOT vacuum system from the main experiment chamber. The other end of this gate valve connects to a flange that is meant to connect directly to the main experiment chamber.

A picture of the stainless cell is shown in Figure 18. Attaching the glass windows to the stainless steel frame in a vacuum tight way proved to be quite difficult, and this picture was taken during one of the attempts to do so using epoxy. The clamps around the cell served to keep the windows in place as the epoxy was curing. In the final design, the seal was made with indium, with gaskets custom machined to press the windows onto the cell. We roughly followed the indium sealing method presented in [99], with gaskets above and below the windows. We

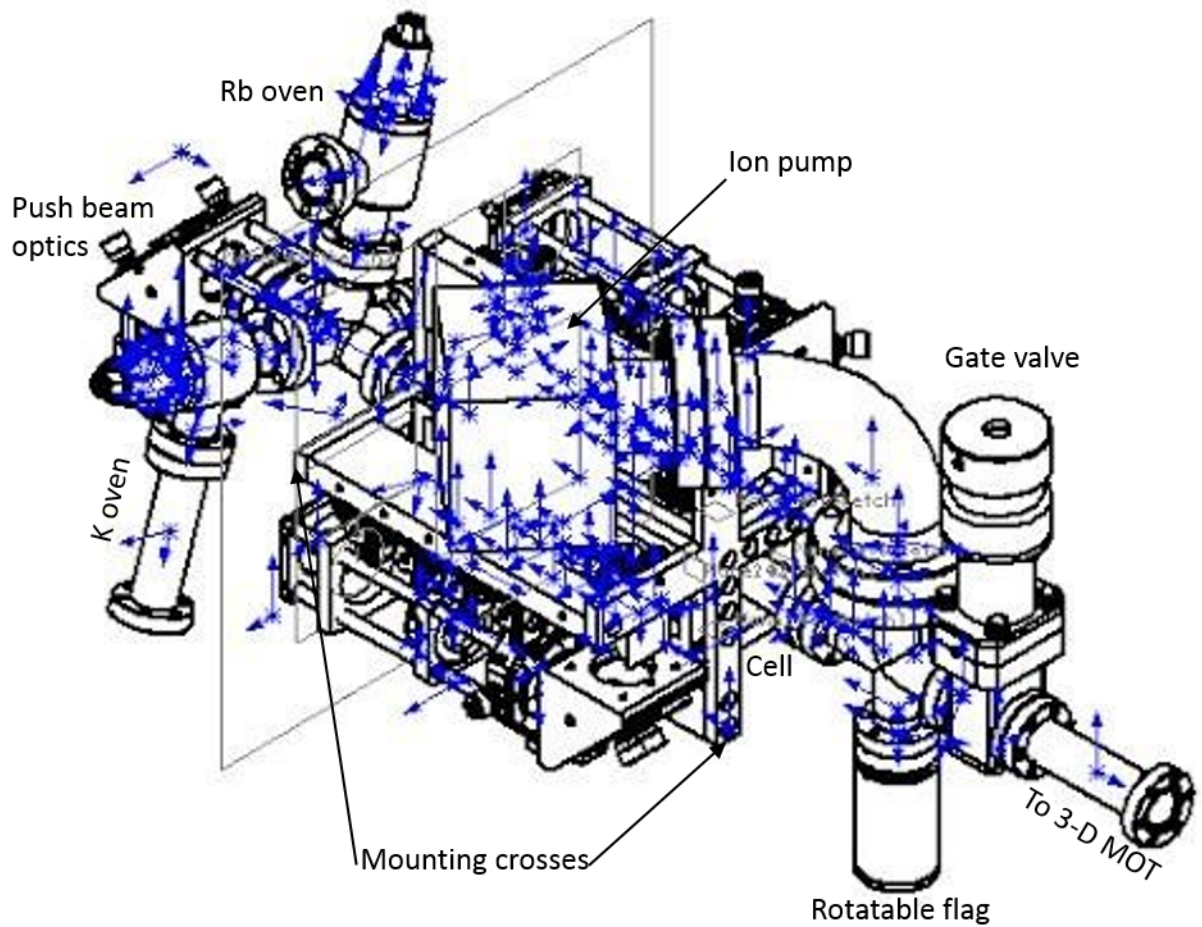


Figure 17: Schematic of the 2D MOT setup. The mini-conflat on the right is to be attached to the existing experiment chamber, directing the atomic beam into the 3D MOT.

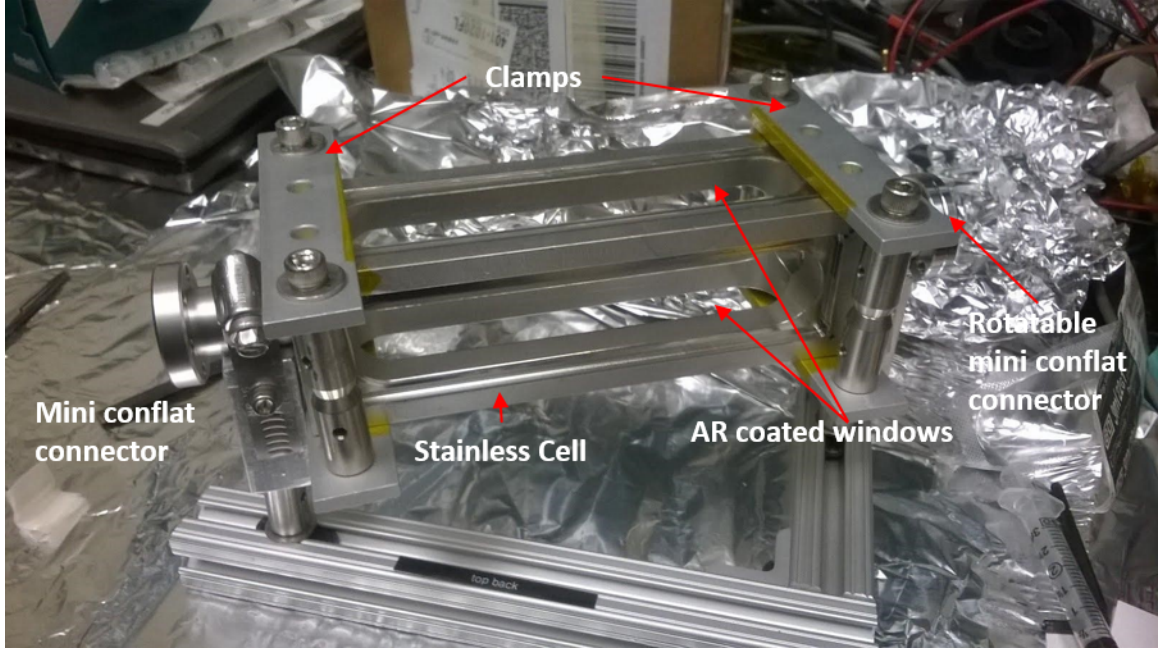


Figure 18: Picture of 2D MOT cell during an attempt to epoxy AR coated windows onto the stainless steel frame. The clamps serve to hold the windows in place while epoxy cures.

also employed pre-squashing, where a metal piece in the shape of the window was first pressed onto the indium wire to flatten it and minimize the amount of pressure that needed to be applied to the glass window.

The main 2D MOT optics direct the cooling and repump beams into the cell from two directions, and retro-reflect them on the other end, producing cooling along those two directions (hence the name 2D MOT). The optical set-up along one of those directions is presented schematically in Figure 19. The cell is elongated along the atomic beam direction, to maximize the time the atoms are cooled while travelling to the 3D MOT. Because of this, instead of a highly elliptical cooling beam, four MOT beams are launched in a row, almost overlapping, from each of the two directions. This is accomplished by splitting one beam into four with four sequential beam-splitting cubes (BSs).

The 2D MOT cooling and repump light is first periscoped over from a fiber and lens assembly (designed to shape the beam to be roughly 1 inch in diameter).

It then goes through a half-wave plate (HWP) before entering the first 70/30 beam splitter. 30% of the light is sent through a quarter-wave plate (QWP) tuned to provide circularly polarized light into the cell. On the other side of the cell, the beam hits another QWP before being retro-reflected back into the cell. Since the beam hits the QWP on the other side of the cell twice, the circular polarization is preserved. The remaining 70% of the light goes into the next 70/30 BS, sending 21% of the total beam power into the second arm going into the cell, to be retro-reflected in the same way. The remaining 49% hits a 50/50 BS, sending 25.5% of the total beam power into the third retro-reflected arm. The final cube is a polarizing beam-splitter (PBS), and the HWP before the cubes is tuned to ensure all of the light is sent into the cell on this last, fourth, arm.

The push beam enters from the oven direction and serves to provide some velocity to the atoms along the long direction of the cell to ensure they continue to travel to the 3D MOT, while still providing some cooling along the longitudinal direction. In order to provide this cooling, the push beam is also retro-reflected, with the help of a custom machined differential pumping tube (on the right in fig. 19). The differential pumping tube is machined to have a 45° angled polished end, reflecting all of the light except for the central part towards a retro-reflecting mirror outside the cell. Along the other 2D-MOT cooling direction (up and down in fig. 19), this whole set of optics is replicated, with the exception of the push beam retro-reflection.

The current 2D-MOT setup is pictured in Figure 20. The vacuum system has been assembled and successfully pumped down, with a octagonal test chamber in place of the main experimental chamber. This test chamber is intended to be used to send probe light through and detect fluorescence to characterize the atomic beam coming out of the 2D MOT. The optics have been assembled and the quarter-wave plates lightly epoxied onto the BS cubes and mirrors, although as can be seen in the

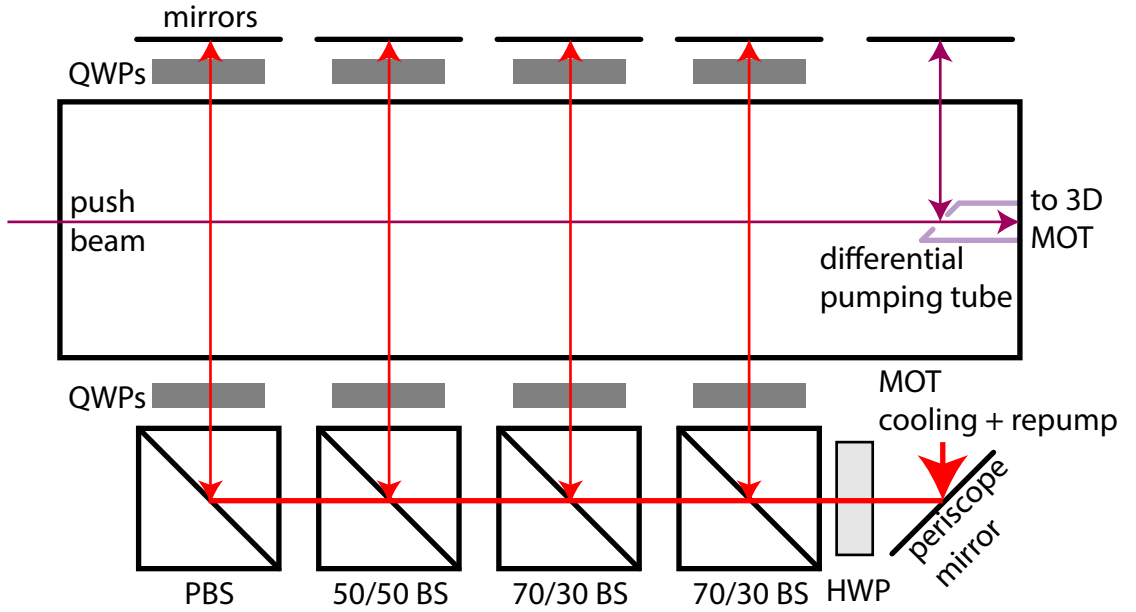


Figure 19: Schematic of 2D MOT optics along one direction. The main cooling and repump beam is split into four parallel arms by four beam splitter cubes. The push beam enters from the oven direction and is retro-reflected via a custom machined and polished differential pumping tube. These optics are mounted on crosses attached to the 2D MOT cell.

picture some have regrettably fallen off. Quadropole coils have been wound around each of the four windows, onto 3D printed coil winding forms. Bias Z coils have also been wound to cancel out stray gradients along the atomic beam direction.

The two Toptica TA-pro systems that were used to provide all ^{40}K light in the past are still operational, and need to be re-purposed to provide both 2D MOT and 3D MOT cooling and repump light. A new Toptica TA-pro was also purchased, with the intent to implement gray molasses cooling on the ^{40}K D1 line as described in [100].

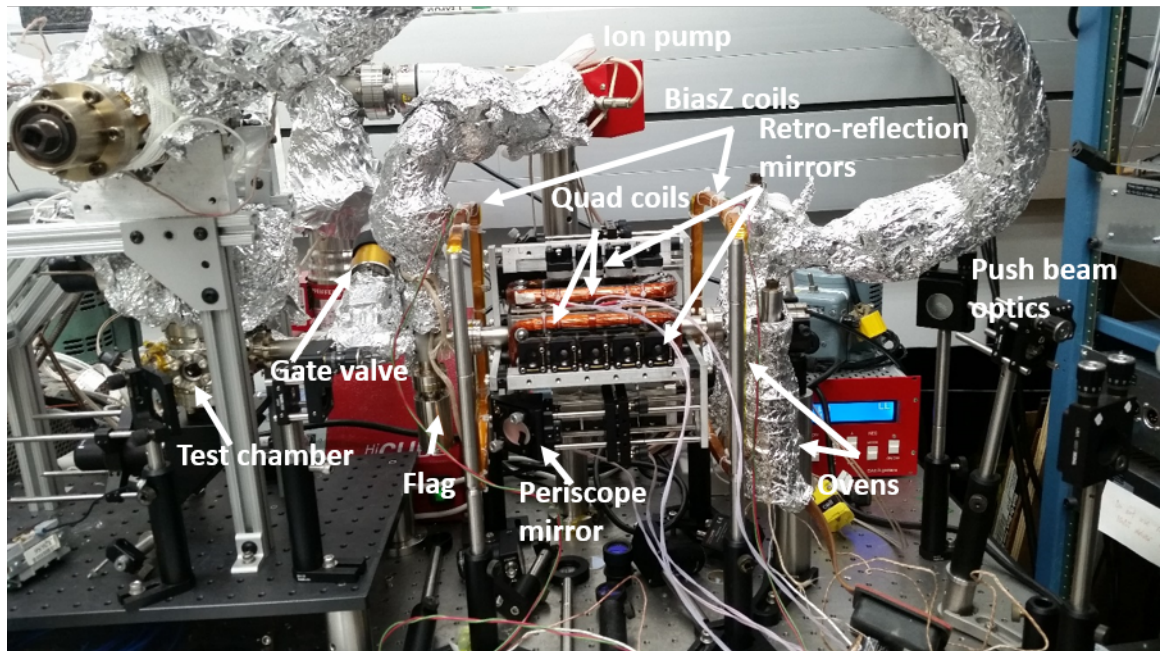


Figure 20: Picture of current 2D MOT apparatus. The vacuum system is in place, optics are (mostly) mounted and coils to generate the quadrupole trap and cancel gradients along the atomic beam direction have been wound.

Chapter 4: Absorption Imaging with Recoil Induced Detuning

In this Chapter, we describe the simulations we performed in order to interpret absorption images in a non-standard regime: at long imaging times, where the recoil induced detuning needed to be taken into account. This simulation was necessary to interpret data collected for our s-wave scattering experiment, described in Chapter 5. In this Chapter, we first describe the recoil-induced detuning effect and derive the equations to be solved. Then, we solve these equations perturbatively, and show that this treatment is insufficient in the regime of interest. We then perform two versions of numerical simulations: one where the atoms are assumed to remain stationary relative to each other during imaging, and one where they are free to move. We show that although the atoms do move significantly during the imaging time, this does not have a strong effect on the final observed intensity. Finally, we use our simulated results to calibrate the saturation intensity in our camera units, and find the parameters for optimal signal-to-noise (SNR) ratio imaging. This work was previously reported in [101].

4.1 Recoil-induced detuning

After absorbing a number of photons N all traveling in the same direction, an atom will obtain an average recoil velocity of Nv_r . Via the Doppler effect, this will result in a detuning $\delta = Nk_r v_r$. This detuning will increase as more photons are absorbed, and therefore depend on time. Since detuning affects the absorption cross section, the absorbed intensity will also become time dependent. We can generalize

Eq. 2.35 to include a time dependence on the detuning term and therefore also the intensity:

$$\frac{d}{dz} \frac{I(z, t)}{I_{\text{sat}}} = -\rho(z)\sigma_0 \frac{I(z, t)/I_{\text{sat}}}{1 + 4\delta(z, t)^2/\Gamma^2 + I(z, t)/I_{\text{sat}}}. \quad (4.1)$$

The number of photons absorbed per atom will depend on the intensity lost, up until the current time, at that location. The detuning will therefore be proportional to the total number of photons lost up until time t at that location, given by the absorbed intensity divided by the single photon energy $\hbar\omega_L$, divided by the number of atoms that participated in the absorption $\rho(z)$ times the detuning $k_r v_r$:

$$\delta(t, z) = \frac{k_r v_r}{\hbar\omega_L \rho(z)} \int_0^t \frac{dI(z, \tau)}{dz} d\tau. \quad (4.2)$$

These equations are interdependent, and cannot be in general solved analytically.

Figure 1a shows the velocity and detuning as a function of position in space for three different imaging times, calculated numerically. All calculations in this chapter were done for a cloud of ^{40}K atoms, as that is relevant to our experiment described in the next chapter. The resonant wavelength is $\lambda_L = 770.11$ nm, the natural linewidth of the transition is $\Gamma = 6.035$ MHz, the resulting saturation intensity and recoil velocity are $I_{\text{sat}} = 17.5$ W/m² and $v_r = 0.01297$ m/s.

4.2 Perturbative treatment

We can treat these equations perturbatively in time, assuming the light is initially on resonance $\delta(z, 0) = 0$. To first order, we can set the detuning in Eq. 4.1 to $\delta = 0$, assume $I(z)$ is time independent, and plug that into Eq. 4.2 to obtain

$$\delta(t, z) = \frac{k_r v_r}{\hbar\omega_L \rho(z)} \int_0^t -\rho(z)\sigma_0 \frac{I(z)}{1 + I(z)/I_{\text{sat}}} d\tau \quad (4.3)$$

$$= \frac{k_r v_r \sigma_0}{\hbar\omega_L} \frac{I(z)}{1 + I/I_{\text{sat}}} t. \quad (4.4)$$

This can then be recursively plugged into Eq. 4.1 to obtain

$$\frac{d}{dz} \frac{I(z, t)}{I_{\text{sat}}} = -\rho(z) \sigma_0 \frac{I(z, t)/I_{\text{sat}}}{1 + 4 \left(\frac{k_r v_r \sigma_0}{\hbar \omega_L \Gamma} \frac{I(z)}{1+I/I_{\text{sat}}} \right)^2 t^2 + I(z, t)/I_{\text{sat}}}. \quad (4.5)$$

Integrating both sides of the above equation, we obtain a perturbative equation to second order in time [102]:

$$\sigma_0 n = \ln(I_0/I_f) + \frac{I_0 - I_f}{I_{\text{sat}}} + \frac{(k_r v_r t)^2}{3} \left(\frac{I_{\text{sat}}}{I_f + I_{\text{sat}}} - \frac{I_{\text{sat}}}{I_0 + I_{\text{sat}}} + \ln \left(\frac{I_f + I_{\text{sat}}}{I_0 + I_{\text{sat}}} \right) \right). \quad (4.6)$$

In Fig. 1b, we examine for what imaging times the above perturbative equation, as well as the model that completely ignores recoil induced detuning, is valid. We do this by performing numerical simulations to extract a value for the final intensity I_f and using Eq. 2.36 and Eq. 4.6 to extract values $\sigma_0 n$ that would be deduced from experiment. We find that within the recoil time, both analytic expressions start to differ from the true atomic column density by over 5%, and the perturbative model of Eq. 4.6 quickly diverges thereafter.

In the following sections, we describe two versions of numerical simulations that we have performed in order to appropriately extract atomic column densities from experimental data.

4.3 Stationary atom model

In order to numerically simulate the imaging process, we assumed a Gaussian distribution of atoms along the propagation direction, $\rho(z) = n/\sqrt{2\pi}w e^{-z^2/2w^2}$. The dependence of the result on the choice of cloud width w is discussed in the next section. We divided the cloud into small spatial bins of atoms along the imaging direction z . For the initial version of the simulation, the atoms were assumed to stay within their original bins for the entire duration of the imaging pulse, i.e. the cloud

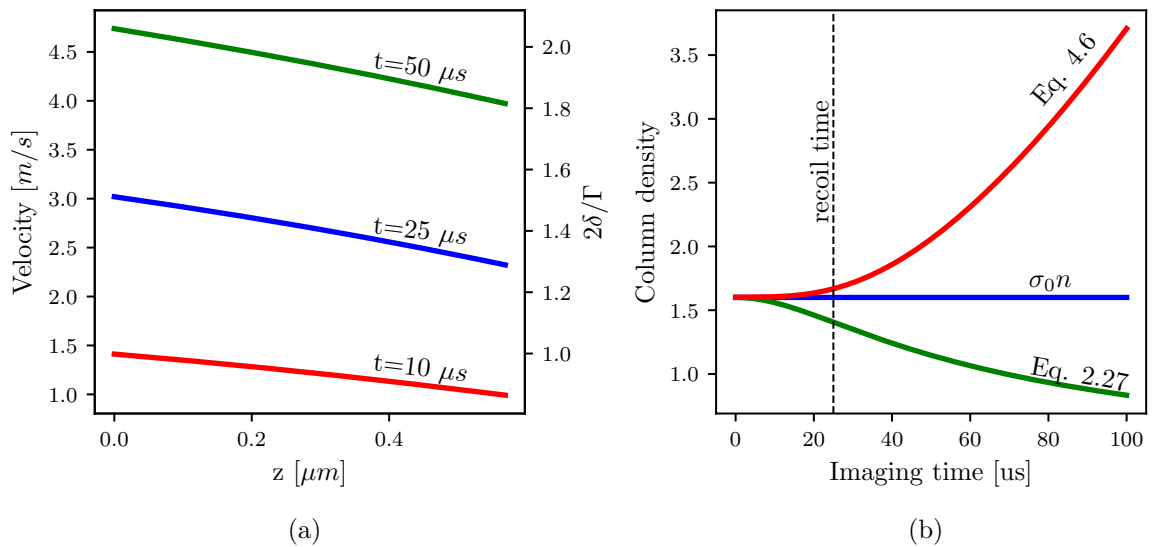


Figure 1: (a) Dependence of velocity and detuning on position simulated for ^{40}K at three different imaging times and a probe intensity $I_0 = 0.8I_{\text{sat}}$. (b) Column densities deduced from optical depths obtained from recoil detuning corrected simulation of imaging ^{40}K atoms at probe intensity $I_0 = 0.8I_{\text{sat}}$. The blue line is the true column density $\sigma_0 n = 1.6$. The green line is the high probe intensity corrected column density given by Eq. (2.36). The red line is the column density as expanded to second order in time, Eq. (4.6).

shape remained constant. We then used eqns. 4.1-4.2 to numerically propagate the probe intensity and detuning as a function of both time and space. The algorithm used is detailed by Alg. 1.

Algorithm 1 Stationary atom model

```

 $I[n = 0, t] = I_0$  { $n$  is the bin index,  $t$  is the time index,  $I$  is in units of  $I_{\text{sat}}$ }
```

 $\delta[n, t = 0] = 0$ {light initially resonant, δ in units of $\Gamma/2$ }
 $H_f = 0$ {Radiant fluence seen by camera after passing through cloud}
for $t = 0$ to t_f **do** {loop over time steps}
 for $n = 1$ to N **do** {loop over bins, N is total bin number}
 $A = \sigma_0 \rho[n] dz$ { dz is the size of spatial step}
 $B = v_r dt / (\hbar c \rho[n])$ { dt is the size of the time step}
 $I[n, t] = I[n - 1, t] - AI[n - 1, t] / (1 + \delta[n, t - 1]^2) + I[n - 1, t]$ {Eq. (4.1)}
 $\delta[n, t] = \delta[n, t - 1] + B(I[n - 1, t] - I[n, t])$ {Eq. (4.2)}
end for
 $H_f = H_f + I[N, t] dt$ {collecting total fluence seen by the camera}
end for
 $OD^{\text{sim}1} = -\ln(H_f / I_0 t_f)$

We call the optical depth obtained in this way $OD^{\text{sim}1}$, to distinguish if from the simulated optical depth via the method described in the next section.

The validity of this model can be checked by considering limits where the equations are analytically solvable. For short imaging times, the recoil-induced detuning should not contribute to the optical depth, and therefore Eq. 2.36 should become exact. This is seen in Fig. 2a, where the imaging pulse is only $3 \mu\text{s}$ long and the simulated optical depth (blue dots) agrees with that given by Eq. 2.36 for all intensity regimes.

Even at longer imaging times, the problem can be analytically solved for limits of both high and low intensity compared to the saturation intensity. At intensities $I \gg I_{\text{sat}}$, even far detuned atoms will scatter light at their maximum, and we can assume $\delta^2/\Gamma^2 \ll I/I_{\text{sat}}$, reducing back to Eq. 2.36. At extremely low intensities, atoms will scatter very little light and the detuning $\delta^2/\Gamma^2 \ll 1$, again reducing back to Eq. 2.36. As seen in Fig. 2 b,c the simulation agrees with the analytic Eq. 2.36 in the limit of both high and low intensities. But, as the imaging time increases,

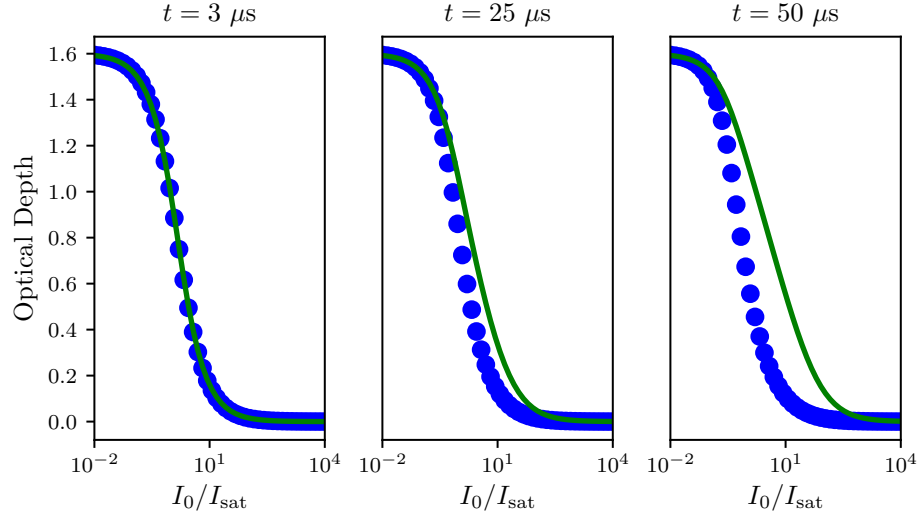


Figure 2: Optical depth as a function of probe intensity as predicted by the simulation (blue symbols) and by Eq. (2.36) (green curves), for three different imaging times. As expected, the predictions agree in both the high and low intensity limits, and differ for probe intensities comparable to the saturation intensity and longer imaging times.

the disagreement due to recoil induced detuning grows.

The simulation allows us to extract both the intensity and the detuning as a function of both time and position. We can use this information to infer the velocity and therefore the displacement of the atoms during the imaging pulse, and check if our assumption that the atoms stay in their original bins during the image pulse is valid. Figure 3a shows the position, deduced by integrating the recoil-induced velocity, as a function of time of the first (closest to light source), middle, and last (furthest from light source) spatial bin for a probe intensity slightly above saturation, $I = 1.2I_{\text{sat}}$. As seen in the figure, not only do the atoms move beyond their bins, but also at long imaging times the first atoms (which have absorbed the most light) overtake the last ones. Therefore, the atomic cloud does not maintain shape during the imaging pulse, and our initial assumption is invalid.

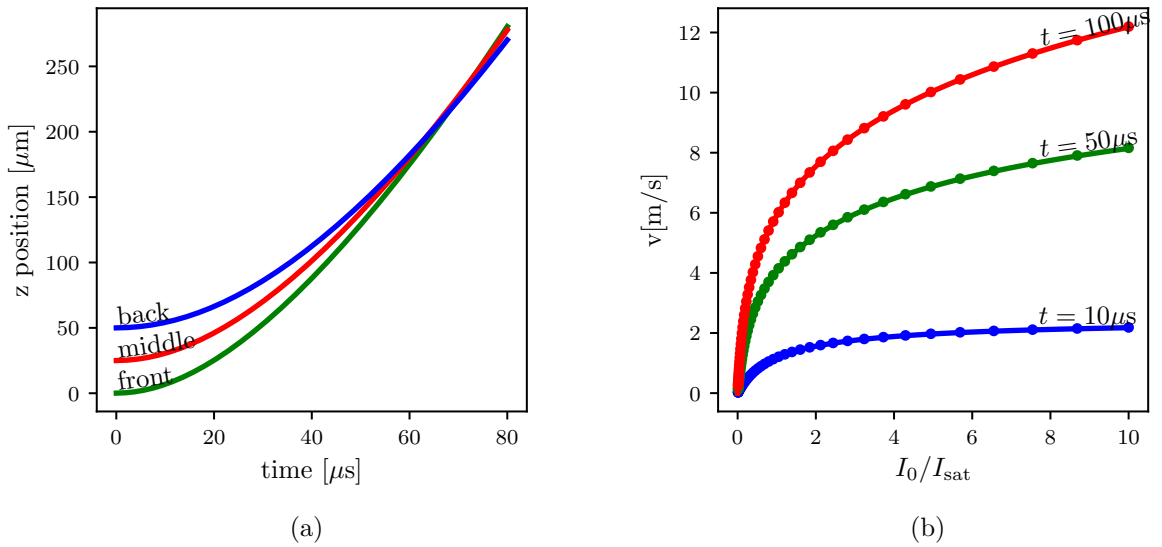


Figure 3: (a) Position of atoms as a function of imaging time for atoms in the first (solid green), middle (dashed red), and last (dotted blue) bins of the simulated density distribution for an initial cloud $50 \mu\text{m}$ in extent. The probe intensity used in this calculation was $1.2 I_{\text{sat}}$, and the column density was $\sigma_0 n = 1.6$. (b) The velocity of a single composite atom as a function of probe intensity for various imaging times. Simulation data (dots) and numerical solutions of Eq. (4.7) (lines) are in agreement.

4.4 Traveling atom model

To model the recoil-induced detuning effect during the imaging pulse taking into account the potentially significant spatial displacement of the atoms, we performed a second version of our simulation. In this version, we clumped $N_{\text{ca}} \approx 10^{11}$ atoms per unit transverse area into a single composite atom, and then tracked the detuning, velocity and position of each composite atom as a function of imaging time. Tacking individual atoms would be computationally inaccessible for reasonable cloud sizes. The algorithm used is given by Alg. 2.

Algorithm 2 Travelling atom model

```

 $z[n] = z_0, \delta[n] = 0$  {initialize position and detuning for each composite atom,
labeled by index  $n$ }
 $O[i] = n$  {make a list of composite atom indexes, ordered by position}
 $I[n = 0, t] = I_0$  {  $t$  is the time index,  $I$  is in units of  $I_{\text{sat}}$ }
 $H_f = 0$  {Radiant fluence seen by camera after passing through cloud}
for  $t = 0$  to  $t_f$  do {loop over time steps}
    for  $i = 1$  to  $N$  do {loop over superatoms}
         $n = O[i]$  {apply probe intensity to composite atoms in order of appearance}
         $A = \sigma_0 N_{sa} dz$  {dz is length over which atoms were grouped into single com-
        posite atom}
         $B = v_r dt / (\hbar c N_{sa})$  {dt is the time step}
         $I[n, t] = I[n - 1, t] - AI[n - 1, t] / (1 + \delta[n]^2 + I[n - 1, t])$  {Eq. (4.1)}
         $\delta[n] += B(I[n - 1, t] - I[n, t])$  {Eq. (4.2), detuning in units of  $\Gamma/2$ }
         $z[n] += dt \Gamma \delta / 2k$  { $k$  is the wavenumber,  $\Gamma \delta / 2k$  is the velocity at  $\delta$  detuning}
    end for
     $O[i] = \text{sort}(n, \text{key} = z[n])$  {sort composite atom indexes by current position}
     $H_f H_f + I[N, t] dt$  {collecting total fluence seen by the camera}
end for
 $OD^{\text{sim2}} = -\ln(H_f / I_0 t_f)$ 

```

To check the validity of this version of the simulation, we check the velocity of a composite atom as a function of time in an analytically solvable limit. In this case, we take the limit of a single composite atom, such that the intensity seen by the composite atom becomes time independent. This simplifies Eqs. 4.1 and 4.2 to only carry time dependence in the detuning term, and we can then plug Eq. 4.1

into Eq. 4.2 and differentiate both sides with respect to time to obtain

$$\frac{d\delta(t)}{dt} = \frac{\Gamma k_r v_r}{2} \frac{I/I_{\text{sat}}}{1 + 4\delta^2/\Gamma^2 + I/I_{\text{sat}}}. \quad (4.7)$$

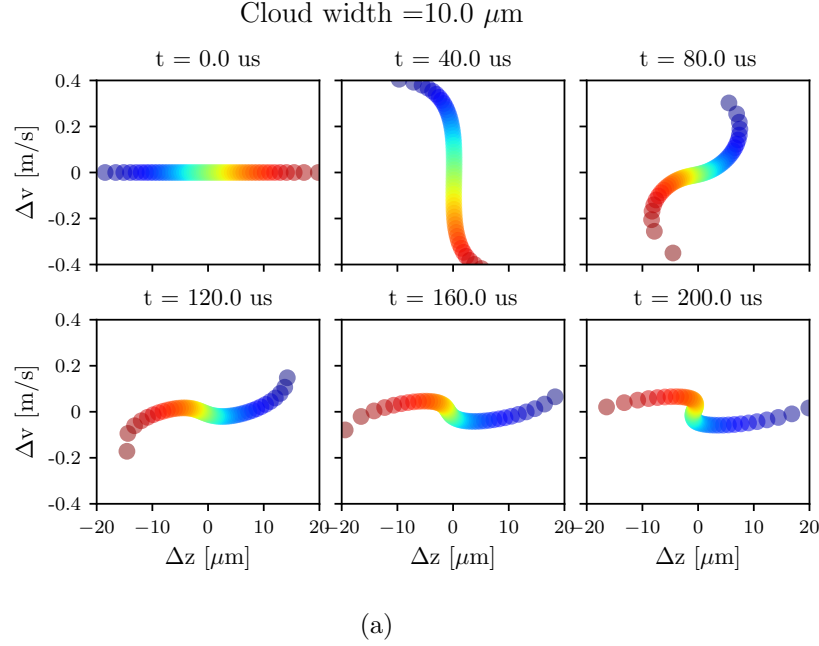
Equation (4.7) can be solved numerically, and is in agreement with our simulation, as seen in Fig. 3(b).

We then used this version of the simulation to look at the motion of composite atoms as a function of imaging time in phase space (i.e., velocity and position). Some examples of this motion can be seen in Fig. 4. As seen in the figure, the atomic cloud is significantly distorted during the imaging pulse and the atoms perform some crazy acrobatics.

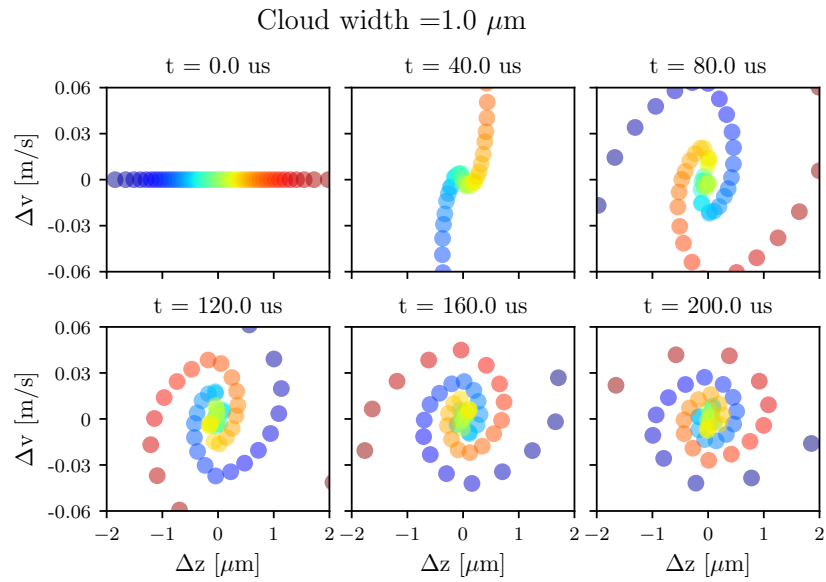
It remains to check how the atoms' acrobatics affect the resulting optical depth, ie the attenuation of the probe beam. To do this, we compare the optical depths generated by our stationary atom model, OD^{sim1} , and by our traveling atom model, OD^{sim2} . The results of this comparison are seen in Fig. 5(a). As seen from the figure, the optical depths predicted by the two versions of the simulation are negligibly small - $|OD^{\text{sim1}} - OD^{\text{sim2}}| / OD^{\text{sim1}} \leq 0.005$. We also checked the effect of having different initial distributions of atoms in space by varying the initial function $\rho(z)$ and keeping the total atom number constant. We found the effect of this to be negligible as well. Therefore, to infer atomic column densities from observed optical depths, it is sufficient to use the stationary atom model.

4.5 Calibration of saturation intensity

Saturation intensity is an intrinsic property of the atom, so the idea of calibrating it may be confusing. However, there are several experimental parameters that may influence exactly what value of I_{sat} is appropriate to use in eqn. 4.1 and 4.2, such as losses in the imaging system and polarization of the probe beam. In



(a)



(b)

Figure 4: Phase space evolution of an atomic cloud exposed to probe light with intensity $\tilde{I}_0 = 1.2$. We defined $\Delta v = v - \langle v(t) \rangle$ and $\Delta z = z - \langle z(t) \rangle$, subtracting out the center of mass position and velocity of the cloud. The column density $\sigma_0 n$ is 1.6, and the initial cloud is a Gaussian with a width of $10 \mu\text{m}$ in (a) and $1 \mu\text{m}$ in (b). The center of mass velocities $\langle v \rangle$ are $(0, 3.41, 5.26, 6.52, 7.50, 8.32) \text{ m/s}$ sequentially, and are the same for both initial cloud widths. Color represents original position of the composite atom along e_z .

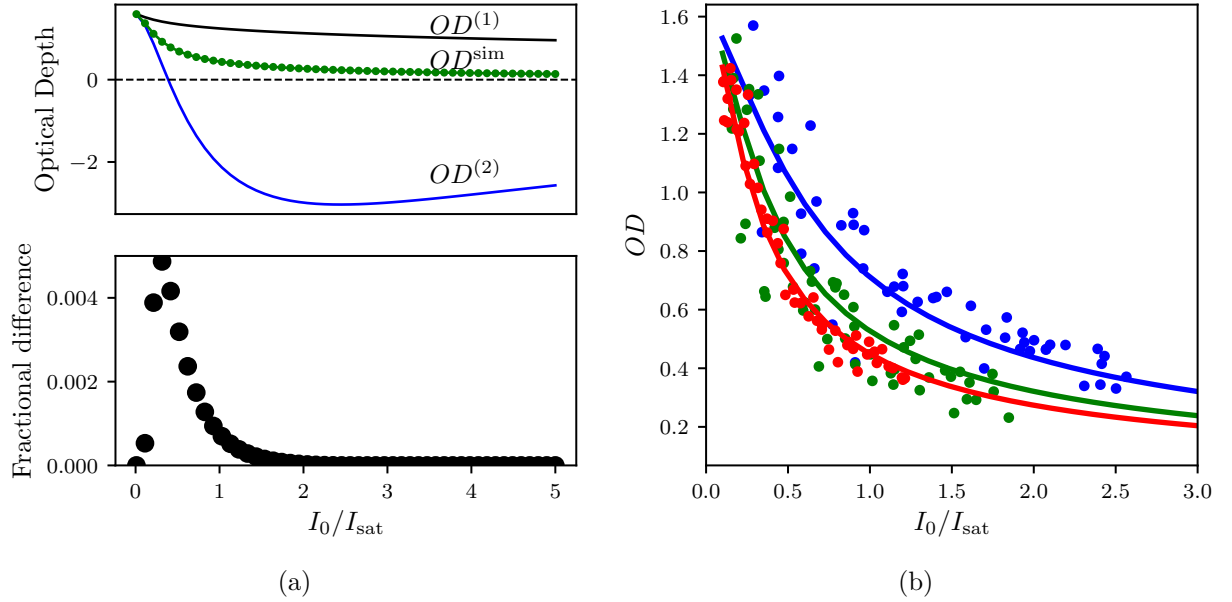


Figure 5: (a) Top. Optical depth as a function of probe intensity for an imaging time $t = 100 \mu\text{s}$. $OD^{(1)}$ and $OD^{(2)}$ are optical depths predicted from a given column density by Eq. (2.36) and (4.6) respectively. The two versions of simulated optical depth, $OD^{\text{sim}1}$ (green curve) and $OD^{\text{sim}2}$ (green dots) are plotted and overlapping each other. Bottom. The fractional difference between two versions of the simulated OD , $|OD^{\text{sim}1} - OD^{\text{sim}2}| / OD^{\text{sim}1}$. (b) The optical depth as a function of probe intensity for three imaging times: $t = 40 \mu\text{s}$ (blue), $t = 75 \mu\text{s}$ (green), $t = 100 \mu\text{s}$ (red). The dots represent experimental data and the lines represent the best fit of simulated data. The optimal fit parameters pictured are a $\sigma_0 n$ of 1.627(5) and saturation intensity of 29(7) counts/ μs .

addition, we have no direct experimental access to the total radiant fluence (time integral of intensity) seen by the camera. Instead, the light hitting the charge-coupled device (CCD) camera triggers some number of photoelectrons to be registered. The proportionality between the number of photons hitting the camera and the number of photoelectrons it triggers is called the quantum efficiency q_e of the camera. The number of these photoelectrons, after some electronic gain and noise introduced during the readout process, is then read out as a number of ‘counts’ registered on each pixel. The camera-dependent factors influencing how the number of counts depends on the number of incoming photons can be convolved with the experimental factors such as probe polarization and optical loss into a single calibration of the effective saturation intensity in units of ‘counts’ output by the camera per unit time.

To calibrate this effective I_{sat} in camera counts per unit time, we absorption imaged our cloud of ^{40}K atoms for a range of probe intensities for three different values of imaging time: $40 \mu\text{s}$, $100 \mu\text{s}$, and $200 \mu\text{s}$. We select a small region in the center of the cloud, where we can assume the atomic column density $\sigma_0 n$, and the initial probe intensity I_0 to be roughly constant. We then average the values of I_0 and I_f over this region and plot the final intensity I_f as a function of I_0 . We then used the optical depth predicted by our simulation OD^{sim} and used that to simultaneously fit the three curves with I_{sat} and $\sigma_0 n$ as fit parameters, as shown in Fig. 5(b). As can be seen from the figure, this procedure not only allows us to read off I_{sat} in units of camera counts per μs , but also shows that our simulation accurately reproduces the differences in OD dependence on imaging time.

4.6 SNR optimization

We consider Poisson distributed photon shot noise, converting into shot noise on photoelectrons triggered inside the CCD. The standard deviation will then be proportional to $q_e \sqrt{N_p}$, where q_e is the quantum efficiency of the camera and N_p is

the photon number. This uncertainty can be then propagated via the lookup table into uncertainty on the measured atomic column density $\delta_{\sigma_0 n}$. The signal-to-noise ratio (SNR) can then be expressed as $\sigma_0 n / \delta_{\sigma_0 n}$.

We study the SNR as a function of imaging time and initial probe intensity for a few different atomic column densities. Some representative data is shown in Fig. 6. As seen in Fig. 6(a), for a wide range of atomic column densities, extending the imaging time beyond 40 μs no longer yields significant improvements in SNR. There is, however, a factor of 1.5 improvement between using an imaging time of 10 μs , where the simple model given by Eq. 2.36 is appropriate, and 40 μs . Therefore, there are significant gains that can be made by going to longer imaging times and making use of the simulated lookup table.

This simulation allowed us to interpret experimental data. For a given imaging time, we created a look-up table of predicted optical depth as a function of probe intensity and atomic column density. We then found the observed optical depth on this table, with the given probe intensity, and inferred the atomic density. The uncertainty in the measured intensities can be propagated through this procedure, and we established optimal imaging parameters to maximize the SNR of this detection scheme. Figure 6(b) illustrates that the optimal initial probe intensity is different for different atom numbers. For low atom numbers, $\sigma_0 n \approx 0.1$, a probe intensity of $I_0 \approx 0.6 I_{\text{sat}}$ is best.

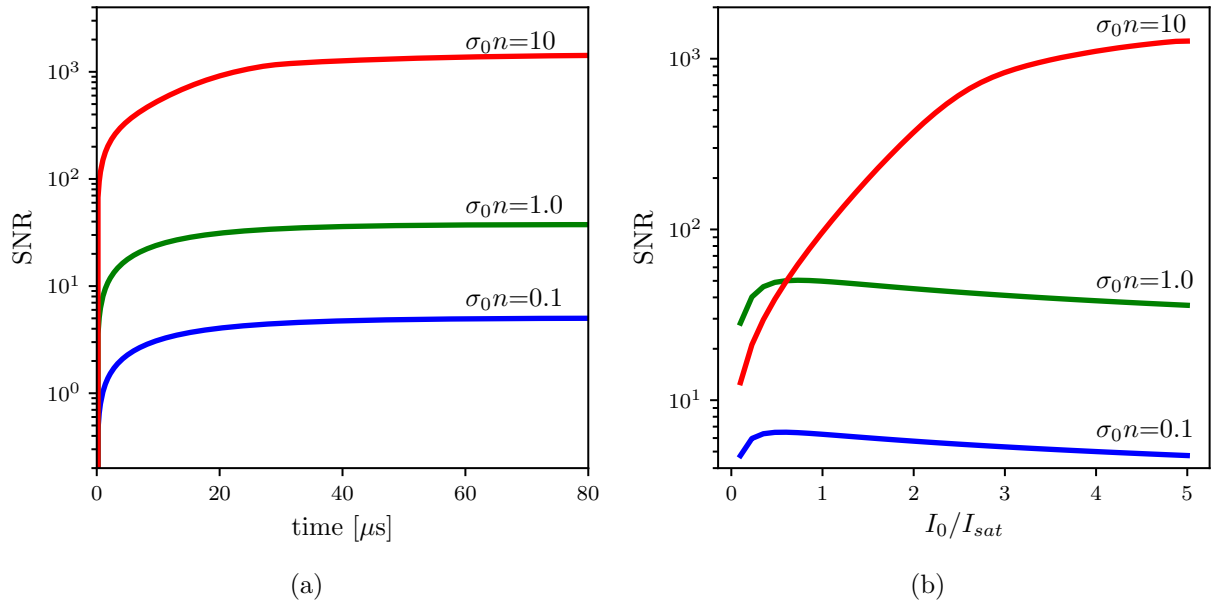


Figure 6: SNR for three different column densities after correcting for recoil induced detuning. (a) SNR as a function of imaging time for a probe intensity of $I_0 = 5.0I_{\text{sat}}$ and (b) SNR as a function of probe intensity for an imaging time of $50 \mu\text{s}$.

Chapter 5: Imaging of Scattering Near a Feshbach Resonance

In this chapter, we describe our experiment directly imaging *s*-wave scattering halos of ^{40}K atoms in the vicinity of a Fesbach resonance between the $|F = 9/2, m_F = -9/2\rangle$ and $|F = 9/2, m_F = -7/2\rangle$ internal states. We used this data to extract the location of the magnetic fields resonance of $20.206(15)$ mT and a width of $1.0(5)$ mT, similar to the accepted values of $20.210(7)$ mT and $0.78(6)$ mT [44]. The data presented in this chapter was previously reported in [101].

We first introduced Feshbach resonances in section 3.2.2. Although Feshbach resonances are extremely useful for studying and manipulating Fermi gases, their resonant magnetic field values are difficult to predict analytically and are commonly computed via numerical models based on experimental input parameters [103–105] or determined experimentally [41, 106]. There have been a variety of experimental techniques used to characterize Feshbach resonances, including measuring atom loss due to three-body inelastic scattering, measurement of re-thermalization timescales, and anisotropic expansion of the cloud upon release from a confining potential, all of which infer the elastic scattering cross section from collective behavior of the cloud [80, 107, 108].

Here, we present an alternative technique, where we directly image the enhancement in elastic scattering due to the resonance. We collided pairs of ultra-cold Fermi gases and directly imaged the resulting *s*-wave scattered atoms as a function of magnetic field strength. This allowed us to observe the enhancement in scattering without relying on proxy effects. We measured the fraction of atoms scattered

during the collision, and from this fraction deduced the resonant magnetic field and the width of the resonance.

In our dilute DFGs, even with the resonant enhancement of the scattering cross section, only a small fraction of the atoms scattered as the clouds passed through each other. This made direct detection of scattered atoms difficult due to detection uncertainty that disproportionately affected regions of low atomic density. To optimize the signal-to-noise ratio (SNR) for low atom numbers, we absorption imaged with fairly long, high-intensity pulses — a non-standard regime, where the atoms acquired a velocity during imaging and the resulting Doppler-shift was non-negligible. Simulation of the absorption imaging process was necessary for an accurate interpretation of these images, as described in Chapter 4. Using the simulation-corrected images, we extracted the fraction of atoms scattered in our collision experiment.

5.1 Experimental procedure

We prepared our degenerate ${}^{40}\text{K}$ clouds as described in section 3.3.5. After this preparation, we used adiabatic rapid passage (ARP) to transfer the degenerate cloud of ${}^{40}\text{K}$ atoms in the $|F = 9/2, m_F = 9/2\rangle$ state into the $|F = 9/2, m_F = -9/2\rangle$ state by using a 3.3 MHz rf field and sweeping the bias magnetic field from -0.518 mT to -0.601 mT in 150 ms.

Following the state transfer, we had two versions of the protocol – one for approaching the Feshbach resonance from higher fields and one for approaching it from lower fields. For approaching the resonance from lower fields, we proceeded by ramping the bias magnetic field to 19.05 mT, turning on a 42.42 MHz RF field, and then sinusoidally modulating the bias field at 125 Hz for 0.5 s, with a 0.14 mT amplitude, decohering the ${}^{40}\text{K}$ state into an equal mixture of $|F = 9/2, m_F = -9/2\rangle$ and $|F = 9/2, m_F = -7/2\rangle$. For approaching the resonance from higher fields, the same was done at a bias field of 21.71 mT and an RF frequency of 112.3 MHz. The

depolarization allowed the ^{40}K atoms to interact and re-thermalize, allowing us to further evaporate in the dipole trap [109]. Since ^{87}Rb is heavier than ^{40}K , we were able to evaporate the ^{40}K atoms past the point where ^{87}Rb atoms were no longer suspended against gravity and had been completely removed. These hyperfine states of ^{40}K were then used to study their Feshbach resonance.

After evaporation, we ramped the bias field in a two-step fashion to the desired value B near the Feshbach resonance. We approached the field using our quad coils in Helmholtz configuration (0.19 mT/A, see sec. 3.3.2) to bring the magnetic field to a setpoint 0.59 mT away from B , $B - 0.59$ mT when approaching from below and $B + 0.59$ mT from above. We held the atoms at this field for 100 ms to allow the eddy currents induced by the large quad coils to settle, and then flipped the current of our lower inductance biasZ coils from -18 to 18 A (0.017 mT/A, see sec. 3.3.2) to quickly change the field the remaining 0.59 mT. This allowed us to study the resonance from both sides without the added losses associated with going through the resonance [40].

Once at the intended bias field, we split the cloud into two spatially overlapping components with opposing momenta and observed scattering as they moved through each other and separated. These counter-propagating components were created using an $8E_{\text{L}}$ deep near resonant ($\lambda_{\text{L}}=766.704$ nm) 1-d retro-reflected optical lattice (see sec. 3.3.1), where $E_{\text{L}} = \hbar^2 k_{\text{L}}^2 / 2m_{\text{K}}$ is the lattice recoil energy and $\hbar k_{\text{L}} = 2\pi\hbar/\lambda$ is the recoil momentum. We rapidly pulsed this lattice on and off with a double-pulse protocol [110, 111]. The pulse sequence was optimized to transfer most of the atoms into the $\pm 2\hbar k_{\text{L}}$ momentum states. Since the initial Fermi gas had a wide momentum spread (in contrast to a BEC, which has a very narrow momentum spread), and the lattice pulsing is a momentum dependent process [110], not all the atoms were transferred into the target momentum states. We experimentally optimized our pulse times to minimize the atoms remaining in the zero momentum

state. The optimized pulse times were $23\ \mu\text{s}$ for the first pulse, $13\ \mu\text{s}$ off interval, and $12\ \mu\text{s}$ for the second pulse [111].

We then released the atoms from the trap and allowed 1 ms for the two opposite momentum states within the cloud to pass through each other, scattering on the way. For the data taken coming from below the Feshbach resonance, we then simply ramped down the field and imaged the atoms. For the data taken coming from above the Feshbach resonance, we ramped the field back up, retreating through the resonance if it had been crossed and thereby dissociating any molecules that were created, and then quickly ramped the field back down and imaged the atoms. We used a $40\ \mu\text{s}$ imaging pulse with $I_0/I_{\text{sat}} \approx 0.6$ at the center of the probe laser. The total time-of-flight was $t_{TOF} = 6.8\ \text{ms}$.

The magnetic fields produced by the combination of our quad and biasZ coils in the regime of interest were independently calibrated by rf-spectroscopy. We prepared ^{40}K atoms in the $|F = 9/2, m_F = -9/2\rangle$ state and illuminated them with an rf-field with some frequency ν_{rf} . We then ramped our high-inductance coils to variable set points, followed by an adiabatic $250\mu\text{s}$ ramp of $2.84\ \text{mT}$ in the lower inductance coils. We then used Stern-Gerlach and observed the fractional population in the $|F = 9/2, m_F = -9/2\rangle$ and $|F = 9/2, m_F = -7/2\rangle$ states as a function of the high-inductance coil current. We fit the fractional population curve to a Gaussian, and considered the center of the fit to be on-resonant, with an uncertainty given by the Gaussian width. We used the Breit-Rabi formula (see sec. 2.1.2) to determine the resonant field value at ν_{rf} . We did this for 5 different rf frequencies, and acquired a field calibration with an uncertainty of $0.3\ \text{mT}$, which was included in the listed uncertainty on the center field of the Feshbach resonance.

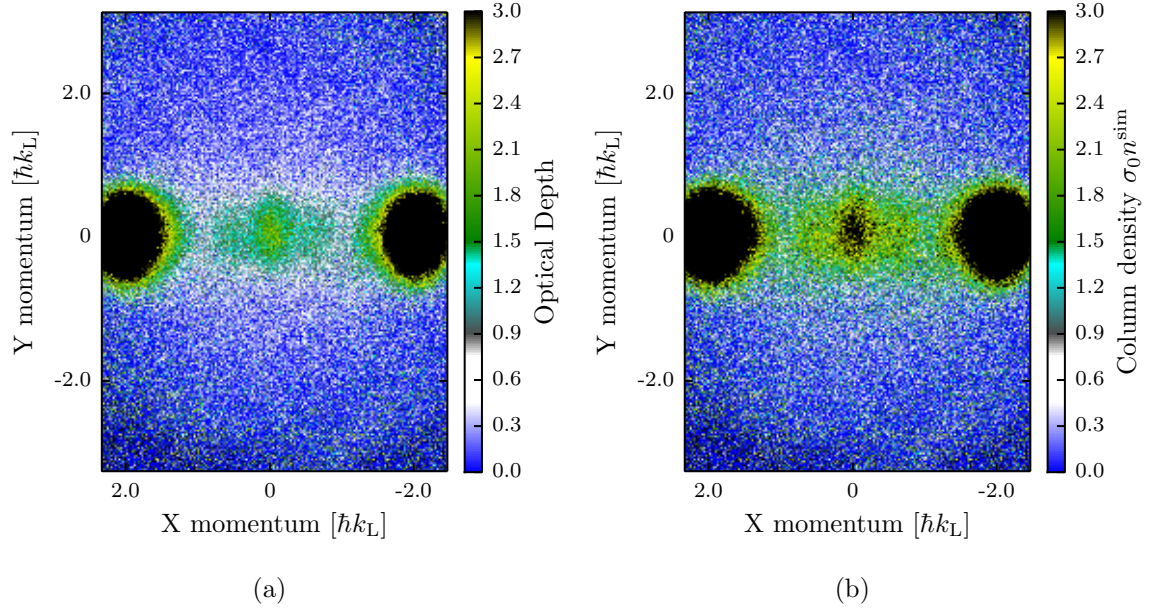


Figure 1: An example of our absorption image after 6.8 ms TOF. The 1-D lattice imparts momentum along e_x . The two large clouds on the left and right are the atoms in the $\pm 2k_L$ momentum orders that passed through each other unscattered. The smaller cloud in the center is the atoms that remained in the lowest band of the lattice after pulsing, and thus obtained no momentum. The thin spread of atoms around these clouds is the atoms that underwent scattering. This image was taken coming from below the Feshbach resonance at 20.07 mT. (a) Raw optical depth, (b) atomic column density obtained by comparing to simulated ODs , $\sigma_0 n^{\text{sim}}$

5.2 Data analysis

We first processed each image by comparing the observed ODs to simulations taking into account the recoil induced detuning as described in Chapter 4. An example of images before and after processing are shown in Fig. 1. To improve the signal and mitigate our shot to shot number fluctuations, we took 15 nominally identical images for each data point.

We counted the fraction of atoms that experienced a single scattering event for each of the fifteen images at a given bias magnetic field. Single scattering events are easily identified, as two atoms that scatter elastically keep the same amplitude of momentum, but depart along an arbitrary direction. Therefore, an atom traveling

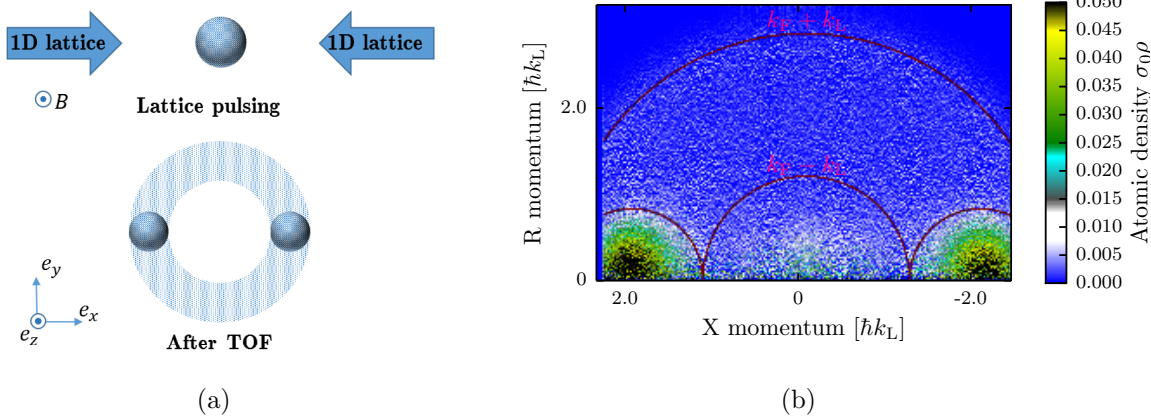


Figure 2: (a) Our experimental setup. After time-of-flight, the two clouds traveling along $\pm \hat{e}_x$ directions have separated and the atoms that underwent a single scattering event were evenly distributed in a scattering halo around the unscattered clouds. The 1-D lattice defined the axis of cylindrical symmetry. (b) Inverse Abel transformed image. The atoms within the Fermi momentum k_F of each unscattered cloud center are in the unscattered region and counted towards the total unscattered number. The atoms outside the radius $k_L - k_F$ but inside $k_L + k_F$ while also being outside the unscattered region are counted towards the number of single scattered atoms.

at $2\hbar k_L$ to the right that collides elastically with an atom traveling at $-2\hbar k_L$ to the left will depart with equal and opposite momenta $2\hbar k_L$ at an arbitrary angle, and in a time-of-flight image such atoms will lie in a spherical shell, producing the scattering halo pictured in Fig. 2(a).

Absorption images captured the integrated column density along e_z , a projected 2D atomic distribution. To extract the radial dependence of the 3D distribution from the 2D image, we performed a standard inverse Abel transform. The inverse Abel transform assumes cylindrical symmetry, which was present in our case, with the axis of symmetry along e_x , defined by the lattice. We neglect the initial asymmetry of the trap, as during time-of-flight the atoms travel far beyond the initial extent of the cloud ($r_x, r_y, r_z \approx (45, 48, 15)$ μm), while the cloud width after TOF is $\approx 82 \mu\text{m}$ in each direction. We thus obtained the atomic distribution $\rho(r, \theta)$ as a function of r , the radial distance from the scattering center, and θ , the angle

between r and symmetry axis e_x , integrated over ϕ , the azimuthal angle around the x axis.

We then extracted the number of scattered atoms N_{scat} as a fraction of the total atom number N_{tot} for each image, as shown in Fig. 2(b). The unscattered atom number was the number of atoms in the two unscattered clouds. The number of atoms that underwent a single scattering event was the number of atoms outside the Fermi radius of the unscattered clouds, but inside the arc created by rotating the Fermi momentum k_F around the original center of the cloud (red arcs in Fig. 2(b)). For both the scattered and unscattered numbers, we accounted for atoms that fell outside the field of view of our camera by multiplying the counted atom number by a factor of the total area as defined by the radii divided by the visible area on the camera. The atoms in the center region were not counted as they were originally in the zero momentum state and could not contribute to the scattering halo under study.

We fit the fraction of scattered atoms versus the total atom number for each of the 15 images taken at the same bias magnetic field to a line constrained to be zero at zero. The slope of this fit was taken to be the value of $N_{\text{scat}}/N_{\text{tot}}^2$ at that bias magnetic field, and the variance of the fit gave the uncertainty on that data point. This uncertainty reflected our shot to shot number fluctuations, which produced variable atomic densities and thus influence the scattered fraction.

We then deduced the resonant field value B_0 and width of the resonance Δ , the parameters in Eq. (3.26). Since we were in the low energy regime (the atomic momentum was much smaller than the momentum set by the van der Waals length $k_L + k_F \ll 1/l_{\text{vdW}}$, and we were well below the p-wave threshold temperature [109]), the scattering cross-section was given by $\sigma = 4\pi a^2$.

The scattering cross-section σ gives the probability $P_{\text{scat}} = \sigma N/A$ that a single particle will scatter when incident on a cloud of atoms with a surface density of

N/A , where A is the cross-sectional area of the cloud and N is the number of atoms in the cloud. In our case, each half of the initial cloud, with atoms number $N_{\text{tot}}/2$, is incident on the other half. Thus, the number of expected scattering events is $N_{\text{scat}} = (N_{\text{tot}}/2)\sigma(N_{\text{tot}}/2) = \sigma N_{\text{tot}}^2/4A$. Assuming A is constant for all our data, we can define a fit parameter $b_0 = 4\pi a_{\text{bg}}^2/4A$, where a_{bg} is the background scattering length. We can thus adapt Eq. (3.26) to obtain the fit function

$$\frac{N_{\text{scat}}}{N_{\text{tot}}^2} = b_0 \left(1 - \frac{\Delta}{B - B_0}\right)^2 + C. \quad (5.1)$$

We found that our imaging noise skewed towards the positive, giving rise to a small background offset. We accounted for this in our fit by including a constant offset parameter C .

5.3 Results

Our final data is presented in Fig. 3. The red curve depicts a best fit of the model given in Eq. (5.1). The fit parameters we extracted were $\Delta = 1(5)$ mT, $B_0 = 20.206(15)$ mT, $b_0 = 5(3) \times 10^{-3}$ and $C = 8(1) \times 10^{-4}$. To obtain the fit, we used data taken by approaching the resonance from above for points above where we expected the resonance to be and data taken approaching the resonance from below for points below. We also excluded from the fit data points very near the resonance, as there the assumption $\sigma\rho \ll 1$, where ρ is the atom number per unit area, is no longer valid and the problem must be treated hydrodynamically.

The accepted values for the ${}^{40}K$ s-wave Feshbach resonance for the $|9/2, -9/2\rangle$ and $|9/2, -7/2\rangle$ states are $B_0 = 20.210(7)$ mT and $\Delta = 0.78(6)$ mT [44], which is in good agreement with our findings. Some potential sources of systematic uncertainty that we did not account for include scattering with atoms that did not receive a momentum kick from the lattice pulsing or the impact of multiple scattering events.

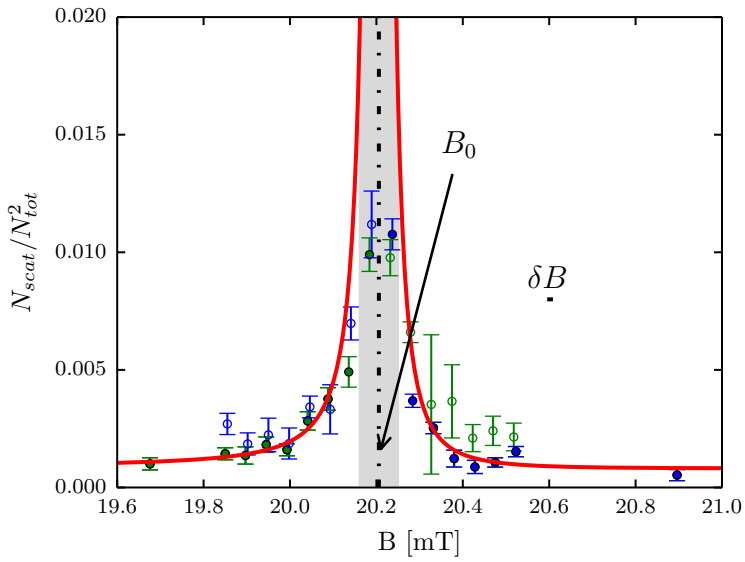


Figure 3: Normalized scattered population plotted versus bias field B . Green dots represent data taken coming from below the resonance, and blue dots represent the data taken coming from above the resonance. The red curve depicts the best fit, where data coming from above the resonance was used above the resonance and data coming from below the resonance was used below the resonance to create the fit; the unused data points are indicated by hollow dots. The regime where the scattering length is likely large enough for the atoms to behave hydrodynamically is shaded in gray, and data points in that area were also excluded from the fit. Resonant field value B_0 as found in this work and our systematic uncertainty in the bias magnetic field δB are indicated.

Chapter 6: Synthetic Magnetic Fields in Synthetic Dimensions

In condensed matter, 2-D systems in high fields have proved to be of great technological use and scientific interest. The integer quantum Hall effect (IQHE) [20], with its quantized Hall resistance, has given rise to an ultra-precise standard for resistivity. It was also one of the first examples of topology playing an important role in physics—the precise quantization of the Hall conductance is guaranteed by the non-trivial topology of the system [6]. This leads to the precisely quantized ‘plateaus’ in the transverse resistivity that occur as different multiples of the magnetic flux quantum $\Phi_0 = h/e$, where e is the electron charge, are threaded through the material.

In the IQHE system, the underlying lattice structure of the host semiconductor is effectively washed out—the magnetic flux per individual lattice plaquette is negligible. However, new physics arises when the magnetic flux per plaquette is increased to some non-negligible fraction of the flux quantum, giving rise to the Hofstadter butterfly [16]. These regimes are hard to reach experimentally, since the typical plaquette size in crystalline material is of order a square Angstrom, and the magnetic field necessary to thread a magnetic flux of Φ_0 through such a narrow area is of order $\approx 10^4$ Tesla, not accessible with current technology.

Several platforms have however reached the Hofstadter regime by engineering systems with large effective plaquette size, in engineered materials [17, 18], and in atomic [51, 54–58] and optical [112] settings. Here, we use the approach of synthetic dimensions [61] in atomic BEC of ^{87}Rb to reach the Hofstadter regime. We

demonstrate the non-trivial topology of the system created, and use it to image skipping orbits at the edge of the 2-D system—a hallmark of 2-D electron systems in a semi-classical treatment.

We first describe the experimental setup of the effective 2D lattice with a large effective magnetic flux through it created with synthetic dimensions in sec. 6.1. We write down the Hamiltonian of the system, calculate the band structure and discuss its basic features in sec. 6.2.1. We then describe the results of our experiments. First, we describe the measured eigenstates of the system in sec. 6.3. Second, we detail the measurement of chiral edge motion when atoms are loaded into the central site of the lattice along the synthetic direction. Finally, we describe our observation of skipping orbits along the edges of the system, when atoms are loaded into the edge sites along the synthetic direction. This measurement represents the first direct observation of the phenomenon of skipping orbits. The work described in this chapter was published in [62].

6.1 Synthetic dimensions setup

Any internal degree of freedom can be thought of as a synthetic dimension—the different internal states can be treated as sites along this synthetic direction. As long as one can define a metric along this direction, i.e. some of the internal states are ‘nearest neighbors’ while others are not, it is sensible to consider it is a dimension. In our case, an effective 2-D lattice is formed by sites formed by a 1-D optical lattice along a ‘real’ direction, here e_x , and the atom’s spin states forming sites along a ‘synthetic’direction, \mathbf{e}_s .

The experimental setup for this system is schematically represented in Fig. 1a. The BEC is subject to a 1-D optical lattice, formed by a retro-reflected beam of $\lambda_L = 1064$ nm along e_x . A bias magnetic field B_0 along e_z energetically separates the different spin states. The spin states can be thought of as sites along a synthetic

dimension even without any coupling field. However, only once a coupling field is present do they acquire a sense of distance. We couple them via rf or Raman coupling, which only couples adjacent spin states. The Raman beams illuminating the atoms are shining in opposite directions along the same e_x axis as the 1-D optical lattice. The rf field has components both along the e_x and e_y .

Figure 1b sketches out the effective 2-D lattice created. Here, we have labeled the lattice sites along the ‘real’ direction e_x by site index j . In the tight binding approximation, we can describe a lattice hopping between adjacent sites with tunneling amplitude t_x . Similarly, the sites along the ‘synthetic’ dimension are labeled by site index m (identical to spin projection quantum number m_F), and the rf or Raman coupling here plays the role of a tunneling amplitude t_s . In the case of rf coupling, there is no momentum kick associated with spin exchange, and both t_x and t_s are real.

In the case of Raman coupling, however, there is a momentum kick of $2k_R$ associated with every spin transfer, and therefore a phase factor of $\exp(2ik_Rx)$ with every spin ‘tunneling’ event. Since position x is set by the 1-D lattice, $x_j = j\lambda_L/2 = j\pi/k_L$, and the space dependent phase factor is $\exp(2\pi ik_R/k_L j)$. An absolute phase change in the wavefunction is not meaningful. However, a phase acquired when going around a plaquette and coming back to the same place is meaningful, as one could imagine one atom staying at the same site and the other going around a plaquette and coming back to detect the phase difference. In this setup, the phases acquired while going around a single plaquette are, starting at some lattice site $|j, m\rangle$, are: 0 (for tunneling right to $|j + 1, m\rangle$), $2\pi ik_R/k_L(j + 1)$ (for tunneling up to $|j + 1, m + 1\rangle$), 0 (for tunneling left to $|j, m + 1\rangle$) and $-2\pi ik_R/k_L j$ (for tunneling back down to $|j, m\rangle$). The total phase acquired is thus $\phi_{AB} = 2\pi k_R/k_L$, independent of the starting lattice site. Since the absolute phase does not matter and only the value of ϕ_{AB} , we can perform a phase transformation that shifts the tunneling phase

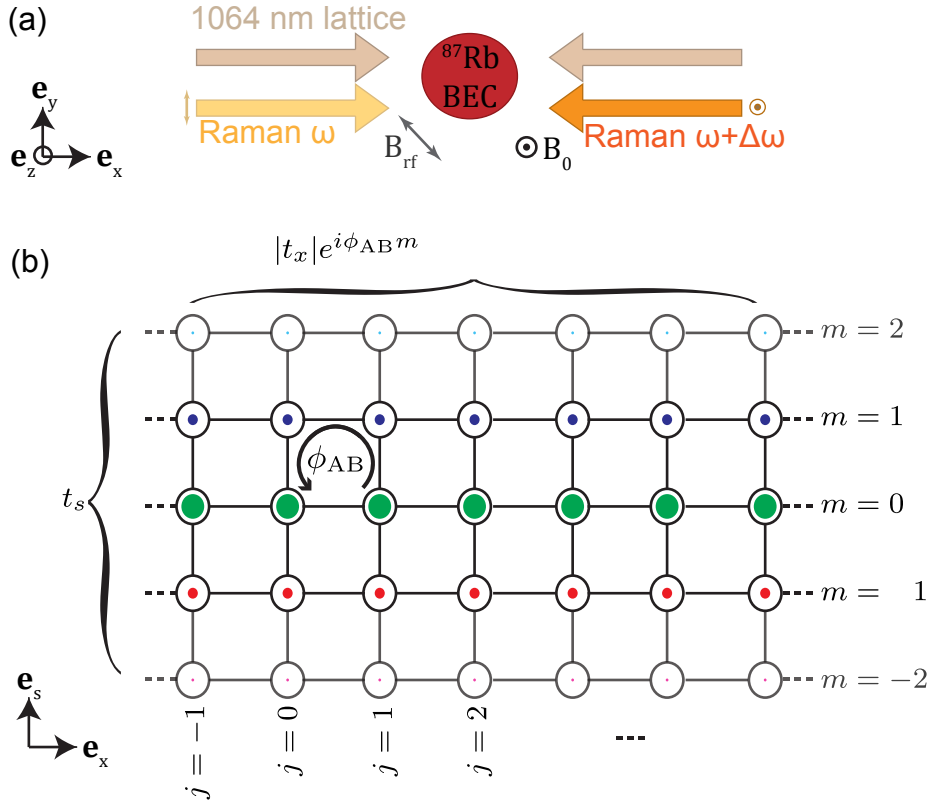


Figure 1: Setup of effective 2-D lattice. (a) Beam geometry. The BEC is subject to a bias magnetic field B_0 in the e_z direction. The 1-D lattice beam and Raman beams are both along the e_x direction, and the rf field can be applied with projections onto both e_x and e_y . (b) Schematic of the effective 2-D lattice. Sites along e_x are formed by the 1-D optical lattice and labeled by site number j . Sites along the synthetic direction e_s are formed by the spin states: 3 sites for atoms in the $F = 1$ manifold and 5 sites for atoms in $F = 2$. These sites are labeled by m . Raman transitions induce a phase shift, which can be gauge transformed into a tunneling phase along the e_x direction. This leads to a net phase when hopping around a single lattice plaquette of ϕ_{AB} .

onto the spatial direction, defining $t_x = |t_x| \exp(i\phi_{AB}m)$ and $t_s = |t_s|$, as labeled in Figure 1b.

To see how this phase implies an effective magnetic field, we draw an analogy to the Aharonov-Bohm effect [15, 113] from quantum mechanics. This effect considers an infinite solenoid with an electric current running through it. The magnetic field B in this setup exists only inside the solenoid, while the magnetic vector potential persists outside the solenoid. However, if two electrons are sent on a trajectory around the solenoid, even though they never pass through any magnetic field, they nevertheless acquire a relative phase that can be detected by interfering them with each other. This relative phase is given by $\phi_{AB} = 2\pi\Phi/\Phi_0$, where $\Phi = B * A$ is the magnetic flux through the solenoid (A is the area inside the solenoid, pierced by the magnetic field) and $\Phi_0 = h/e$ is the flux quantum, with e the electron charge. Since in our system, the atoms acquire a phase when they perform a closed loop around a single lattice plaquette. Therefore, they behave as though there was an infinite solenoid piercing each plaquette with a magnetic field going through it, and the flux per plaquette in units of the flux quantum is $\Phi/\Phi_0 = \phi_{AB}/2\pi = k_R/k_L$. For the case of rf coupling, the phase acquired at every transition is 0 and the flux $\Phi/\Phi_0 = 0$. In this way, we are able to engineer large fluxes per individual plaquette simply by adjusting the ratio k_R/k_L , allowing us to sidestep the need for experimentally inaccessible field strengths and reach the Hofstadter regime.

6.2 Hamiltonian of the effective 2-D system

6.2.1 Hamiltonian

The full Hamiltonian of this system, without making the tight binding approximation, can be written down by combining the lattice Hamiltonian (eqn. 2.43) and

the rf (eqn. 2.53) or Raman Hamiltonian (eqn. 2.56):

$$H = \frac{\hbar\vec{k}^2}{2m} - V_0 \sin^2(k_L x) + \hbar\delta F_z + \hbar\epsilon F_z^2 + \frac{\Omega}{2} F_x \quad (6.1)$$

for rf coupling and

$$H = \frac{\hbar k_y^2 + \hbar k_z^2}{2m} + \hbar^2 \frac{k_x \mathcal{I} + k_R F_z)^2}{2m} - V_0 \sin^2(k_L x) + \hbar\delta F_z + \hbar\epsilon F_z^2 + \frac{\Omega}{2} F_x \quad (6.2)$$

for Raman coupling. Here, k is the wavenumber, V_0 is the lattice depth, $\hbar k_L$ is the lattice recoil momentum, $\hbar k_R$ is the Raman recoil momentum, F_z and F_x are the angular momentum matrices, δ is the rf or Raman detuning, Ω is the rf or Raman Rabi frequency, ϵ is the quadratic Zeeman shift, and \mathcal{I} is the identity matrix. To find eigenstates of these Hamiltonians, we write them in a new basis that encompasses both the momentum and the spin degrees of freedom. For the lattice Hamiltonian, we used the momentum basis

$$\begin{pmatrix} \vdots \\ |q + 4k_L\rangle \\ |q + 2k_L\rangle \\ |q\rangle \\ |q - 2k_L\rangle \\ |q - 4k_L\rangle \\ \vdots \end{pmatrix}. \quad (6.3)$$

For the Raman Hamiltonian in the $F = 1$ manifold, we used the spin and momentum basis

$$\begin{pmatrix} |k_x - 2k_R, -1\rangle \\ |k_x, 0\rangle \\ |k_x + 2k_R, 1\rangle \end{pmatrix}. \quad (6.4)$$

In a lattice, the momentum k_x becomes crystal momentum q . For every state

in the lattice basis, we now expand to three states, one for each spin state, with the appropriate momentum shifts, giving

$$\left(\begin{array}{c} \vdots \\ |q + 2k_L - 2k_R, -1\rangle \\ |q + 2k_L, 0\rangle \\ |q + 2k_L + 2k_R, 1\rangle \\ |q - 2k_R, -1\rangle \\ |q, 0\rangle \\ |q + 2k_R, 1\rangle \\ |q - 2k_L - 2k_R, -1\rangle \\ |q - 2k_L, 0\rangle \\ |q - 2k_L + 2k_R, 1\rangle \\ \vdots \end{array} \right) . \quad (6.5)$$

In this basis, we combine the lattice and Raman Hamiltonians (omitting the kinetic energy in the other two directions) in an infinite block matrix form as

$$H = \left(\begin{array}{ccc} \ddots & & \\ & \mathbf{H}_R(2k_L) & \frac{\mathbf{v}_0}{4} & \mathbf{0} \\ & \frac{\mathbf{v}_0}{4} & \mathbf{H}_R(0) & \frac{\mathbf{v}_0}{4} \\ & \mathbf{0} & \frac{\mathbf{v}_0}{4} & \mathbf{H}_R(-2k_L) \\ & & & \ddots \end{array} \right) , \quad (6.6)$$

where $\mathbf{H}_R(x)$ is the Raman Hamiltonian with a momentum shift of x :

$$\mathbf{H}_R(n2k_L) = \begin{pmatrix} \frac{\hbar^2(q+n2k_L-2k_R)^2}{2m} + \hbar\delta & \hbar\Omega/2 & 0 \\ \hbar\Omega/2 & \frac{\hbar^2(q+n2k_L)^2}{2m} - \hbar\epsilon & \hbar\Omega/2 \\ 0 & \hbar\Omega/2 & \frac{\hbar^2(q+n2k_L+2k_R)^2}{2m} - \hbar\delta \end{pmatrix}, \quad (6.7)$$

the matrix $\frac{\mathbf{V}_0}{4}$ is a 3x3 diagonal matrix lattice coupling strength $\frac{V_0}{4}$ on the diagonal, and $\mathbf{0}$ is a 3x3 matrix of zeros. This extends in both directions with $\mathbf{H}_R(2nk_L)$ on the diagonal blocks and $\frac{\mathbf{V}_0}{4}$ as the first off-diagonal blocks and $\mathbf{0}$ everywhere else.

This Hamiltonian is easily extended to higher F values by replacing the Raman blocks $\mathbf{H}_R(x)$ with the corresponding Raman coupling Hamiltonian from eqn. 2.57, and extending the diagonal matrix $\frac{\mathbf{V}_0}{4}$ and the zero matrix $\mathbf{0}$ to be $(2F+1)\times(2F+1)$.

For computational convenience, we convert to lattice recoil units, $E_L = \hbar^2 k_L^2 / 2m$, $k_L = 2\pi/\lambda_L$. Then the diagonal blocks become

$$\mathbf{H}_R(n)/E_L = \begin{pmatrix} (q + 2n - 2\phi_{AB}/2\pi)^2 + \hbar\delta & \hbar\Omega/2 & 0 \\ \hbar\Omega/2 & (q + 2n)^2 - \hbar\epsilon & \hbar\Omega/2 \\ 0 & \hbar\Omega/2 & (q + 2n + 2\phi_{AB}/2\pi)^2 - \hbar\delta \end{pmatrix}, \quad (6.8)$$

where $\hbar\delta$, $\hbar\Omega$ and $\hbar\epsilon$ are now written in units of E_L , q is written in units of k_L and we have used the fact that $\phi_{AB}/2\pi = k_R/k_L$. The off-diagonal blocks $\frac{\mathbf{V}_0}{4}$ will be the same 3x3 diagonal matrices, with $\frac{V_0}{4}$ in units of E_L .

This Hamiltonian can be written for general values of F in the presence of Raman coupling and a 1-D optical lattice as

$$H = \sum_{m=-F, n=-\infty}^{F, \infty} H_0 + H_R + H_L,$$

where the diagonal term

$$H_0 = (\hbar^2 (q - 2m\Phi/\Phi_0 - 2n)^2 k_L^2 / 2m + \hbar\delta m + \hbar\epsilon m^2) |q + n2k_L, m\rangle \langle q + n2k_L, m|$$

includes the kinetic energy as well as the two-photon Raman detuning from resonance δ and the quadratic Zeeman shift ϵ . The second term represents the Raman coupling with coupling strength $\hbar\Omega$, with anisotropic tunneling arising from the spin-dependent prefactor (Clebsch-Gordan coefficient):

$$H_R = \hbar\Omega\sqrt{F(F+1) - m(m+1)} / 2\sqrt{2} |q + n2k_L, m\rangle \langle q + n2k_L, m+1| + \text{H.c.}$$

Here, H.c. stands for Hermitian conjugate. The third term represents lattice coupling to higher order lattice states, with lattice depth V_0 :

$$H_L = V_0/4 |q + n2k_L, m\rangle \langle q + (n+1)2k_L, m| + \text{H.c.}$$

6.2.2 Band structure

The band structure of this Hamiltonian is presented in Figure 2. Here, we have restricted ourselves to the lowest lattice band. We can do this because the energy splitting between the lowest and second lowest lattice band is of order $4E_L$ (see Figure 5), while the width of the lowest band, given by the amplitude of the approximate sinusoid, is of order $0.3E_L$ for lattice depths around $5.0E_L$, relevant to our experiment. As long as the Raman coupling stays small compared to the lattice

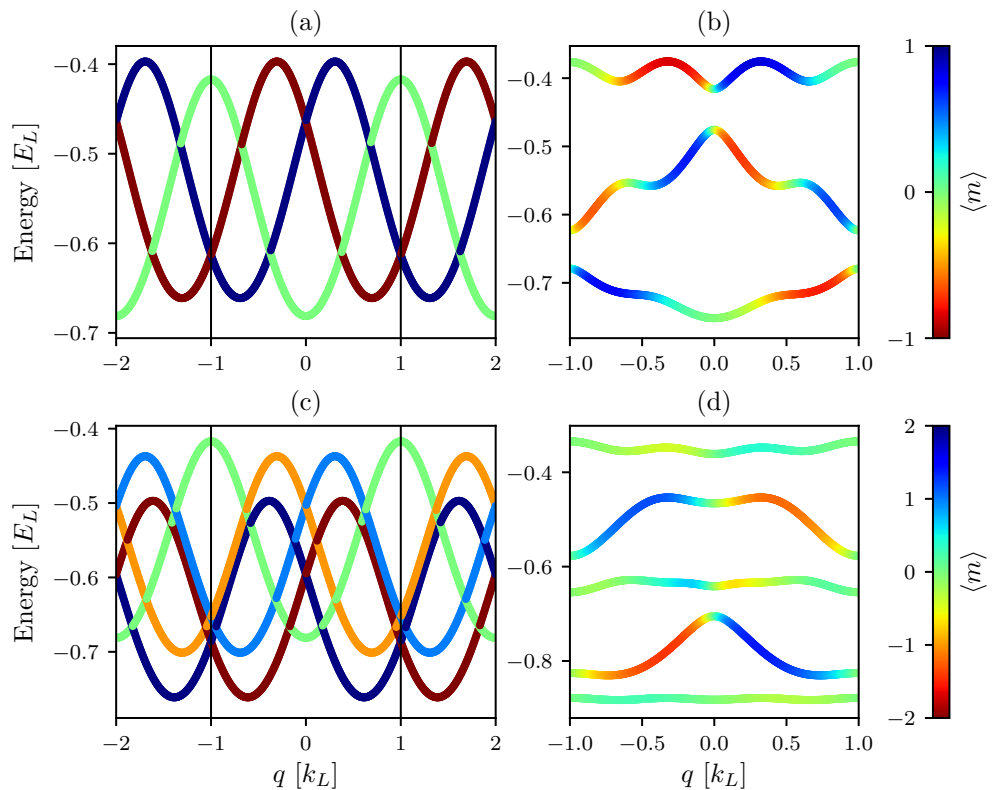


Figure 2: Band structure of the synthetic dimensions Hamiltonian, eqn. 6.6. For all panels, the detuning $\hbar\delta = 0$ and the quadratic shift $\hbar\epsilon = 0.02E_L$. (a) $F = 1$, $\hbar\Omega = 0.0$. The color represents $\langle m \rangle$, magnetization along \mathbf{e}_s . (b) $F = 1$, $\hbar\Omega = 0.5$. (c) $F = 2$, $\hbar\Omega = 0.0$. (d) $F = 2$, $\hbar\Omega = 0.5$.

band spacing, the higher lattice bands are energetically separated enough that they can be ignored.

Therefore, we can think of the Raman coupling analogously to the free space Raman coupling (see section 2.6.2), except instead of free space parabolas each spin state gets a lowest lattice band sinusoid. Figure 2a shows this in the limit of no Raman coupling, $\Omega = 0$, but with the 1D lattice on at $V_0 = 4.0E_L$. The quadratic Zeeman shift is $\hbar\epsilon = 0.02E_L$ and the detuning $\delta = 0$. The $m_F = -1$ sinusoid is shifted $2k_R$, similarly to section 2.6.2, but since the sinusoid is periodic with $2k_L$, it folds into the first Brillouin zone of the lattice, such that the nearest minimum to $q = 0$ is at $q = 2k_R - 2k_L = (2\phi_{AB}/2\pi - 2)k_L$. The edges of the Brillouin zone are marked by horizontal lines. The color indicates magnetization $\langle m \rangle = \sum_{m_F} m_F n_{m_F}$, where n_{m_F} is the fractional population in the m_F state. In synthetic dimensions language, $\langle m \rangle$ is the expectation value of position along \mathbf{e}_s .

In Figure 2b, we have restricted ourselves to the first Brillouin zone and turned the Raman coupling to $\hbar\Omega = 0.5E_L$. This results in avoided crossings in Figure 2a, and the lowest band now has a spin dependence on crystal momentum. Figure 2c-d shows the same progression for the $F = 2$ manifold. Figure 2c is taken in the limit of $\hbar\Omega = 0$. All of the 5 spin states get ‘folded’ back into the first Brillouin zone due to the lattice periodicity of the bands. The different overall energies of the sinusoids are due to the quadratic Zeeman shift $\hbar\epsilon = 0.02E_L$. The lattice depth is again $V_0 = 5.0E_L$ and detuning $\hbar\delta = 0$. In Figure 2d we have restricted ourselves to the first Brillouin zone and turned on the Raman coupling to $\hbar\Omega = 0.5E_L$. Note that the inverted hyperfine structure in Fig. 2c (meaning that the quadratic shift pushed the $m_F = 0$ state up rather than down in energy compared to the others), combined with the Raman coupling serves to make the lowest band in the $F = 2$ manifold close to flat. This makes the band more similar to a quantum Hall Landau level, and also shows promise for potential simulation of fractional quantum Hall physics,

which require bands to be very flat.

6.2.3 Calibration

To calibrate the lattice depth V_0 in the synthetic dimensions system, we can simply calibrate the lattice depth without Raman or rf coupling as described in Section 2.5.3. However, we are operating at very low Raman coupling strengths, $\hbar\Omega \approx 0.5E_L$. This is necessary because in the synthetic dimensional system the Raman coupling plays the role of tunneling, which has to be small, $t_s \approx 0.1E_L$, to approximate the tight binding limit. At these low Raman couplings, simple pulsing as described in Section 2.6.3 is not useful for calibration, as the contrast of the Rabi oscillations would be too low to resolve. Therefore, we calibrate the Raman coupling and detuning with the full synthetic dimensions system. The ‘folding in’ effect of the lattice (meaning, the folding in of the sinusoids into the first Brillouin zone, or Umklapp processes) makes the higher Raman bands much closer energetically than without the lattice, leading to larger contrast and allowing for accurate calibration.

To do this, we must first adiabatically load the lowest 1-D lattice band. To do that, we must ramp on the lattice potential on a time scale slow compared to the band spacing, $\approx 4E_L$. This gives $t \approx h/4E_L = 0.12$ ms. Figure 3a shows the full ramping scheme. We ramp the lattice on in ≈ 20 ms. Then, we must pulse on the Raman coupling on a time scale fast compared to the spin sub-band level spacing to produce Rabi oscillations, but still adiabatic with respect to the lattice spacing to avoid exciting to the higher lattice band. We ramp the Raman beams on in $300\ \mu\text{s}$. Then, the system is held on for a variable amount of time before all light is snapped off and the atoms are allowed to expand in time-of-flight. For the case of $F = 2$ atoms, the transfer to the $F = 2$ manifold is done in the 1-D lattice before the Raman beams are ramped on to minimize the time spend in the $F = 2$ manifold.

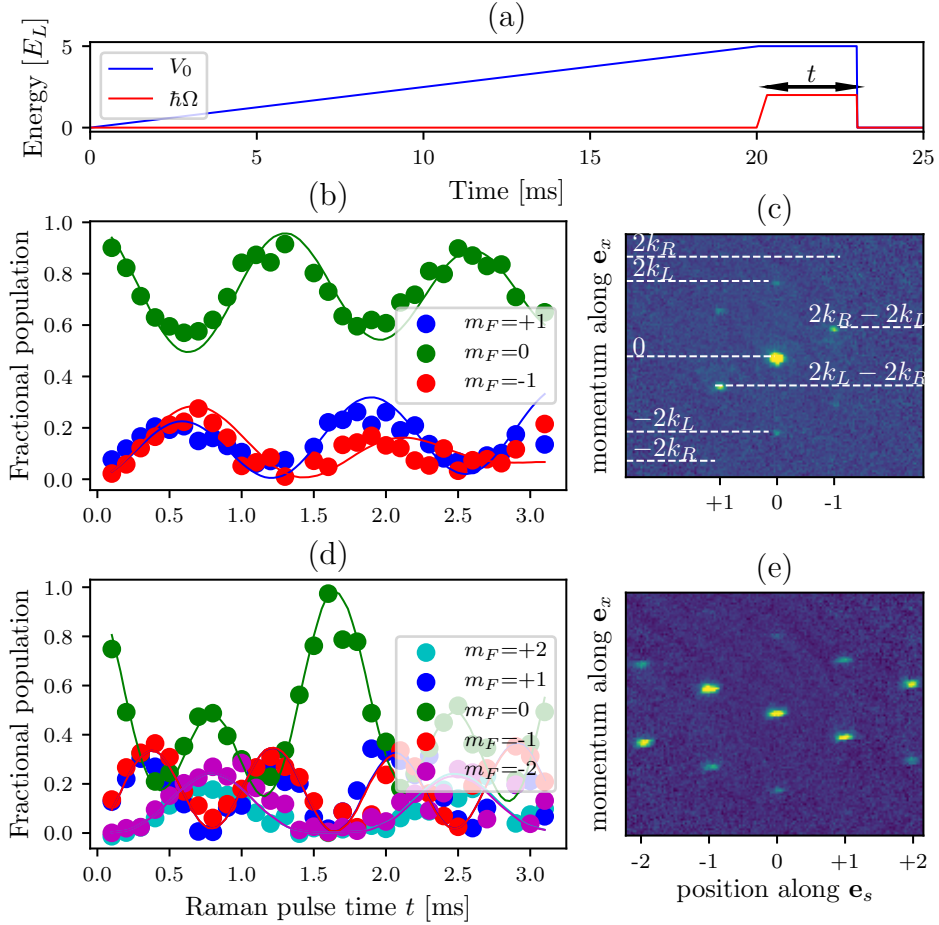


Figure 3: Calibration of synthetic dimensions lattice. (a) Ramping procedure. The blue line represents the 1-D lattice depth as a function of time and the red line represents Raman coupling as a function of time. Both are held on for a variable amount of time t , producing Rabi oscillations. (b) Example of fractional populations in different m states as a function of time t in the $F = 1$ manifold. Dots indicate data and lines indicate the best fit to theory, with parameters $\hbar\Omega = 0.56 \pm 0.01 E_L$ and $\hbar\delta = 0.029 \pm 0.002 E_L$. The quadratic shift was constrained at the calibrated value $\hbar\epsilon = 0.02 E_L$. (c) Example time-of-flight image in the $F = 1$ manifold. A Stern-Gerlach gradient pulse separates different m states along the horizontal axis, while the lattice and Raman beams give momentum along the vertical axis. (d) Example of fractional populations in different m states as a function of time t in the $F = 2$ manifold. Dots indicate data and lines indicate the best fit to theory, with parameters $\hbar\Omega = 0.61 \pm 0.002 E_L$ and $\hbar\delta = 0.002 \pm 0.001 E_L$. The quadratic shift was constrained at the calibrated value $\hbar\epsilon = 0.02 E_L$. (e) Example time-of-flight image in the $F = 2$ manifold. A Stern-Gerlach gradient pulse separates different m states along the horizontal axis, while the lattice and Raman beams give momentum along the vertical axis.

Figure 3c,d shows sample time-of-flight images during the calibration procedure for $F = 1$ and $F = 2$ respectively. The vertical axis is e_x , aligned with the lattice and Raman beams. Since the atoms have expanded in time-of-flight, this axis corresponds to the momentum k_x . The horizontal axis of the image is the axis along which a Stern-Gerlach magnetic field gradient, separating the different spin states, is applied. Therefore, this axis is the position m along the synthetic dimension \mathbf{e}_s . In the effectively 2-D synthetic dimensions lattice language, this is a ‘hybrid’ imaging technique, imaging momentum along one lattice direction and position along the other.

Figure 3c labels some notable momentum orders. The central order is at $k_x = 0$, where the atoms start before the experiment. Two higher lattice orders, at $k_x = \pm 2k_L$, are populated for the same spin $m = 0$. $k_x = \pm 2k_R$ is labeled, but not visibly populated, to indicate where the orders would appear if only Raman coupling was present with a higher coupling strength. Due to the ‘folding in’ effect of the lattice, the brightest orders of the $m = \pm 1$ states appear at $k_x = \pm(2k_L - 2k_R)$. The $F = 2$ states follow the same pattern, not labeled in Figure 3e as there are too many orders.

For each value of the time t we sum up the total optical depth in all of the orders of each spin state to obtain fractional populations for each spin state as a function of time. An example scan in the $F = 1$ manifold is shown in Figure 3 b. The colored dots represent the data for different spin states, and the lines represent the best fit to theory. Here, the significant detuning makes populations in the $m = \pm 1$ states unequal. An example scan in the $F = 2$ manifold is shown in Figure 3e. Here, the detuning is small and states with opposite spin oscillate in approximate unison. This technique allows us to calibrate our experimental parameters.

6.2.4 Tight binding approximation

The synthetic dimensions Hamiltonian can be approximated in the tight binding limit as:

$$H = - \sum_{j,m} |t_x| e^{i\phi_{AB}m} |j+1, m\rangle \langle j, m| + t_s(m) |j, m+1\rangle \langle j, m| + A_m |j, m\rangle \langle j, m| + h.c., \quad (6.9)$$

where j and m label sites along e_x and \mathbf{e}_s respectively, as shown in Figure 1b. $t_s = |t_s|$ and $t_x = |t_x| \exp(i\phi_{AB}m)$ are the associated tunnelings. A_m captures the spin dependent diagonal elements, detuning $\hbar\delta$ and quadratic shift $\hbar\epsilon$. Here, we have implicitly restricted ourselves to the lowest 1-D lattice band, and assumed that tight binding, i.e. confinement at discrete lattice sites, is a good approximation (see 2.5.2). t_s is not a spin dependent quantity for $F = 1$ atoms, but is for $F = 2$, where differences in Clebsch-Gordan coefficients create non-uniform tunneling. In the limit of zero detuning and neglecting the quadratic shift as well as the t_s dependence on spin, this becomes the traditional Harper-Hofstadter Hamiltonian 1.7 with a synthetic dimension:

$$H = - \sum_{j,m} t_x e^{i\phi_{AB}m} |j+1, m\rangle \langle j, m| + t_s |j, m+1\rangle \langle j, m| + h.c. \quad (6.10)$$

We can transform this Hamiltonian into momentum space along e_x by plugging the Fourier transform formula

$$|j, m\rangle = \frac{1}{\sqrt{N}} \sum_{k_j} e^{-ik_j j} |k_j, m\rangle, \quad (6.11)$$

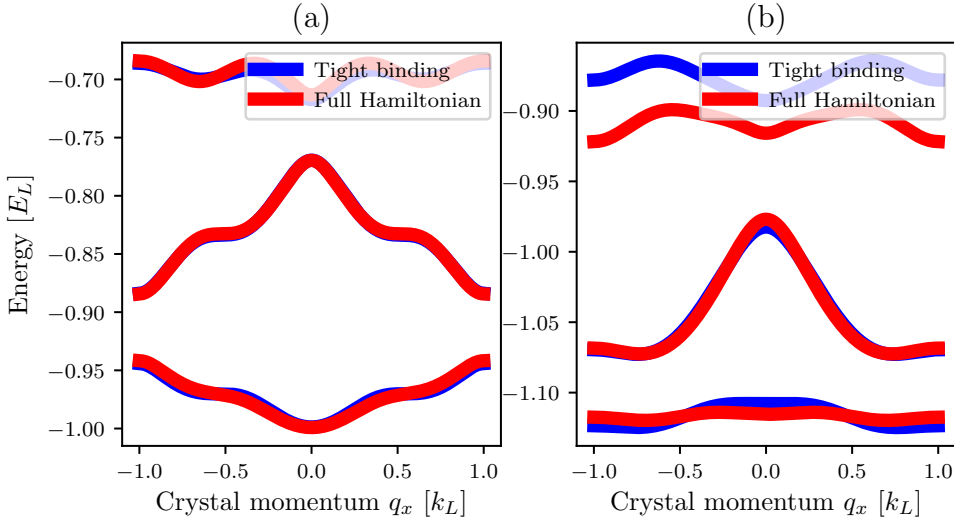


Figure 4: Band structure of the tight binding versus full Hamiltonian. $V_0 = 6.0E_L$, giving $|t_x| = 0.1E_L$, $\hbar\delta = 0$, $\hbar\epsilon = 0.02E_L$, $\hbar\Omega = 0.5E_L$. (a) $F = 1$, fitted value $t_s = 0.154E_L$. (b) $F = 2$, fitted value $t_s = 0.284$. Here, the tight-binding Hamiltonian included anisotropic tunneling t_s due to Clebsch-Gordan coefficients.

with N the number of sites j , into the above Hamiltonian to obtain

$$H = -\frac{1}{N} \sum_{k_j, m} t_s |k_j, m+1\rangle \langle k_j, m| + h.c. + 2|t_x| \cos(k_j - \phi_{AB}) |k_j, m\rangle \langle k_j, m| + A_m |k_j, m\rangle \langle k_j, m| \quad (6.12)$$

To approximate the full Hamiltonian, eqn. 6.6, by the tight binding Hamiltonian, eqn. 6.9, we must find appropriate values for t_s and t_x . We find $|t_x|$ by treating the 1-D lattice independently, and matching the tight binding band to the lowest full lattice band. For most of the experiments described in the chapter, the lattice depth was $V_0 = 6E_L$, corresponding to $|t_x| \approx 0.01E_L$. To find the appropriate value of t_s , we fit the lowest 3 bands of the full synthetic dimensions band structure to the tight binding band structure eqn. 6.12 with t_s as fitting free parameter.

Figure 4 shows the overlayed band structure of the full Hamiltonian, eqn. 6.6, and the best fit tight binding band structure, eqn. 6.12. To fit, we minimize the square difference between the energies in the lowest two bands, relevant to our

experiment.

6.3 Eigenstates of the synthetic 2-D lattice

After calibrating the synthetic dimensional lattice via pulsing, we can study the eigenstates of the lowest band of the system by adiabatically loading, i.e. ramping both the lattice and Raman or rf coupling on on a time scale slow compared to the magnetic band spacing. Along the synthetic direction, in the $F = 1$ manifold, there are no $m = \pm 2$ sites. This can be thought of as hard wall boundary conditions at the $m = \pm 2$ sites, confining the atoms in the allowed $m = 0, \pm 1$ sites. Therefore, we can consider the position eigenstates along the synthetic direction in relation to eigenstates of a square-well potential.

Figure 5a shows a time-of-flight image of an adiabatically loaded synthetic dimensions lattice eigenstate with rf coupling along the synthetic direction. The vertical axis is single site resolved spin states m . The horizontal axis is momentum along the e_x direction. Note that for each site m the distribution of momenta k_x is symmetric. Figure 5b shows the fractional population in each site m , summed over all momenta k_x . In the case of rf coupling, $\phi_{AB} = 0$ and the effective magnetic flux $\Phi_{AB}/\Phi_0 = 0$. Therefore, the fractional population along the spin direction looks simply like a discretized ground state probability distribution of the square well potential.

Figure 5c-h shows analogous data with Raman coupling along the synthetic direction. Figure 5d,g are the time-of-flight image and corresponding fractional populations of atoms adiabatically loaded from the $m_F = 0$ spin state, corresponding to the central minimum ($q = 0$) of the lowest band in Figure 2b. There are two key differences between this case and the rf case in Figure 5a-b. First, the momenta of the different spin states are no longer symmetric, as explained in sec. 6.2.3. Second, the fractional populations in Figure 5g are no longer simply the discretized ground

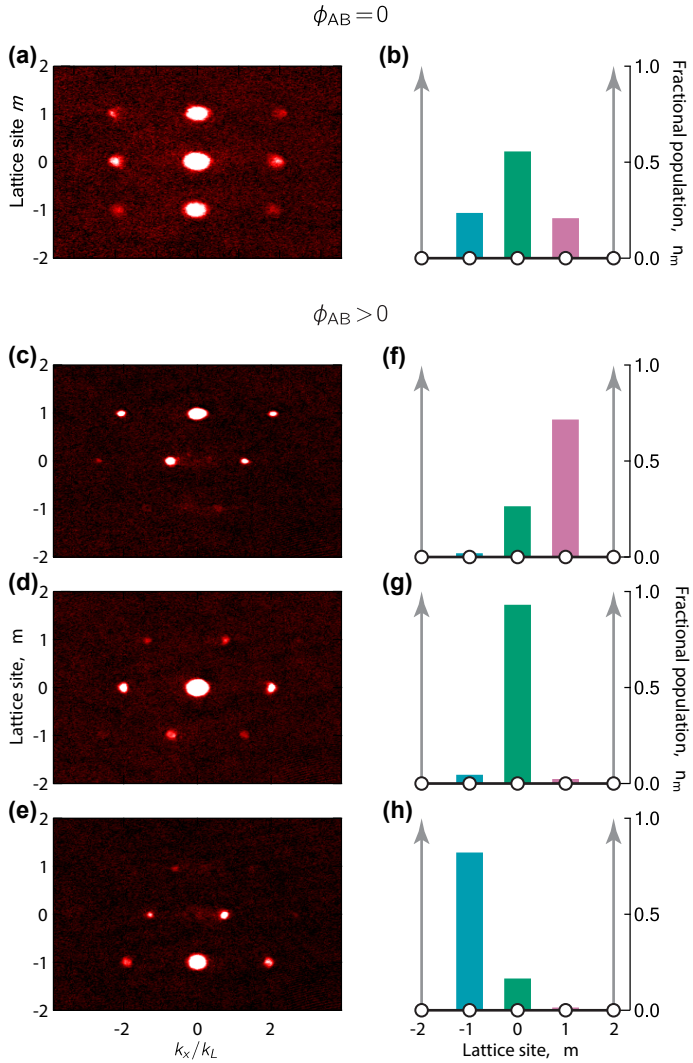


Figure 5: Eigenstates of the synthetic dimensions lattice. Left column: time-of-flight images, with position along \mathbf{e}_s on the vertical axis and momentum along \mathbf{e}_s on the horizontal. Right column: fractional populations in each site m . (a,b) rf coupling, resulting in $\phi_{AB} = 0$. (c,f) Raman coupling, resulting in $\phi_{AB} > 0$, adiabatically loaded from the $m_F = 1$ state. (d,g) Raman coupling, resulting in $\phi_{AB} > 0$, adiabatically loaded from the $m_F = 0$ state. (e,h) Raman coupling, resulting in $\phi_{AB} > 0$, adiabatically loaded from the $m_F = -1$ state.

state probability distribution of the square well potential: they are a narrowed version of it, more strongly concentrated in the $m = 0$ site.

This can be understood by analogy with a 2D electron system in a perpendicular magnetic field, confined in one dimension with hard walls. Along the confined direction, the wavefunction is localized to the scale of the magnetic length $l_B = \sqrt{\hbar/qB}$, with the center position at $k_x l_B^2$ in the bulk state, where $\hbar k_x$ is the electrons canonical momentum. In our system, the magnetic length $l_B = \sqrt{a^2\Phi_0/2\pi\Phi_{AB}}$, or in units of the lattice period a , $l_B^* = \sqrt{3/2\pi}$; this explains the narrowing of the bulk state in Figure 5g.

In the 2D electron system, at large $|k_x|$, the electron becomes localized near the edges, lifting the degeneracy of the otherwise macroscopically degenerate Landau levels. In our case, stable edge states appeared as the additional minima in Figure 2b, at $q \approx \pm 0.66k_L$. We loaded these edge states by starting in the $m_F = \pm 1$ states before adiabatically turning on the synthetic dimensions lattice to obtain the eigenstates displayed in Figure 5c,f and Figure 5e,h respectively. These edge states predominantly occupy the edge sites in the synthetic direction, and are strongly confined there due to the narrow magnetic length. These localized edge states are the analog to the current-carrying edge states in Fermionic integer quantum Hall effect systems [114].

6.4 Chiral edge currents

The same pulsing procedure that was used for calibration (sec. 6.2.3) can also be interpreted by analogy with the 2-D electron system. Figure 6a shows schematically what happens when atoms are loaded from the $m = 0$ site into the lattice and tunneling along the synthetic dimension is pulsed on. Atoms begin analogues of cyclotron orbits, tunneling out into the edge $m = \pm 1$ sites and tunneling back to the bulk $m = 0$ state. The fractional populations in the three m sites as a

function of time are shown in Figure 6b.

We performed this experiment for three different magnetic flux values: with rf coupling giving $\Phi_{AB}/\Phi_0 = 0$, with Raman coupling giving $\Phi_{AB}/\Phi_0 \approx 4/3$ and with inverted Raman coupling giving $\Phi_{AB}/\Phi_0 \approx -4/3$. The inverted Raman coupling was accomplished by switching the roles of the two Raman beams (see Figure 1a): the right going beam frequency was changed to $2\pi(\omega + \Delta\omega)$ and the left going beam frequency was change to $2\pi\omega$, resulting in the opposite recoil momentum for the same spin flip, flipping the direction of the effective magnetic field.

We define the current $I_{m=\pm 1} = n_m \langle v_m \rangle$, where n_m is the fractional population in site m and $\langle v_m \rangle$ is the expectation value of velocity along e_x for atoms in sites m , as depicted in Figure 6a. The velocity is derived from the momentum measured in time-of-flight images. The chiral current of the system is then defined as $\mathcal{I} = I_1 - I_{-1}$. We calculate this chiral current for data in Figure 6b, with $\Phi_{AB}/\Phi_0 \approx 4/3$, displayed in red dots in Figure 6c. Atoms in the edge sites $m = \pm 1$ exhibit chiral motion, therefore the resulting chiral current is directly proportional to the fractional population in those sites and oscillates as a function of time in concert with the oscillation in Figure 6b. in Figure 6c also includes data for the $\Phi_{AB}/\Phi_0 \approx -4/3$ (solid black dots indicate data and solid gray lines are from theory) and $\Phi_{AB}/\Phi_0 = 0$ (empty black dots). As seen in the figure, reversing the direction of the effective magnetic flux reverses the direction of the chiral currrent, and turning off the magnetic flux results in no net chiral current. The chiral current \mathcal{I} is normalized here by the tunneling velocity $2t_x/\hbar k_L$.

As the chiral current \mathcal{I} is proportional to the edge state population, we plot it as a function of the expectation value of the absolute value of m , $\langle |m| \rangle$, in Figure 6d. As expected, the chiral current is linear, with slope \mathcal{S} . \mathcal{S} is positive for $\Phi_{AB}/\Phi_0 \approx 4/3$, negative for $\Phi_{AB}/\Phi_0 \approx -4/3$, and zero for $\Phi_{AB}/\Phi_0 = 0$. We then study the dependence of the chiral current on the strength of tunneling along the

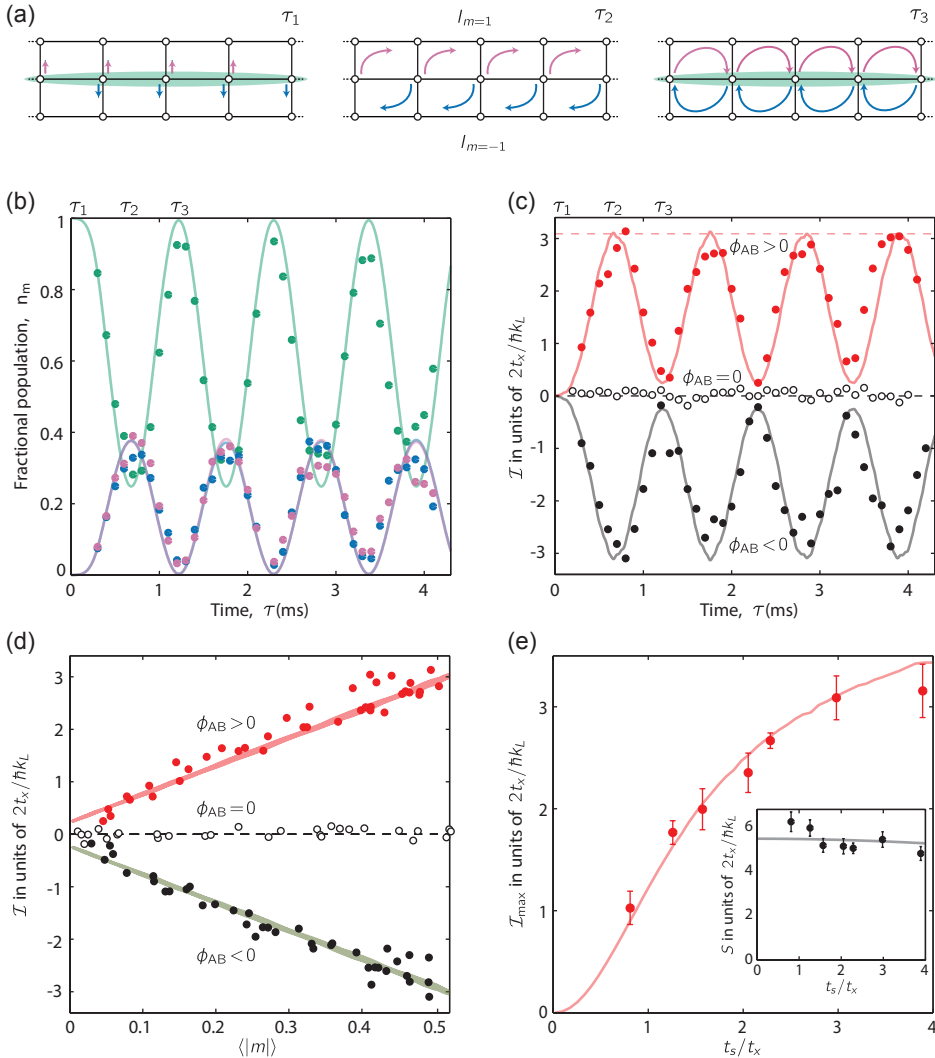


Figure 6: Measuring chiral currents in synthetic dimensions. (a) Schematic of the formation of chiral currents when the system is loaded into the bulk $m = 0$ site and tunneling along \mathbf{e}_s is turned on suddenly. They start to tunnel both towards the $m = 1$ sites (pink arrows), moving towards the right along e_x , and the $m = -1$ sites (blue arrows), moving towards the left along e_x . They then return to $m = 0$, completing cyclotron orbits. (b) Fractional population in each spin state ($m = 0, +1$, and -1 in green, pink, and blue respectively) as a function of time for a system with $\phi_{AB} > 0$. Dots represent data and lines represent theory calculated from the full Hamiltonian, eqn. 6.2.1, with parameters $\hbar\Omega = 0.5E_L$, $V_0 = 6E_L$, $\hbar\delta = 0.001E_L$, and $\hbar\epsilon = 0.05E_L$. (c) Chiral current \mathcal{I} as a function of time for $\phi_{AB} > 0$ (red) $\phi_{AB} = 0$ (empty black dots) and $\phi_{AB} < 0$ (solid black). (d) Chiral current \mathcal{I} as a function of $\langle |m| \rangle$ for the three values of ϕ_{AB} . Solid lines calculated from theory, with the same parameters as in (b) for $\phi_{AB} \neq 0$, and with parameters $\hbar\Omega = 0.33E_L$, $V_0 = 6E_L$, $\hbar\delta = -0.01E_L$, and $\hbar\epsilon = 0.05E_L$ for $\phi_{AB} = 0$. (e) Peak chiral current \mathcal{I}_{\max} as a function of tunneling asymmetry t_s/t_x , as measured experimentally (red dots) and calculated from the full Hamiltonian (red line). Inset: slope of best fit lines of current \mathcal{I} as a function of $\langle |m| \rangle$ (as in (d)) as a function of tunneling asymmetry t_s/t_x : nearly independent.

synthetic dimension, in units of the real axis tunneling t_s/t_x . We refer to this as the tunneling anisotropy: the asymmetry between the two dimensions. As shown in the inset to Figure 6e, the slope \mathcal{S} of the chiral current as a function of $\langle|m|\rangle$ is practically independent of the tunneling anisotropy. The small deviation from a flat line is explained by the deviation of our system from the tight binding model. However, the maximal chiral current attained during the pulsing experiment, \mathcal{I}_{\max} , depends strongly on the tunneling anisotropy (see Figure 6e). This is because the maximum fractional population in the edge states $\langle|m|\rangle$ increases with increased t_s . The increase is approximately linear at first, and then saturates at large t_s/t_x when the fractional population in the edge states $m = \pm 1$ approaches 1.

6.5 Observation of skipping orbits

Semi-classically, electrons in a 2-D material pierced by a magnetic field can be described in terms of cyclotron orbits in the bulk, as described in the previous section, and skipping orbits on the edge. Skipping orbits arise from electrons on the edge beginning cyclotron orbits, but hitting the edge of the system and being reflected and beginning the next cyclotron orbit. Due to the chirality of the cyclotron orbits, this results in the skipping orbits traveling in one direction along the top edge and in the opposite direction along the bottom edge.

We observed an analogue of these skipping orbits in our system. We performed the same experiment, pulsing on tunneling along the synthetic dimension, but this time initializing the system on the edge, as shown schematically in Figure 7a. To populate these states, we initially applied a detuning $\hbar\delta = \pm 0.087E_L$, tilting the potential along the synthetic direction as shown in Figure 7b. This made the initial state, $m = -1$ in the figure, a potential minimum. We then pulsed on the tunneling and observed the resulting dynamics.

Figure 7c shows the expectation value of position along \mathbf{e}_s as a function of time

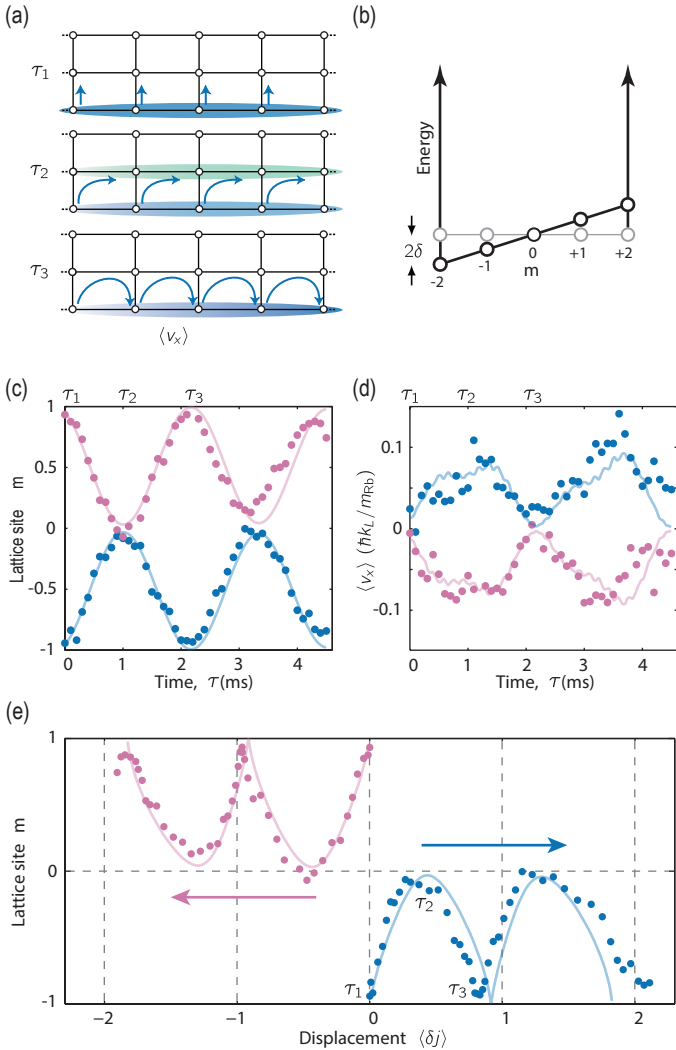


Figure 7: Imaging skipping orbits. (a) Schematic of pulsing experiment when atoms are initialized on the $m = -1$ edge. The atoms move towards the $m = 0$ site, while moving to the right along e_x (blue arrows). They then continue their semi-cyclotron orbits back to $m = -1$, from where they cannot finish the circle, forming skipping orbits. (b) Schematic of the tilted box potential applied along the synthetic direction. (c) Expectation value of position along e_s , $\langle m \rangle$, as a function of pulse time for atoms initialized in the $m = +1$ (red) and $m = -1$ (blue) states. Dots represent data and lines are from theory calculated from the full Hamiltonian, eqn. 6.2.1, with parameters $\hbar\Omega = 0.41E_L$, $V_0 = 5.2E_L$, $\hbar\delta = \pm 0.087E_L$, and $\hbar\epsilon = 0.13E_L$. (d) Expectation value of the group velocity along e_x , $\langle v_x \rangle$, for the same data as in (c). (e) Expectation value of displacement along e_x , $\langle \delta j \rangle$ in units of lattice spacing, for the same data as in (c) and (d). The displacement was obtained by integrating $\langle v_x/a \rangle$, where a is the period of the optical lattice. Atoms initialized in $m = -1$ performed skipping orbits to the left, while atoms starting in $m = +1$ traveled to the right.

during the pulsing experiment. This expectation value is obtained by calculating the fractional population n_m on each site m and summing $\langle m \rangle = \sum_m mn_m$. The red dots were obtained from an experiment where the atoms were initialized in the $m = 1$ site. The blue dots were obtained by starting in the $m = -1$ site. The expected position oscillated with time, as expected for Rabi oscillations. The same data was then used to extract the expected group velocity along e_x , $\langle v \rangle = \sum_m n_m \langle v_m \rangle$ as a function of time. This is shown in Figure 7d. The group velocity oscillated with the expected position $\langle m \rangle$, and was positive for experiments starting in $m = -1$ and negative for experiments starting in $m = 1$.

We obtain the expected displacement in units of the lattice spacing a , $\langle \delta j \rangle$ along e_x as a function of time by directly integrating the expected group velocity. The resulting displacement is shown in Figure 7e. As seen in the figure, for experiments initialized in $m = 1$, the atoms began cyclotron orbits, but reflected off the edge and performed skipping orbits towards the left. Likewise, atoms initialized in $m = -1$ performed skipping orbits along the opposite edge and in the opposite direction. This experiment presents the first direct observation of skipping orbit motion.

Chapter 7: Measuring Chern Number in Synthetic Dimensions

As discussed in Chapter 1, the 2D topological invariant as applied to band topology, the Chern number, is well defined for an infinite 2D system. For any finite system, the Chern number can be thought of as the Chern number of an infinite system that locally looks like the bulk of the finite system. This begs the question, how narrow can a system get for this extension of the definition of Chern number to still be meaningful?

In this chapter, we describe our experiment in measuring Chern number in the effectively 2D synthetic dimensional lattice, as described in Chapter 6. This lattice was elongated along the real direction and extremely narrow along the synthetic direction, only 3 or 5 sites wide. We performed a transport experiment to sample the band structure of this system as a function of crystal momentum k_x along the real direction, and observed the resulting motion along the transverse, synthetic, direction, as shown schematically in Figure 1.

Similarly to Chapter 6, our system was qualitatively well described by the tight binding limit Harper-Hofstadter Hamiltonian (see eqn. 6.10) [16, 115]

$$\hat{H} = - \sum_{m,j} (t_x e^{i\phi m} |j, m\rangle\langle j+1, m| + t_s |j, m\rangle\langle j, m+1|) + \text{H.c.}, \quad (7.1)$$

where j and m label lattice sites along e_x and e_s , with tunneling strengths t_x and t_s respectively. Figure 1a sketches the atoms loaded into the lowest band of the synthetic dimensions lattice in the $F = 2$ manifold of ^{87}Rb , creating 5 sites along

the synthetic direction. As in Chapter 6, there was a 1D optical lattice along the longitudinal e_x direction, with lattice tunneling t_x between adjacent sites labelled by j . Internal spin states of the atoms defined sites along the transverse e_s direction, with tunneling t_s induced by either rf or Raman coupling. In the case of rf coupling, no phase was imprinted, $\phi_{AB} = 0$. In the case of Raman coupling, an overall phase $\phi_{AB} \neq 0$ was imprinted, and we choose the Landau gauge in which the phase is written on the longitudinal tunneling coefficient $t_x = |t_x|e^{i\phi_{AB}m}$.

The histogram in Figure 1a shows the fractional populations n_m in each site m . An example hybrid TOF image (see sec. 6.2.3) is shown below in Figure 1c, with the central $m = 0$ order marked by red cross-hairs. Then, a force is applied along the long (real) dimension of the system for some time Δt , and a transverse response is observed, as seen in Figure 1b. The fractional population has become maximized in the $m = 1$ site, and the sample hybrid TOF image in Figure 1d shows a displacement along the longitudinal momentum axis of Δq_x .

Due to the extremely narrow widths in the synthetic dimension, our measurement cannot be readily interpreted as a quantum Hall conductivity measurement, and a meaningful Chern number is not readily extracted in that manner, as discussed in sec. 7.2. However, we leverage the TKNN Diophantine equation [6] to perform an alternative measurement of the Chern number, discussed in 7.3. We show how this equation arises naturally in our synthetic dimensional system, and claim that with this metric we can extend the definition of the Chern meaningfully to systems as narrow as ours.

7.1 Experimental procedure

The setup for this experiment followed closely that of the original synthetic dimensions experiment, as described in sec. 6.1. In contrast with the experiment described in Chapter 6, we performed this experiment in both the $F = 1$ and $F = 2$

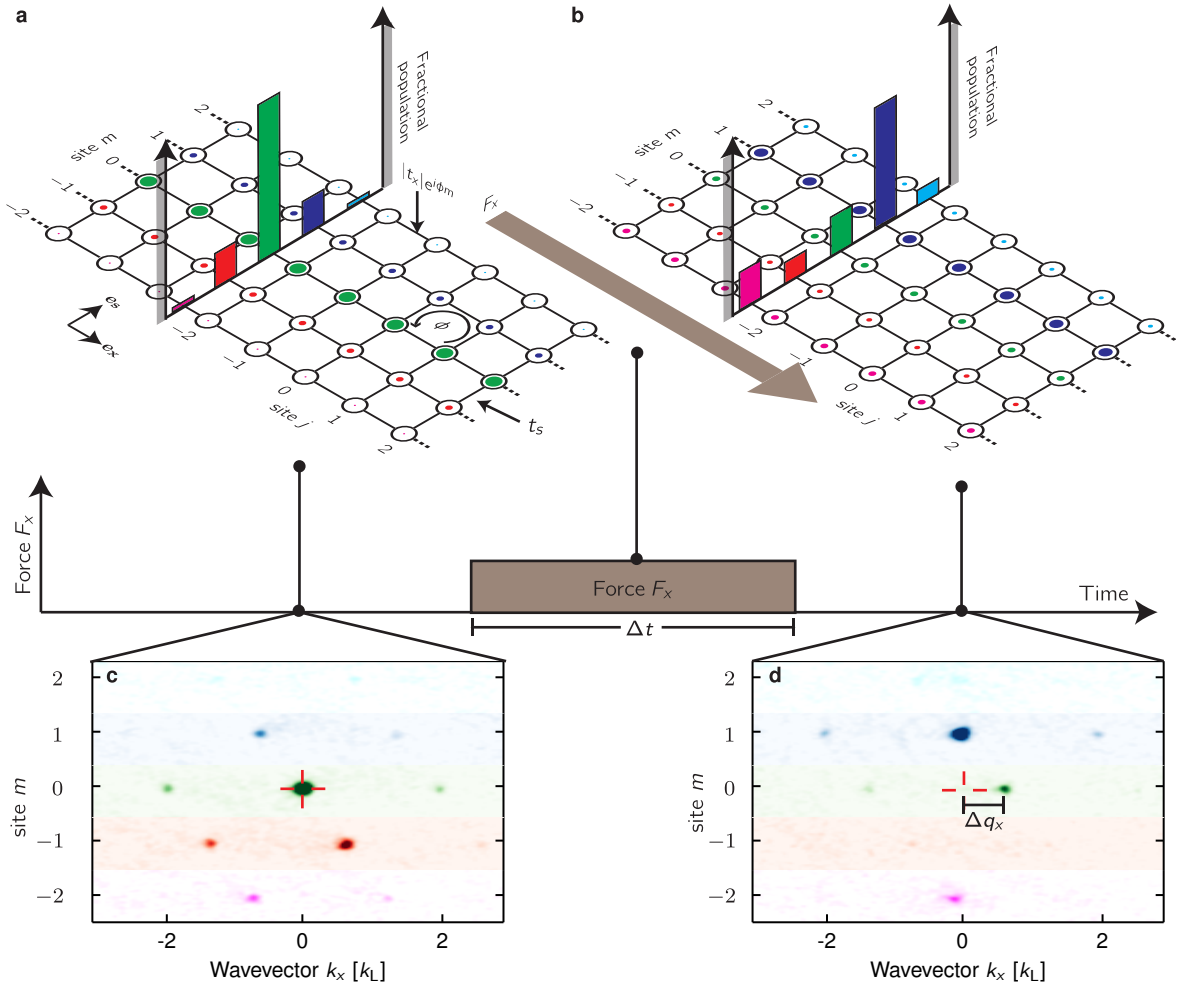


Figure 1: Quantum Hall effect in Hofstadter ribbons. (a) 5-site wide ribbon with real tunneling coefficients along e_s and complex tunneling coefficients along e_x , creating a non-zero phase ϕ around each plaquette. (b) After applying a force along e_x for a time Δt , atomic populations shift transversely along e_s , signaling the Hall effect. (c,d) TOF absorption images giving hybrid momentum/position density distributions $n(k_x, m)$. Prior to applying the force (c), the $m = 0$ momentum peak is at $k_x = 0$, marked by the red cross. Then, in (d), the force directly changed q_x , evidenced by the displacement Δq_x of crystal momentum, and via the Hall effect shifted population along e_s .

hyperfine manifolds of ^{87}Rb , creating both 3-site and 5-site wide strips. We began the experiment by adiabatically loading the full synthetic dimensional system for both $F = 1$ and $F = 2$, with both Raman coupling ($\Phi_{\text{AB}} \neq 0$) and rf coupling ($\Phi_{\text{AB}} = 0$).

7.1.1 Loading procedures

The loading procedure for the Raman coupled case was as follows. We prepared a ^{87}Rb BEC (see sec. 3.3.3) in the $m_F = -1$ hyperfine state of the $F = 1$ manifold, or in the $|1, 0\rangle$ state for Raman data in $F = 1$ only. We ramped on the 1D optical lattice along e_x adiabatically in 300 ms. For experiments in the $F = 2$ manifold, we then applied a microwave pulse for 0.55 ms to transfer $|1, -1\rangle \rightarrow |2, 0\rangle$ manifold while already in the lattice. This was done after lattice loading to minimize the amount of time the atoms spent in the $F = 2$ manifold and thereby limit the spin-changing collisions and losses associated with that state as observed in our experiment. Then, the Raman coupling field was ramped on adiabatically in 30 ms.

Loading the ground state of the $F = 2$ manifold presented a unique restriction, as illustrated by Figure 2. For the experiments described in Chapter 6, a bias magnetic field B_z was chosen such that the quadratic Zeeman shift was $\hbar\epsilon = 0.05E_{\text{L}}$, in lattice recoil energy units. However, in the $F = 2$ case at this field, with a lattice depth of $4.4E_{\text{L}}$, the $m_F = 0$ ground state does not adiabatically connect to the Raman-coupled ground state. This is because, as shown in the band structure in Figure 2a, the $m_F = \pm 2$ energies of the lattice-coupled system at $q_x = 0$ are lower in energy than the $m_F = 0$ state. Therefore, to avoid this issue, we chose a bias field such that the quadratic Zeeman shift was $\hbar\epsilon = 0.02E_{\text{L}}$. The band structure for this case is shown in Figure 2b. Here, the $m_F = 0$ sinusoid at crystal momentum $q_x = 0$ is still the lowest energy, and therefore connects adiabatically to the Raman coupled ground state.

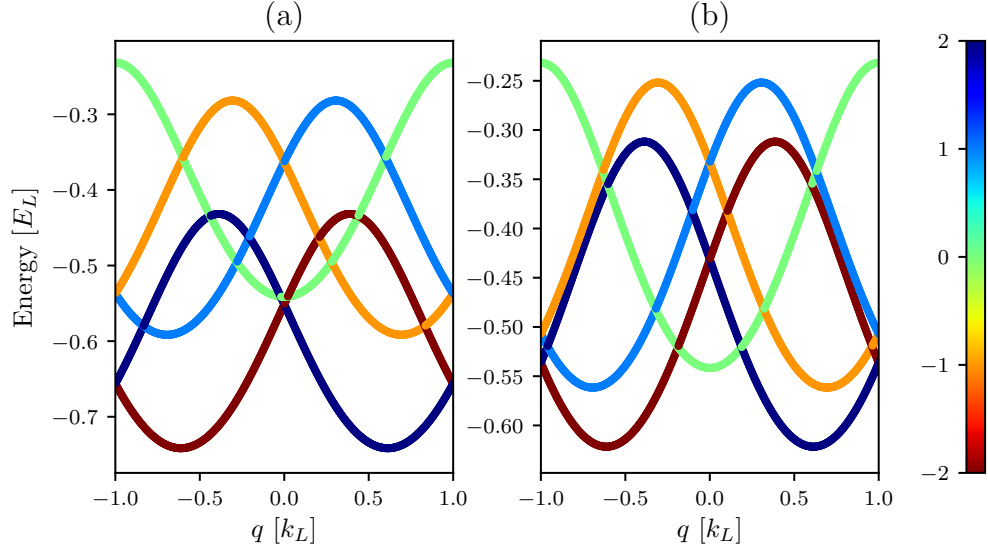


Figure 2: Band structure of the lattice-coupled system in $F = 2$. Here, lattice depth $V_0 = 4.4E_L$, Raman coupling $\hbar\Omega = 0$, and detuning $\hbar\delta = 0$. (a) Quadratic shift $\hbar\epsilon = 0.05E_L$. At $q_x = 0$, $m_F = 0$ is not the ground state. (b) Quadratic shift $\hbar\epsilon = 0.02E_L$. At $q_x = 0$, $m_F = 0$ is the ground state.

For the case where tunneling along the synthetic dimension was provided by rf coupling ($\Phi_{AB} = 0$), the loading procedure was as follows. We started in the $F = 1, m_F = -1$ state and turned the 1D optical lattice on adiabatically in 300 ms, same as in the Raman case. For $F = 2$, we then transferred to the $F = 2, m_F = -2$ state with a 0.55 ms microwave pulse. Then, we set the bias field to a large detuning $\hbar\delta > 1E_R$. Implementing adiabatic rapid passage (see sec. 2.2.3), we then swept the field to resonance in ≈ 50 ms, thereby loading the rf coupled ground state. This was necessary in the rf case as opposed to the Raman case, because there is no momentum shift in the band structure, and therefore turning on the rf coupling opens up an avoided crossing at every point in the band, making it impossible to be adiabatic with respect to this turn-on while on resonance.

7.1.2 Application of force and measurement

After adiabatically loading the ground state at $q_x = 0$ for all the configurations, we applied a constant force to the atoms, inducing a linear evolution of the crystal momentum given by

$$F_x = \hbar \frac{dq_x}{dt}. \quad (7.2)$$

To apply this force, we displaced the crossing beam of the ODT, such that instead of being held at the potential minimum, the atoms were on an edge of the Gaussian beam, with a locally linear optical potential. This displacement was achieved by frequency shifting the AOM that controlled the split between the two ODT orders (see fig. 7). Note that the ODT is far detuned and this frequency shift of < 1 MHz had no effect on the trapping potential depth. This is shown schematically in Figure 3. Figure 3a shows the atoms (indicated by a black dot) at the minimum of the Gaussian crossing beam (potential in blue), with no force applied. Figure 3b shows the beam displaced to the right relative to the atoms, and the locally linear potential experienced by the atoms results in a positive force. Similarly, in Figure 3c the beam is displaced to the left resulting in a negative force.

An example of the resulting evolution of the system is shown in Figure 4. Figure 4a shows the lowest three bands of the Raman coupled synthetic dimensions band structure in the $F = 2$ manifold, for our approximate experimental parameters of $V_0 = 4.4E_L$, $\hbar\Omega = 0.5E_L$, $\hbar\delta = 0E_L$ and $\hbar\epsilon = 0.02E_L$. The starting point of the BEC at $q_x = 0$ is indicated by the black dot in the lowest band. The color indicates the modal position \bar{m} along the synthetic direction. Modal position is a slight variant on the magnetization used in sec. 6.2.2. The modal position was found by taking the fractional populations n_m in the different m sites at a given crystal momentum, and fitting them to a Gaussian distribution. The peak of the Gaussian distribution was taken as the modal position \bar{m} . In this experiment, we use \bar{m} as the

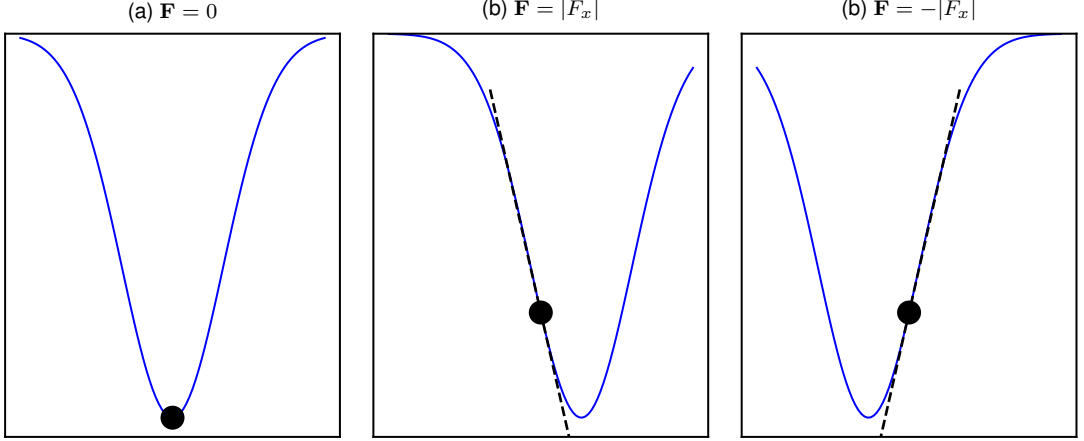


Figure 3: Application of a constant force by displacing a Gaussian beam potential. (a) Atoms are at the minimum of the Gaussian potential, not experiencing a force. (b) Beam is displaced to the right, atoms experience a local linear potential resulting in a constant positive force. (c) Beam is displaced to the left, atoms experience a local linear potential resulting in a constant negative force.

metric of location along \mathbf{e}_s in favor of the more conventional magnetization given by $\langle m \rangle = \sum_m m n_m$ to avoid the large uncertainties introduced in the magnetization from number fluctuations in the extremal $m = \pm F$ sites.

We displaced the crossing ODT beam to one side to apply a positive force, inducing motion to the right $q_x \rightarrow q_x > 0$ in the band structure, for various amounts of time Δt inducing various changes in crystal momentum Δq_x . We then followed the same measurement protocol as described in sec. 6.2.3: we abruptly turned off the lattice, Raman or rf, and trapping ODT beams and allowed the atoms to expand in time-of-flight for 16 ms, mapping initial momentum k_x to position on the TOF images. During TOF, we applied a 2 ms Stern-Gerlach gradient pulse of ≈ 39 G/cm (80 A quad coil current), separating the atoms according to site m along an axis perpendicular to e_x . We therefore performed a hybrid measurement of momentum k_x along the longitudinal e_x axis and single site resolved position m along the transverse \mathbf{e}_s direction.

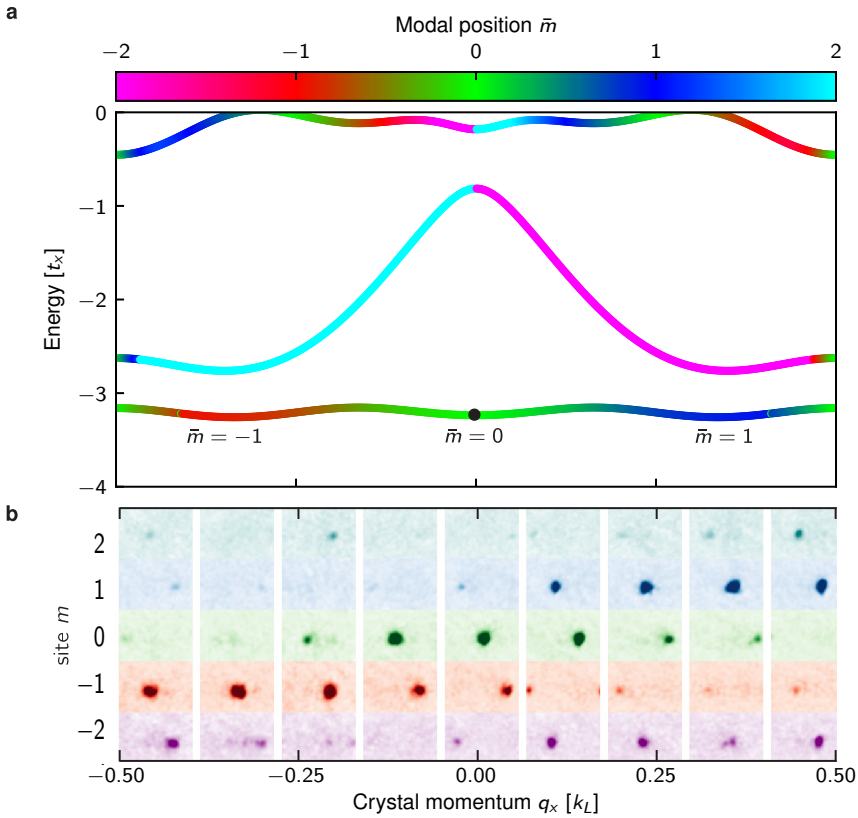


Figure 4: Band structure in a 5-site wide ribbon. (a) Band structure computed using full Hamiltonian for a $4.4E_L$ deep 1-D lattice ($\lambda_L = 1064$ nm), $0.5E_L$ Raman coupling strength ($\lambda_R = 790$ nm), and quadratic Zeeman shift $\epsilon = 0.02E_L$, giving $\Phi/\Phi_0 \approx 4/3$, $t_x = 0.078(2)E_L$, $t_s = 2.3(1)t_x$. The color indicates modal position \bar{m} . The black dot indicates the initial loading parameters. (b) TOF absorption images $n(k_x, m)$ for varying longitudinal crystal momenta q_x .

From these hybrid TOF images, we extracted the fractional population in each site m . In addition, from the change in position along the momentum axis k_x we detected the crystal momentum Δq_x for each image, as shown in Figure 1c,d. We therefore observed the evolution in the fractional populations and modal position as a function of q_x . Sample TOF images at different values of the crystal momentum are shown in Figure 4, with different single-site resolved imaging along \mathbf{e}_s represented in the vertical direction, different m sites shaded in different colors, corresponding to the colorbar in Figure 4a. Similarly, the ODT crossing beam was displaced to the opposite side an equal amount, applying the same magnitude of force in the opposite direction and including motion to the left $q_x \rightarrow q_x < 0$ in the band structure. In this way, we obtained a complete map of the fractional populations n_m in each transverse site m for each value of the longitudinal crystal momentum q_x .

7.1.3 Density reduction

When force was applied to the atoms, their crystal momentum q_x evolved, and they were no longer confined to a minimum of the band structure. This opened up the possibility for two-body collisions between the atoms that conserved the overall momentum and energy of the pair while changing the crystal momentum of each atom [116]. This lead to a smearing of the atoms along the crystal momentum axis, obscuring the measurement.

To mitigate this problem, it was necessary to reduce the atomic density as much as possible while retaining enough atoms to observe a signal. In addition to reshaping the ODT beam (see sec. 3.3.4.4), we also cut down the overall atom number after creating the BEC before loading the synthetic dimensional lattice. Starting in $F = 1, m_F = 0$, we applied a microwave pulse resonant with the $|F = 1, m_F = 0\rangle \rightarrow |F = 2, m_F = -1\rangle$ transition for 355 μs , until $\approx 80\%$ of the atoms were transferred to the $F = 2$ manifold. We then shined on the XZ probe beam to selectively blow

away the $F = 2$ atoms, leaving ≈ 1000 atoms in the condensate.

7.1.4 Rf correction

For rf-coupled experiments, our loading procedure into the lowest band at $q_x = 0$ resulted in some latent non-adiabaticity that we could not get rid of or fully explain. This non-adiabaticity resulted in oscillations in the fractional populations n_m as a function of time, even though the rf-coupled band structure predicts no dependence of n_m on q_x . However, these oscillations were present as a function of time even when no force was applied to the atoms, indicating that these variations were dependent on time and not q_x . Therefore, we used data obtained with no force applied to correct the time-dependent variation in data where the force was applied.

Our correction procedure is shown in Figure 5. Figure 5a-c show the raw fractional populations as a function of time for the case where a force was applied to the right, to the left, and not at all, respectively. Note that the observed oscillations are quite large, but consistent between the three cases. This implies that whatever mechanism is causing these oscillations is a time dependent one and not a consequence of any change in longitudinal crystal momentum q_x .

To correct the data and extract the change in fractional populations caused by varying q_x , we first calculate the change in fractional population as a function of time for the data with no force applied. This is given by $\Delta n_m^{F=0}(t) = n_m^{F=0}(t) - n_m^{F=0}(0)$. We then subtract this change from the data with force applied via $n_m^{F \neq 0, \text{corrected}}(t) = n_m^{F \neq 0}(t) - \Delta n_m^{F=0}(t)$. These corrected fractional populations as a function of time are shown in Figure 5d,e for positive and negative force, respectively. In Figure 5f, we have combined the corrected positive and negative force data and plotted it as a function of crystal momentum, effectively mapping out the fractional populations everywhere in the lowest band.

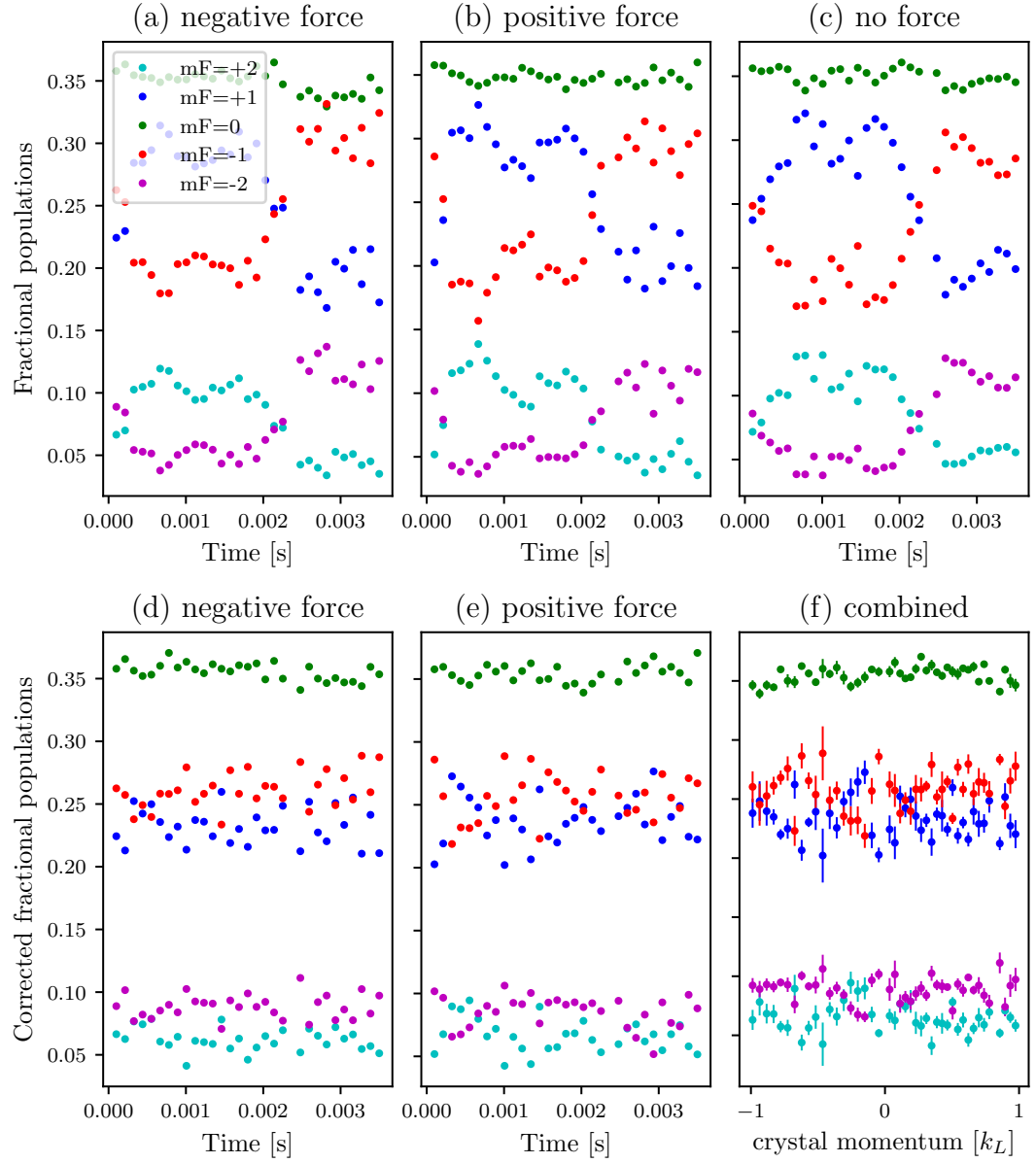


Figure 5: Correction of oscillations in rf coupled data. (a,b,c) Raw fractional populations n_m observed as a function of time Δt with (a) positive force applied, (b) negative force applied, and (c) no force applied. (d,e) Corrected fractional populations $n_m^{\text{corrected}}$ with (d) positive force applied, (e) negative force applied. (f) Corrected data as a function of crystal momentum for both force directions combined.

7.2 Quantum Hall Effect interpretation

The measurement we performed is similar to a quantum Hall conductivity measurement: we pierced a 2D material with an effective magnetic field, applied a force (an electric field in a conventional quantum Hall setup), and observed a transverse response. To draw a more direct analogy, we can describe the quantum Hall effect(QHE) from the microscopic perspective.

7.2.1 Microscopic view of QHE

In the quantum Hall effect, a longitudinal force F_{\parallel} , induced by an electric field $F_{\parallel} = eE_{\parallel}$, drives a transverse ‘Hall’ current density

$$j_{\perp} = \sigma_H E_{\parallel}, \quad (7.3)$$

where σ_H is the Hall conductivity. This transverse current density can be expressed as

$$j_{\perp} = n_{2D} v_{\perp} e, \quad (7.4)$$

where n_{2D} is the 2-D charge carrier density, v_{\perp} is the transverse velocity of the charge carriers and e is the electron charge. Choosing some increment of time Δt , we can express v_{\perp} and F_{\parallel} as

$$v_{\perp} = \frac{\Delta x_{\perp}}{\Delta t}, \quad (7.5)$$

and

$$F_{\parallel} = \hbar \frac{\Delta q_{\parallel}}{\Delta t}, \quad (7.6)$$

where q_{\parallel} is the crystal momentum along the direction of the force. Plugging this into eqn. 7.3, we obtain

$$n_{2D} e \frac{x_{\perp}}{\Delta t} = \hbar \frac{\Delta q_{\parallel}}{\Delta t} \frac{\sigma_H}{e} \quad (7.7)$$

Re-expressing n_{2D} in number of carriers N per plaquette, defining Δx_\perp as transverse displacement in units of lattice periods, we plug the above definitions into eqn. 7.3 to obtain

$$NG \frac{\Delta x_\perp}{\Delta q_\parallel} = \sigma_H \frac{h}{e^2}, \quad (7.8)$$

where G is the reciprocal lattice vector.

In addition, we know that the quantum Hall conductivity can be expressed in terms of the Chern numbers C_n of the occupied bands n as

$$\sigma_H = \frac{e^2}{h} \sum_n C_n. \quad (7.9)$$

In the conventional case of Landau levels, where each Landau level has a Chern number $C_n = 1$, this amounts to the number of filled bands ν , giving $\sigma_H = \nu e^2/h$. In our case, where the Chern number is not necessarily 1 and only the lowest band is occupied, this instead reduces to the Chern number of the lowest band which we will just call C , giving $\sigma_H = Ce^2/h$. Plugging this into eqn. 7.8, we can write

$$NG \frac{\Delta x_\perp}{\Delta q_\parallel} = C \quad (7.10)$$

Therefore, if we observe (as was done in our measurement) the ratio of transverse displacement Δx_\perp to the longitudinal crystal momentum Δq_\parallel , we should be able to fit that to a line and directly extract the Chern number C .

7.2.2 Chern number from Hall conductivity

We used the prescription given in the previous section to extract a Hall conductivity and therefore a Chern number from our data. The results for a 5-site wide strip ($F = 2$) are shown in Figure 6a,b,c (top) for all values of flux studied: $\Phi/\Phi_0 = 0, \approx -4/3$, and $\approx 4/3$, respectively. We calculated the modal position

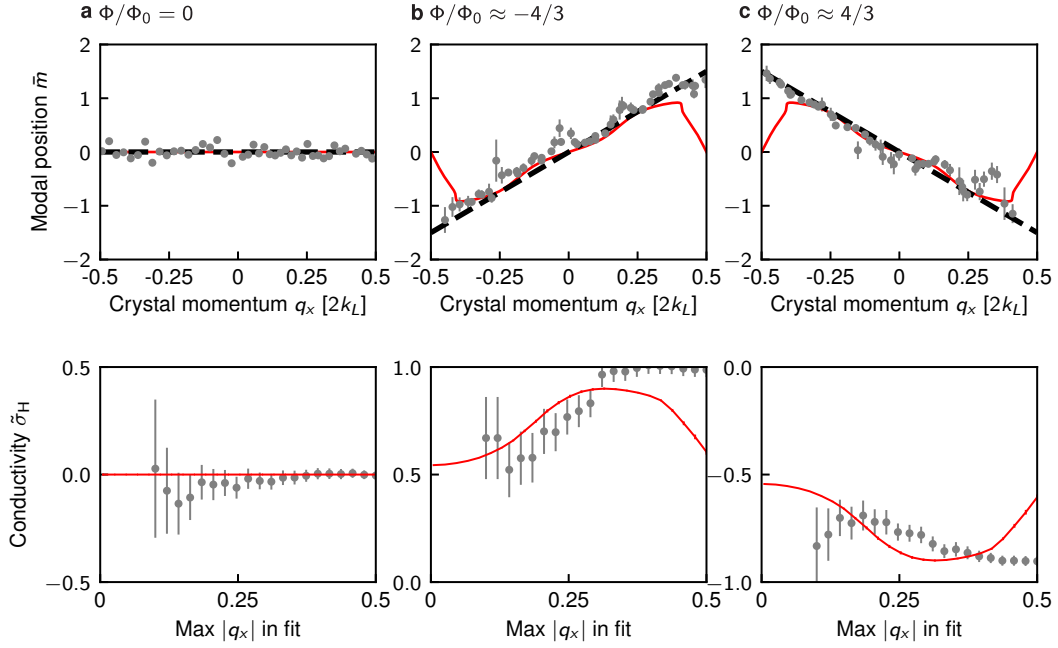


Figure 6: Hall displacement. Top: modal position \bar{m} is plotted as a function of q_x for the 5-site ribbon with flux **a.** $\Phi/\Phi_0 = 0$, **b.** $\Phi/\Phi_0 \approx -4/3$, **c.** $\Phi/\Phi_0 \approx 4/3$. Gray circles depict the measurements; black dashed lines are the prediction of our simple $\tilde{\sigma}_H$ and red curves are the expectation from the band structure of our thin ribbon. Bottom: Extracted conductivity from the slope of a line of best fit to the data (gray circles) and theory (red lines) as a function of maximum $|q_x|$ included in the fit range, for each flux value. As discussed in sec. 7.1.4, the $\Phi/\Phi_0 = 0$ data was compensated to account for non-adiabaticity in the loading procedure.

\bar{m} (see sec. 7.1.2) of our atoms along \mathbf{e}_s as a function of longitudinal crystal momentum q_x . The data is represented by gray dots, with uncertainty bars reflecting the propagated standard uncertainty from averaging six identical runs. For zero flux $\Phi/\Phi_0 = 0$ (Fig. 6a), \bar{m} was independent of q_x ; in contrast, for non-zero flux $\Phi/\Phi_0 \approx \pm 4/3$ (Fig. 6b,c), \bar{m} depends linearly on q_x with non-zero slope.

Here, the change in \bar{m} was a transverse displacement Δx_\perp . We fit the modal position as a function of q_x to a line (black dashes in the figure). From the slope of the line, we used eqn. 7.10 to extract the Chern number. We obtained $C = 0.01(1)$, $0.87(3)$, and $-0.85(3)$ for zero, negative and positive flux respectively. This shows the correct qualitative behavior, but differs significantly from expected values of $0, \pm 1$.

7.2.3 Inadequacy for narrow systems

The red curves in Figure 6(top) show the expected behavior for our 5-site wide system for adiabatic changes in q_x as calculated from exact diagonalization of the full Hamiltonian (see sec. 6.2.1), always within the lowest band (Fig. 4a), i.e., Bloch oscillations. This theory predicts a nearly linear slope for small q_x sharply returning to $\bar{m} = 0$ at the edges of the Brillouin zone. A linear fit to this theory produces $\tilde{\sigma}_H \approx 0, 0.6$, and -0.6 for zero, negative and positive flux respectively, far from the Chern number. In addition, they differ significantly both from the data and from the linear fit at the edges of the Brillouin zone.

This discrepancy is resolved by recalling that Bloch oscillations require adiabatic motion, meaning no transition to higher bands can happen. This is possible in the narrow system under study, but quickly becomes impossible as the size of the system grows. This is illustrated in Figure 7. Figure 7a shows the band structure of our 5-site ($F = 2$) strip, with parameters used in the experiment. Here, there are non-negligible band gaps at the edges of the Brillouin zone between the lowest and second bands. With a weak enough force, the atoms could traverse this region slowly enough to be adiabatic with respect to this band gap. However, for a larger system, such as the 41-site wide system whose band structure is shown in Figure 7b, these band gaps become negligibly small and adiabaticity is impossible.

The departure of the data in Fig. 6(top) from the adiabatic theory (red lines) at the edges of the Brillouin zone indicates a partial break down of adiabaticity was present in our data. However, it is not a complete breakdown as the data also differs from the linear fit at the edges of the Brillouin zone. The data was somewhere in the partially adiabatic regime, only possible for our narrow system. This made neither the adiabatic theory, nor the linear fit assuming perfect non-adiabaticity, applicable to our system. Therefore, the linear fit is not a good measure of the Chern number

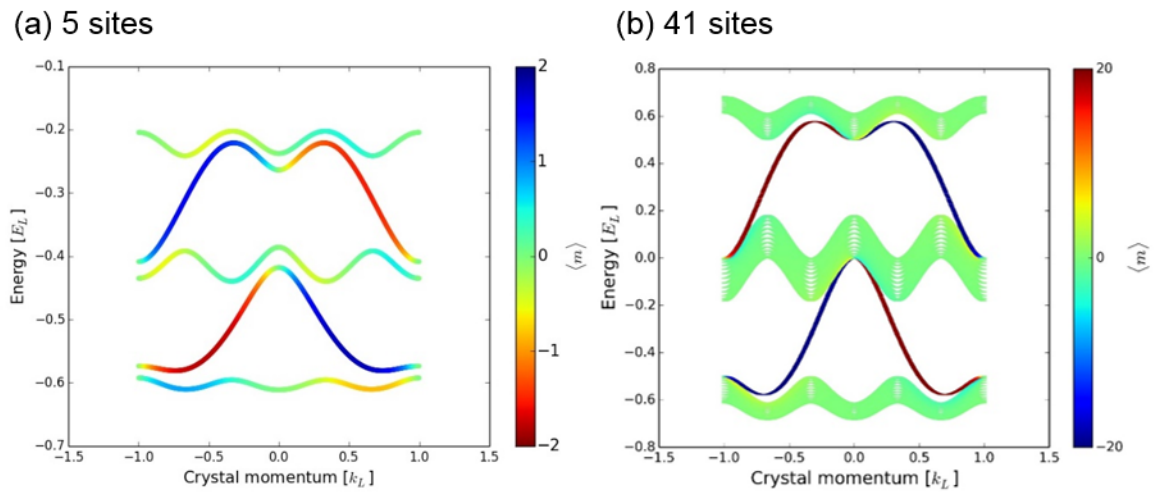


Figure 7: Band structure of the synthetic dimesnions lattice with flux $\Phi/\Phi_0 = -4/3$. (a) 5-site wide system with experimental parameters $V_0 = 4.4$, $\hbar\Omega = 0.5$, $\hbar\delta = 0$, and $\hbar\epsilon = 0.02$. There is a band gap between the first and second bands at the edge of the Brillouin zone. (b) 41-site wide system with parameters $V_0 = 4.4$, $\hbar\Omega = 0.5$, $\hbar\delta = 0$, and $\hbar\epsilon = 0$ and no Clebsch-Gordan coefficients included. The band gap between the first and second bands at the edge of the Brillouin zone is negligibly small.

for our system.

One might suspect that limiting the domain of the linear fit such that band edge effects are excluded would still provide a good measure of the Chern number. This is not the case, as can be seen in Fig. 6(bottom). Here, we plot the measured Chern number for a linear fit to our data (grey) and the adiabatic theory (red) for a limited range of crystal momenta q_x . The range of the fit is plotted on the x axis, ranging from only the center to the entire Brillouin zone. The slope of the best fit line for non-trivial topologies ($\Phi/\Phi_0 \neq 0$), and thus the measured Chern number, depends highly on the selected domain for both the theoretical (red) and experimental (black) data, and the appropriate choice of range is ambiguous. We conclude that for an extremely narrow system such as ours, a conductivity measurement is insufficient for determining the Chern number at reasonable tunneling strengths [117].

7.3 Measuring Chern number via Diophantine equation

To better identify the Chern number in our system, following theoretical work [117–121], we leveraged the TKNN Diophantine equation (see sec. 1.1.5) to determine the Chern number of our system. This equation states that for rational flux $\Phi/\Phi_0 = P/Q$ (for relatively prime integers P and Q) the integer solutions s and C to the Diophantine equation

$$1 = Qs - PC \tag{7.11}$$

uniquely¹ determine the Chern number C of the lowest band.

¹Subject to the constraint $|C| \leq |Q|/2$ [6, 22]. The integer s has no bearing on our argument, but has been interpreted as the charge transported when the periodic potential is adiabatically displaced [122, 123].

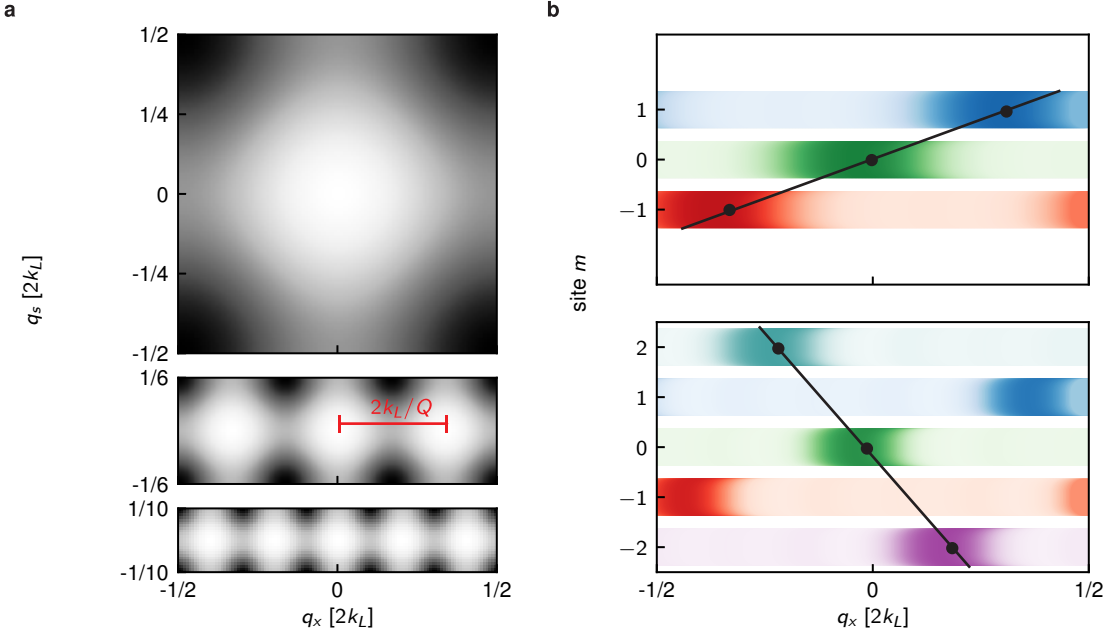


Figure 8: Chern number from the TKNN equation. (a). Lowest band energy within the Brillouin zone in an extended 2-D system, where q_x and q_s are crystal momenta along e_x and e_s , respectively. Top. $\Phi/\Phi_0 = 0$. Middle. $\Phi/\Phi_0 = 1/3$: Brillouin zone shrinks by a factor of 3 and becomes 3-fold degenerate, distance between adjacent energy minima spaced by $2k_L/Q$ is labeled. Bottom. $\Phi/\Phi_0 = 2/5$. (b). Fractional population in each spin state in the lowest band at $q_s = 0$. Top. $\Phi/\Phi_0 = 1/3$. Bottom. $\Phi/\Phi_0 = 2/5$. A momentum shift along e_x of $2k_L/Q$ is accompanied by an integer number of spin flips C . A line connecting magnetic states separated by $2k_L/Q$, with slope $C = 1$ (top) and -2 (bottom), is indicated.

7.3.1 TKNN Diophantine equation in synthetic dimensions

Surprisingly, the TKNN equation (Eqn. 7.11) has a direct interpretation in the physical processes present in our system. Although the Hofstadter Hamiltonian in eqn. 7.1 is only invariant under m -translations that are integer multiples of Q , a so-called ‘‘magnetic-displacement’’ by $\Delta m = 1$ accompanied with a crystal momentum shift $\Delta q_x/2k_R = P/Q$ leaves Eqn. 7.1 unchanged. Together, these symmetry operations give a Q -fold reduction of the Brillouin zone along e_s , and add a Q -fold degeneracy, as illustrated in Fig. 8a for $\Phi/\Phi_0 = 0, 1/3$, and $2/5$. Recalling that the Brillouin zone is $2\hbar k_L$ periodic along e_x , it follows that a displacement

by $2k_L/Q$ to the nearest symmetry related state involves an integer C magnetic displacements, shown in Fig. 8b for $\Phi/\Phi_0 = 1/3$ and $2/5$, given by solutions to $2k_L s - 2k_R C = 2k_L/Q$, where s counts the number of times the Brillouin zone was “wrapped around during the C vertical displacements. Because this is exactly the TKNN equation (7.11), we identify C as the Chern number.

Both C and s directly relate to physical processes. First, each time the Brillouin zone is wrapped around implying a net change of momentum by $2\hbar k_L$ a pair of photons must be exchanged between the optical lattice laser beams. Second, each change of m by 1 must be accompanied by a $2\hbar k_R$ recoil kick imparted by the Raman lasers as they change the spin state. This physical motivation of the TKNN equation remains broadly applicable even for our narrow lattice, providing an alternate signature of the Chern number.

7.3.2 Prescription for identifying Chern number

The prescription we used to identify the Chern number from our data and theoretical calculations through the Diophantine equation argument is detailed in Figure 9. Figure 9a shows the fractional populations in each m site as a function of q_x for a 3-site wide strip ($F = 1$ data) with flux $\Phi/\Phi_0 \approx -4/3$. Each of the fractional populations (red, green, and blue representing $m = -1, 0$, and 1 respectively) was fit to a parabola to extract the peak. These peak locations were interpreted as the band structure minima corresponding to each m site. These points were then plotted as in Figure 9c, with site m as a function of its maximizing crystal momentum q_x . These points were then fit to a line, whose slope was identified as the Chern number C . The same prescription was used to obtain the theoretical predictions, as shown in Figure 9b,d. The theoretical fractional populations were obtained from the eigenvectors corresponding to the lowest band of the full Hamiltonian, eqn. 6.2.1.

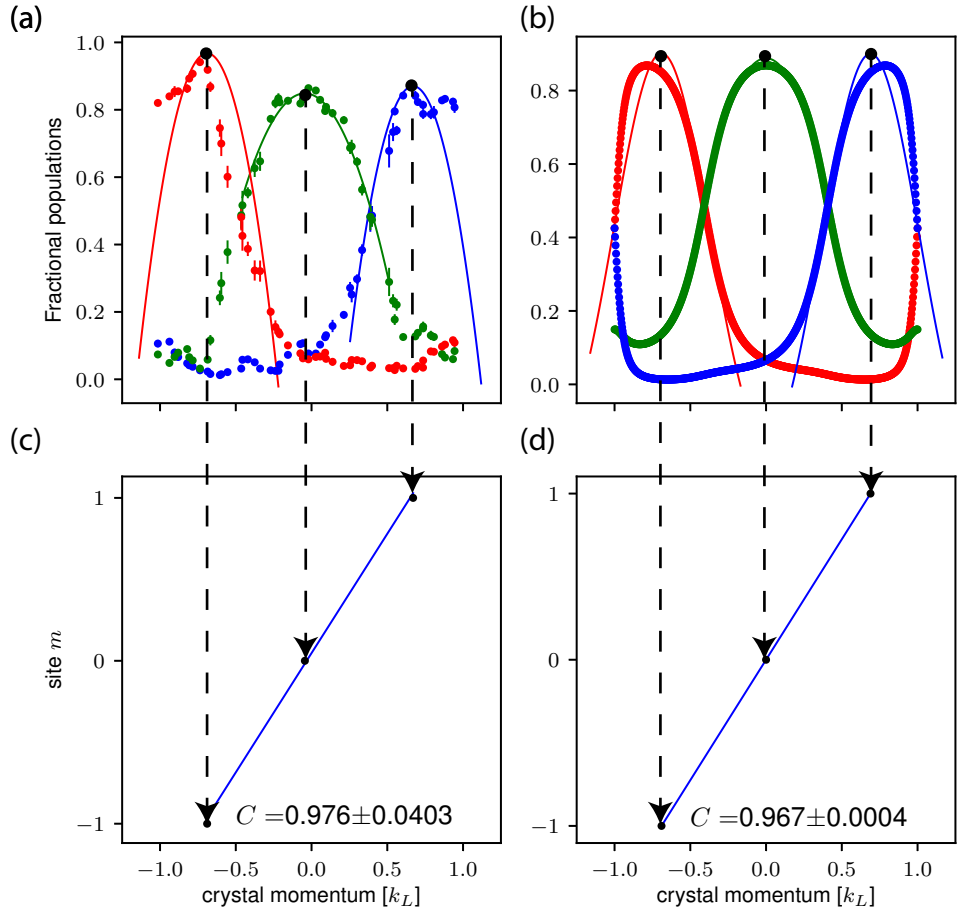


Figure 9: Calculating Chern number. (a) Fractional populations in $m = -1, 0$ and 1 sites (red, green, and blue respectively) as a function of q_x for data taken in a 3-site wide strip ($F = 1$ data) with flux $\Phi/\Phi_0 \approx -4/3$. Dots represent data, lines represent parabolic fits. (b) Theoretically calculated fractional populations for the same system. (c) Site m as a function of maximizing q_x from fits to data in (a). Best fit line to the three points has a slope corresponding to the Chern number C . (d) Site m as a function of maximizing q_x from fits to theory in (b). Best fit line to the three points has a slope corresponding to the Chern number C .

7.3.3 Properties of the method

This prescription for identifying the Chern number in narrow system can only be considered meaningful if it converges to the more traditional exact integer value in the limit of an infinite system. We study the behavior of the Chern number, as identified through the prescription defined in the previous section, as a function of width along the synthetic direction \mathbf{e}_s . We solve this in the tight binding limit in momentum space along e_x , eqn. 6.12. We also set the detuning $\hbar\delta = 0$, quadratic shift $\hbar\epsilon = 0$, allowing us to drop the last diagonal term in eqn. 6.12. Additionally, we neglect the variability in t_s as a function m due to Clebsch-Gordan coefficients by setting them to 1, assuming uniform coupling as in the Harper-Hofstadter Hamiltonian.

The resulting Chern number dependence on synthetic dimension size is presented in Figure 10a. Here, the flux $\Phi/\Phi_0 = -4/3$, leading to an expected Chern number of 1. We used a value of tunneling $t_x = 0.5E_L$ and synthetic direction coupling $\hbar\Omega = 0.5E_L$. As seen in the figure, for narrow lattices the measured Chern number differs from unity, but converges to unity as the system size grows. There also appears to be a three distinct convergence curves, caused by the slightly differing band structures depending on the number of sites modulo q .

We also study the dependence of the measured Chern number on the coupling strength along the synthetic direction $\hbar\Omega$ for lattice widths relevant to our experiment—3 and 5 sites. We used the same Hamiltonian and parameter values listed above. The results are shown in Figure 10b. In the limit of vanishing tunneling, both the 3 and 5-site wide Chern number converge to the exact integer value of 1. This supports the hypothesis that deviation from unity at non-zero coupling strengths is a consequence of the hybridization of edge states, which is facilitated by stronger couplings.

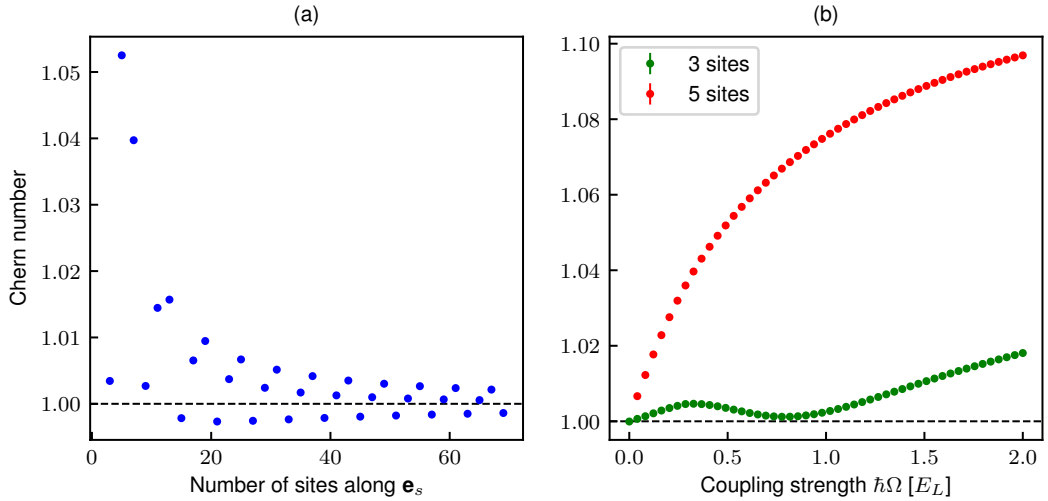


Figure 10: Chern number dependence on (a) system size and (b) coupling strength.

7.4 Results and conclusion

Figure 11 shows the full evolution of fractional population in each m site as a function of crystal momentum q_x in the lowest band, for all preparations studied in the experiment: 3- and 5-site wide strips, with fluxes $\Phi/\Phi_0 = 0, \approx \pm 4/3$. The black circles locate the peak of the fractional population in each spin state. From these data, we extract the Chern number through the procedure described in the previous section.

For the 3-site wide ribbon ($F = 1$ data), we measured a Chern number of $0.99(4), -0.98(5)$ for negative and positive flux respectively², in agreement with the exact theory which predicts $\pm 0.97(1)$, with uncertainties reflecting fit uncertainty of peak locations. For the 5-site wide ribbon, we measured $1.11(2), -0.97(4)$, close to the theoretical prediction of $\pm 1.07(1)$. The deviation from unity results from $\Phi/\Phi_0 - 4/3 \approx 0.01$, a non-zero quadratic Zeeman shift, and $t_s > t_x$ allowing hybridization of the edge states [117].

²Our Chern number extraction scheme fails for the rf case as the fractional populations are flat and there is no peak. We therefore assign a Chern number of 0 to flat distributions.

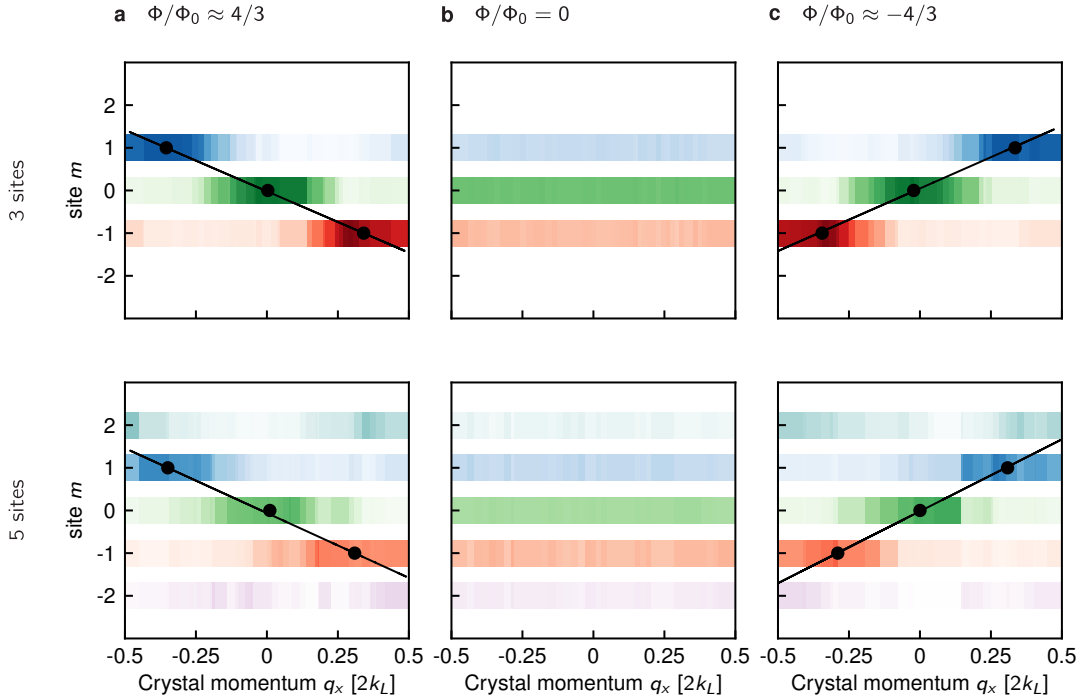


Figure 11: Chern number measurement. Lowest band fractional population measured as a function of crystal momentum in the e_x and position in the e_s . Darker color indicates higher fractional population. In the Raman-coupled cases, the points represent the fitted population maxima and the Chern number is extracted from the best fit line to those points. (a). 3-site (left) and 5-site (right) systems with positive flux. (b) 3-site (left) and 5-site (right) system with zero flux. (c). 3-site (left) and 5-site (right) systems with negative flux. The parameters for 3-site data were identical to those for 5-site data, see Fig. 6 a, except $t_s = 2.880(1)t_x$.

Our direct microscopic observations of topologically driven transverse transport demonstrate the power of combining momentum and site-resolved position measurements. With the addition of interactions, these systems have been shown to display chiral currents [124], and with many-body interactions are predicted to give rise to complex phase diagrams supporting vortex lattices and charge density waves [125–127]. Realizations of controlled cyclic coupling giving periodic boundary conditions [61] along e_s could elucidate the appearance of edge modes as the coupling between two of the three states is smoothly tuned to zero. In addition, due to the non-trivial topology as well as the low heating afforded by synthetic dimensional systems, a quantum Fermi gas dressed similarly to our system would be a good candidate for realizing fractional Chern insulators [128].

Appendix A: Brownian motion of solitons in a Bose–Einstein Condensate

Brownian motion of solitons in a Bose–Einstein condensate

Lauren M. Aycock^{a,b}, Hilary M. Hurst^{a,c}, Dmitry K. Efimkin^d, Dina Genkina^a, Hsin-I Lu^a, Victor M. Galitski^{a,c}, and I. B. Spielman^{a,1}

^aJoint Quantum Institute, National Institute of Standards and Technology and University of Maryland, Gaithersburg, MD, 20899; ^bDepartment of Physics, Cornell University, Ithaca, NY 14850; ^cCondensed Matter Theory Center, Department of Physics, University of Maryland, College Park, MD 20742; and ^dThe Center for Complex Quantum Systems, The University of Texas at Austin, Austin, TX 78712-1192

Edited by Alain Aspect, Institut d'Optique, Palaiseau, France, and approved January 10, 2017 (received for review September 7, 2016)

We observed and controlled the Brownian motion of solitons. We launched solitonic excitations in highly elongated ^{87}Rb Bose–Einstein condensates (BECs) and showed that a dilute background of impurity atoms in a different internal state dramatically affects the soliton. With no impurities and in one dimension (1D), these solitons would have an infinite lifetime, a consequence of integrability. In our experiment, the added impurities scatter off the much larger soliton, contributing to its Brownian motion and decreasing its lifetime. We describe the soliton's diffusive behavior using a quasi-1D scattering theory of impurity atoms interacting with a soliton, giving diffusion coefficients consistent with experiment.

soliton | Brownian motion | Bose–Einstein condensate | diffusion | fluctuation dissipation

We studied the diffusion and decay of solitons in the highly controlled quantum environment provided by atomic Bose–Einstein condensates (BECs), where density maxima can be stabilized by attractive interactions [i.e., bright solitons (1, 2)] or, as here, where density depletions can be stabilized by repulsive interactions [i.e., dark solitons such as kink solitons (3, 4) and solitonic vortices (5)]. By contaminating these BECs with small concentrations of impurity atoms, we quantitatively studied how random processes destabilize solitons.

Our BECs can be modeled by the one-dimensional (1D) Gross–Pitaevski equation (GPE): an integrable nonlinear wave equation with soliton solutions as excitations above the ground state. For a homogeneous 1D BEC of particles with mass m_{Rb} with density ρ_0 , speed of sound c , and healing length $\xi = \hbar/\sqrt{2m_{\text{Rb}}c}$, the dark soliton solutions

$$\varphi(z, t) = \sqrt{\rho_0} \left[i \frac{v_s}{c} + \frac{\xi}{\xi_s} \tanh \left(\frac{z - v_s t}{\sqrt{2}\xi_s} \right) \right] \quad [1]$$

are expressed in terms of time t , axial position z , soliton velocity v_s , and soliton width $\xi_s = \xi/\sqrt{1 - (v_s/c)^2}$. Such dark solitons have a minimum density $\rho_0(v_s/c)^2$ and a phase jump $-2\cos^{-1}(v_s/c)$, both dependent on the soliton velocity v_s . These behave as classical objects with a negative inertial mass $m_s \approx -4\hbar\rho_0/c$, essentially the missing mass of the displaced atoms. The negative mass implies that increasing the soliton velocity reduces its kinetic energy; thus, dissipation accelerates dark solitons (6). This can be seen from the soliton equation of motion

$$-|m_s|\ddot{z}(t) = -\gamma\dot{z}(t) - \partial_z V + f(t), \quad [2]$$

where $-\gamma\dot{z}$ is the friction force and V is the confining potential due to the mean-field effects of the condensate. The random Langevin force $f(t)$ has a white noise correlator $\langle f(t)f(t') \rangle = 2\gamma k_B T \delta(t - t')$, where T is temperature and k_B is Boltzmann's constant. The connection between the friction coefficient γ and $f(t)$ derives from the same microscopic

dynamics that yield the fluctuation–dissipation theorem for positive mass objects— $f(t)$ is responsible for Brownian motion, whereas γ describes friction, but both have contributions from impurity atoms.

Conventionally, the diffusion coefficient D is inversely proportional to the friction coefficient: $D \propto 1/\gamma$. For negative mass objects, we show that the diffusion coefficient is instead proportional to the friction coefficient $D \propto \gamma$; this reflects that friction is an antidamping force for negative mass objects. The interplay between friction and confinement drives diffusive behavior with linear-in-time variance in soliton position, $\text{Var}(z) = Dt$, the same Brownian motion present for positive mass objects.

Solitons are infinitely long lived because of the integrability of the 1D GPE. Integrability breaking is inherent in all physical systems—for example, from the nonzero transverse extent of quasi-1D systems. Indeed, the kink soliton in 3D—the direct analogue to the 1D GPE's dark soliton solution—is only long-lived in highly elongated geometries (7–9), where integrability breaking is weak. Cold atom experiments have profoundly advanced our understanding of soliton instability by controllably lifting integrability by tuning the dimensionality (5, 10). Here, we studied the further lifting of integrability by coupling solitons to a reservoir of impurities.

Experimental System

Our system (11) consisted of an elongated ^{87}Rb BEC, confined in a nominally flat-bottomed time-averaged potential, created by spatially dithering one beam of our crossed dipole trap. We

Significance

Solitons, spatially localized, mobile excitations resulting from an interplay between nonlinearity and dispersion, are ubiquitous in physical systems from water channels and oceans to optical fibers and Bose–Einstein condensates (BECs). From our pulse throbble at our wrists to rapidly moving tsunamis, solitons appear naturally at a wide range of scales. In nonlinear optical fibers, solitons can travel long distances with applications for communication technology and potential for use in quantum switches and logic. Understanding how random processes contribute to the decay and the diffusion of solitons is essential to advancing these technologies.

PHYSICS

Author contributions: V.M.G. and I.B.S. designed research; V.M.G. proposed the initial theoretical concept that I.B.S. refined into a working experimental concept; H.M.H., D.K.E., and V.M.G. developed the final theoretical framework; L.M.A. configured the apparatus for this experiment; L.M.A. led the data acquisition and analysis effort to which D.G. and H.-I.L. contributed; H.M.H. performed detailed simulations for our experiment; I.B.S. contributed to the understanding of experimental data; H.M.H. prepared the theory discussions in the manuscript; and L.M.A., H.M.H., D.G., H.-I.L., V.M.G., and I.B.S. wrote the paper.

The authors declare no conflict of interest.

This article is a PNAS Direct Submission.

¹To whom correspondence should be addressed. Email: ian.spielman@nist.gov.

prepared $N = 8(2) \times 10^5$ atoms* in the $|F = 1, m_F = 0\rangle$ internal state at $T = 10(5)$ nK. Our system's $\approx 250\text{ }\mu\text{m}$ longitudinal extent was approximately 30 times its transverse Thomas-Fermi diameter $2R_{\perp}$ set by the radial trap frequency $\omega_r = 2\pi \times 115(2)$ Hz and chemical potential $\mu \approx \hbar \times 1$ kHz. We controllably introduced a uniform (12) gas of N_I impurity atoms in thermal equilibrium, with our BECs using an rf pulse resonant with the $|F = 1, m_F = 0\rangle$ to $|F = 1, m_F = +1\rangle$ transition before evaporation to degeneracy (13). This gave impurity fractions N_I/N from 0 to 0.062 in our final BECs.

We then launched long-lived solitonic excitations using a phase-imprinting technique (3, 4). Because our trap geometry had a finite transverse extent, quantified by the ratio $\mu/\hbar\omega_r \approx 9$, planar kink solitons could be dynamically unstable and decay into 3D excitations (14). Our soliton's initial velocity $v_s \approx 0.3$ mm/s, approximately 1/5 the 1D speed of sound $c \approx 1.4$ mm/s (15), implies that it is in an unstable regime (6), where it will convert from a planar kink soliton to a nearly planar solitonic vortex. For highly anisotropic geometries such as ours, the density profile of these two types of solitons is nearly the same—as given by the 1D GPE—reflecting that they become formally indistinguishable at large velocity (14).

We absorption-imaged our solitons after a sufficiently long time-of-flight (TOF) that their initial width $\xi_s \approx 0.24\text{ }\mu\text{m}$ expanded beyond our $\approx 2\text{ }\mu\text{m}$ imaging resolution. Fig. 1A shows our elongated BEC with no soliton present, and, in contrast, Fig. 1B displays a BEC with a soliton taken 0.947 s after its inception. The soliton is the easily identified density depletion sandwiched between two density enhancements. We quantitatively identified the soliton position as the minimum of the density depletion from 1D distributions (Fig. 1B, Right). Our phase-imprinting process launched several excitations in addition to the soliton of interest. After a few hundred milliseconds, the additional excitations dissipated, and the remaining soliton was identified. By backtracking the soliton trajectory, we were able to identify the soliton, even at short times.

Fig. 1E shows a series of 1D distributions taken from time $t \approx 0$ s to 4 s after the phase imprint. These images show three salient features: (i) The soliton underwent approximately sinusoidal oscillations; (ii) the soliton was often absent at long times; and (iii) there was significant scatter in the soliton position. Items ii and iii suggest that random processes were important to the soliton's behavior. The solitons' position z_i —when present—is represented by the light pink symbols in Fig. 1D, and the darker pink symbols mark the average position $\langle z_i \rangle$ for each time t .

Coupling to Impurities

Having established a procedure for creating solitons, we turned to the impact of coupling to a reservoir of impurities, thus further breaking integrability. Fig. 2 displays the soliton position vs. time for a range of impurity fractions. Adding impurities gave two dominant effects[†]: further increasing the scatter in the soliton position z and further decreasing the soliton lifetime. These effects manifested as a reduced fraction f_s of images with a soliton present and an increase in the sample variance $\text{Var}(z) = \sum (z_i - \langle z \rangle)^2 / (M - 1)$ computed by using the number M of measured positions z_i at each time.

Reduced Lifetime. The addition of impurities had a dramatic impact on the soliton lifetime. Although we lack a quantita-

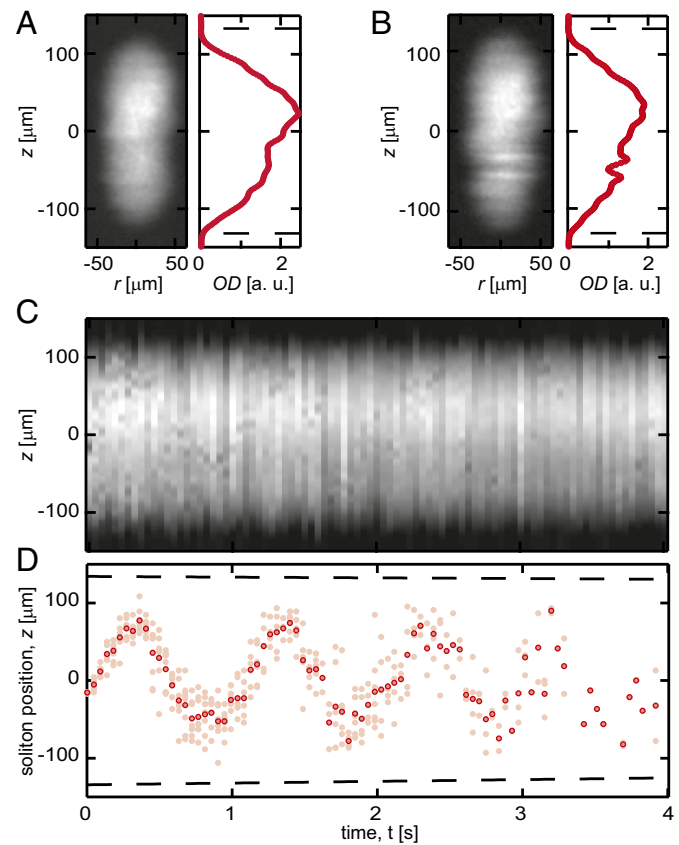


Fig. 1. Soliton oscillations. (A) An absorption image after a 19.3 ms TOF of an elongated condensate without a soliton and a longitudinal density distribution obtained by averaging over the remaining transverse direction. (B) An absorption image and 1D distribution at time $t = 0.942$ s with a soliton with $\approx 30\%$ imaged contrast. (C) A subset of the data where each 1D distribution is a unique realization of the experiment plotted vs. time t . Notice a soliton was often absent at longer times. (D) The axial position z_i of the soliton (light pink) vs. time t for different realizations of the experiment. We repeated each measurement 8 times. Dashed lines represent the edges of the elongated condensate. The dark markers represent the average soliton position $\langle z_i \rangle$ at each time t . In A and B the longitudinal densities are given in arbitrary units (a.u.).

tive model of the soliton's decay mechanism, there are several reasons to expect a finite lifetime. When dissipation is present, solitons accelerate to the speed of sound and disintegrate. Furthermore, numerical simulations show that, in anharmonic traps, solitons lose energy by phonon emission, accelerate, and ultimately decay (16). All of these decay mechanisms can contribute to the soliton lifetime, even absent impurities.

The added impurities act as scatterers impinging on the soliton, further destabilizing it. This effect is captured in Fig. 3A, showing the measured survival probability f_s vs. time for a range of impurity fractions. We fit to our data a model of the survival probability

$$f_s(t) = 1 - \frac{1}{2} \operatorname{erfc} \left[\frac{-\ln(t/\tau)}{\sqrt{2}\sigma} \right], \quad [3]$$

essentially the integrated lognormal distribution of decay times, suitable for decay due to accumulated random processes (17). The survival probability $f_s(t)$ has a characteristic width parameterized by σ and reaches 1/2 at time τ , which we associate with the soliton lifetime. Fig. 3B shows the extracted lifetime τ vs. impurity fraction N_I/N , showing a monotonic decrease. Our maximum N_I/N gives a factor of four decrease in lifetime τ .

* In our system, number fluctuations increased at the lowest trap depth (*Materials and Methods*).

[†]The soliton oscillation frequency was slightly shifted with impurities resulting from an unintentional change in the underlying optical potential. This change also slightly reduced the BECs' longitudinal extent.

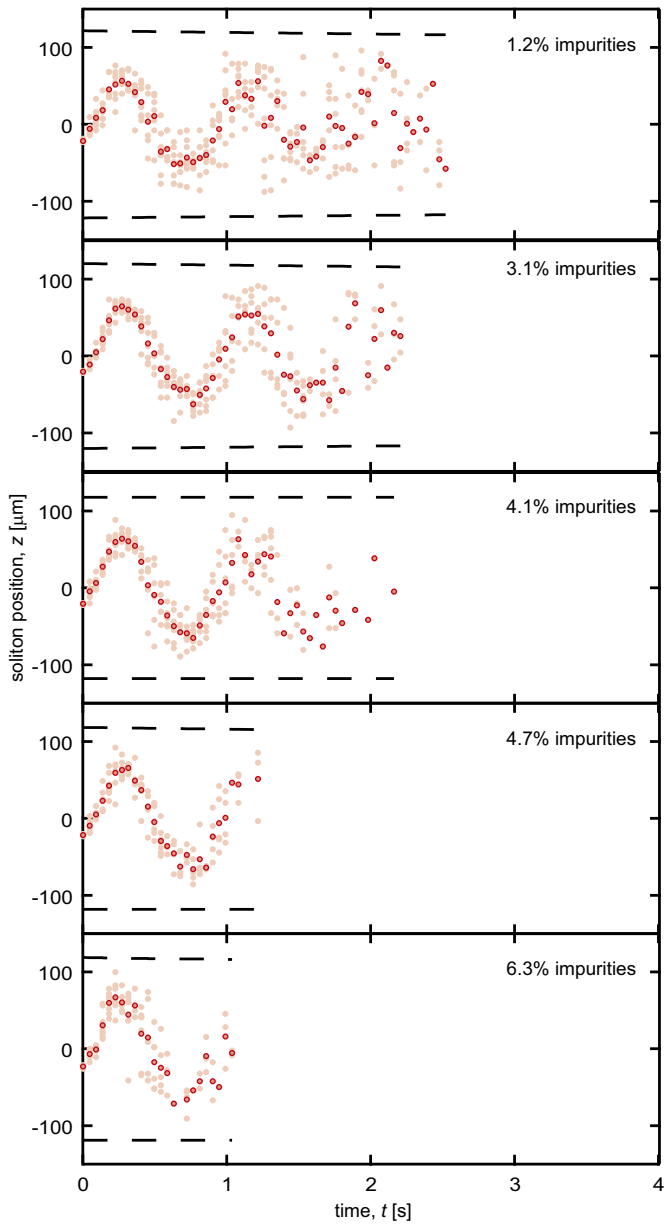


Fig. 2. Impact of impurities. Here, we plot the position z_i of the soliton (light pink) vs. time t after the phase imprint for different impurity levels. The dark pink markers represent the average position $\langle z_i \rangle$ for each time t . Dashed lines represent the endpoints of the condensate vs. t .

Soliton Diffusion. The second important consequence of adding impurities was an increased scatter in soliton position z , reminiscent of Brownian motion. Indeed, as shown in Fig. 4B, this scatter, quantified by $\text{Var}(z)$, increased linearly with time. We obtained the diffusion coefficient D as the slope from linear fits to these data and calculated D using a quasi-1D scattering theory. The energy of the infinitely long 1D system is given by the GPE energy functional

$$E[\varphi, \psi] = \int \left(\frac{\hbar^2 |\nabla \varphi|^2}{2m_{\text{Rb}}} + \frac{\hbar^2 |\nabla \psi|^2}{2m_{\text{Rb}}} + \frac{g}{2} |\varphi|^2 |\varphi|^2 + \frac{g'}{2} |\varphi|^2 |\psi|^2 \right) dz, \quad [4]$$

describing the majority gas interacting with itself along with the impurities with interaction coefficients g and g' , respectively. The fields φ and ψ denote the condensate and impurity wave functions. Because the impurities are very dilute, we do not

include interactions between impurity atoms. A soliton (Eq. 1) acts as a supersymmetric Pöschl–Teller (18, 19) potential for the impurity atoms with exact solutions in terms of hypergeometric functions (20). Impurity scattering states with momentum k_z in the rest frame of the soliton are described by the reflection coefficient

$$R(k_z) = \frac{1 - \cos(2\pi\lambda)}{\cosh(2\pi k_z \xi) - \cos(2\pi\lambda)}, \quad [5]$$

where $\lambda(\lambda - 1) = g'/g$. In ^{87}Rb , we have $g \approx g'$, giving $\lambda \approx 1.5$. The scattering problem is fully characterized by $R(k_z)$, and the problem is reduced to that of a classical heavy object moving through a gas of lighter particles.

To understand soliton diffusion over many experimental runs, we studied their distribution function $f(t, z, v_s)$. We used a kinetic equation equivalent to Eq. 2 with a stochastic force due to elastic collisions with the impurity atoms and a harmonic confining potential $V(z) \approx -|m_s|\omega^2 z^2/2$, where $\omega = \omega_{\text{trap}}/\sqrt{2}$ is the effective frequency (21, 22). In the limit of small soliton velocity $(v_s/c)^2 \ll 1$, the time-dependent distribution function can be calculated exactly (*Materials and Methods*). The kinetic equation has no stable solutions: Eventually, all solitons accelerate and disappear. However, the timescale for acceleration is set by $\Gamma^{-1} = |m_s|/\gamma$, was many seconds in our experiment. In the limit of $\Gamma t \ll 1$ and $\Gamma \ll \omega$, the variance in position grew linearly with time and diffusive behavior emerges (i.e., $\text{Var}(z) \approx Dt$). We calculate the diffusion coefficient

$$D \approx \frac{\gamma + \gamma_0}{|m_s|\omega^2} \left(\frac{k_B T}{|m_s|} + \frac{v_i^2}{2} \right), \quad [6]$$

where v_i is the soliton's initial velocity. The offset γ_0 accounts for any diffusion present without impurities. The friction coefficient γ is given by

$$\gamma = \frac{2\hbar}{k_B T} \sum_{m,l} \int_{-\infty}^{\infty} \frac{dk_z}{2\pi} k_z^2 \left| \frac{\partial \epsilon}{\partial k_z} \right| R(k_z) n(\epsilon) [1 + n(\epsilon)], \quad [7]$$

an extension of ref. 23. $\epsilon_{m,l}(k_z) = \hbar^2 k_z^2 / 2m_{\text{Rb}} + \hbar^2 j_{m,l}^2 / 2m_{\text{Rb}} R_\perp^2$ is the impurities' quasi-1D dispersion along with quantized states in the radial direction, described by Bessel functions. We account for radial confinement by summing over quantum numbers m and l . $n(\epsilon)$ is the Bose–Einstein distribution for impurity atoms[†].

Fig. 4B plots D measured experimentally (markers) and computed theoretically (curves; colored for different temperatures) as a function of N_I/N . The theory provides rather accurate estimates of the experimentally observed diffusion coefficient, with a single fitting parameter given by $\gamma_0 = 5.32 \times 10^{-4} \text{ mm}^2/\text{s}$. γ_0 is set by the diffusion coefficient at $N_I/N = 0$, where D is suppressed in agreement with our theory. Diffusion at zero impurity concentration could be due to a number of factors, including scattering of thermal phonons from the soliton, as well as trap anharmonicity (6, 16). In our quasi-1D system, the soliton is not reflectionless to phonons in the majority gas as it would be in 1D.

Conclusion and Outlook

Our data show that added uncondensed impurity atoms contribute to soliton diffusion; however, the soliton lifetime falls monotonically with increasing impurity fraction, even when the additional impurities all enter the condensate. We speculate that this might arise from two independent effects: (i) A static soliton forms a potential minimum for impurity atoms, implying that, after some time, impurities will congregate in these

[†]In our model, the condensed atoms do not contribute to the stochastic force underlying diffusion because they are all in the ground state. The impurity atoms are condensed for impurity fraction $\gtrsim 0.2\%$; thus, the number of thermal impurity atoms is constant, leading to constant friction coefficient.

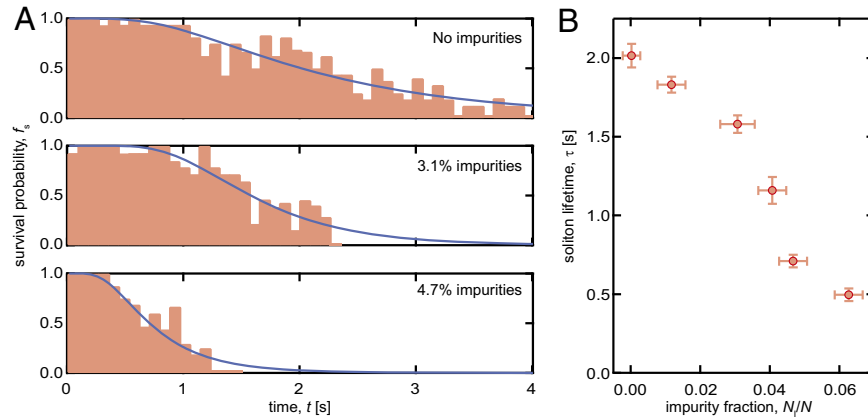


Fig. 3. Soliton lifetime in the presence of impurities. (A) Histograms of soliton occurrence probability f_s vs. time t after phase imprint. The blue solid curves are fits to the lognormal-based survival function, from which we extract the lifetime τ . For each impurity fraction, we stopped collecting data when f_s fell below approximately 0.2. (B) Lifetime τ extracted from fit to the survival fraction f_s vs. impurity fraction N_i/N .

minima (7), broadening and destabilizing the soliton; or (ii) because the soliton moves in excess of the speed of sound for the impurity atoms, even condensed atoms can reflect from the moving soliton. Although this coherent reflection process would not add to diffusion, it would transfer momentum, thereby increasing the apparent damping coefficient and thereby reducing the soliton lifetime. This latter model predicts a reduction of lifetime qualitatively similar to, but quantitatively in excess of, that observed in experiments.

Solitons in spinor systems with impurity scatterers is an exciting playground for studying integrability breaking and diffusion of quasiclassical, negative-mass objects. Our observed reduction in soliton lifetime with increasing impurity fraction is in need of a quantitative theory. For the case of no impurities, there is a further open question for both theory and experiment of whether friction and diffusion can be present, even in the case of preserved integrability, for example, due to non-Markovian effects, as was recently discovered for bright solitons (24). Future experiments could study the impact of different types of impurities on soliton dynamics by introducing impurities of a different atomic mass. Lastly, mixtures with tunable interactions could freely tune the amount of impurity scattering, offering an additional way to change D .

Materials and Methods

BEC Creation. We created BECs in the optical potential formed by a pair of crossed horizontal laser beams of wavelength $\lambda = 1064$ nm (11). The beam traveling orthogonal to the elongated direction of the BEC was spatially dithered by modulating the frequency of an acoustic-optic modulator at a few hundred kHz. This created an anharmonic, time-averaged potential. To reach the extremely cold temperatures necessary to realize long-lived solitons, we evaporated to the lowest dipole trap depth in which our technical stability allowed us to realize uniform BECs.

Temperature Measurement. We measured temperature below the majority atom's condensation temperature $T_c = 350$ nK by removing the majority atoms and fitting the TOF expanded impurity atoms to a Maxwell-Boltzmann (MB) distribution (13). Once the temperature was below T_c for the impurity atoms, MB fits systematically underestimated the temperature. Fitting the small number of impurity atoms to a Bose distribution was technically challenging due to low signal-to-noise ratio and the addition of another free parameter, the chemical potential. To limit the number of free parameters, we performed a global fit on the different impurity fractions, where we constrained the chemical potential μ to be negative. This provided an estimate of the temperature with large uncertainties. We found for our usual operating parameters, and, based on information from both temperature measurements, $T = 10(5)$ nK.

Impurity Characterization. We used a Blackman enveloped rf pulse at a ~ 9 G magnetic field to transfer the $|F = 1, m_F = 0\rangle$ atoms primarily to the $|F = 1, m_F = +1\rangle$ internal state (25). We varied the impurity fraction by tuning the rf amplitude. Even though the fraction of impurity atoms before evaporation determined the fraction after evaporation, they were not equal due to more effective evaporation of the minority spin state (13). We characterized the impurity fraction through careful, calibrated absorption imaging with a Stern-Gerlach technique during TOF to measure the relative fraction of the impurity atoms after evaporation.

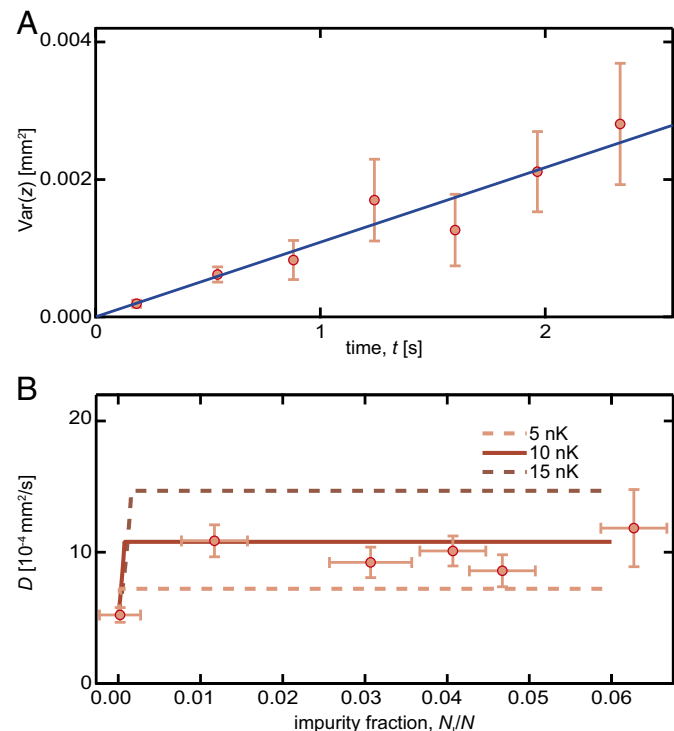


Fig. 4. Brownian diffusion constant dependence on impurities. (A) An example for the linear fit of $\text{Var}(z)$ vs. t for 1.2% impurities. Data are binned into 0.36-s bins; the uncertainties are the sample SD. (B) The diffusion coefficient D vs. impurity fraction N_i/N . The experimental results (markers) are extracted from the slope of a linear fit of the sample variance $\text{Var}(z)$ vs. time t . The uncertainty in D is the uncertainty from that fit. See Materials and Methods for an explanation of uncertainty in N_i/N . The theory curves (solid and dashed curves) plot the calculated D for our measured temperature.

Soliton Creation. We applied a phase shift to half of a condensate by imaging a back-lit, carefully focused razor edge with light red detuned by ≈ 6.8 GHz from the D₂ transition for 20 μ s.

Scattering Theory of Impurities. Minimizing Eq. 4 with respect to φ^* , ψ^* gives the coupled equations of motion

$$i\hbar\partial_t\varphi(z, t) = -\frac{\hbar^2}{2m_{\text{Rb}}}\partial_z^2\varphi(z, t) + g|\varphi|^2\varphi + \frac{g'}{2}|\psi|^2\varphi, \quad [8]$$

$$i\hbar\partial_t\psi(z, t) = -\frac{\hbar^2}{2m_{\text{Rb}}}\partial_z^2\psi(z, t) + \frac{g'}{2}|\varphi|^2\psi. \quad [9]$$

In the experiment, we observed that the soliton remained stable for long times in the presence of impurities. Therefore, we neglect the last term of Eq. 8, giving the well-known solitonic solution in Eq. 1. We seek a solution for the impurity wavefunction $\psi(z)$ in the soliton rest frame. In the radial direction, the single-particle wave functions are the usual Bessel functions for a particle in a cylindrical well. For $\psi(z)$, we combine Eqs. 1 and 9 with $\psi(z, t) = e^{-iE_z t/\hbar} e^{im_{\text{Rb}} v_s z'/\hbar} \psi(z')$. This gives a Schrödinger equation with a Pöschl-Teller potential (18, 20),

$$\frac{\partial^2\psi(z')}{\partial z'^2} + \left[\frac{\gamma_s^2\lambda(\lambda-1)}{\cosh^2(\gamma_s z')} + k_z^2 \right] \psi(z') = 0. \quad [10]$$

The dimensionless parameters are $z' = (z - v_s t)/\sqrt{2}\xi$, $k_z^2 = 4m_{\text{Rb}}\xi^2/\hbar^2(E_z + m_{\text{Rb}}v_s^2/2 - g'\rho_0/2)$, $\lambda(\lambda-1) = 2m_{\text{Rb}}\xi^2g'\rho_0/\hbar^2 = g'/g$, and $\gamma_s = \sqrt{1 - (v_s/c)^2}$. g and g' are the effective 1D interaction parameters after integrating over the transverse degrees of freedom in ψ and φ . Because the transverse wave functions are different, in general, $g'/g \lesssim 1$. However, $R(k_z)$ is periodic in g'/g (through λ), and small variations in this parameter do not strongly affect the result. Solving for $\psi(z')$ and the scattering matrix then gives $R(k_z)$ Eq. 5. For $\lambda \approx 1.5$, this potential also has a single, shallow bound state. Occupation of the bound state by an impurity atom can only occur through three body collisions (two impurity atoms and soliton), scenarios that we did not consider here.

Kinetic Theory of the Soliton. To define a diffusion coefficient, we studied the distribution function of many solitons, $f(t, z(t), v_s(t))$ (corresponding to many experimental runs). The distribution function of solitons follows a Boltzmann equation with a collision integral in Fokker-Planck form

$$\frac{df}{dt} = \frac{\partial}{\partial p} \left(Af + B \frac{\partial f}{\partial p} \right), \quad [11]$$

where A and B are the drift and diffusion transport coefficients, and the left-hand side is a total time derivative. For $v_s \ll c$, we can write $A \approx \gamma v_s$ and $B \approx \gamma k_B T$, where v_s is the soliton velocity and γ is the friction coefficient given in Eq. 7. Finally, we write the soliton momentum as $p = -|m_s|v_s$ (23). The kinetic equation then takes the form

$$\frac{\partial f}{\partial t} + v_s \frac{\partial f}{\partial z} = \frac{\partial}{\partial v_s} \left(-\Gamma v_s f - \frac{\partial_z V}{|m_s|} f + \Gamma v_{\text{th}}^2 \frac{\partial f}{\partial v_s} \right), \quad [12]$$

where $\Gamma = \gamma/|m_s|$ and $v_{\text{th}}^2 = k_B T/|m_s|$ is the thermal velocity. This equation can be solved analytically by using the method of characteristics in the case of a harmonic potential $V(z) = -|m_s|\omega^2 z^2/2$. The solution is the time-dependent distribution function $f(t, z, v_s)$, parametrized by functions

- Strecker KE, Partridge GB, Truscott AG, Hulet RG (2002) Formation and propagation of matter-wave soliton trains. *Nature* 417(6885):150–153.
- Khaykovich L, et al. (2002) Formation of a matter-wave bright soliton. *Science* 296(5571):1290–1293.
- Burger S, Bongs K, Dettmer S, Ertmer W, Sengstock K (1999) Dark solitons in Bose-Einstein condensates. *Phys Rev Lett* 83(25):5198–5201.
- Denschlag J, et al. (2000) Generating solitons by phase engineering of a Bose-Einstein condensate. *Science* 287(5450):97–101.
- Ku MJH, et al. (2014) Motion of a solitonic vortex in the BEC-BCS crossover. *Phys Rev Lett* 113(6):065301.
- Muryshev A, Shlyapnikov GV, Ertmer W, Sengstock K, Lewenstein M (2002) Dynamics of dark solitons in elongated Bose-Einstein condensates. *Phys Rev Lett* 89(11):110401.
- Becker C, et al. (2008) Oscillations and interactions of dark and dark-bright solitons in Bose-Einstein condensates. *Nat Phys* 4(6):496–501.
- Weller A, et al. (2008) Experimental observation of oscillating and interacting matter wave dark solitons. *Phys Rev Lett* 101(13):130401.
- Hasegawa A, Matsumoto M (2003) Optical Solitons in Fibers, eds Kamiya T, Venghaus H, Monemar B, Yamamoto Y (Springer, Heidelberg), 3rd Ed, Vol 2, p 205.
- Anderson BP, et al. (2001) Watching dark solitons decay into vortex rings in a Bose-Einstein condensate. *Phys Rev Lett* 86(14):2926–2929.
- Lin Y-J, Perry AR, Compton RL, Spielman IB, Porto JV (2009) Rapid production of ⁸⁷Rb Bose-Einstein condensates in a combined magnetic and optical potential. *Phys Rev A* 79(6):063631.
- Fang F, Olf R, Wu S, Kadau H, Stamper-Kurn DM (2016) Condensing magnons in a degenerate ferromagnetic spinor Bose gas. *Phys Rev Lett* 116:095301.
- Olf R, Fang F, Marti GE, MacRae A, Stamper-Kurn DM (2015) Thermometry and cooling of a Bose-Einstein condensate to 0.02 times the critical temperature. *Nat Phys* 11:06196.

$g_i(t, \omega)$, with Gaussian form

$$f(t, z, v_s) = \frac{1}{2\pi\sqrt{4g_1g_3 - g_2^2}} \exp \left\{ -\frac{1}{4g_1g_3 - g_2^2} \left[g_1v_s^2 + g_3z^2 + g_2v_s z + v_i v_s (g_2g_4 + 2g_1g_5) + v_i z (g_2g_5 + 2g_3g_4) + v_i^2 (g_3g_4^2 + g_1g_5^2 + g_2g_4g_5) \right] \right\}. \quad [13]$$

where v_i is the soliton initial velocity and functions $g_i(t, \omega)$ are given by

$$g_1(t, \omega) = \frac{1 + 4\omega^2(e^t - 1) - e^t [\cos(t\bar{\omega}) + \bar{\omega} \sin(t\bar{\omega})]}{2\omega^2\bar{\omega}^2} \quad [14]$$

$$g_2(t, \omega) = -\frac{2e^t}{\bar{\omega}^2} [1 - \cos(t\bar{\omega})] \quad [15]$$

$$g_3(t, \omega) = \frac{1 + 4\omega^2(e^t - 1) + e^t [\bar{\omega} \sin(t\bar{\omega}) - \cos(t\bar{\omega})]}{2\omega^2\bar{\omega}^2} \quad [16]$$

$$g_4(t, \omega) = -\frac{2e^{t/2}\bar{\omega}^2}{\bar{\omega}} \sin\left(\frac{t\bar{\omega}}{2}\right) \quad [17]$$

$$g_5(t, \omega) = -\frac{e^{t/2}}{\bar{\omega}} \left[\sin\left(\frac{t\bar{\omega}}{2}\right) + \bar{\omega} \cos\left(\frac{t\bar{\omega}}{2}\right) \right], \quad [18]$$

where we work in dimensionless units $t \rightarrow t/\Gamma$, $\omega \rightarrow \omega\Gamma$, $v_s \rightarrow v_{\text{th}}v_s$, $z \rightarrow v_{\text{th}}z/\Gamma$, and $\bar{\omega} = \sqrt{4\omega^2 - 1}$. Eq. 12 does not have a stable solution where $\partial f/\partial t \rightarrow 0$, due to the fact that the soliton is inherently unstable. The solution given in Eq. 13 is valid for $v_s \ll c$. Finally, we calculate the variance in soliton position, $\text{Var}(z)(t) = \int dv_s \int dz z^2 f(t, z, v_s) = 2g_1 + v_i^2 g_4^2$, finding the exact expression (with restored units)

$$\text{Var}(z)(t) = \frac{4v_i^2(e^{\Gamma t} - 1)}{4\omega^2 - \Gamma^2} + \frac{4v_i^2 e^{\Gamma t}}{4\omega^2 - \Gamma^2} \sin^2\left(\frac{t\bar{\omega}}{2}\right) + \frac{v_{\text{th}}^2 \Gamma^2 e^{\Gamma t}}{\omega^2(4\omega^2 - \Gamma^2)} \left[1 - e^{\Gamma t} \left(\cos(t\bar{\omega}) + \frac{\bar{\omega}}{\Gamma} \sin(t\bar{\omega}) \right) \right] \quad [19]$$

where $\bar{\omega} = \sqrt{4\omega^2 - \Gamma^2}$. In the limits $\Gamma t \ll 1$, $\Gamma \ll \omega$, we find diffusive behavior $\text{Var}(z) \approx D(t)t$, with the time-dependent diffusion coefficient

$$D(t) \approx \frac{v_{\text{th}}^2 \Gamma}{\omega^2} + \frac{v_i^2 \Gamma}{\omega^2} \sin^2\left(\frac{t\bar{\omega}}{2}\right). \quad [20]$$

Setting $\sin^2(t\bar{\omega}/2) \approx 1/2$, we find the diffusion coefficient D presented in Eq. 6. We note that in the limit $\Gamma t \ll 1$, $\omega \rightarrow 0$, we have $\text{Var}(z) \propto \Gamma t^3$ —the variance has no linear in t dependence, and the soliton undergoes ballistic motion, followed by exponential increase of $\text{Var}(z)$ and soliton death[§].

ACKNOWLEDGMENTS. We thank Martin Link and Stephen Eckel for carefully reading our manuscript; and Joachim Brand for greatly beneficial conversations. This work was partially supported by the Army Research Office's Atomtronics Multidisciplinary University Research Initiative, by the Air Force Office of Scientific Research's Quantum Matter Multidisciplinary University Research Initiative, National Institute of Standards and Technology, and the National Science Foundation through the Physics Frontier Center at the Joint Quantum Institute. H.M.H. received additional fellowship support from the National Physical Science Consortium and National Security Agency. V.M.G. was supported by the Simons Foundation.

[§]Our trap was not strictly harmonic; however, the restoring force emerges for any trap with nonzero slope $\partial_z V \neq 0$, making our results qualitatively applicable to our experimental set.

14. Mateo AM, Brand J (2015) Stability and dispersion relations of three-dimensional solitary waves in trapped Bose-Einstein condensates. *New J Phys* 17(12):125013.
15. Zaremba E (1998) Sound propagation in a cylindrical Bose-condensed gas. *Phys Rev A* 57(1):518–521.
16. Parker NG, Proukakis NP, Adams CS (2010) Dark soliton decay due to trap anharmonicity in atomic Bose-Einstein condensates. *Phys Rev A* 81(3):033606.
17. Cockburn SP, et al. (2011) Fluctuating and dissipative dynamics of dark solitons in quasicondensates. *Phys Rev A* 84(4):43640.
18. Pöschl G, Teller E (1933) Bemerkungen zur Quantenmechanik des anharmonischen Oszillators. *Z Phys* 83(3):143–151.
19. Cooper F, Khare A, Sukhatme U (1995) Supersymmetry and quantum mechanics. *Phys Rep* 251(5-6):267–385.
20. Cevik D, Gadella M, Kuru S, Negro J (2016) Resonances and antibound states of Pöschl-Teller potential: Ladder operators and SUSY partners. *Phys Lett A* 380(18-19):1600–1609.
21. Lifschitz E, Pitaevskii L (1981) *Physical Kinetics* (Butterworth-Heinemann, Oxford).
22. Konotop VV, Pitaevskii L (2004) Landau dynamics of a grey soliton in a trapped condensate. *Phys Rev Lett* 93(24):240403.
23. Fedichev PO, Muryshev AE, Shlyapnikov GV (1999) Dissipative dynamics of a kink state in a Bose-condensed gas. *Phys Rev A* 60(4):3220–3224.
24. Efimkin DK, Hofmann J, Galitski V (2016) Non-Markovian quantum friction of bright solitons in superfluids. *Phys Rev Lett* 116:225301.
25. Jiménez-García K, et al. (2010) Phases of a two-dimensional bose gas in an optical lattice. *Phys Rev Lett* 105(11):110401.

Appendix B: Geometrical pumping with a Bose–Einstein condensate

Geometrical Pumping with a Bose-Einstein Condensate

H.-I Lu,¹ M. Schemmer,^{1,2} L. M. Aycock,^{1,3} D. Genkina,¹ S. Sugawa,¹ and I. B. Spielman^{1,*}

¹*Joint Quantum Institute, National Institute of Standards and Technology,
and University of Maryland, Gaithersburg, Maryland 20899, USA*

²*École Normale Supérieure de Lyon, F-69364 Lyon, France*

³*Cornell University, Ithaca, New York 14850, USA*

(Received 17 August 2015; revised manuscript received 21 April 2016; published 20 May 2016)

We realized a quantum geometric “charge” pump for a Bose-Einstein condensate (BEC) in the lowest Bloch band of a novel bipartite magnetic lattice. Topological charge pumps in filled bands yield quantized pumping set by the global—topological—properties of the bands. In contrast, our geometric charge pump for a BEC occupying just a single crystal momentum state exhibits nonquantized charge pumping set by local—geometrical—properties of the band structure. Like topological charge pumps, for each pump cycle we observed an overall displacement (here, not quantized) and a temporal modulation of the atomic wave packet’s position in each unit cell, i.e., the polarization.

DOI: 10.1103/PhysRevLett.116.200402

Ultracold atoms in optical lattices provide a unique setting for experimentally studying concepts that lie at the heart of theoretical condensed matter physics, but are out of reach of current condensed matter experiments. Here, we focus on the connection between topology, geometry, and adiabatic charge pumping [1–7] for Bose-Einstein condensates (BECs) in cyclically driven lattice potentials.

Particles in periodic potentials form Bloch bands with energy $\epsilon_n(q)$ and eigenstates $|\Psi_n(q)\rangle = \exp(iq\hat{x})|u_n(q)\rangle$ labeled by the crystal momentum q along with the band index n . The states $|u_n\rangle$ retain the underlying periodicity of the lattice, set by the unit cell size a . Motion in lattices is conventionally understood in terms of these bands: metals are materials with partially filled bands, while insulators have completely filled bands. In this context, a topological charge pump is a counterintuitive device, where charge motion—conduction—accompanies the adiabatic and cyclic drive of an insulating lattice’s parameters. Thouless showed that this conduction is quantized, completely governed by the band topology [8,9]. Although various charge pumps have been realized in condensed matter devices—such as modulated quantum dots [10–12], one-dimensional (1D) channels driven by surface acoustic waves [13], and superconducting qubits [14]—Thouless pumps remain unrealized in condensed matter settings but have been demonstrated in recent experiments with cold-atom insulators [15,16].

Here, we break from this established paradigm for insulators and create a quantum charge pump for a BEC in a 1D lattice [17–19] occupying a single crystal momentum state q . This charge pump gives nonquantized motion sensitive to the Berry curvature at q integrated over the whole pump cycle, a local geometric quantity, rather than a global topological quantity. Berry curvatures play an important role in condensed matter systems. An iconic

example is the integer quantum Hall effect, where the electrons acquire an anomalous transverse velocity proportional to the Berry curvature and the quantized Hall conductance is given by the Berry curvature integrated over the whole two-dimensional (2D) Brillouin zone (BZ) [20]; recent cold-atom experiments in 2D have measured such curvatures integrated over part [21,22] or all [23] of the BZ. In an analogous way, 1D lattice systems, driven cyclically in time t , have a generalized Berry curvature defined on the 2D effective BZ in q, t space. This curvature is the source of an anomalous velocity [24], utilized to drive an adiabatic quantum pumping process.

The Rice-Mele model [25–28] of a bipartite lattice with a unit cell consisting of A and B sites is the paradigmatic system for understanding quantum pumps. The Hamiltonian for this tight-binding model is

$$\begin{aligned} \hat{H}_{\text{RM}} = & - \sum_j [(t + \delta t) \hat{b}_j^\dagger \hat{a}_j + (t - \delta t) \hat{a}_{j+1}^\dagger \hat{b}_j + \text{H.c.}] \\ & + \Delta \sum_j (\hat{a}_j^\dagger \hat{a}_j - \hat{b}_j^\dagger \hat{b}_j), \end{aligned} \quad (1)$$

where \hat{a}_j^\dagger and \hat{b}_j^\dagger describe the creation of a particle in unit cell j and sublattice site A or B , respectively. The nominal tunneling strength t is staggered by δt , and the sublattice sites are shifted in energy by Δ .

We investigated quantum pumping in a novel 1D (along e_x) bipartite magnetic lattice (building on Refs. [29,30]) that in effect allowed independent control of t , δt , and Δ . As shown in Figs. 1(a) and 1(b), our magnetic lattice for ^{87}Rb arose from the interplay of one rf and two Raman fields that coupled the $|f = 1; m_F = \pm 1, 0\rangle$ “spin” states comprising the $f = 1$ ground state hyperfine manifold, which were Zeeman split by $\hbar\omega_Z$. The natural units of momentum and energy are given by the single photon recoil momentum

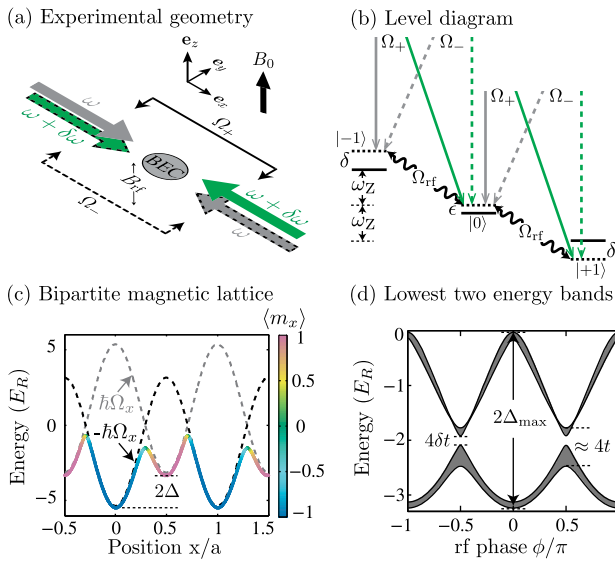


FIG. 1. Bipartite magnetic lattice. [(a) and (b)] Dipole trapped ^{87}Rb BECs subject to a bias magnetic field $B_0\mathbf{e}_z$ had a Zeeman splitting $\omega_Z/2\pi = 0.817$ MHz and a quadratic shift $\hbar\epsilon = 0.03E_R$. These BECs were illuminated by four Raman beams and an rf magnetic field. Each of the two Raman couplings (strengths Ω_{\pm}) was derived from two cross-polarized Raman laser beams with frequency components ω and $\omega + \delta\omega$. (c) Adiabatic potentials colored according to $\langle m_x \rangle$ computed for $\hbar(\bar{\Omega}, \Omega_{\text{rf}}, \delta) = (6, 2.2, 0)E_R$, $\delta\Omega/\bar{\Omega} = -0.1$, and $\phi = \pi/4$. The dashed curves plot the $\pm\hbar\Omega_x$ contributions to the potential experienced by states $|m_x = \pm 1\rangle$. (d) Lowest two energy band energies plotted as a function of ϕ , otherwise with the same parameters as (c).

$\hbar k_R = 2\pi\hbar/\lambda_R$ and its corresponding energy $E_R = \hbar^2 k_R^2/2m$, where m is the atomic mass. In the frame rotating at the rf frequency $\delta\omega$ and under the rotating wave approximation, the combined rf-Raman coupling lead [31] to the overall Hamiltonian

$$\hat{H} = \frac{\hbar^2 \hat{k}_x^2}{2m} + \Omega(\hat{x}) \cdot \hat{\mathbf{F}} + \hat{H}_Q, \quad (2)$$

where $\hat{\mathbf{F}}$ is the total angular momentum vector operator. We interpret $\Omega(\hat{x}) = [\Omega_{\text{rf}} \cos(\phi) + \bar{\Omega} \cos(2k_R\hat{x}), -\Omega_{\text{rf}} \sin(\phi) - \delta\Omega \sin(2k_R\hat{x}), \sqrt{2}\delta]/\sqrt{2}$ as a spatially periodic effective Zeeman magnetic field, in which Ω_{rf} is the rf coupling strength; $\bar{\Omega} = \Omega_+ + \Omega_-$ and $\delta\Omega = \Omega_+ - \Omega_-$ are derived from the individual Raman coupling strengths Ω_{\pm} ; $\delta = \delta\omega - \omega_Z$ is the detuning from Raman-rf resonance; and ϕ is the relative phase between the rf and Raman fields. Additionally, $H_Q = -\epsilon(\hbar^2 \hat{\mathbb{I}} - \hat{F}_z^2)/\hbar$ describes the quadratic Zeeman shift, where $\hat{\mathbb{I}}$ is the identity operator.

This spatially varying effective magnetic field produces a 1D bipartite lattice [2,32] with lattice constant $a = \lambda_R/2$ and with adiabatic (Born-Oppenheimer) potentials depicted in Fig. 1(c). This magnetic lattice is most easily conceptualized for small $\delta\Omega$: the $\bar{\Omega} \cos(2k_R\hat{x})$ term provides

periodic potentials for the $|m_x = \pm 1\rangle$ states spatially displaced from each other by $a/2$ [dashed curves in Fig. 1(c)]; the resulting $m_x = \pm 1$ sites are then staggered in energy, giving $\Delta \approx \Delta_{\text{max}} \cos(\phi)$, with $\Delta_{\text{max}} = \Omega_{\text{rf}}/\sqrt{2}$. The Ω_y term couples these sublattices together: the rf term $-\Omega_{\text{rf}} \sin(\phi)$ generates constant height barriers (largely specifying t), which become staggered by the $-\delta\Omega \sin(2k_R\hat{x})$ contribution (largely specifying δt).

Figure 1(d) plots the energies of the resulting lowest two bands as a function of ϕ (modulating Δ cosinusoidally). Although our lattice is not in the tight-binding limit, the band structure qualitatively matches that of the Rice-Mele model. In the remainder of this Letter, we focus on the lowest band $n = 0$ and henceforth omit the band index.

As illustrated by the shading in Fig. 1(c), in each unit cell the sublattice sites are labeled by their \hat{F}_x spin projection with the $|m_x = -1\rangle$ site on the left and $|m_x = +1\rangle$ site on the right. To confirm this, we adiabatically loaded $|m_z = -1\rangle$ BECs into the lattice's ground state by simultaneously ramping the detuning from $5E_R$ to 0 while ramping on the coupling fields in 10 ms. Following preparation, our measurement sequence began with a $\pi/2$ spin rotation along \mathbf{e}_y , allowing us to measure the eigenstates of \hat{F}_x in our \hat{F}_z measurement basis. We achieved this $\pi/2$ rotation (rot) with a $44\ \mu\text{s}$ pulse from an additional rf field with phase $\phi_{\text{rot}} = \pi/2$ and strength $\hbar\Omega_{\text{rf,rot}} = 2.2E_R$, applied while the Raman coupling was greatly reduced ($\bar{\Omega} \ll \Omega_{\text{rf,rot}}$) and the lattice rf coupling was off ($\Omega_{\text{rf}} = 0$). We then abruptly removed the remaining control fields along with the confining potential and absorption imaged the resulting spin-resolved momentum distribution after a 20 ms time-of-flight period in the presence of a magnetic field gradient along \mathbf{e}_y .

Figure 2 shows the measured \hat{F}_x spin composition [33] and magnetization for adiabatically loaded BECs as a function of ϕ with $\delta\Omega = 0$. Because $\Delta(\phi)$ controls the relative depth of the $|m_x = \pm 1\rangle$ wells, we observe ground state spin populations that follow this "tilt." For example, when $\phi = 0$ or π the double well is strongly tilted and we observe the near perfect spin magnetization, consistent with atoms residing in the individual sublattices; in contrast, when $\phi = \pi/2$, the double wells are balanced and we observe equal populations in each $|m_x\rangle$ state as expected for equal occupancy of both sublattices. Thus, the magnetization [Fig. 2(b)] measures the mean atomic position within each unit cell, i.e., the polarization.

Having constructed a physical realization of the Rice-Mele model, and demonstrated the requisite control and measurement tools, we now turn our attention to topological and geometrical charge pumping. These fundamentally quantum mechanical effects rely on the canonical commutation relation between position and momentum. Consider a finite wave packet with a center of mass (c.m.) position $\langle x \rangle = \langle \Psi | \hat{x} | \Psi \rangle$, subject to a lattice Hamiltonian \hat{H} that is

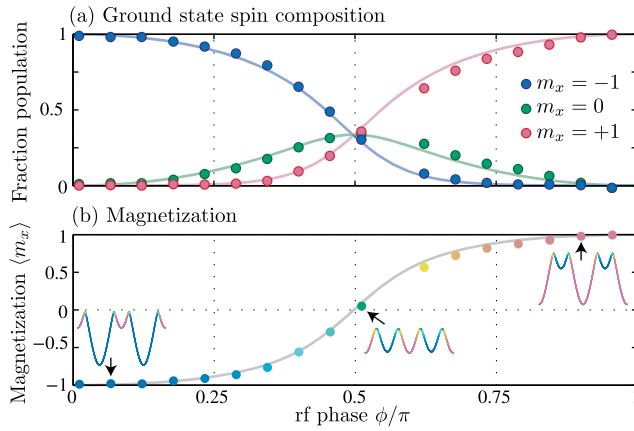


FIG. 2. Ground state spin projections. (a) Ground state spin projections at various ϕ along with the predicted populations for $\hbar(\bar{\Omega}, \delta\Omega, \Omega_{\text{rf}}, \delta) = (4.4, 0, 2.2, 0)E_R$. The associated adiabatic potentials [insets in (b)] have minima with spin projection following the observed population's trends. (b) Magnetization derived from data in (a).

adiabatically modulated with period T , i.e., $\hat{H}(t) = \hat{H}(t+T)$. After one cycle, any initial crystal momentum state is transformed, $|\Psi(q)\rangle \rightarrow \exp[i\gamma(\hat{q})]|\Psi(q)\rangle$, at most acquiring a phase, where \hat{q} is the crystal momentum operator; this defines the single-period evolution operator $\hat{U}_T = \exp[i\gamma(\hat{q})]$. The time-evolved position operator $\hat{U}_T^\dagger \hat{x} \hat{U}_T = \hat{x} - \partial_q \gamma(\hat{q})$ is displaced after a single pump cycle.

The displacement is particularly simple in two limits: when just a single crystal momentum state is occupied or when every crystal momentum state in the BZ, $-\pi/a \leq q < \pi/a$, is occupied with equal probability. As for our BEC, when a single $|q_0\rangle$ state is occupied the displacement is $\Delta x(q_0) = -\partial_q \gamma(q)|_{q_0}$. Both the dynamical (D) phase $\gamma_D(q) = -\bar{e}(q)T/\hbar$ from the time-average energy $\bar{e}(q)$ and the geometric Berry (B) phase $\gamma_B(q) = i \int_0^T \langle u | \partial_t u \rangle dt$ contribute to $\gamma(q) = \gamma_D(q) + \gamma_B(q)$. In agreement with conventional descriptions [18,24,27], this predicts a mean velocity $\bar{v}(q) = \partial_q \bar{e}(q)/\hbar - T^{-1} \int_0^T F(q, t) dt$. The first term is the usual group velocity and the second term—the anomalous velocity—derives from the Berry curvature $F(q, t) = i(\langle \partial_q u | \partial_t u \rangle - \langle \partial_t u | \partial_q u \rangle)$. In our experiment, the BEC occupied the minimum of $e(q, t)$ at $q = 0$ during the whole pump cycle giving $\partial_q \bar{e}(q) = 0$, so only the geometric phase $\gamma_B(q)$ contributed to the per-cycle displacement $\Delta x(q = 0) = -\int_0^T F(q = 0, t) dt$.

In the contrasting case of a filled band, the average group velocity is also 0 and the displacement is $\Delta x = -a \int_{\text{BZ}} \partial_q \gamma_B(q) dq / 2\pi$; this is often expressed as $\Delta x = a \int_0^T \partial_t \gamma_{\text{Zak}}(t) dt / 2\pi$. The Zak phase $\gamma_{\text{Zak}} = i \int_{\text{BZ}} \langle u | \partial_q u \rangle dq$, a topological property of 1D bands, is the Berry's phase associated with traversing the 1D BZ once, in the same way that $\gamma_B(q)$ is a Berry's phase taken over a pump cycle.

Our lattice's Zak phase is plotted in Fig. 3(a); this Zak phase is qualitatively indistinguishable from that of the Rice-Mele model, with singularities at $\phi = \pm\pi/2$ and $\delta\Omega = 0$, signaling topological phase transitions across these points. For filled band experiments, pumping trajectories encircling these points give quantized charge pumping [15,16]. Figure 3(b) shows the richly structured Berry curvature $F(q = 0, \phi)$ relevant to our experiment, which is explored next.

For our charge pump experiments, we linearly ramped the pump control parameter $\phi(t) = 2\pi t/T$, effectively modulating the lattice potential in two qualitatively different regimes (separated by a critical $|\delta\Omega/\bar{\Omega}| \approx 0.63$). In the first [Fig. 3(c), left panel] the sublattice sites rise and fall but the local potential minima are essentially fixed in space; in the second [Fig. 3(c), right panel] each minimum is only present for part of the pump cycle (the potential appears to “slide” by $\pm a$ per cycle). As these schematics imply, the associated pumping process gives either no displacement or a quantized per-cycle displacement $\pm a$ for classical trajectories [34]. In quantum systems, however, geometrical

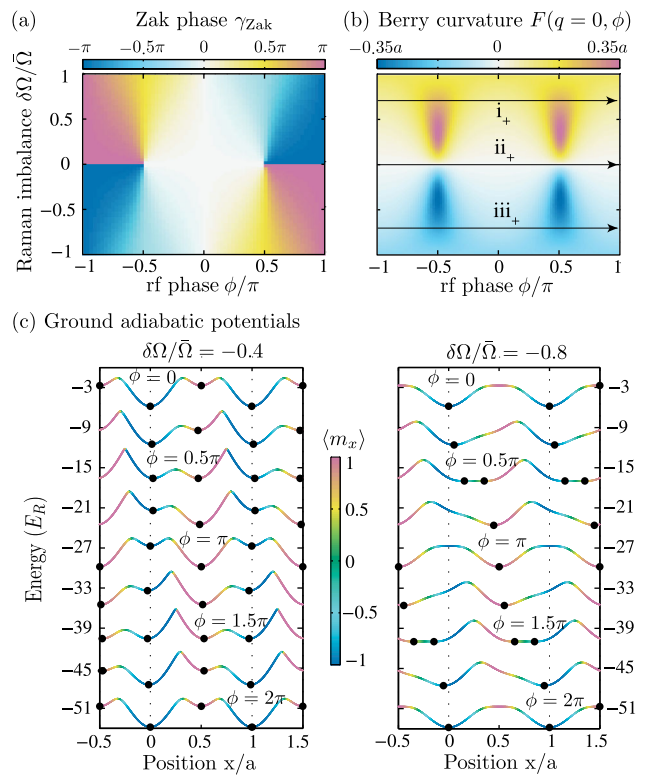


FIG. 3. Band geometry and topology computed for $\hbar(\bar{\Omega}, \Omega_{\text{rf}}, \delta) = (6, 2.2, 0)E_R$. [(a) and (b)] Zak phase and $q = 0$ Berry curvature showing the dependence on both $\delta\Omega/\bar{\Omega}$ and ϕ . In (b), the arrows show experimental charge pump trajectories in Fig. 4(b). (c) Adiabatic potentials (displaced vertically for clarity) computed for a range of ϕ constituting a complete pump cycle at $\delta\Omega/\bar{\Omega} = -0.4$ (left panel) and -0.8 (right panel). Filled circles mark the local energy minima.

pumping is controlled by the Berry curvature, giving nonquantized per-cycle displacements that can, in principle, take on any value.

We studied adiabatic charge pumping in this lattice in two ways: in the first we observed the \hat{F}_x magnetization, giving the polarization within the unit cells, and in the second we directly measured the displacement Δx of our BEC. In both cases we loaded into the lattice's ground state and linearly ramped $\phi = 2\pi t/T$, driving the Hamiltonian with period T [34]. As shown in Fig. 4(a), the magnetization oscillated with the $T = 2$ ms period, demonstrating the periodic modulation of polarization per cycle. In good agreement with our data, the solid curves in Fig. 4(a) show the predicted behavior given our known system parameters. This agreement persists to long times: for example, after 50 pumping cycles (for $t = 100$ ms to 110 ms) the contrast is unchanged, confirming the adiabaticity of the process [34].

Lastly, we performed a charge pumping experiment by directly measuring the cloud's position *in situ* for a range of $\delta\Omega/\bar{\Omega}$. We obtained *in situ* density distributions using partial-transfer absorption imaging [35] in which ≈ 6.8 GHz microwave pulses transferred $\approx 5\%$ of the atoms from $|f, m_z\rangle = |1, -1\rangle$ to $|2, 0\rangle$ where they were absorption imaged. This technique allowed us to repeatedly measure the *in situ* density distribution for each BEC. Each observed displacement was derived from differential measurements of the cloud position taken just before and just after the pumping process, rendering our observations insensitive to micron-level drift in the trap position between different realizations.

Figure 4(b) shows data taken for $\delta\Omega/\bar{\Omega} = 0.7, 0$, and -0.7 along trajectories i, ii, and iii, respectively, with both increasing and decreasing phases. Our data display two expected symmetry properties. First, since the displacement $\Delta x(q = 0) = - \int F(q, \phi) d\phi$ depends on the sign of the acquired phase, the direction of motion is reversed when the ramp direction is inverted. Second, as shown in Fig. 3(b),

$F(q = 0, \phi)$ is an odd function of $\delta\Omega/\bar{\Omega}$, so the direction of motion is also reversed when $\delta\Omega/\bar{\Omega} \rightarrow -\delta\Omega/\bar{\Omega}$. Thus, Δx is an odd function of both ϕ and $\delta\Omega/\bar{\Omega}$, and as expected we observe no motion when $\delta\Omega/\bar{\Omega} = 0$.

The displacement was markedly nonlinear when the pumping time became comparable to our trap's 80 ms period, showing the influence of the confining potential [36]. We included the harmonic potential in our real-space simulations by directly solving the time-dependent Schrödinger equation for our system [37]. The simulated results [Fig. 4(b), solid curves] agree with our observations. To extract the per-cycle displacement due to geometric pumping, we fit the sinusoidal predictions of our model to each data trace, with only the overall amplitudes and a small vertical offset as free parameters, giving the short-time per-cycle displacement [34]. Figure 4(c) shows these per-cycle displacements for a range of Raman imbalances.

The *in situ* cloud typically had a Thomas-Fermi radius of $30 \mu\text{m}$, corresponding to a small momentum width of $0.004k_R$ for our BEC. We estimated the thermal fraction to be $\approx 5\%$ given by our ≈ 20 nK temperature (momentum width of $0.24k_R$). Moreover, the per-cycle displacement is nearly independent of q for $|q| < 0.25k_R$ [34]. These allow us to compare the data with the expected displacement from integrating $q = 0$ Berry curvature [Fig. 4(c), solid line], showing an excellent agreement and confirming the geometric origin of our quantum charge pump.

Our magnetic lattice enables new experiments with 1D topological lattices. Berry curvatures at $q \neq 0$ can be probed by performing the charge pump pairwise at $\pm|q|$ (for example, prepared via Bloch oscillations [38]). The dynamical phases in these cases are opposite and therefore cancel while Berry curvatures (even in q) contribute equally to the displacements [34]. Furthermore, protected edge states, a hallmark of topological systems, are present at the interface between regions characterized by different

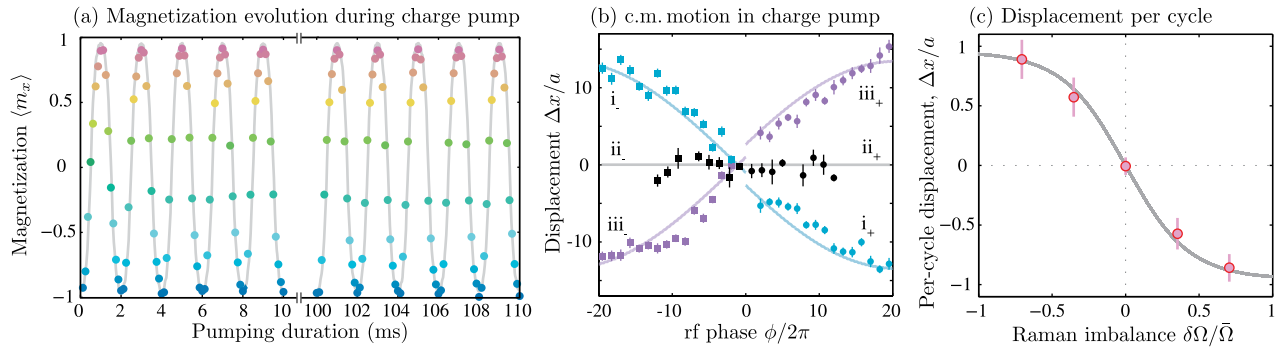


FIG. 4. Geometric charge pumping. (a) Magnetization measured while linearly ramping ϕ with period $T = 2$ ms, along with the prediction for $\hbar\bar{\Omega} = 6.38(2)E_R$, $\hbar\delta\Omega = 4.50(2)E_R$, and $\hbar\Omega_{\text{rf}} = 2.20(3)E_R$. (b) Displacement plotted versus $\phi/2\pi$ (number of pump cycles). Trajectories i–iii are taken at $\delta\Omega/\bar{\Omega} = 0.7, 0$, and -0.7 , respectively; in each case $\hbar\bar{\Omega} \approx 6E_R$ and $\hbar\Omega_{\text{rf}} = 2.20(3)E_R$. Solid curves: simulation of a charge pump in the trap. The small displacement near $\phi = 0$ is introduced by our loading procedure. (c) Measured displacement Δx per pump cycle (symbols), along with the prediction obtained by integrating the Berry curvature over our pumping trajectory (solid curve). The uncertainty bars represent the 95% confidence interval.

topological invariants [39–41]. Since in our lattice the topological index is set by the rf phase, a bulk topological junction can be generated by replacing the rf field with an additional copropagating pair of Raman laser beams in which just one beam has an abrupt π phase shift in its center. This provides a static model of the soliton excitation mode in polyacetylene [25,42]. Terminating our lattice with hard-wall boundaries gives rise to similar end states—somewhat analogous to Majorana fermions in 1D topological superconductors [40,43]—with a spin character.

We appreciate the constructive discussions with W. D. Phillips, E. Mueller, L. J. LeBlanc, and L. Wang. This work was partially supported by the ARO’s Atomtronics MURI, and by the AFOSR’s Quantum Matter MURI, NIST, and the NSF through the PFC at the JQI. M. S. was supported by Ampère Scholarships of Excellence of the École Normale Supérieure (ENS) de Lyon. S. S. acknowledges support from JSPS Postdoctoral Fellowship for research abroad.

^{*}ian.spielman@nist.gov

- [1] F. Mei, J.-B. You, D.-W. Zhang, X. C. Yang, R. Fazio, S.-L. Zhu, and L. C. Kwek, *Phys. Rev. A* **90**, 063638 (2014).
- [2] D.-W. Zhang, F. Mei, Z.-Y. Xue, S.-L. Zhu, and Z. D. Wang, *Phys. Rev. A* **92**, 013612 (2015).
- [3] L. Wang, M. Troyer, and X. Dai, *Phys. Rev. Lett.* **111**, 026802 (2013).
- [4] R. Wei and E. J. Mueller, *Phys. Rev. A* **92**, 013609 (2015).
- [5] T.-S. Zeng, C. Wang, and H. Zhai, *Phys. Rev. Lett.* **115**, 095302 (2015).
- [6] P. Marra, R. Citro, and C. Ortix, *Phys. Rev. B* **91**, 125411 (2015).
- [7] N. R. Cooper and A. M. Rey, *Phys. Rev. A* **92**, 021401 (2015).
- [8] D. J. Thouless, *Phys. Rev. B* **27**, 6083 (1983).
- [9] Q. Niu and D. J. Thouless, *J. Phys. A* **17**, 2453 (1984).
- [10] M. Switkes, C. M. Marcus, K. Campman, and A. C. Gossard, *Science* **283**, 1905 (1999).
- [11] M. D. Blumenthal, B. Kaestner, L. Li, S. Giblin, T. J. B. M. Janssen, M. Pepper, D. Anderson, G. Jones, and D. A. Ritchie, *Nat. Phys.* **3**, 343 (2007).
- [12] B. Kaestner, V. Kashcheyevs, S. Amakawa, M. D. Blumenthal, L. Li, T. J. B. M. Janssen, G. Hein, K. Pierz, T. Weimann, U. Siegner *et al.*, *Phys. Rev. B* **77**, 153301 (2008).
- [13] V. I. Talyanskii, J. M. Shilton, M. Pepper, C. G. Smith, C. J. B. Ford, E. H. Linfield, D. A. Ritchie, and G. A. C. Jones, *Phys. Rev. B* **56**, 15180 (1997).
- [14] M. Möttönen, J. J. Vartiainen, and J. P. Pekola, *Phys. Rev. Lett.* **100**, 177201 (2008).
- [15] S. Nakajima, T. Tomita, S. Taie, T. Ichinose, H. Ozawa, L. Wang, M. Troyer, and Y. Takahashi, *Nat. Phys.* **12**, 296 (2016).
- [16] M. Lohse, C. Schweizer, O. Zilberberg, M. Aidelsburger, and I. Bloch, *Nat. Phys.* **12**, 350 (2016).
- [17] E. Yaschenko, L. Fu, L. Resca, and R. Resta, *Phys. Rev. B* **58**, 1222 (1998).
- [18] R. Resta, *J. Phys. Condens. Matter* **12**, R107 (2000).
- [19] Y. Qian, M. Gong, and C. Zhang, *Phys. Rev. A* **84**, 013608 (2011).
- [20] D. J. Thouless, M. Kohmoto, M. P. Nightingale, and M. den Nijs, *Phys. Rev. Lett.* **49**, 405 (1982).
- [21] G. Jotzu, M. Messer, R. Desbuquois, M. Lebrat, T. Uehlinger, D. Greif, and T. Esslinger, *Nature (London)* **515**, 237 (2014).
- [22] L. Duca, T. Li, M. Reitter, I. Bloch, M. Schleier-Smith, and U. Schneider, *Science* **347**, 288 (2015).
- [23] M. Aidelsburger, M. Lohse, C. Schweizer, M. Atala, J. T. Barreiro, S. Nascimbène, N. R. Cooper, I. Bloch, and N. Goldman, *Nat. Phys.* **11**, 162 (2015).
- [24] S.-Q. Shen, *Topological Insulators: Dirac Equation in Condensed Matters* (Springer, New York, 2012), Vol. 174.
- [25] W. P. Su, J. R. Schrieffer, and A. J. Heeger, *Phys. Rev. Lett.* **42**, 1698 (1979).
- [26] M. J. Rice and E. J. Mele, *Phys. Rev. Lett.* **49**, 1455 (1982).
- [27] D. Xiao, M.-C. Chang, and Q. Niu, *Rev. Mod. Phys.* **82**, 1959 (2010).
- [28] M. Atala, M. Aidelsburger, J. T. Barreiro, D. Abanin, T. Kitagawa, E. Demler, and I. Bloch, *Nat. Phys.* **9**, 795 (2013).
- [29] K. Jiménez-García, L. J. LeBlanc, R. A. Williams, M. C. Beeler, A. R. Perry, and I. B. Spielman, *Phys. Rev. Lett.* **108**, 225303 (2012).
- [30] L. W. Cheuk, A. T. Sommer, Z. Hadzibabic, T. Yefsah, W. S. Bakr, and M. W. Zwierlein, *Phys. Rev. Lett.* **109**, 095302 (2012).
- [31] G. Juzeliūnas and I. B. Spielman, *New J. Phys.* **14**, 123022 (2012).
- [32] N. Lundblad, S. Ansari, Y. Guo, and E. Moan, *Phys. Rev. A* **90**, 053612 (2014).
- [33] The data presented in Fig. 2 contain a small correction from the known imperfect state rotation.
- [34] See Supplemental Material at <http://link.aps.org/supplemental/10.1103/PhysRevLett.116.200402> for simulations of classical pumps, Berry curvatures and geometric pumps at nonzero, and other experimental details.
- [35] A. Ramanathan, S. R. Muniz, K. C. Wright, R. P. Anderson, W. D. Phillips, K. Helmerson, and G. K. Campbell, *Rev. Sci. Instrum.* **83**, 083119 (2012).
- [36] The effective mass in the lattice can increase the period.
- [37] W. Bao, D. Jaksch, and P. A. Markowich, *J. Comput. Phys.* **187**, 318 (2003).
- [38] M. B. Dahan, E. Peik, J. Reichel, Y. Castin, and C. Salomon, *Phys. Rev. Lett.* **76**, 4508 (1996).
- [39] J. Ruostekoski, J. Javanainen, and G. V. Dunne, *Phys. Rev. A* **77**, 013603 (2008).
- [40] M. Z. Hasan and C. L. Kane, *Rev. Mod. Phys.* **82**, 3045 (2010).
- [41] S. Ganeshan, K. Sun, and S. D. Sarma, *Phys. Rev. Lett.* **110**, 180403 (2013).
- [42] A. J. Heeger, S. Kivelson, J. R. Schrieffer, and W. P. Su, *Rev. Mod. Phys.* **60**, 781 (1988).
- [43] S. Nadj-Perge, I. K. Drozdov, J. Li, H. Chen, S. Jeon, J. Seo, A. H. MacDonald, B. A. Bernevig, and A. Yazdani, *Science* **346**, 602 (2014).

Bibliography

- [1] Elbio Dagotto. Correlated electrons in high-temperature superconductors. *Rev. Mod. Phys.*, 66:763–840, Jul 1994.
- [2] Patrick A. Lee, Naoto Nagaosa, and Xiao-Gang Wen. Doping a mott insulator: Physics of high-temperature superconductivity. *Rev. Mod. Phys.*, 78:17–85, Jan 2006.
- [3] Horst L. Stormer. Nobel lecture: The fractional quantum hall effect. *Rev. Mod. Phys.*, 71:875–889, Jul 1999.
- [4] Ganpathy Murthy and R. Shankar. Hamiltonian theories of the fractional quantum hall effect. *Rev. Mod. Phys.*, 75:1101–1158, Oct 2003.
- [5] Ludovic Berthier and Giulio Biroli. Theoretical perspective on the glass transition and amorphous materials. *Rev. Mod. Phys.*, 83:587–645, Jun 2011.
- [6] D. J. Thouless, M. Kohmoto, M. P. Nightingale, and M. den Nijs. Quantized hall conductance in a two-dimensional periodic potential. *Phys. Rev. Lett.*, 49:405–408, Aug 1982.

- [7] Xiao-Liang Qi and Shou-Cheng Zhang. Topological insulators and superconductors. *Rev. Mod. Phys.*, 83:1057–1110, Oct 2011.
- [8] P. Grinfeld. *Introduction to Tensor Analysis and the Calculus of Moving Surfaces*. Springer, New York, 2014.
- [9] Marcel Franz and Laurens Molenkamp. *Contemporary Concepts of Condensed Matter Science: Topological Insulators*, volume 6. Elsevier Science, Burlington, 1 edition, 2013.
- [10] N.W. Ashcroft and N.D. Mermin. *Solid State Physics*. Saunders College, Philadelphia, 1976.
- [11] Michael Victor Berry. Quantal phase factors accompanying adiabatic changes. *Proceedings of the Royal Society of London. A. Mathematical and Physical Sciences*, 392(1802):45–57, 1984.
- [12] S Y Cheng, P Li, and G Tian. *A Mathematician and His Mathematical Work*. WORLD SCIENTIFIC, 1996.
- [13] L. J. Alty. The generalized gaussbonnetchern theorem. *Journal of Mathematical Physics*, 36(6):3094–3105, 1995.
- [14] S. Datta. *Electronic transport in mesoscopic systems*. Cambridge University Press, 1995.
- [15] Y. Aharonov and D. Bohm. Significance of electromagnetic potentials in quantum theory. *Phys. Rev.*, 115:485, 1959.
- [16] Douglas R. Hofstadter. Energy levels and wave functions of bloch electrons in rational and irrational magnetic fields. *Phys. Rev. B*, 14:2239–2249, Sep 1976.

- [17] M. C. Geisler, J. H. Smet, V. Umansky, K. von Klitzing, B. Naundorf, R. Ketzmerick, and H. Schweizer. Detection of a landau band-coupling-induced rearrangement of the hofstadter butterfly. *Phys. Rev. Lett.*, 92:256801, Jun 2004.
- [18] B. Hunt, J. D. Sanchez-Yamagishi, A. F. Young, M. Yankowitz, B. J. LeRoy, K. Watanabe, T. Taniguchi, P. Moon, M. Koshino, P. Jarillo-Herrero, and R. C. Ashoori. Massive Dirac Fermions and Hofstadter Butterfly in a van der Waals Heterostructure. *Science*, 340:1427, 2013.
- [19] Tsuneya Ando, Yukio Matsumoto, and Yasutada Uemura. Theory of hall effect in a two-dimensional electron system. *Journal of the Physical Society of Japan*, 39(2):279–288, 1975.
- [20] K. v. Klitzing, G. Dorda, and M. Pepper. New method for high-accuracy determination of the fine-structure constant based on quantized hall resistance. *Phys. Rev. Lett.*, 45:494–497, Aug 1980.
- [21] R. B. Laughlin. Quantized hall conductivity in two dimensions. *Phys. Rev. B*, 23:5632–5633, May 1981.
- [22] Mahito Kohmoto. Zero modes and the quantized hall conductance of the two-dimensional lattice in a magnetic field. *Phys. Rev. B*, 39:11943–11949, Jun 1989.
- [23] Bose. Plancks gesetz und lichtquantenhypothese. *Zeitschrift für Physik*, 26(1):178–181, Dec 1924.
- [24] M. H. Anderson, J. R. Ensher, M. R. Matthews, C. E. Wieman, and E. A. Cornell. Observation of bose-einstein condensation in a dilute atomic vapor. *Science*, 269(5221):198–201, 1995.

- [25] K. B. Davis, M. O. Mewes, M. R. Andrews, N. J. van Druten, D. S. Durfee, D. M. Kurn, and W. Ketterle. Bose-einstein condensation in a gas of sodium atoms. *Phys. Rev. Lett.*, 75:3969–3973, Nov 1995.
- [26] B. DeMarco and D. S. Jin. Onset of Fermi degeneracy in a trapped atomic gas. *Science*, 285(5434):1703–1706, 1999.
- [27] Andrew G. Truscott, Kevin E. Strecker, William I. McAlexander, Guthrie B. Partridge, and Randall G. Hulet. Observation of fermi pressure in a gas of trapped atoms. *Science*, 291(5513):2570–2572, 2001.
- [28] Markus Greiner, Immanuel Bloch, Olaf Mandel, Theodor W. Hänsch, and Tilman Esslinger. Exploring phase coherence in a 2d lattice of bose-einstein condensates. *Phys. Rev. Lett.*, 87:160405, Oct 2001.
- [29] C Becker, P Soltan-Panahi, J Kronjger, S Drscher, K Bongs, and K Sengstock. Ultracold quantum gases in triangular optical lattices. *New Journal of Physics*, 12(6):065025, jun 2010.
- [30] J. Struck, C. Olschlager, R. Le Targat, P. Soltan-Panahi, A. Eckardt, M. Lewenstein, P. Windpassinger, and K. Sengstock. Quantum simulation of frustrated classical magnetism in triangular optical lattices. *Science*, 333(6045):996999, 2011.
- [31] Leticia Tarruell, Daniel Greif, Thomas Uehlinger, Gregor Jotzu, and Tilman Esslinger. Creating, moving and merging dirac points with a fermi gas in a tunable honeycomb lattice. *Nature*, Mar 2012.
- [32] Guocai Liu, Shi-Liang Zhu, Shaojian Jiang, Fadi Sun, and W. M. Liu. Simulating and detecting the quantum spin hall effect in the kagome optical lattice. *Phys. Rev. A*, 82:053605, Nov 2010.

- [33] Matthew P. A. Fisher, Peter B. Weichman, G. Grinstein, and Daniel S. Fisher. Boson localization and the superfluid-insulator transition. *Phys. Rev. B*, 40:546–570, Jul 1989.
- [34] Markus Greiner, Olaf Mandel, Tilman Esslinger, Theodor W. Hnsch, and Immanuel Bloch. Quantum phase transition from a superfluid to a mott insulator in a gas of ultracold atoms. *Nature*, 415:39–44, Jan 2002.
- [35] J. Mun. *Bose-Einstein Condensates in Optical Lattices: The Superfluid to Mott Insulator Phase Transition*. PhD thesis, Massachusetts Institute of Technology, 2008.
- [36] Ugo Fano. Sullo spettro di assorbimento dei gas nobili presso il limite dello spettro d'arco. *Il Nuovo Cimento (1924-1942)*, 12(3):154–161, Mar 1935.
- [37] U. Fano. Effects of configuration interaction on intensities and phase shifts. *Phys. Rev.*, 124:1866–1878, Dec 1961.
- [38] Herman Feshbach. Unified theory of nuclear reactions. *Annals of Physics*, 5(4):357 – 390, 1958.
- [39] Herman Feshbach. A unified theory of nuclear reactions. ii. *Annals of Physics*, 19(2):287 – 313, 1962.
- [40] C. Chin, R. Grimm, P. Julienne, and E. Tiesinga. Feshbach resonances in ultracold gases. *Rev. Mod. Phys.*, 82:1225–1286, 2010.
- [41] S. L. Cornish, N. R. Claussen, J. L. Roberts, E. A. Cornell, and C. E. Wieman. Stable Rb-85 Bose-Einstein condensates with widely tunable interactions. *Phys. Rev. Lett.*, 85(9):1795–1798, 2000.

- [42] S. Jochim, M. Bartenstein, A. Altmeyer, G. Hendl, S. Riedl, C. Chin, J. Hecker Denschlag, and R. Grimm. Bose-Einstein condensation of molecules. *Science*, 302(5653):2101–2103, 2003.
- [43] M. W. Zwierlein, C. A. Stan, C. H. Schunck, S. M. F. Raupach, S. Gupta, Z. Hadzibabic, and W. Ketterle. Observation of Bose-Einstein condensation of molecules. *Phys. Rev. Lett.*, 91:250401, 2003.
- [44] C. A. Regal, M. Greiner, and D. S. Jin. Observation of resonance condensation of fermionic atom pairs. *Phys. Rev. Lett.*, 92(4), 2004.
- [45] M. Greiner, C. A. Regal, and D. S. Jin. Emergence of a molecular Bose-Einstein condensate from a Fermi gas. *Nature*, 426(6966):537–540, 2003.
- [46] T. Bourdel, L. Khaykovich, J. Cubizolles, J. Zhang, F. Chevy, M. Teichmann, L. Tarruell, S. J. J. M. F. Kokkelmans, and C. Salomon. Experimental Study of the BEC-BCS Crossover Region in Lithium 6. *Phys. Rev. Lett.*, 93:050401, 2004.
- [47] N.R. Cooper. Rapidly rotating atomic gases. *Advances in Physics*, 57(6):539–616, 2008.
- [48] G. Juzeliūnas, J. Ruseckas, P. Öhberg, and M. Fleischhauer. Light-induced effective magnetic fields for ultracold atoms in planar geometries. *Phys. Rev. A*, 73:025602, Feb 2006.
- [49] Y. J. Lin, R. L. Compton, K. Jimenez-Garcia, J. V. Porto, and I. B. Spielman. Synthetic magnetic fields for ultracold neutral atoms. *Nature*, 462:628–632, 2009.
- [50] Y-J. Lin, K. Jiménez-García, and I. B. Spielman. Spin-orbit-coupled Bose-Einstein condensates. *Nature*, 471:83–86, 2011.

- [51] P. Zoller D. Jaksch. Creation of effective magnetic fields in optical lattices: the hofstadter butterfly for cold neutral atoms. *New Journal of Physics*, 5(1):56, 2003.
- [52] Erich J. Mueller. Artificial electromagnetism for neutral atoms: Escher staircase and Laughlin liquids. *Phys. Rev. A*, 70:041603, Oct 2004.
- [53] Anders S. Sørensen, Eugene Demler, and Mikhail D. Lukin. Fractional quantum hall states of atoms in optical lattices. *Phys. Rev. Lett.*, 94:086803, Mar 2005.
- [54] M. Aidelsburger, M. Atala, M. Lohse, J. T. Barreiro, B. Paredes, and I. Bloch. Realization of the Hofstadter Hamiltonian with ultracold atoms in optical lattices. *Phys. Rev. Lett.*, 111(18):185301–, October 2013.
- [55] Hirokazu Miyake, Georgios A. Siviloglou, Colin J. Kennedy, William Cody Burton, and Wolfgang Ketterle. Realizing the Harper Hamiltonian with laser-assisted tunneling in optical lattices. *Phys. Rev. Lett.*, 111:185302, Oct 2013.
- [56] Gregor Jotzu, Michael Messer, Remi Desbuquois, Martin Lebrat, Thomas Uehlinger, Daniel Greif, and Tilman Esslinger. Experimental realization of the topological Haldane model with ultracold fermions. *Nature*, 515(7526):237–240, Nov 2014.
- [57] M. Aidelsburger, M. Lohse, C. Schweizer, M. Atala, J. T. Barreiro, S. Nascimbène, N. R. Cooper, I. Bloch, and N. Goldman. Measuring the Chern number of Hofstadter bands with ultracold bosonic atoms. *Nature Physics*, 11(2):162–166, December 2014.
- [58] M. Mancini, G. Pagano, G. Cappellini, L. Livi, M. Rider, J. Catani, C. Sias, P. Zoller, M. Inguscio, M. Dalmonte, and L. Fallani. Observation of chi-

- ral edge states with neutral fermions in synthetic hall ribbons. *Science*, 349(6255):1510–, Sep 2015.
- [59] Fangzhao Alex An, Eric J. Meier, and Bryce Gadway. Direct observation of chiral currents and magnetic reflection in atomic flux lattices. *Science Advances*, 3(4), 2017.
- [60] Leonardo Mazza, Alejandro Bermudez, Nathan Goldman, Matteo Rizzi, Miguel Angel Martin-Delgado, and Maciej Lewenstein. An optical-lattice-based quantum simulator for relativistic field theories and topological insulators. *New Journal of Physics*, 14(1):015007, jan 2012.
- [61] A. Celi, P. Massignan, J. Ruseckas, N. Goldman, I.B. Spielman, G. Juzeliunas, and M. Lewenstein. Synthetic gauge fields in synthetic dimensions. *Phys. Rev. Lett.*, 112(4):043001–, Jan 2014.
- [62] B. K. Stuhl, H.-I. Lu, L. M. Aycock, D. Genkina, and I. B. Spielman. Visualizing edge states with an atomic bose gas in the quantum hall regime. *Science*, 349(6255):1514–, Sep 2015.
- [63] Eric J. Meier, Fangzhao Alex An, and Bryce Gadway. Atom-optics simulator of lattice transport phenomena. *Phys. Rev. A*, 93:051602, May 2016.
- [64] David Jeffery Griffiths. *Introduction to Quantum Mechanics*. Pearson Prentice Hall, 2005.
- [65] L. H. Thomas. The motion of the spinning electron. *Nature*, 117(514), Apr 1926.
- [66] Daniel Adam Steck. Rubidium 87 d line data. Available online, <http://steck.us/alkalidata>, April 2018. revision 2.1.5.

- [67] T. G. Tiecke. Properties of potassium. Available online, <http://www.tobiastiecke.nl/archive/PotassiumProperties.pdf>, May 2011. v1.02.
- [68] E. Arimondo, M. Inguscio, and P. Violino. Experimental determinations of the hyperfine structure in the alkali atoms. *Rev. Mod. Phys.*, 49:31–75, Jan 1977.
- [69] G. Breit and I. I. Rabi. Measurement of nuclear spin. *Phys. Rev.*, 38:2082–2083, Dec 1931.
- [70] A. M. Fox. *Quantum optics: an introduction*. Cambridge University Press, Oxford, UK, 2002.
- [71] H.J. Metcalf and P. van der Straten. *Laser Cooling and Trapping*. Graduate Texts in Contemporary Physics. Springer New York, 1999.
- [72] Nicola Marzari, Arash A. Mostofi, Jonathan R. Yates, Ivo Souza, and David Vanderbilt. Maximally localized wannier functions: Theory and applications. *Rev. Mod. Phys.*, 84:1419–1475, Oct 2012.
- [73] Karina Jimenez-Garcia. *Artificial Gauge Fields for Ultracold Neutral Atoms*. PhD thesis, Joint Quantum Institute, National Institute of Standards and Technology, and the University of Maryland, 2012.
- [74] K. Jiménez-García, L. J. LeBlanc, R. A. Williams, M. C. Beeler, A. R. Perry, and I. B. Spielman. Peierls substitution in an engineered lattice potential. *Phys. Rev. Lett.*, 108:225303, May 2012.
- [75] Daniel Adam Steck. Quantum and atom optics. Available online at <http://steck.us/teaching>, January 2015. revision 0.12.2.

- [76] J. R. Ensher, D. S. Jin, M. R. Matthews, C. E. Wieman, and E. A. Cornell. Bose-einstein condensation in a dilute gas: Measurement of energy and ground-state occupation. *Phys. Rev. Lett.*, 77:4984–4987, Dec 1996.
- [77] C.J. Pethick and H. Smith. *Bose-Einstein Condensation of Dilute Gases*. Oxford University Press, Oxford, UK, 2005.
- [78] M. Egorov, B. Opanchuk, P. Drummond, B. V. Hall, P. Hannaford, and A. I. Sidorov. Measurement of *s*-wave scattering lengths in a two-component bose-einstein condensate. *Phys. Rev. A*, 87:053614, May 2013.
- [79] W. Ketterle and M. W. Zwierlein. Making, probing and understanding ultracold Fermi gases. In *Ultracold Fermi Gases, Proceedings of the International School of Physics ‘Enrico Fermi’, Course CLXIV*, Varenna, 20-30 June 2006.
- [80] K. M. O’Hara, S. L. Hemmer, M. E. Gehm, S. R. Granade, and J. E. Thomas. Observation of a strongly interacting degenerate Fermi gas of atoms. *Science*, 298(5601):2179–2182, 2002.
- [81] S. Jochim, M. Bartenstein, G. Hendl, J. Hecker Denschlag, R. Grimm, A. Mosk, and M. Weidemüller. Magnetic field control of elastic scattering in a cold gas of fermionic lithium atoms. *Phys. Rev. Lett.*, 89:273202, Dec 2002.
- [82] K. Dieckmann, C. A. Stan, S. Gupta, Z. Hadzibabic, C. H. Schunck, and W. Ketterle. Decay of an ultracold fermionic lithium gas near a feshbach resonance. *Phys. Rev. Lett.*, 89:203201, Oct 2002.
- [83] T. Loftus, C. A. Regal, C. Ticknor, J. L. Bohn, and D. S. Jin. Resonant control of elastic collisions in an optically trapped fermi gas of atoms. *Phys. Rev. Lett.*, 88:173201, Apr 2002.

- [84] C. A. Regal, C. Ticknor, J. L. Bohn, and D. S. Jin. Tuning p -wave interactions in an ultracold fermi gas of atoms. *Phys. Rev. Lett.*, 90:053201, Feb 2003.
- [85] M. Bartenstein, A. Altmeyer, S. Riedl, S. Jochim, C. Chin, J. Hecker Denschlag, and R. Grimm. Collective excitations of a degenerate gas at the bcs-bcs crossover. *Phys. Rev. Lett.*, 92:203201, 2004.
- [86] M. W. Zwierlein, C. A. Stan, C. H. Schunck, S. M. F. Raupach, A. J. Kerman, and W. Ketterle. Condensation of pairs of Fermionic atoms near a Feshbach resonance. *Phys. Rev. Lett.*, 92:120403, 2004.
- [87] Y.-J. Lin, A. R. Perry, R. L. Compton, I. B. Spielman, and J. V. Porto. Rapid production of ^{87}Rb bose-einstein condensates in a combined magnetic and optical potential. *Phys. Rev. A*, 79:063631, Jun 2009.
- [88] Lauren M. Aycock. *Topological excitations in a Bose gas and sexual harassment reported by undergraduate physicists*. PhD thesis, Cornell University, Ithaca, NY, 1 2017.
- [89] Lauren M. Ayccock, Hilary M. Hurst, Dmitry K. Efimkin, Dina Genkina, Hsin-I Lu, Victor M. Galitski, and I. B. Spielman. Brownian motion of solitons in a bose-einstein condensate. *Proceedings of the National Academy of Sciences*, 114(10):2503–2508, 2017.
- [90] Christopher J. Foot. *Atomic Physics*. Oxford University Press, Cambridge, UK, 2006.
- [91] E. A. Donley, T. P. Heavner, F. Levi, M. O. Tataw, and S. R. Jefferts. Double-pass acousto-optic modulator system. *Review of Scientific Instruments*, 76(6):063112, 2005.

- [92] Ryan Price. *Phase transitions in engineered ultracold quantum systems*. PhD thesis, University of Maryland College Park, Digital Repository at the University of Maryland, 6 2016.
- [93] E. Majorana. Atomi orientati in campo magnetico variabile. *Nuovo Cimento*, 9:43–50, Feb 1932.
- [94] C. V. Sukumar and D. M. Brink. Spin-flip transitions in a magnetic trap. *Phys. Rev. A*, 56:2451–2454, Sep 1997.
- [95] D. M. Brink and C. V. Sukumar. Majorana spin-flip transitions in a magnetic trap. *Phys. Rev. A*, 74:035401, Sep 2006.
- [96] J. Catani, P. Maioli, L. De Sarlo, F. Minardi, and M. Inguscio. Intense slow beams of bosonic potassium isotopes. *Phys. Rev. A*, 73:033415, Mar 2006.
- [97] Thomas Uehlinger. A 2-d magneto-optical trap as a high flux source of cold potassium atoms. Master’s thesis, Swiss Federal Institute of Technology Zurich, Zurich, 5 2008.
- [98] E. Pedrozo-Peafiel, F. Vivanco, P. Castilho, R. R. Paiva, K. M. Farias, and V. S. Bagnato. Direct comparison between a two-dimensional magneto-optical trap and a zeeman slower as sources of cold sodium atoms. *Laser Physics Letters*, 13:065501, May 2016.
- [99] K. J. Weatherill, J. D. Pritchard, P. F. Griffin, U. Dammalapati, C. S. Adams, and E. Riis. A versatile and reliably reusable ultrahigh vacuum viewport. *Review of Scientific Instruments*, 80(2):026105, 2009.
- [100] D. Rio Fernandes, F. Sievers, N. Kretzschmar, S. Wu, C Salomon, and F. Chevy. Sub-doppler laser cooling of fermionic 40k atoms in three-dimensional gray optical molasses. *Europhysics Letters*, 100:63001, Dec 2012.

- [101] D. Genkina, L. M. Aycock, B. K. Stuhl, H-I Lu, R. A. Williams, and I. B. Spielman. Feshbach enhanced s-wave scattering of fermions: direct observation with optimized absorption imaging. *New Journal of Physics*, 18:013001, Dec 2015.
- [102] Lindsey J. LeBlanc. *Exploring many-body physics with ultracold atoms*. PhD thesis, University of Toronto, 2011.
- [103] E. Tiesinga, B. J. Verhaar, and H. T. C. Stoof. Threshold and resonance phenomena in ultracold ground-state collisions. *Phys. Rev. A*, 47(5, B):4114–4122, 1993.
- [104] M. Lysebo and L. Veseth. *Ab initio* calculation of Feshbach resonances in cold atomic collisions: *s*- and *p*-wave Feshbach resonances in ${}^6\text{Li}_2$. *Phys. Rev. A*, 79:062704, 2009.
- [105] B. Gao. Analytic description of atomic interaction at ultracold temperatures. II. Scattering around a magnetic Feshbach resonance. *Phys. Rev. A*, 84:022706, 2011.
- [106] S. Inouye, M. R. Andrews, J. Stenger, H. J. Miesner, D. M. Stamper-Kurn, and W. Ketterle. Observation of Feshbach resonances in a Bose-Einstein condensate. *Nature*, 392(6672):151–154, 1998.
- [107] C. A. Regal and D. S. Jin. Measurement of positive and negative scattering lengths in a Fermi gas of atoms. *Phys. Rev. Lett.*, 90:230404, 2003.
- [108] C. Monroe, E. Cornell, C. Sackett, C. Myatt, and C. Wieman. Measurement of Cs-Cs elastic scattering at $T = 30 \mu\text{K}$. *Phys. Rev. Lett.*, 70:414–417, 1993.

- [109] B. DeMarco, J. L. Bohn, J. P. Burke, M. Holland, and D. S. Jin. Measurement of p -wave threshold law using evaporatively cooled fermionic atoms. *Phys. Rev. Lett.*, 82:4208–4211, 1999.
- [110] S. Wu, Y.-J. Wang, Q. Diot, and M. Prentiss. Splitting matter waves using an optimized standing-wave light-pulse sequence. *Phys. Rev. A*, 71:043602, 2005.
- [111] M. Edwards, B. Benton, J. Heward, and C. W. Clark. Momentum-space engineering of gaseous bose-einstein condensates. *Phys. Rev. A*, 82:063613, 2010.
- [112] M Hafezi, S Mittal, J Fan, A Migdall, and J M Taylor. Imaging topological edge states in silicon photonics. *Nat. Photon.*, 7(12):1001–1005, October 2013.
- [113] Yakir Aharonov and Ady Stern. Origin of the geometric forces accompanying berry’s geometric potentials. *Phys. Rev. Lett.*, 69(25):3593–3597, 1992.
- [114] Dario Hügel and Belén Paredes. Chiral ladders and the edges of quantum Hall insulators. *Phys. Rev. A*, 89(2):023619, 2014.
- [115] P G Harper. Single band motion of conduction electrons in a uniform magnetic field. *Proceedings of the Physical Society. Section A*, 68(10):874, 1955.
- [116] Gretchen K. Campbell, Jongchul Mun, Micah Boyd, Erik W. Streed, Wolfgang Ketterle, and David E. Pritchard. Parametric amplification of scattered atom pairs. *Phys. Rev. Lett.*, 96:020406, Jan 2006.
- [117] Samuel Mugel, Alexandre Dauphin, Pietro Massignan, Leticia Tarruell, Maciej Lewenstein, Carlos Lobo, and Alessio Celi. Measuring chern numbers in hofstadter strips. *SciPost*, 2017.
- [118] Zhoushen Huang and Daniel P. Arovas. Entanglement spectrum and wannier center flow of the hofstadter problem. *Phys. Rev. B*, 86:245109, Dec 2012.

- [119] Xiong-Jun Liu, K. T. Law, T. K. Ng, and Patrick A. Lee. Detecting topological phases in cold atoms. *Phys. Rev. Lett.*, 111:120402, Sep 2013.
- [120] Lei Wang, Alexey A. Soluyanov, and Matthias Troyer. Proposal for direct measurement of topological invariants in optical lattices. *Phys. Rev. Lett.*, 110(16):166802–, Apr 2013.
- [121] Dan-Wei Zhang and Shuai Cao. Measuring the spin chern number in time-reversal-invariant hofstadter optical lattices. *Physics Letters A*, 380(42):3541–3545, Oct 2016.
- [122] A. H. MacDonald. Landau-level subband structure of electrons on a square lattice. *Phys. Rev. B*, 28:6713–6717, Dec 1983.
- [123] H. Kunz. Quantized currents and topological invariants for electrons in incommensurate potentials. *Phys. Rev. Lett.*, 57:1095–1097, Sep 1986.
- [124] M. Eric Tai, Alexander Lukin, Matthew Rispoli, Robert Schittko, Tim Menke, Dan Borgnia, Philipp M. Preiss, Fabian Grusdt, Adam M. Kaufman, and Markus Greiner. Microscopy of the interacting harperhofstadter model in the two-body limit. *Nature*, 546:519–, June 2017.
- [125] S. Greschner, M. Piraud, F. Heidrich-Meisner, I. P. McCulloch, U. Schollwöck, and T. Vekua. Spontaneous increase of magnetic flux and chiral-current reversal in bosonic ladders: Swimming against the tide. *Phys. Rev. Lett.*, 115:190402, Nov 2015.
- [126] S. Greschner, M. Piraud, F. Heidrich-Meisner, I. P. McCulloch, U. Schollwöck, and T. Vekua. Symmetry-broken states in a system of interacting bosons on a two-leg ladder with a uniform abelian gauge field. *Phys. Rev. A*, 94:063628, Dec 2016.

- [127] Marcello Calvanese Strinati, Eyal Cornfeld, Davide Rossini, Simone Barbarino, Marcello Dalmonte, Rosario Fazio, Eran Sela, and Leonardo Mazza. Laughlin-like states in bosonic and fermionic atomic synthetic ladders. *Phys. Rev. X*, 7:021033, Jun 2017.
- [128] Siddharth A. Parameswaran, Rahul Roy, and Shivaji L. Sondhi. Fractional quantum hall physics in topological flat bands. *Comptes Rendus Physique*, 14(9):816–839, 2013.